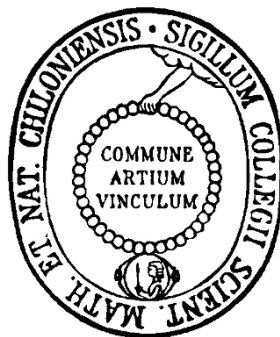


Formation and evolution of a Proterozoic magmatic arc – the Ongole domain of the Eastern Ghats Belt, India.

Dissertation
zur Erlangung des Doktorgrades
der Mathematisch-Naturwissenschaftlichen Fakultät
der Christian-Albrechts-Universität
zu Kiel

vorgelegt von
Tapabrato Sarkar

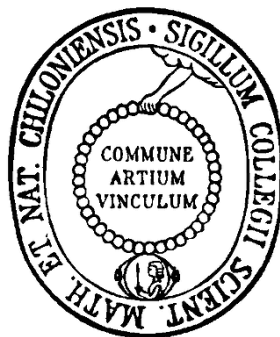


Kiel 2014

Formation and evolution of a Proterozoic magmatic arc – the Ongole domain of the Eastern Ghats Belt, India.

Dissertation
zur Erlangung des Doktorgrades
der Mathematisch-Naturwissenschaftlichen Fakultät
der Christian-Albrechts-Universität
zu Kiel

vorgelegt von
Tapabrato Sarkar



Kiel 2014

Referent: Prof. Dr. Volker Schenk

Korreferentin: Prof. Dr. Astrid Holzheid

Tag der mündlichen Prüfung: 26th May, 2014

Zum Druk genehmigt

Der Dekan

Vorwort

Die vorliegende Arbeit wurde als monographische Dissertation verfasst, jedoch ist in den drei Kapiteln jeweils eine eigenständige Einleitung und Diskussion vorhanden. Für die einzelnen Kapitel wurde bewusst ein unabhängiger Aufbau gewählt, da diese losgelöst voneinander in internationalen Fachzeitschriften publiziert werden sollen. Daher finden sich in jedem Kapitel eine Einleitung, Diskussion und Literaturverzeichnis wieder, auch die Länge und etwaige Formatierungen sind in Hinblick auf die jeweiligen Vorgaben der Fachzeitschriften bewusst gewählt. Der Leser sei darauf hingewiesen, dass es durch den gewählten Aufbau zu Wiederholungen kommen kann und möge diesen Sachverhalt bei der Lektüre berücksichtigen.

Kiel, April 2014
Tapabrato Sarkar

Table of Contents

Zusammenfassung	xi
Abstract	xv
1. Introduction	1
1.1. Importance of magmatic arcs	1
1.2. The Eastern Ghats Belt – A Proterozoic high-grade terrain	3
1.3. The Ongole domain	5
1.4. Study approach and analytical techniques	6
1.5. Outline of this thesis	7
References	9
2. Petrology and pressure-temperature evolution of the granulite-facies rocks of the Ongole domain	13
Abstract	13
2.1. Introduction	14
2.2. Geological background	16
2.3. Field relationships	20
2.4. Petrography	23
2.4.1. Metapelitic granulites	23
2.4.2. Charnoenderbitic gneisses	30
2.4.3. Mafic granulites	31
2.5. Analytical techniques	33
2.6. Mineral chemistry	34
2.6.1. Metapelitic granulites	34
2.6.2. Charnoenderbitic gneisses	44
2.6.3. Mafic granulites	46

2.7. Thermobarometry	48
2.7.1. Feldspar thermometer.....	48
2.7.2. Garnet-orthopyroxene thermometer	51
2.7.3. Al solubility in orthopyroxene thermometer.....	51
2.7.4. Garnet-orthopyroxene-plagioclase-quartz barometer	53
2.7.5. Garnet – Al ₂ SiO ₅ – quartz – plagioclase (GASP) barometer.....	53
2.8. Thermodynamic modeling – P-T pseudosection	54
2.8.1. Grt-Sil-Spl-Qz granulite (TK8-1).....	55
2.8.2. Grt-Sil-Spl-Qz granulite (TK7).....	56
2.9. Discussion and conclusions	58
2.9.1. UHT stage of metamorphism.....	58
2.9.2. Higher pressure - lower temperature stage of metamorphism.....	60
2.9.3. P-T trajectories and geodynamic interpretation.....	61
2.10 Acknowledgements	64
References.....	65
3. Two-stage granulite formation in the Ongole domain: LA-ICP-MS zircon dating and texturally controlled in-situ monazite dating	75
Abstract	75
3.1. Introduction.....	76
3.2. Geological background.....	78
3.3. Petrography of the investigated lithologies.....	81
3.3.1. Charnockite (TK39-4) and enderbite (TK4B2).....	81
3.3.2. Metapelites (TK8-1, TK8C1, TK35-6, TK73-2, TK73-4).....	82
3.4. LA-ICP-MS zircon dating of metapelites.....	83
3.4.1. Analytical techniques	84
3.4.2. TK8C1	85
3.4.3. TK35-6.....	85
3.4.4. TK73-4.....	88
3.4.5. TK22.....	89
3.4.6. TK82-2.....	89

3.4.7. TK46-3.....	91
3.4.8. Zircon data results.....	92
3.5. Th-U-total Pb dating of monazite.....	93
3.5.1. Analytical techniques	94
3.5.2. Monazite texture, chemistry and age	95
3.5.3. Monazite data results.....	106
3.6. Discussion and conclusions	111
3.6.1. Correlation of zircon and monazite age data	111
3.6.2. Possible interpretation of the post 1.54 Ga events	115
3.6.3. Geodynamic interpretation	116
3.7 Acknowledgements	118
References.....	118

4. Formation and evolution of a Proterozoic magmatic arc: geochemical and geochronological constraints from the meta-igneous rocks of the Ongole domain

Abstract	125
4.1. Introduction.....	126
4.2. Geological setting	128
4.3. Field relationship and petrography	130
4.4. Analytical techniques	132
4.4.1. Geochemistry	132
4.4.2. U-Pb zircon geochronology by LA-ICP-MS	133
4.5. Geochemistry	134
4.5.1. Alteration and element mobility	134
4.5.2. Rock classification	135
4.5.3. Major and trace element composition	137
4.6. U-Pb zircon geochronology	143
4.6.1. TK4B2	144
4.6.2. TK21	144
4.6.3. TK28-1	145

4.6.4. TK39-4	147
4.6.5. TK39-3	148
4.6.6. TK66-1	149
4.7. Discussion	152
4.7.1. Timing of formation and metamorphism of the Ongole domain	152
4.7.2. Petrogenesis of the mafic granulites	157
4.7.3. Petrogenesis of the charnoenderbites	160
4.7.4. Geodynamic setting	162
4.8. Conclusions	165
4.9. Acknowledgements	166
References	166
List of Figures	172
List of Tables	174
Appendix A	175
Appendix B	181
Appendix C	190
Publications related to this thesis	201
Acknowledgements	203
Curriculum vitae	207

Zusammenfassung

Im Eastern Ghats Belt (EGB), einem proterozoischen Gebirgsgürtel entlang der indischen Ostküste, befinden sich mehrere polymetamorphe, granulitfazielle Krustenblöcke. Einer dieser Blöcke ist die Ongole Provinz im Südwesten des EGB.

Detaillierte frühere Arbeiten konzentrierten sich hauptsächlich auf den nördlichen Teil des EGB und zeigen deutliche Unterschiede in den Entstehungsgeschichten der einzelnen Blöcke des EGB. Jedoch wurde bislang bei keiner dieser Untersuchungen der südliche Teil des EGB, insbesondere die Ongole Provinz, genauer bearbeitet.

Ziel dieser Arbeit ist es deshalb, dieses Informationsdefizit durch petrologische, geochronologische und geochemische Untersuchungen der granulitfaziellen Gesteine der Ongole Provinz zu beheben, um ein besseres Verständnis der Entstehung und Entwicklung der Ongole Provinz zu erhalten, sodass auch die Rolle dieser Provinz in der präkambrischen Krustenbildung des indischen Kontinents verstanden wird.

Die Ongole Provinz besteht hauptsächlich aus Abfolgen von Charnoenderbiten, in welche pelitische und mafische Granulite eingeschaltet sind. Geochemische Untersuchungen sowohl der Haupt- und Spurenelemente, als auch der Seltenen Erdelemente der metamagmatischen Gesteine, deuten auf eine Bildung in einem magmatischen Inselbogen nahe eines Kontinents hin. Der magmatische Ursprung der Gesteine kann auch durch die oszillierende Zonierung der großen, euhedralen bis subhedralen Zirkone in den Charnoenderbiten erkannt werden. Das an den Zirkonen gemessene paläoproterozoische Alter von 1750 bis 1700 Ma entspricht der Zeit der Magmenbildung und dementsprechend der Entstehung des magmatischen Inselbogens.

Aus der Petrographie der verschiedenen Gesteinstypen kann auf zwei Generationen des metamorphen Mineralwachstums geschlossen werden. Sowohl die Vergesellschaftung von Spinell und Quarz, als auch die Ergebnisse von Feldspat-Thermometrie, Modellierung von Pseudosections und die aus konventioneller Thermobarometrie abgeleiteten Druck- und Temperaturbedingungen, für die erste

Phase des Mineralwachstums sprechen für eine Ultrahochtemperatur-Metamorphose mit Temperaturen $> 950^{\circ}\text{C}$ und Drücken von 6.5–7 kbar. Die Abwesenheit von Cordierit in retrograden Mineralparagenesen weist auf einen Prozess isobaren Abkühlens hin und impliziert einen nahezu isobaren Kurvenverlauf von Aufheizung und Abkühlung. Sowohl die Ergebnisse der Thermobarometrie, als auch die P-T-Pseudosections der petrographisch identifizierten zweiten Generation von Mineralen (besonders Granat), deuten auf höhere Drücke und niedrigere Temperaturen (ca. 780°C und 9.5 kbar) während eines zweiten metamorphen Ereignisses hin. Die im Spätstadium des zweiten Ereignisses entstandenen Niederdruck-Minerale zeigen eine nahezu isotherme Dekompression an, die von einer isobaren Abkühlung gefolgt war. Die petrologischen Beobachtungen alleine reichen aber nicht aus, um festzustellen, ob beide Ereignisse Teile eines einzigen oder zweier verschiedener orogener Zyklen sind.

Altersbestimmungen an metamorphen Anwachsflächen um detritische Zirkonerne, sowie metamorphen Zirkonen aus Metapeliten, zusammen mit den unzonierten Bereichen von metamorph überprägten magmatischen Zirkon-Kernen aus den Charnoenderbitten, ergeben ein konkordantes Alter von 1630–1600 Ma. Dieses entspricht etwa der Dauer einer hochgradigen Metamorphose. Im Gegensatz dazu ergeben texturell kontrollierte, in-situ Mikrosonden-Datierungen an zwei chemisch und texturell identifizierten Monazit-Generationen in Metapeliten zwei metamorphe Ereignisse, die 60-80 Ma auseinander liegen. Dieses Ergebnis wiederum ergänzt die petrologischen Untersuchungen. Einschlüsse von Monazit in porphyroblastischen Granaten, sowie die Kerne einiger Monazite in der Matrix sind auf 1610 Ma datiert, welches dem Alter der konkordanten Zirkone entspricht und dem Ultrahochtemperaturereignis zugeordnet wird. Die Monazitkörner in der Matrix, die in der zweiten Generation von Granat und in späten Symplektiten eingeschlossen vorkommen, sind stark rekristallisiert und weisen ein Alter von 1540 Ma auf. Sie werden dem zweiten Metamorphosereignis bei höheren Drücken und niedrigeren Temperaturen zugeordnet. An den Monaziten aus den Charnoenderbitten lässt sich zwar das zweite metamorphe Ereignis bestätigen,

jedoch sind kaum Alter aus dem frühen Ultrahochtemperatur-Ereignis erhalten. Sie geben aber Hinweise auf noch spätere Überprägungen zwischen ca. 1450 und 1360 Ma und schwächere Ereignisse bei ca. 730 Ma und 510 Ma.

Insgesamt ergeben die kombinierten petrologischen, geochronologischen und geochemischen Daten einen bis dato unerreichten, detaillierten Einblick in die tektono-metamorphe Entstehungsgeschichte des Ongole Blocks. Dieser Block wurde während des Paläoproterozoikums als magmatischer Inselbogen vor dem indischen Kontinent gebildet. Anschließend wurden die Gesteine, durch konstante magmatische Aktivität (*magmatic underplating*) und dem daraus resultierenden Wachstum des Inselbogens, metamorphen Ultrahochtemperatur-Bedingungen ausgesetzt. 60-80 Ma später, zur Zeit des frühen Mesoproterozoikums, erfolgte die Akkretion des Inselbogens an den indischen Kraton, was zu einer Verdickung der kontinentalen Kruste und daraus resultierend dem zweiten metamorphen Ereignis führte. Diese zweigeteilte Entwicklungsgeschichte der Ongole Provinz stimmt mit der generell zu erwartenden Entwicklung magmatischer Inselbögen überein. Im Kontext der Bildung von Superkontinenten kann man die Entstehung und Entwicklung der Ongole Provinz und ihre subduktionsgesteuerte Akkretion mit dem Wachstum von Columbia vor 1.8 bis 1.2 Ma zuordnen. Dagegen ist die Akkretion an den indischen Kraton im globalen Kontext bislang mit keiner anderen Superkontinentbildung zu korrelieren.

Abstract

The Eastern Ghats Belt (EGB), a well known Proterozoic mobile belt along the east coast of Peninsular India, is an assembly of several polymetamorphosed granulite terrains. The Ongole domain is one such terrain in the SW part of the EGB. Detailed studies were mostly concentrated in the northern parts of the EGB, revealing that the different terrains have distinct and apparently unrelated evolutionary histories. However, such comprehensive geological studies are lacking for the southern part of the EGB, especially the Ongole domain. This thesis aims to fulfill this deficit of knowledge through petrological, geochronological and geochemical investigations of granulite-facies rocks from the Ongole domain for a holistic understanding of the formation and evolution of this Proterozoic domain and its connection to Precambrian crustal assemblies involving India.

The Ongole domain is dominated by a suite of charnoenderbites with enclaves of pelitic and mafic granulites. The major, trace and rare earth element geochemistry of the meta-igneous rocks indicate their formation in a magmatic arc setting near a continent. The large, euhedral to subhedral zircon grains from the charnoenderbites showing fine-scale oscillatory zoning also implies a magmatic origin. The Palaeoproterozoic age of ca. 1750-1700 Ma obtained from them indicate the time of magma emplacement and arc formation.

Detailed petrographic and mineral chemical studies of the different rock types reveal at least two generations of mineral growth. The association of spinel and quartz, P-T conditions obtained from conventional thermobarometry, feldspar thermometry and pseudosection modeling suggests that the rocks underwent ultrahigh-temperature (UHT) ($T > 950^{\circ}\text{C}$) peak metamorphism at $P = 6.5\text{-}7$ kbar. The absence of cordierite in retrograde mineral assemblages points to isobaric cooling, giving rise to a near-isobaric heating-cooling trajectory. P-T pseudosections and thermobarometry from the second, chemically distinct generation of minerals (especially garnet) indicate their formation at a higher pressure but lower

temperature (ca. 780°C, 9.5 kbar) during a second metamorphic event. The late-stage low-pressure mineral assemblage including andalusite points to a near-isothermal decompression from the peak pressures followed by isobaric cooling, along a clockwise P-T path. However, petrology alone could not distinguish if the two events are part of the same or different orogenic cycles.

Metamorphic overgrowths over detrital zircon cores and metamorphic zircons from the metapelites, together with unzoned, metamorphic overgrowths surrounding the oscillatory-zoned magmatic zircon cores from some younger charnoenderbites show concordant ages of 1630-1600 Ma, indicating the time and duration of a high-grade metamorphism. In contrast, texturally controlled in-situ EMP monazite dating of two chemically distinct monazite generations in metapelites revealed two metamorphic events separated by 60-80 Ma, thereby complementing the petrologic study. Small monazite inclusions in porphyroblastic garnets and cores of some matrix monazite grains show ages of ca. 1610 Ma, similar to the concordia ages from zircon, thereby confirming the time of the UHT metamorphism. The monazite grains in the matrix, growing along with a second generation of garnet and late-stage symplectites are highly recrystallized and show ages of ca. 1540 Ma, indicating the time of the second metamorphic event at higher pressures but lower temperatures. Monazite in the charnoenderbites records the second metamorphic event but only rarely the earlier UHT event. In addition, they show evidence for later imprints of deformation between ca. 1450 and 1360 Ma and minor disturbances at ca. 730 Ma and ca. 510 Ma.

Thus, the combination of petrological, geochronological and geochemical data unveils the tectono-metamorphic history of the Ongole domain in a hitherto unknown detail. The Ongole domain was formed as a magmatic arc near the Indian continent during the Palaeoproterozoic. Subsequently, the rocks were metamorphosed under UHT conditions during late Palaeoproterozoic (ca. 1610 Ma) due to advective heat from magma underplating during the growth of the arc. Finally, 60 to 80 Ma later (ca. 1540 Ma), during early Mesoproterozoic, the terrain was accreted to the Indian craton leading to crustal thickening and consequently the

second metamorphic event. The two-stage evolutionary history of the Ongole domain fits well to the expected evolution of magmatic arcs in general.

In context of supercontinent cycles, the formation and growth of the magmatic arc (Ongole domain) through subduction related accretion can be correlated with the growth of Columbia (1.8-1.2 Ga) but its accretion to the Indian craton is apparently unrelated to the formation of any supercontinent on a global scale.

Chapter 1

Introduction

1.1. Importance of magmatic arcs

It is generally considered that movement of tectonic plates leads to growth of continents along convergent plate margins through arc-continent collision, continent-continent collision or accretionary processes at subduction zones (Taylor and McLennan, 1985; Rudnick, 1995; Arndt, 2013). Plate tectonics also led to the assembly and break up of continents resulting in the periodic formation of supercontinents like Columbia, Rodinia, Gondwana and Pangea. Nevertheless, there is still a lot of debate about when plate tectonics in its current form started and the nature of plate tectonics in the Precambrian (Polat, 2012). The controversy persists mainly because of the lack of evidence for ancient subduction zones. The key evidence used to infer convergent margin settings in the Phanerozoic is the presence of high-pressure rocks such as blueschists and eclogites. However, these rocks are rare or missing at ancient subduction zones, the scarcity of which has been attributed to a preservation problem by Möller et al. (1995). Magmatic arcs on the other hand have a better preservation potential than subduction zone eclogites (Korsch et al., 2011) and consequently they have become increasingly important as an alternative evidence for ancient subduction zones. Magmatic arcs have figured prominently in models of continental growth and preserve unique geochemical characters (Kelemen et al., 2003) and tectono-metamorphic history. They have often

been correlated to the processes accompanying continental amalgamation through the subduction of intervening oceanic lithosphere in a prolonged subduction-accretion-collision regime. Thus, the pathways along which magmatic arcs evolve provide important clues about the formation and amalgamation of continental crust, which led to supercontinent formations in geological history.

To gain a thorough knowledge about the formation and evolution of a magmatic arc a combination of detailed petrological, geochronological and geochemical work is required. Results thus obtained allow for making statements about the nature and timing of processes that operated at active continental margins, for example the timing of formation and the tectonic setting of growth due to subduction related accretion, nature and timing of subsequent metamorphism of the arc due to advective heat prior to collision and the timing of collision leading to the amalgamation of the arc and a continent. However, detailed petrological, geochronological and geochemical studies have been rarely combined. The approach is particularly powerful when it includes reconstruction of petrological pressure-temperature (P-T) paths and texturally controlled in-situ dating of metamorphic minerals, as it then provides information not only about the timings but also the geodynamic settings of different metamorphic events.

The recognition of magmatic arcs in ancient rock records indicate that subduction processes at convergent plate margins were operating very early in the earth's history and provide missing links between larger continental blocks that were together in the past but are now geographically separated.

1.2. The Eastern Ghats Belt – A Proterozoic high-grade terrain

The Eastern Ghats Belt is an assembly of several granulite-facies terrains that extends for ca. 1000 km along the eastern margin of peninsular India in a roughly NE-SW direction. It is bounded to the north by the Singhbhum craton and to the

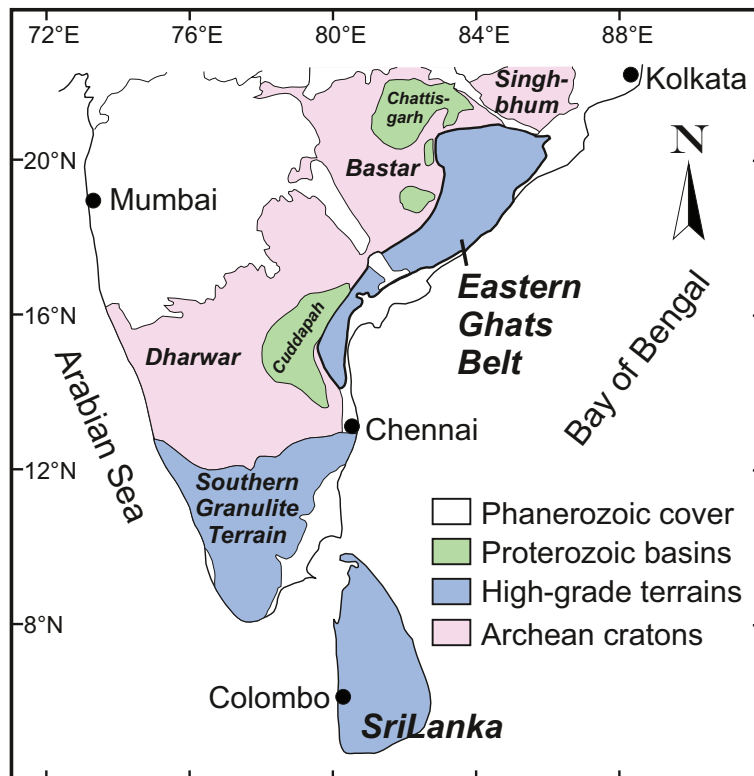


Figure 1.1: Main geological units in the southern part of the Indian subcontinent

west by the Bastar craton and the Eastern Dharwar craton, and is juxtaposed against them along several shear zones (see Dobmeier and Raith, 2003). The cratons are of Archean age and are composed of TTG gneiss. Ramakhishnan et al. (1998) presented the first geological map of the Eastern Ghats Belt in which they divided the EGB into four longitudinal litho-tectonic domains, followed by Rickers et al.

(2001) whose subdivisions were based on isotopic signatures. Shortly after, Dobmeier and Raith (2003) divided the whole Eastern Ghats Belt into four crustal provinces, which themselves were divided into several crustal domains on the basis of their different crustal histories (Figure 1 in Chapter 1) . These crustal provinces are the Rengali Province (northern part), the Eastern Ghats Province (central part), the Jeypore Province (western part) and the Krishna Province (southern part). While the Rengali and the Jeypore Province are Archean in age, the largest Eastern Ghats Province is dominantly Neoproterozoic and the Krishna Province is dominantly Palaeoproterozoic. In the Eastern Ghats Province UHT metamorphism of preexisting rocks, the subsequent emplacement of charnockites and granites in a subduction zone setting and the final collision of East Antarctica with India, all occurred between 1.03 and 0.9 Ga as a part of the Rodinia supercontinent formation (Mukhopadhyay and Basak, 2009). Before the breakup of the latter, the Eastern Ghats Province was contiguous with the high-grade terrains of the Napier and Rayner complexes of East Antarctica. On the other hand, the Krishna Province being older, its evolution has been vaguely attributed to the Columbia supercontinent formation. It is therefore evident that the various provinces of the EGB have very different histories, which are apparently unrelated to each other. Though there is evidence for Pan-African overprints from the EGB, no major tectono-metamorphic events of that age have been reported till date.

Thus, understanding the tectono-metamorphic history of the Eastern Ghats Belt is vital for the reconstruction of supercontinent assemblies involving India during the Precambrian and early Palaeozoic.

1.3. The Ongole domain

The granulite-facies Ongole domain is a part of the Krishna Province along with two other domains, namely the Vinjamuru and the Udayagiri domain, dominated by greenschist to amphibolite-facies schists. It is presently squeezed between the Eastern Ghats Province and the Eastern Dharwar craton. The Ongole domain essentially consists of huge volumes of multi intrusive intermediate to felsic granulites (charnoenderbites), covering a substantial area, with enclaves of mafic granulites and migmatitic metapelites constituting a small portion (<10 vol %). The geological evolution of the Ongole domain, so far is based on a limited dataset. It is characterized by felsic magmatism at ~1.7 Ga (Kovach et al., 2001) and a high-grade metamorphic event at ~1.6 (Bose et al., 2011; Kovach et al., 2001; Simmat and Raith, 2008). Geochemical data from discrete magmatic bodies around and within the Ongole domain indicate their formation in a magmatic arc setting. A N-S array of alkaline rocks, interpreted to have been emplaced during rifting at 1.5-1.3 Ga, marks the boundary of the Ongole domain and the Eastern Dharwar craton to the west (Upadhyay, 2008). It is hence dominantly a late Palaeoproterozoic terrain.

From the available data it appears that the Ongole domain is an exotic polymetamorphic granulite terrain whose formation and metamorphic age neither matches with that of the neighboring crustal blocks nor does it fit exactly to the period of amalgamation of Columbia supercontinent. In order to gain a thorough knowledge about this high-grade terrain, a comprehensive petrological, geochronological and geochemical study is much needed, which is expected to provide important but missing clues about the evolution of the EGB, thereby shedding light on the growth of continental crust in Peninsular India.

1.4. Study approach and analytical techniques

To solve the above mentioned problems, first extensive field work was performed in the entire Ongole domain as well as some areas in the northern part of the adjoining Vinjamuru domain. The main focus was laid on systematic sampling the different rock types. Thin sections of all samples were produced and examined using polarizing microscopy. Metapelites were of particular interest because they have the highest potential to preserve the metamorphic history in form of reaction textures and mineral compositions, which in turn are necessary for geodynamic interpretations. Observations of mineral assemblages and reaction textures provided first ideas about the metamorphic history. Samples were then selected for analyzing mineral compositions. Polished thin sections were produced and analyzed using the electron microprobe at the University of Kiel. Geothermobarometric calculations performed using the analyzed mineral compositions helped to quantitatively constrain the P-T conditions for metamorphism.

Whole rock major element compositions of certain samples were analyzed using the X-ray fluorescence (XRF) technique at the University of Kiel. The major element concentrations of metapelites were used to perform thermodynamic modeling in the form of pseudosections using THERIAK-DOMINO (de Capitani and Brown, 1987) to better constrain the P-T conditions of metamorphism. For the meta-igneous rocks (charnoenderbites and mafic granulites) whole rock major, trace and rare earth element concentrations were used to determine the tectonic setting of melt generation, leading to the magmatic protoliths of the charnoenderbites and mafic granulites. For analyzing trace element concentrations, samples were dissolved using acid digestion bombs and subsequently analyzed by means of Inductively Coupled Plasma Mass Spectrometry (ICP-MS) at GeoForschungZentrum in Potsdam. For analyzing rare earth elements (REE), the samples were decomposed and dissolved using the Na₂O₂ sinter method and REE were separated using ion-

exchange methods. The samples were subsequently measured by means of Inductively Coupled Plasma Atomic Emission Spectroscopy (ICP-AES) also at GeoForschungZentrum in Potsdam.

Geochronological techniques were applied to unravel the timing of magmatic and metamorphic events. Two different approaches were used: U-Pb isotope dating of zircon by means of Laser Ablation Inductively Coupled Plasma Mass Spectrometry (LA-ICP-MS) at the University of Münster and U-Th-total Pb in-situ monazite dating using the electron microprobe at the University of Kiel. For LA-ICP-MS zircon dating samples were crushed, the zircon grains were separated and mounted on epoxy resin discs. The discs were polished and each zircon grain was photographed using cathodoluminescence (CL) before analysis. Monazite dating was applied to Pb-free polished sections resulting in texturally controlled in-situ analyses with a high spatial resolution (spot diameter ca. 2 μ m). The application of both geochronological techniques on the same samples helped to reveal the polymetamorphic nature of the rocks, providing the timing of different events in a multiply deformed and metamorphosed high-grade terrain.

1.5. Outline of this thesis

This thesis focuses on reconstructing the evolutionary history of a magmatic arc (Ongole domain) from its growth via subduction related accretion followed by high-grade metamorphism by magmatic heat advection to its attachment with the craton via collision. This study thus provides new insights into the evolution of Proterozoic continental crust in Peninsular India. The evolutionary history is presented in three chapters, which are briefly described below. Each chapter is independent on its own, resulting in some repetitions in a few segments of the chapters.

Chapter 2 deals with the detailed petrological and pressure-temperature evolution of metapelitic granulites, charnoenderbites and mafic granulites of the Ongole domain. The results demonstrate that the Ongole domain experienced two distinct high-grade metamorphic events giving rise to two different pressure-temperature paths. The first metamorphic event at low pressures and ultrahigh temperature conditions was due to magma accretion while the second metamorphic event was due to crustal thickening during collision. Such two-stage metamorphism is expected in a magmatic arc.

Chapter 2 has been submitted to Precambrian Research and is currently under review:

Sarkar, T. and Schenk, V. (in review). Two-stage granulite formation in a Proterozoic island arc (Ongole domain of the Eastern Ghats Belt, India): Part 1. Petrology and pressure-temperature evolution.

Chapter 3 focuses on high-quality LA-ICP-MS zircon dating and texturally controlled in-situ monazite dating with an electron microprobe and the correlation of the geochronological results with the petrological results. We can distinctly relate the ages obtained from monazite and zircon to the two different P-T paths and the corresponding textures established in the first manuscript. The unambiguous correlation enables us to develop a geodynamic evolution model of the studied magmatic arc (Ongole domain) that may represent a likely evolution of magmatic arcs in general.

Chapter 3 has been submitted to Precambrian Research and is currently under review:

Sarkar, T., Schenk, V., Appel, P., Berndt, J. and Sengupta, P. (in review). Two-stage granulite formation in a Proterozoic island arc (Ongole domain of the Eastern Ghats Belt, India): Part 2. LA-ICP-MS zircon dating and texturally controlled *in-situ* monazite dating.

Chapter 4 provides geochemical data of charnoenderbites and the mafic granulites and zircon geochronological data of the charnoenderbites. The major, trace and REE geochemistry indicates the geodynamic setting in which the magmatic protoliths of the meta-igneous rocks were emplaced. LA-ICP-MS U-Pb zircon data provide the emplacement age of the magmas, thereby constraining the timing of crustal growth. The zircon ages also constrain the time and duration of high-grade metamorphism, supporting the ages obtained from metapelites presented in chapter 3.

Chapter 4 has been submitted to Contributions to Mineralogy and Petrology and is currently under review:

Sarkar, T., Schenk, V. and Berndt, J. (in review). Formation and evolution of a Proterozoic magmatic arc: geochemical and geochronological constraints from meta-igneous rocks of the Ongole domain, Eastern Ghats belt, India.

References

- Arndt, N., 2013. Formation and Evolution of the Continental Crust. *Geochemical Perspectives* 2, 405–533.
- Bose, S., Dunkley, D.J., Dasgupta, S., Das, K., Arima, M., 2011. India-Antarctica-Australia-Laurentia connection in the Paleoproterozoic-Mesoproterozoic

- revisited: Evidence from new zircon U-Pb and monazite chemical age data from the Eastern Ghats Belt, India. *Geological Society of America Bulletin* 123, 2031–2049.
- de Capitani, C., Brown, T.H., 1987. The computation of chemical equilibrium in complex systems containing non-ideal solutions. *Geochimica et Cosmochimica Acta* 51, 2639–2652.
- Dobmeier, C.J., Raith, M.M., 2003. Crustal architecture and evolution of the Eastern Ghats Belt and adjacent regions of India. Geological Society, London, Special Publications 206, 145–168.
- Kelemen, P.B., Hanghøj, K., Greene, A.R., 2003. One View of the Geochemistry of Subduction-Related Magmatic Arcs, with an Emphasis on Primitive Andesite and Lower Crust, in: *Treatise on Geochemistry*. Elsevier, pp. 593–659.
- Korsch, R.J., Kositcin, N., Champion, D.C., 2011. Australian island arcs through time: Geodynamic implications for the Archean and Proterozoic. *Gondwana Research* 19, 716–734.
- Kovach, V.P., Simmat, R., Rickers, K., Berezhnaya, N.G., Salnikova, E.B., Dobmeier, C., Raith, M.M., Yakovleva, S.Z., Kotov, AB, 2001. The western charnockite zone of the Eastern Ghats Belt, India-an independent crustal province of late Achaean (2.8 Ga) and Palaeoproterozoic (1.7-1.6 Ga) terrains. *Gondwana Research* 4, 666–667.
- Möller, A., Appel, P., Mezger, K., Schenk, V., 1995. Evidence for a 2 Ga subduction zone: eclogites in the Usagaran belt of Tanzania. *Geology* 23, 1067–1070.
- Mukhopadhyay, D., Basak, K., 2009. The Eastern Ghats Belt... A Polycyclic Granulite Terrain. *Journal Geological Society of India* 73, 489–518.
- Polat, A., 2012. Growth of Archean continental crust in oceanic island arcs. *Geology* 40, 383–384.
- Ramakrishnan, M., Nanda, J.K., Augustine, P.F., 1998. Geological evolution of the Proterozoic Eastern Ghats mobile belt. Geological Survey of India Special Publications 44, 1–21.

-
- Rickers, K., Mezger, K., Raith, M.M., 2001. Evolution of the continental crust in the Proterozoic Eastern Ghats Belt, India and new constraints for Rodinia reconstruction: implications from Sm–Nd, Rb–Sr and Pb–Pb isotopes. *Precambrian Research* 112, 183–210.
- Rudnick, R.L., 1995. Making continental crust. *Nature* 378, 571–578.
- Simmat, R., Raith, M.M., 2008. U–Th–Pb monazite geochronometry of the Eastern Ghats Belt, India: Timing and spatial disposition of poly-metamorphism. *Precambrian Research* 162, 16–39.
- Taylor, S.R., McLennan, S.M., 1985. *The continental crust: Its composition and evolution*. Blackwell Scientific Publications, Oxford.
- Upadhyay, D., 2008. Alkaline magmatism along the southeastern margin of the Indian shield: Implications for regional geodynamics and constraints on craton–Eastern Ghats Belt suturing. *Precambrian Research* 162, 59–69.

Chapter 2

Petrology and pressure-temperature evolution of the granulite-facies rocks of the Ongole domain, Eastern Ghats Belt, India.

Abstract

The Ongole domain of the Proterozoic Eastern Ghats Belt, India, is dominated by charnockites and enderbites with enclaves of migmatitic metapelites. Conspicuous reaction textures indicate two generations of mineral growth. Spinel+quartz bearing Fe-Al granulites provide critical evidence for an ultrahigh-temperature (UHT) metamorphism in the Ongole domain. The association of spinel and quartz, now separated by garnet and sillimanite coronas, suggests that the rocks underwent $T > 950^{\circ}\text{C}$ peak metamorphism at $P = 6.5\text{-}7$ kbar, as constrained from P-T pseudosection. Coarse-grained orthopyroxene in garnet+cordierite bearing metapelites show the highest Al_2O_3 content up to 8.2 wt.%, suggesting $T = 950\text{-}1000^{\circ}\text{C}$. Temperatures estimated from mesoperthite and plagioclase pairs and other geothermometers ($T = 900\text{-}1000^{\circ}\text{C}$) further support ultrahigh-temperature metamorphism in the Ongole domain. The absence of cordierite in retrograde mineral assemblages points to isobaric cooling, giving rise to a near isobaric heating-cooling trajectory. The second generation of garnet, occurring as thick overgrowths over coarse-grained garnet porphyroblasts, in metapelites and especially in

charnoenderbites have higher grossular contents than the porphyroblasts. Thermobarometry and P-T pseudosections indicate that they formed at a higher pressure but lower temperature (ca. 780°C, 9.5 kbar) during a second metamorphic event. Orthopyroxene+sillimanite±kyanite±spinel symplectites replacing cordierite is most likely formed during this second metamorphic event. The presence of sillimanite, kyanite as well as andalusite along with coarse-grained retrograde biotite in the same rock marks the last stage of the second metamorphic event characterized by isobaric cooling just below the aluminosilicate triple point. This further suggests near-isothermal decompression from higher pressures. UHT metamorphism at low pressures during the first metamorphic event is most likely caused by magma emplacement. The higher pressure but lower temperature conditions achieved during the second metamorphic event is due to crustal thickening during collision of continental blocks. Near-isothermal decompression to pressures of ca. 4 kbar points to subsequent rapid exhumation of the over thickened crust. The two-stage evolutionary history of the Ongole domain fits well to the expected evolution of a magmatic arc, in which the first can be attributed to magmatic heat advection during arc growth and the second to crustal thickening during collision.

2.1. Introduction

The periodic assembly and breakup of ancient continental fragments since late Archean times has been well documented (Zhao et al., 2002; 2003; 2004; Veevers, 2004; Rogers and Santosh, 2009) and has led to the reconstruction of several Precambrian supercontinents including Columbia, Rodinia, and Gondwana. The continental assemblies are believed to be driven by subduction related processes similar to those occurring during the Phanerozoic, and its evidence is seen in high-

pressure subduction zone rocks or in magmatic arc rocks. However, the high-pressure rocks are rare or even missing in many ancient subduction zones. The scarcity of old eclogite-facies rocks at ancient subduction zones may be attributed to a 'hot early earth' or a mere preservation problem. But careful petrological studies and discovery of old subduction zones had led Möller et al. (1995) to ascribe the scarcity of high-pressure rocks to a mere preservation problem. Thus, the study of magmatic arcs have become increasingly important as an alternative evidence for ancient subduction zones, and have a better preservation potential than subduction zone eclogites (Korsch et al., 2011). A magmatic arc is formed prior to collision of crustal blocks and should preserve a unique tectono-metamorphic history and geochemical character.

The Eastern Ghats Belt bordering the Archean Dharwar, Bastar and Singhbhum cratonic blocks of peninsular India is a classic Proterozoic geological entity and takes a key position in the reconstruction models of Columbia, Rodinia and Gondwana supercontinents (Sengupta et al., 1999; Rickers et al., 2001; Zhao et al., 2002; 2003; 2004; Dasgupta and Sengupta, 2003; Bose et al., 2011). The age of its attachment with the craton is still debated to be either Mesoproterozoic (Dasgupta et al., 2013) or Neoproterozoic (Simmat and Raith, 2008). The Ongole domain in the southern part of the Eastern Ghats Belt (Dobmeier and Raith, 2003), occurring between the Eastern Ghats Province and the Archean cratons, exposes a multitude of granulite-facies rocks dominated by charnoenderbites. The crustal segment seems to be quite different in lithological and geochemical character from the adjoining crustal blocks as a mafic ultramafic complex within the Ongole domain is interpreted to have formed in a magmatic arc setting (Dharma Rao and Santosh, 2011). Moreover, the late Palaeoproterozoic age of crust formation is unrelated to the age of Columbia and Rodinia supercontinent formation.

To gain a better knowledge about the geodynamic setting, the timing of its formation, the metamorphic history as well as the regional extent of this crustal block detailed petrology combined with geochemistry and geochronology is required.

Incidentally no comprehensive petrological, geochemical and geochronological study encompassing the entire Ongole domain has been attempted so far to understand the history and nature of the geological events in this crustal domain.

It is shown in an accompanying study that the rocks of the Ongole domain formed in a magmatic arc setting. In this contribution we have estimated the physical conditions of metamorphism of the rocks of the magmatic arc (charnoenderbites and the metapelites) by combining the results from conventional geothermobarometry, petrogenetic grids and numerically computed phase diagrams (pseudosections). Integrating this information with geochronological constraints (chapter 3), a suitable P-T trajectory followed by the rocks of the Ongole domain has been constructed. Our study highlights that the rocks of the Ongole domain underwent a UHT metamorphism that was followed by a lower temperature but high-pressure metamorphism. Combining the P-T trajectory with the available geological and petrological data for the adjoining crustal blocks the geodynamic situations during the two metamorphic events have been explored.

2.2. Geological background

The Eastern Ghats Belt extends for ~1000 km along the eastern margin of the peninsular India in a roughly NE-SW direction. It is an assembly of several granulite-facies terrains juxtaposed against the Archean cratons of the Indian shield along several shear zones (summary: Dobmeier and Raith, 2003). Ramakhishnan et al. (1998) presented the first geological map of the Eastern Ghats Belt in which they established four longitudinal litho-tectonic domains named as Eastern and Western Khondalite Zones, Central Migmatite Zone and Western Charnockite Zone. Based on the Nd model ages and supporting Rb-Sr and Pb isotopic data Rickers et al. (2001) demonstrated that the Eastern Ghats Belt is a

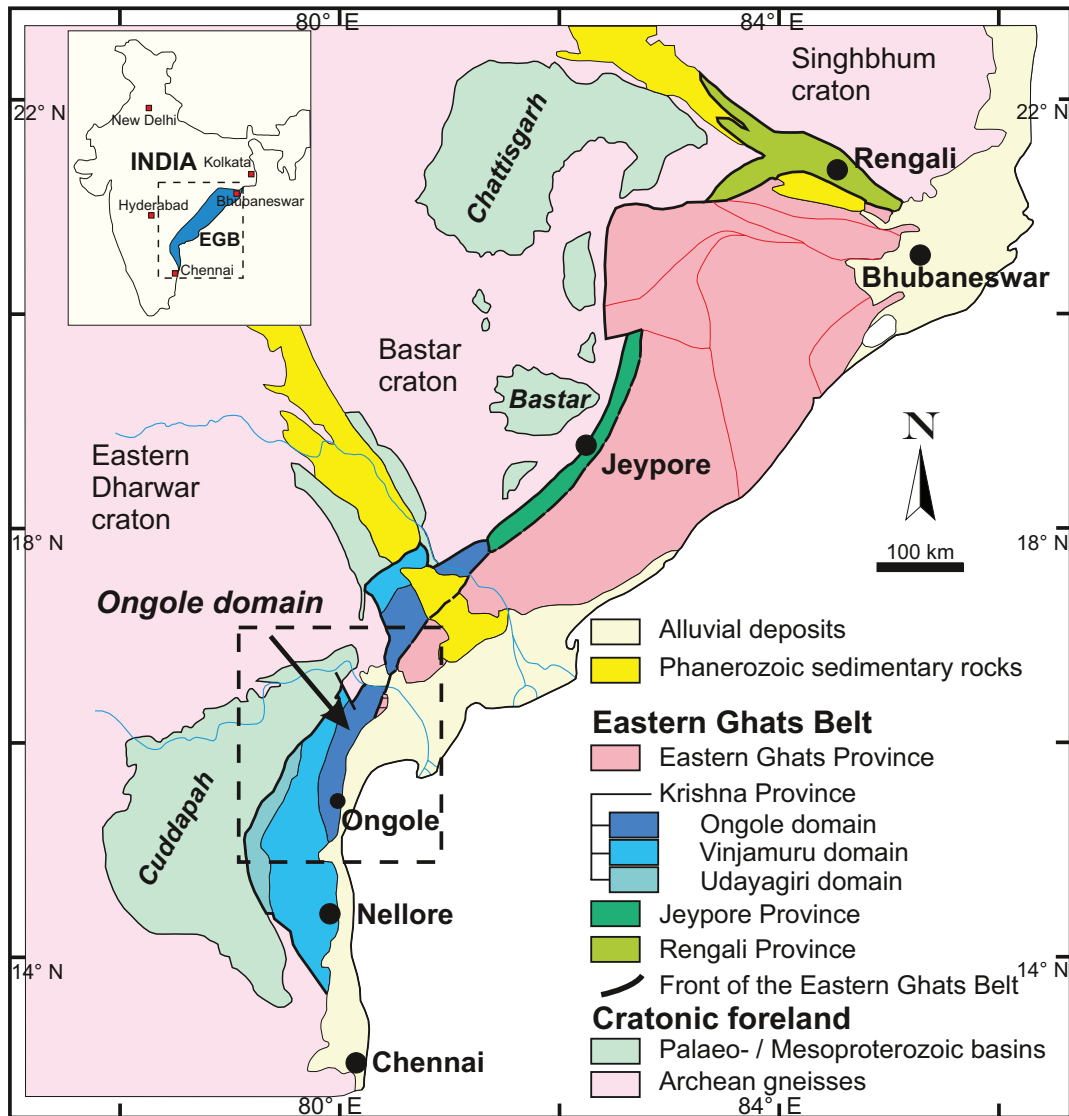


Figure 2.1: Simplified geological map of the Eastern Ghats Belt (EGB) after Dobmeier and Raith (2003). The map shows subdivision in crustal provinces with distinct geological evolution. The provinces are further subdivided into domains separated by megalineaments and shearzones (for details see Dobmeier and Raith, 2003). Only the subdivisions of Krishna province are shown here.

collage of former crustal domains bounded by major lineaments identified by Chetty and Murthy (1994). However, it is to be noted that these domains cut across the lithotectonic units of Ramakrishnan et al. (1998). Shortly after, Dobmeier and Raith (2003) divided the whole Eastern Ghats Belt into several crustal provinces, which themselves were divided into several crustal domains on the basis of their different crustal histories (Fig. 2.1). The major crustal provinces of Dobmeier and Raith

(2003) are the Rengali Province (northern part), the Eastern Ghats Province (central part), the Jeypore Province (western part) and the Krishna Province (southern part). The granulite-facies Ongole domain is a part of the Krishna Province along with two other domains, namely the Vinjamuru and the Udayagiri domain, together known as the Nellore-Khammam Schist Belt as they are dominated by greenschist to amphibolite-facies schists.

The geological evolution of the Ongole domain (Fig. 2.2), so far is based on a limited dataset. It is characterized by felsic magmatism at ~ 1.7 Ga (Kovach et al., 2001) and a high-grade metamorphic event at ~ 1.6 (Bose et al., 2011; Kovach et al., 2001; Simmat and Raith, 2008). This was followed by alkaline magmatism on the western margin of the domain at ~ 1.5 - 1.3 Ga, interpreted as related to rifting (Upadhyay, 2008).

Sengupta et al. (1999) documented a UHT metamorphism ($>1000^{\circ}\text{C}$) and deep crustal heating cooling trajectory for Fe-Al granulites from Kondapalle, in the northern Ongole domain. The cause of the UHT metamorphism was tentatively attributed to the emplacement of voluminous mafic magma represented by a mafic-ultramafic suite near Kondapalle. From field relations Bhui et al. (2007) concluded that the high-grade metamorphism was followed by the emplacement of charnoenderbites at ~ 1.7 Ga indicating that the age of metamorphism should be older. Following this, Bose et al. (2011) interpreted U-Pb zircon ages of concentrically zoned detrital grains from Kondapalle to reflect an older UHT metamorphism (1.76 Ga) prior to the established granulite-facies metamorphism at ~ 1.6 Ga. Very recently the emplacement of the Kondapalle ultramafic complex has been dated at ~ 1.69 - 1.63 Ga (Dharma Rao et al., 2012) and was inferred to be emplaced in a continental arc environment (Dharma Rao and Santosh, 2011; Vijaya Kumar et al., 2011).

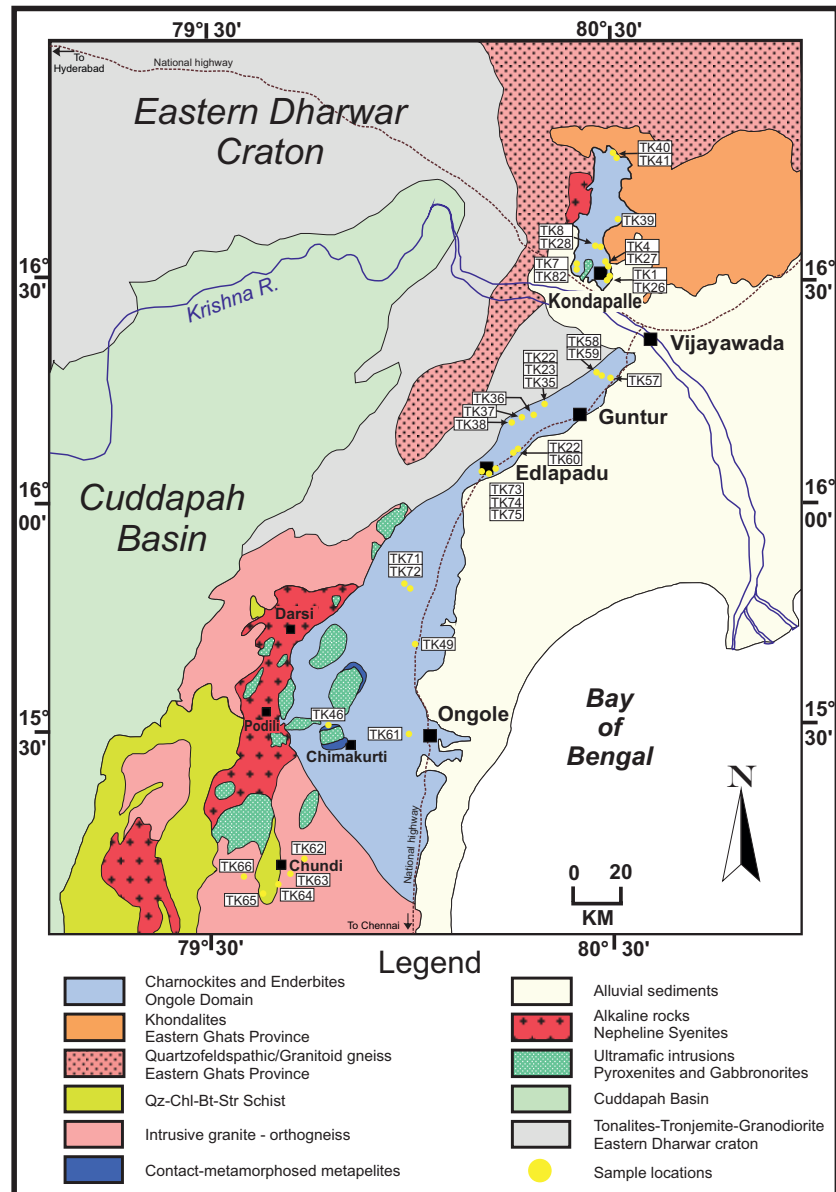


Figure 2.2: Geological map of the southern part of the Eastern Ghats Belt showing the position of the Ongole domain and the adjoining areas (adapted and simplified from the Geological Survey of India map of Andhra Pradesh, published in 2001), showing the locations of samples.

Interestingly, the Ongole domain did not experience major tectonothermal reworking during the Neoproterozoic orogeny, but possibly only minor disturbances reflected in the Ar-Ar age of ~ 1.1 Ga (Mezger and Cosca, 1999). Most recently, Dasgupta et al. (2013) integrated all available data into a geodynamic model.

2.3. Field relationships

The Ongole domain (Fig. 2.2) essentially consists of huge volumes of multi intrusive intermediate to felsic granulites with enclaves of migmatitic metapelites ranging from meter to outcrop scale, well exposed along freshly cut huge quarry faces throughout the Ongole domain.

The intermediate (enderbite) and the felsic rock type (charnockite) together cover the substantial part of the Ongole domain. Both these types have a dark, homogenous and massive appearance in the quarry exposures. Only careful observation reveals that these rocks occur in several modes. The enderbites (garnet + orthopyroxene + plagioclase + quartz \pm perthite) occur as fine-grained massive to medium-grained gneissic rocks, whereas the charnockites (garnet + orthopyroxene + perthite + quartz \pm plagioclase) occur as coarse-grained gneissic to pegmatoidal rocks. However, the essentially gneissic nature of the rocks is only evident on bleached or weathered surfaces. Lineations and sometimes the porphyric augen gneiss nature of the charnockites are mainly visible on weathered surfaces. Dark grey bands and lenses of basic rocks are also present within these charnoenderbites. Complex cross cutting relationships among the various rocks are commonly encountered in the outcrops (Fig. 2.3a). The textural relationship between a charnockitic augen gneiss being intruded sequentially by a fine-grained massive enderbite, a basic rock and a coarse-grained charnockite is nicely preserved (Fig. 2.3a). Fine-grained enderbite being intruded and completely engulfed by coarse-grained charnockite is rather common. The pegmatoidal charnockites, crosscutting the gneissic fabric, are characterized by the presence of blue quartz, coarse-grained orthopyroxene, and occur as ramifying veins within enderbites. Coarse-grained, light colored bleached (decharnockitized) charnoenderbites with streaky gneissic foliation occur frequently as small to large patches within the charnoenderbite or

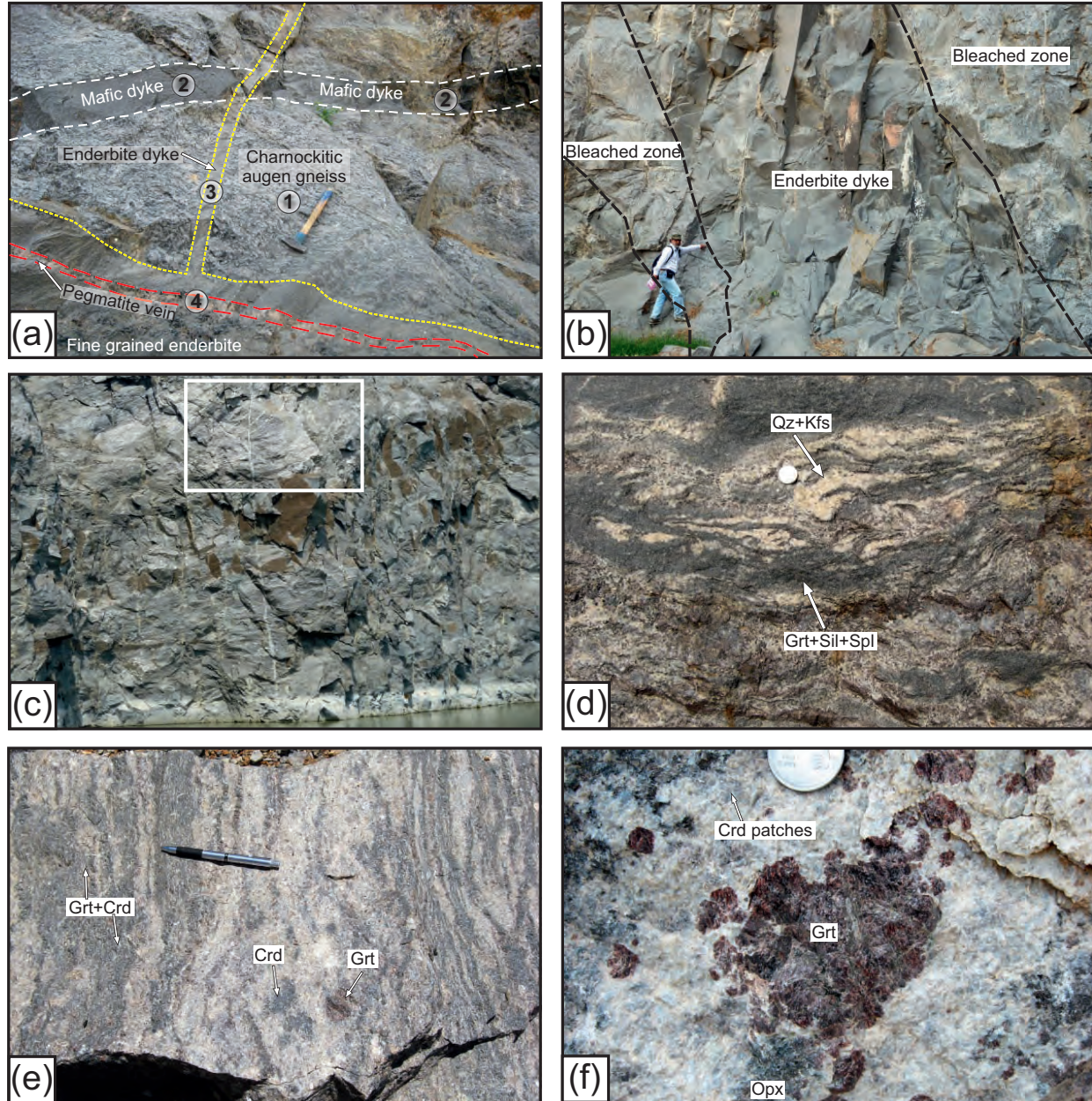


Figure 2.3: Field photographs illustrating the mode of occurrence and interrelation of the different rock types in the Ongole domain. (a) Interrelation among the different generations of magmatic rocks. A Charnockitic augen gneiss (1) has been intruded by a basic dyke (2) and a fine-grained enderbite (3). A pegmatite vein (4) has cut through all the rock units. (b) An enderbite dyke with partially bleached zones along the contact with the host charnockite. (c) An enclave of a migmatitic metapelite completely engulfed within massive enderbite. (d) Grt-Sil-Spl-Qz granulite, mainly showing a stromatic migmatite structure with cm scale leucosomes. (e) Grt-Crd granulite also showing a stromatic migmatite structure. (f) Leucosome of a diatexitic Grt-Opx-Crd migmatite with porphyroblastic garnet and orthopyroxene. Cordierite is also present in the leucosome patches.

along contacts of later dykes (Fig. 2.3b). These are decharnockitized portions that seem to be the result of fluids released from the intruding dykes. This seems to indicate that the country rocks were already in the granulite-facies at the time of dyke intrusion.

The metapelitic granulites constitute only a small portion (<10 vol %) of the exposed rocks and occur as enclaves within the charnoenderbites and have sharp contacts with the host rock (Fig. 2.3c). Despite the locally clear intrusive relationship, the possibility that some other metapelites represent a cover series of the charnoenderbites cannot be excluded. The metapelitic granulites are migmatitic showing prominent layers of leucosome and melanosome ranging from centimeter to decimeter scale, mostly deformed and folded (Fig. 2.3d,e). The prominent gneissic fabric of the metapelites differs from that of the surrounding charnoenderbites. These textural features could be interpreted as evidence for an older metamorphic event, prior to the charnoenderbite intrusion. However, it cannot be excluded that the migmatitic fabric developed during the intrusion. Coarse-grained leucosome patches with porphyroblastic garnet are sometimes found to be interlayered with charnockites (Fig. 2.3f).

A km-scale layered mafic-ultramafic complex with gabbro-norite, leucogabbro-norite and anorthosite containing clinopyroxenite and chromitite layers is present in the northern part of Ongole domain near Kondapalle (Sengupta et al., 1999). These have been invaded and dismembered by intrusive charnoenderbites.

The adjoining Vinjamuru domain in the south mainly comprises metamorphosed felsic to intermediate volcanic gneisses associated with continental rocks consisting of medium to high-grade schistose to gneissic metapelites, metapsammites and amphibolites. The metapelites are dominated by Qz-Ms-Bt-Str±Grt schists, sometimes containing 4-5 cm porphyroblasts of staurolite.

In the southern part near Ongole several tens of meters thick banded-iron formation containing ferrosilite-garnet assemblages is present. The emplacement of a suite of alkaline rocks ranging from quartz syenite to alkali granite marks the

boundary between Ongole domain and the Eastern Dharwar craton to the west (Upadhyay, 2008).

2.4. Petrography

Based on mineral assemblages and bulk composition three rock types have been distinguished: Metapelitic granulites, Charnoenderbitic gneisses and Mafic granulites.

2.4.1. Metapelitic granulites

The metapelitic granulites may be subdivided on the basis of their mineral assemblages into Grt-Sil-Spl-Qz granulites and Grt-Crd±Opx granulites (Table 2.1).

Grt-Sil-Spl-Qz granulite

The ferromagnesian layers in these migmatitic granulites are some millimeters to some centimeters thick and occur alternating with leucosome layers of similar thickness. The mineral assemblage in the melanosome layers is essentially garnet-sillimanite-spinel-quartz-ilmenite±magnetite-perthite-plagioclase-biotite±corundum±rutile, while the leucosome layers consist dominantly of coarse-grained perthite and quartz with minor amounts of plagioclase.

Two generations of garnet occur in the rocks: porphyroblastic (garnet 1) and corona garnet (garnet 2). Garnet 1 (0.1-0.5 cm) forms cluster with medium grained prismatic or elongated sillimanite, coarse-grained spinel and ilmenite (Fig. 2.4a).

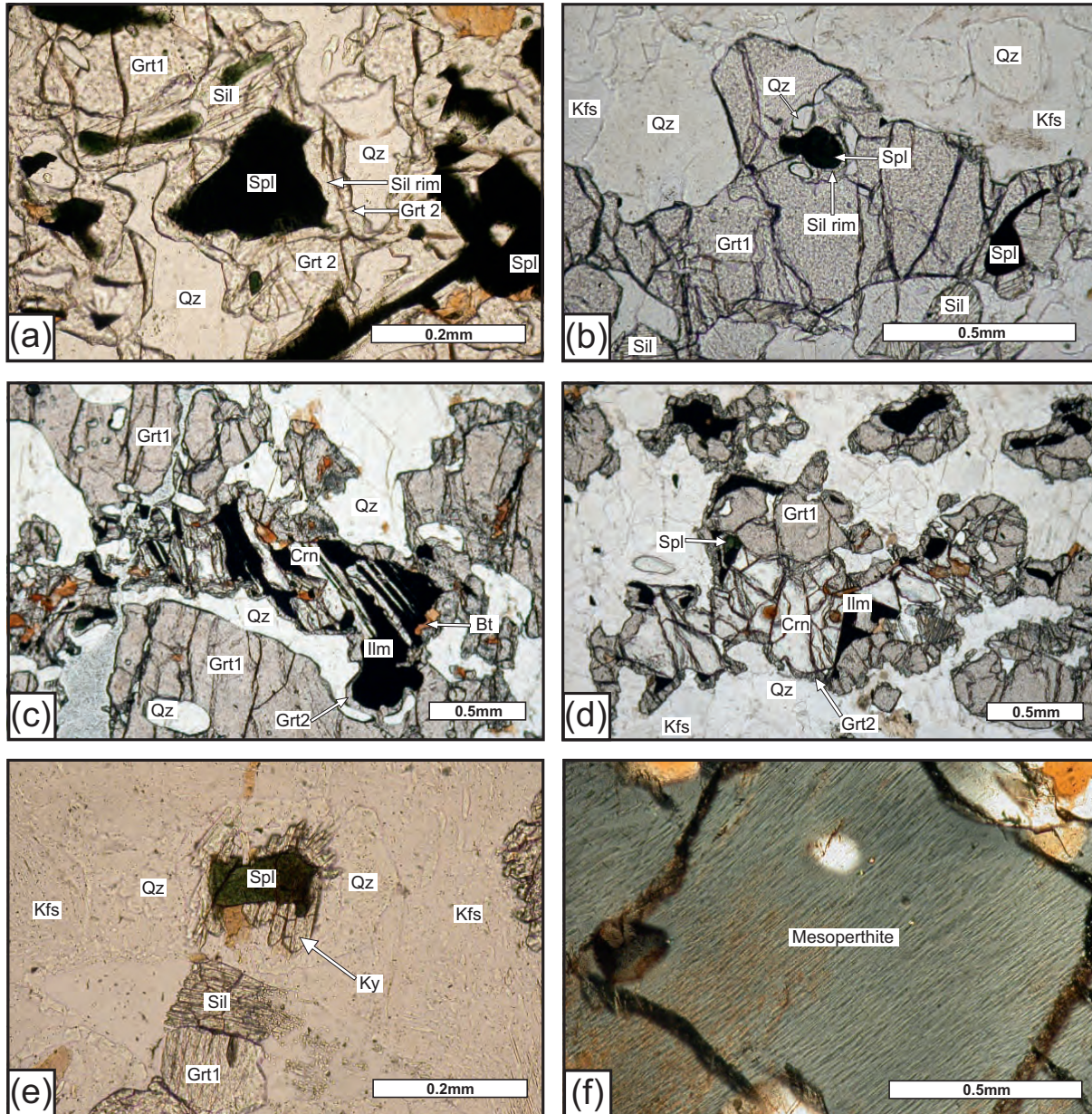


Figure 2.4: Photomicrographs illustrating the reaction textures from the metapelites and charnoenderbites of the Ongole domain. (a) – (f) : Textures from Grt-Sil-Spl-Qz granulite; (a) Spinel and quartz being separated by double coronas of sillimanite and garnet. (b) Inclusion of spinel and quartz separated by sillimanite within porphyroblastic garnet (garnet 1). (c) Lamellar intergrowth of corundum and ilmenite, clustering with garnet 1, is separated from quartz by thin coronal garnet. The association is marginally replaced by late biotite. (d) Cluster of coarse-grained corundum and garnet 1. Corundum associated with very little spinel and ilmenite is rimmed by a continuous garnet corona against quartz and K-feldspar. Note that ilmenite is also shielded by coronal garnet against quartz and K-feldspar. (e) Kyanite overgrowth separating spinel and quartz. (f) Mesoperthite. (continued on page 28)

Quartz, perthite and minor amounts of plagioclase occur in the interstitial spaces of the clusters. Small and rounded grains of spinel, quartz and biotite are the dominant inclusions in garnet (Fig. 2.4b) and sillimanite is less common. Garnet 1 is occasionally overgrown by narrow rims (garnet 2). However, garnet 2 is more common as corona around oxide phases like spinel, ilmenite and corundum (Fig. 2.4a).

Coarse-grained hercynitic spinel is separated from quartz and sometimes feldspar by double coronas of garnet 2 and sillimanite (Fig. 2.4a). If spinel and quartz are present together as inclusions in garnet 1, they are also separated by a narrow corona of sillimanite (Fig. 2.4b). In a few samples rutile is also present in the matrix. There are two main types of oxide aggregates. Coarse-grained spinel with magnetite exsolution often forms coarse aggregates with ilmenite, which formed as a result of oxidation from preexisting spinel that was rich in Fe_2TiO_4 (ulvöspinel). Lamellar intergrowths of ilmenite-corundum±spinel (Fig. 2.4c) are interpreted as exsolution from Fe-Ti-Al±Mg bearing homogeneous spinel. These textures indicate metamorphism at temperatures in excess of 1000°C (Sengupta et al., 1999). These composite intergrowths are always rimmed by garnet 2 separating them from quartz and/or feldspar. Porphyroblastic corundum without any exsolution texture coexists with garnet 1 and coarse-grained sillimanite. It is separated from quartz or feldspar by continuous coronas of garnet 2 (Fig. 2.4d). Exsolved magnetite needles are always confined within the grain boundaries of spinel. Magnetite grains are never found in the matrix.

Sillimanite has several textural modes of occurrence. Small needles as inclusions in garnet 1 and in K-feldspar may represent early sillimanite. The most abundant variety forms coarse, prismatic or elongated grains clustering with garnet 1. Sillimanite also forms coronas around spinel along with garnet, separating spinel from quartz. In a very similar fashion kyanite crystals form a reaction rim around spinel and separating spinel from quartz (Fig. 2.4e). Kyanite is documented here for the first time from the Ongole domain.

Two generations of biotite are identified but they are not part of the peak assemblage. Prograde biotite occurs only as small rounded inclusions in garnet 1. Retrograde biotite developed replacing anhydrous peak phases.

K-feldspar is mesoperthitic (Fig. 2.4f). It occurs as very coarse grains along with quartz in the leucosome and as medium to coarse grains in the melanosome. Plagioclase occurs dominantly in the leucosome.

The coarse-grained mineral assemblages are forming the main gneissic fabric and have subsequently been deformed, resulting in recrystallization and sometimes replacement textures. These features are attributed to a second phase of metamorphism. Quartz, K-feldspar and plagioclase show strain induced extensive recrystallization along the grain boundaries forming a very fine-grained granoblastic texture. The preserved porphyroblastic quartz and K-feldspar show undulose extinction. Retrograde biotite develops in these zones of deformation. Biotite-quartz with or without fibrolitic sillimanite replaces the peak metamorphic minerals like garnet 1, sillimanite and spinel. Patches of symplectitic biotite-kyanite is found to replace feldspar.

Grt-Crd±Opx granulites

Similar to the Grt-Sil-Spl-Qz granulites, these migmatitic metapelites also show melanosome and leucosome domains. The melanosome domains are dominated by garnet-cordierite±orthopyroxene-spinel-ilmenite-biotite±quartz±plagioclase, while the leucosome domains are dominated by quartz-perthite-plagioclase±cordierite.

In this mineral assemblage too, two generations of garnet are present. Garnet 1 forms porphyroblasts (up to 0.6 cm) and forms clusters with cordierite in the melanosome. Garnet 2 occurs as small granular overgrowths around garnet 1 or as small grains replacing retrograde biotite that formed after the first phase of prograde mineral growth.

Coarse-grained cordierite (up to 0.3 cm) containing inclusions of hercynitic spinel and biotite is most common. Cordierite occurs also as medium sized inclusions in garnet 1 (Fig. 2.4g). Coarse-grained orthopyroxene forms isolated grains in Grt-Crd-Spl bearing melanosomes in some samples (Fig. 2.4g). Orthopyroxene is commonly found in garnet rich, cordierite poor domains and not in cordierite rich patches. The grains are altered and may partially (Fig. 2.4g) or completely replaced by biotite. Small, rounded orthopyroxene inclusions (now completely altered) are also present in garnet 1.

Coarse-grained hercynitic spinel (Fig. 2.4h) with magnetite exsolution occurs in the garnet-cordierite domains but is not found in orthopyroxene bearing domains. Tiny inclusions of hercynitic spinel in coarse-grained cordierite are found throughout the rock.

Three generations of biotite are identified. Prograde, rounded biotite grains occur as small to medium grained inclusions in garnet 1 and cordierite. Two generations of retrograde biotite developed abundantly in some zones replacing prograde anhydrous phases. The first generation is overgrown by garnet 2 during the second phase of metamorphism. In addition there seems to be a younger biotite generation that is associated with andalusite and kyanite and formed after the second phase of metamorphism.

K-feldspar is perthitic, coarse-grained and dominant in the leucosome along with coarse-grained quartz and some plagioclase. Medium-grained plagioclase, sometimes antiperthitic, is more common in the melanosome together with some quartz and perthite.

Partial recrystallization of quartz and feldspar along the grain boundaries and undulose extinction provide ample evidence for high-temperature post peak deformation. Coarse-grained cordierite is partially replaced along grain boundaries by extremely fine-grained ($\sim 2\text{-}5\mu\text{m}$) spectacular symplectitic intergrowths of $\text{Opx}+\text{Sil}+\text{Ky}+\text{Spl}\pm\text{Bt}\pm\text{Grt}$ (Fig. 2.4i). Retrograde biotite-sillimanite-quartz

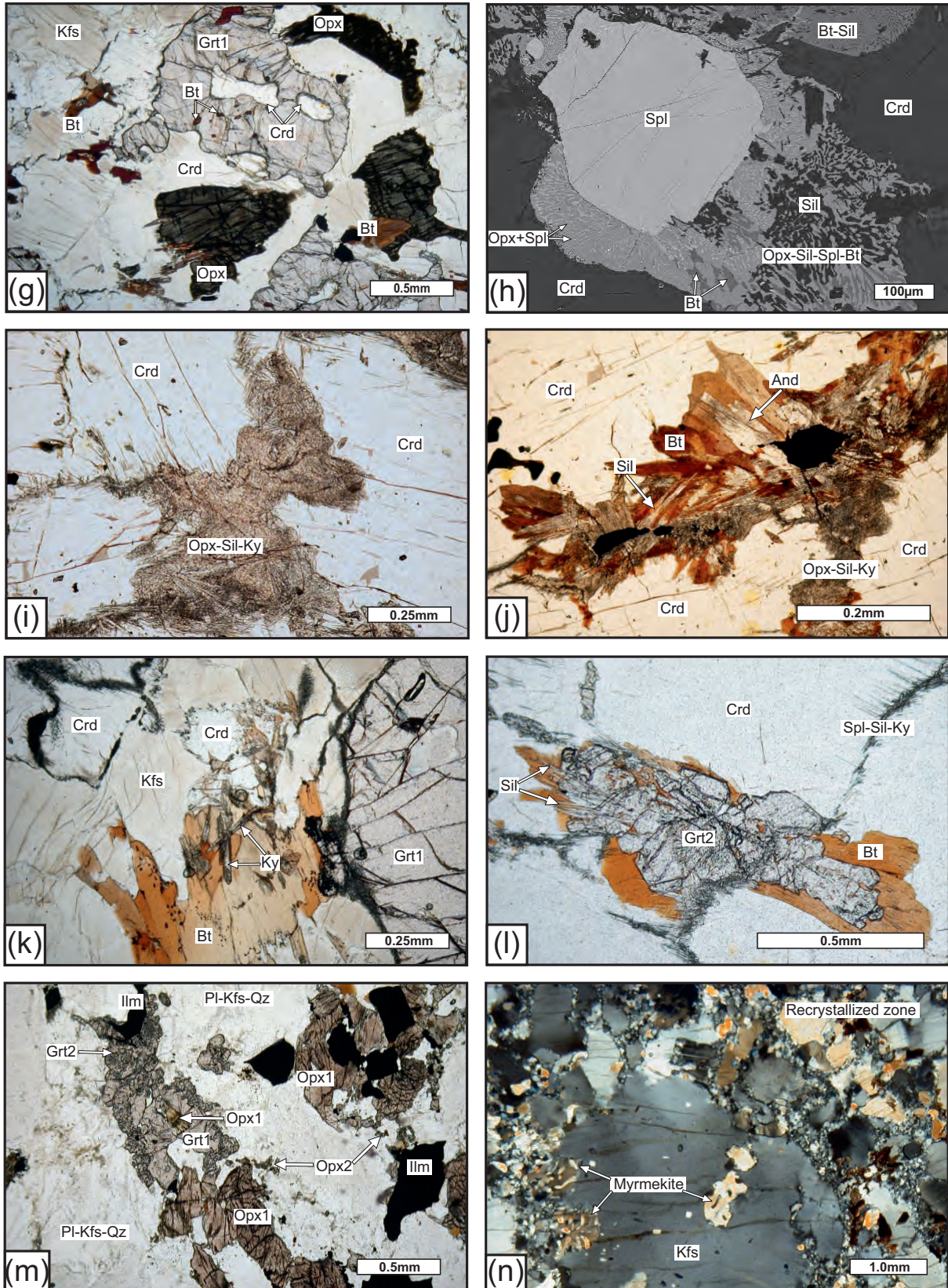


Figure 2.4

Figure 2.4 (continued from page 24): (g) – (l) : Textures from Grt-Crd-Sil±Opx granulite; (m) – (n): Textures from charnockites. (g) Grt-Crd-Opx assemblage. Cordierite inclusions are present in garnet 1 along with rounded, primary inclusions of biotite. Late biotite replaces parts of orthopyroxene and K-feldspar. (h) Coarse-grained cordierite is replaced by symplectites of Opx-Sil-Spl-Bt. Coarse-grained spinel does not take part in the reaction. (i) Partial replacement of cordierite by symplectitic intergrowth of Opx+Si±Ky. The aggregates are projecting from the margin towards the central parts of the cordierite grain, leaving an unreplaced relict of cordierite. (j) Partial replacement of cordierite by late-stage biotite, sillimanite and andalusite. (k) Late-stage biotite and kyanite assemblage replacing porphyroblastic garnet and cordierite. (l) Second generation of garnet (garnet 2) growing over symplectitic aggregates of biotite and sillimanite replacing cordierite. (m) Garnet 1, orthopyroxene and ilmenite in the matrix of plagioclase, K-feldspar and quartz in an enderbite. Inclusion of orthopyroxene in garnet 1. (p) Myrmekite development along the margin of coarse grained K-feldspar. Porphyroblastic quartz and K-feldspar have been recrystallized along the margins and show a fine-grained granoblastic texture.

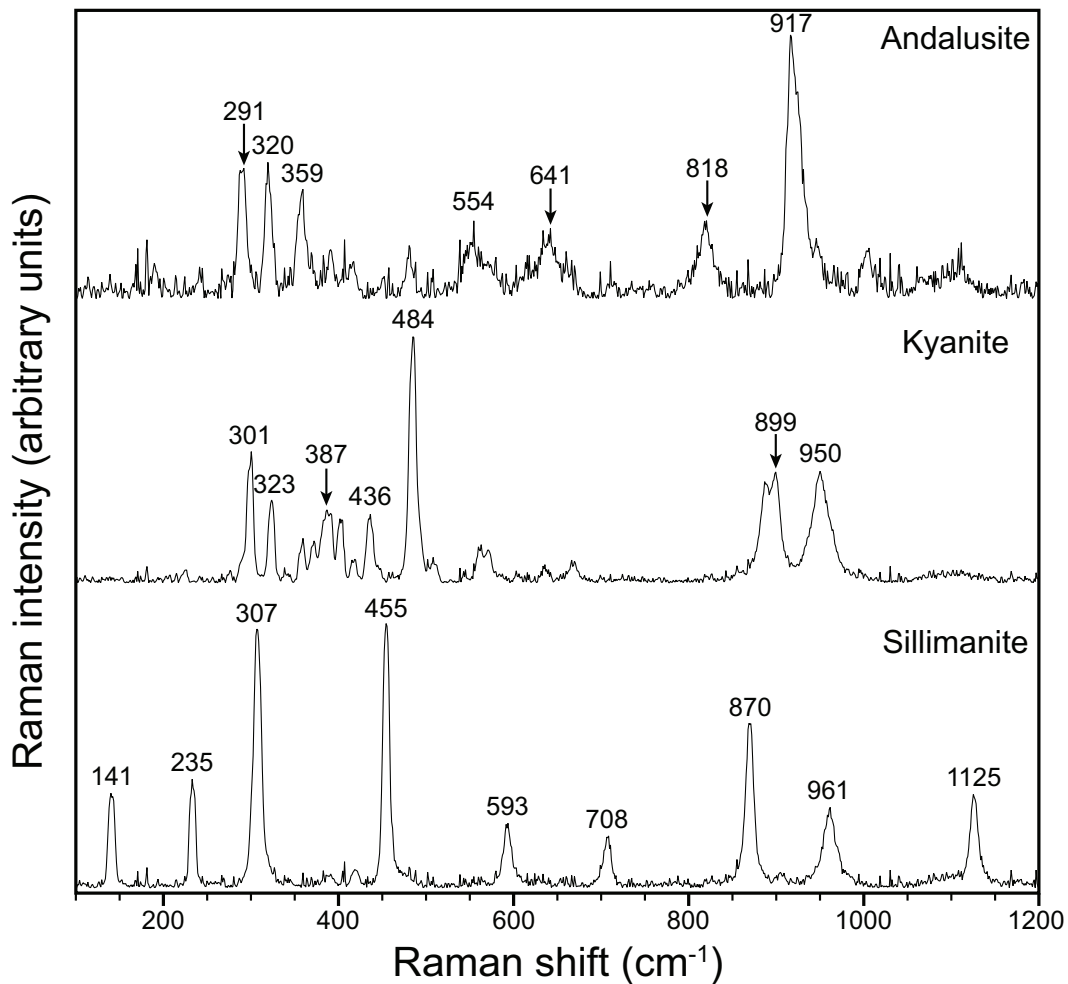


Figure 2.5: Typical Raman spectra of fine-grained aluminosilicate symplectites associated with biotite in the Grt-Crd-Opx granulites.

intergrowths, likely to be formed after the first phase of metamorphism, replace garnet, orthopyroxene, cordierite and spinel. These intergrowths are overgrown by garnet 2 that formed during the second phase of metamorphism (Fig. 2.4l). Another replacement texture occurs in the same rocks replacing cordierite as well as garnet, consisting mainly of coarse-grained, second generation of retrograde biotite intergrown with kyanite, sillimanite (Fig. 2.4j) and even andalusite (Fig. 2.4k). The different polymorphs of aluminosilicate are coarse enough to be identified optically. It was confirmed with Raman spectroscopy (Fig. 2.5).

2.4.2. Charnoenderbitic gneisses

The most common mineral assemblage of the charnoenderbitic gneisses of the Ongole domain is quartz-K-feldspar-plagioclase-orthopyroxene \pm garnet-biotite-ilmenite \pm magnetite \pm sulfides (Table 2.1). The relative proportions of K-feldspar and plagioclase vary considerably depending on the rock type. The charnoenderbitic gneisses are dominantly granoblastic with an equigranular to inequigranular texture. Grain size varies from very coarse-grained to fine-grained. K-feldspar is always perthitic.

Porphyroblastic garnet (garnet 1) commonly occurs in association with orthopyroxene or as isolated grains in the matrix (Fig. 2.4m). Like in metapelites, a distinct second generation of garnet (garnet 2) is also present in the charnoenderbitic gneisses. Small bead shaped garnet occurs as thin to thick overgrowths around garnet 1 and occasionally also around orthopyroxene and ilmenite (Fig. 2.4m). Garnet 2 has numerous small inclusions of quartz (Fig. 2.4m) making it texturally distinct from garnet 1. Inclusions within garnet 1 are less common, among which quartz, feldspar and fine-grained ilmenite are most common.

Orthopyroxene occurs in two textural settings. Coarse-grained orthopyroxene (orthopyroxene 1) and very fine-grained recrystallized orthopyroxene (orthopyroxene

2) occur around these coarse grains (Fig. 2.4m). Biotite is a retrograde phase partially or completely replacing garnet, orthopyroxene and K-feldspar.

The coarse-grained quartz and feldspars showing recrystallization along the grain boundaries (Fig. 2.4n) are evidence for late-stage deformation. Undulose extinction in quartz, feldspar and myrmekite are common in all the samples.

2.4.3. Mafic granulites

The most common mineral assemblage of the less abundant mafic rocks of the Ongole domain is orthopyroxene-clinopyroxene-plagioclase-ilmenite±hornblende±garnet along with minor amounts of biotite and quartz. The mafic rocks are dominantly fine to medium grained. Orthopyroxene, clinopyroxene, plagioclase (occasionally antiperthitic) and ilmenite form the granoblastic fabric.

Porphyroblastic garnet (garnet 1) is rare and is documented only in a single sample. It occurs in association with orthopyroxene and clinopyroxene. A bead shaped second generation of fine-grained garnet (garnet 2) occurs as narrow overgrowth around some zones of garnet 1 and occasionally around orthopyroxene and ilmenite.

Hornblende is present in varying amounts as a retrograde phase partially replacing orthopyroxene, clinopyroxene and garnet. Minor amounts of biotite are present in a few samples replacing pyroxene, garnet and hornblende.

2.5. Analytical techniques

Microprobe analyses of the constituent minerals of different rock types were performed using a JEOL Superprobe JXA 8900R at the Institute for Geosciences, University of Kiel. Operating conditions were 15-20kV accelerating voltage and a beam current of 15nA. The raw data were corrected using the CITZAF method (Armstrong, 1995).

To distinguish between the different fine-grained polymorphs of aluminosilicate occurring in the same samples, Raman spectroscopy measurements were conducted at the Institute for Mineralogy, University of Münster in Germany, using a Jobin Yvon HR800 Raman spectrometer and the 532.18 nm line of a Nd-YAG laser as the excitation source. The scattered Raman light was corrected in 180° backscattering geometry and dispersed by a grating of 1800 grooves/mm after passing through a 100µm entrance slit. The spectrometer was calibrated using a first order Raman band of silica at 520.7cm⁻¹ (King et al., 2011). Among the three polymorphs of aluminosilicate, sillimanite is characterized by the occurrence of four strong peaks at 236, 313, 872 and 963 cm⁻¹ and weaker peaks at 457, 595, 710 and 1128 cm⁻¹ (Downs, 2006). Andalusite is characterized by the presence of two intense peaks at 290 and 920 cm⁻¹ and weaker peaks at 320, 358, 551, 640, 818 and 1065 cm⁻¹. Kyanite is characterized by two strong peaks at 484 and 951 cm⁻¹, a range of weaker peaks from 301 to 435 cm⁻¹ and two small peaks at 900 and 1000 cm⁻¹ (Downs, 2006).

2.6. Mineral chemistry

2.6.1. Metapelitic granulites (Grt-Sil-Spl-Qz and Grt-Crd±Opx granulite)

Garnet

Porphyroblastic garnet (garnet 1) of Grt-Sil-Spl-Qz granulites is almandine rich, pyrope-almandine solid solution with minor amounts of spessartine ($X_{\text{Sps}} < 0.02$) (Table 2.2; Fig. 2.6a). It shows considerable variation in composition (X_{Alm} : 0.56-0.65, X_{Prp} : 0.30-0.39, X_{Grs} : 0.020-0.028, X_{Mg} : 0.32-0.40). However, garnet 1 of individual samples is chemically homogeneous. The garnet 2 corona is richer in Ca (X_{Grs} : up to 0.07) and slightly poorer in Mg and Fe than garnet 1 (Fig. 2.6a).

Garnet 1 of the Grt-Crd±Opx granulite is usually homogeneous and is slightly richer in Fe than the garnet of Sp-Qz bearing type (X_{Alm} : 0.61-0.65, X_{Prp} : 0.29-0.35, X_{Mg} : 0.31-0.36) (Table 2.2). The Ca content is fairly constant (X_{Grs} : 0.025-0.035) in the broad cores. Compared to garnet 1, a slight increase in the Fe contents is seen in garnet 2 (X_{Alm} : 0.65-0.67) accompanied by a slight decrease in the Mg contents (X_{Prp} : 0.27-0.33). Almost ideal cation sums for most garnet analyses in both metapelitic types indicate the absence of ferric iron.

Orthopyroxene

Orthopyroxene in the Grt-Crd-Opx granulites is rich in Fe (X_{Mg} : 0.50-0.56) and Al (Al_2O_3 : 6.5-8.2 wt.%; $\text{Al}^{\text{total}} = 0.30-0.37$ cations p.f.u) (Table 2.3; Fig. 2.6b), which correlates well with the Fe-Al rich bulk composition of the rock. The cores have a broad plateau and uniform Al_2O_3 content (7.5-8.2 wt.%) with a slight decrease

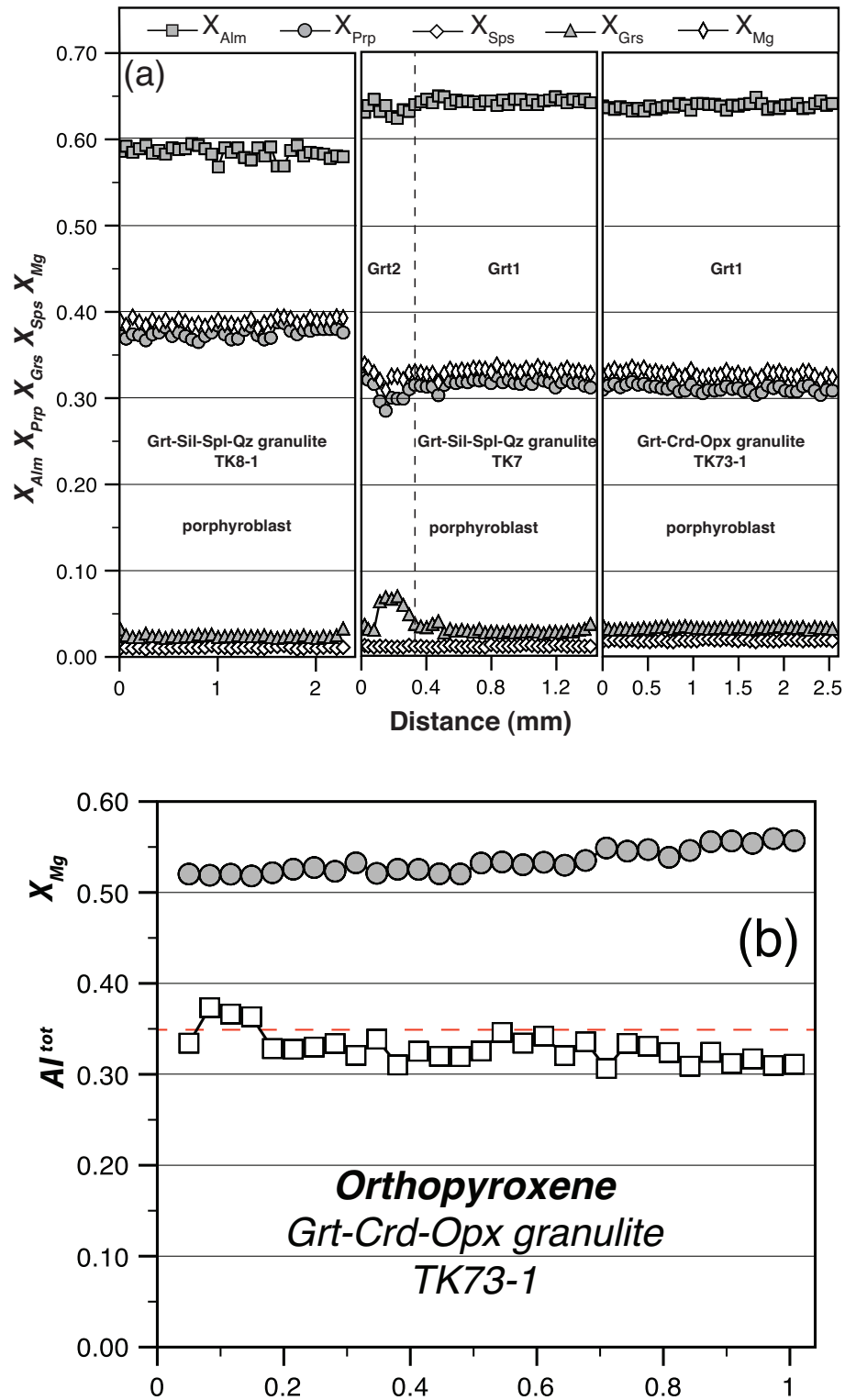


Figure 2.6: (a) Zoning profiles of garnet in Fe-Al rich metapelitic granulites. (b) Variation of X_{Mg} and Al^{tot} (p.f.u) in orthopyroxene from a Grt-Crd-Opx granulite (TK73-1).

towards the rim. Orthopyroxene in Opx-Al₂SiO₅-Spl-Bt symplectite shows similar X_{Mg} (0.51-0.54) and Al₂O₃ content (6.5-7.5wt.%), locally going up to ca. 9 wt.% (Table 2.3).

Porphyroblastic orthopyroxene in a Grt-Opx granulite is unzoned with respect to X_{Mg} having broad core plateau (ca. 0.50) and a slight increase towards the rim (up to 0.56).

Cordierite

Cordierite in the Grt-Crd±Opx granulite is always the most Mg rich phase (X_{Mg}: 0.70-0.82) (Table 2.4). Coarse-grained cordierite in the matrix surrounded by non Fe-Mg phase like plagioclase is strongly zoned with Mg poor cores (X_{Mg}: 0.70) to Mg rich rims (X_{Mg}: 0.80). Coarse-grained cordierite in contact with garnet 1 or orthopyroxene seems to have partially to completely re-equilibrated with only occasionally preserved Mg poor cores. Cordierite inclusions in garnet 1 are compositionally similar to cordierite rims (X_{Mg}: 0.80-0.82). The moderate analytical totals (97.25 – 98.9 wt.%) indicate the presence of some fluids (H₂O and CO₂) in the structural channels.

Spinel

Spinel in the Grt-Sil-Spl-Qz granulites (X_{Mg}: 0.30-0.40) is almost pure hercynite-spinel solid solutions (Hc: 56-67 mol %, Spl: 30-40 mol %) with low contents of gahnite (1-3.5 mol %), magnetite (1.3-4.6 mol %) and chromite (<1 mol %). X_{Mg} of spinel is lower than that of the coexisting garnet 1 (Table 2.5).

Coarse-grained spinel in Grt-Crd±Opx granulites (X_{Mg}: 0.22-0.30) is also hercynite rich (Hc: 64-67 mol %), hercynite-spinel solid solution (Spl: 20-30 mol %) (Table 2.5). These are richer in gahnite (1.7-6.6 mol %) and chromite (up to 3.6 mol %) than that of the Grt-Sil-Spl-Qz granulite with similar amounts of magnetite (up

to 5.5 mol %). Spinel (X_{Mg} : 0.20-0.22) occurring in Opx-Al₂SiO₅ symplectites replacing cordierite is richer in hercynite (Hc: 71-75 mol %, Spl: 20-21 mol %) and poorer in gahnite (2.3-2.5 mol %) than their coarse-grained counterparts (Table 2.5). The symplectitic spinel does not have chromite but the magnetite content is similar (1.5-4.8 mol %).

Feldspar

Mesoperthitic to perthitic K-feldspar in the metapelitic granulites show Na+Ca rich exsolution lamella (An₂₄₋₂₇Ab₇₂₋₇₄Or₁) in a K rich host (An₀₁Ab₀₆₋₁₁Or₈₈₋₉₄). Plagioclase is Na rich (An₂₈₋₃₉Ab₅₄₋₇₀Or₀₁). Antiperthite exhibits K rich exsolved blebs (An₁Ab₁₄Or₈₅) in a Na+Ca rich host (An₃₁Ab₆₇Or₂) (Table 2.6).

Biotite

In Grt-Sil-Spl-Qz granulites prograde biotite, found as rare inclusions in garnet 1, is rich in TiO₂ (ca. 5.5 wt.%) and has high X_{Mg} (0.75-0.77) values (Table 2.7). Retrograde biotite in the matrix replacing coarse-grained phases has similar TiO₂ contents and lower X_{Mg} values (0.68-0.70).

In Grt-Crd±Opx granulites prograde biotite included in garnet 1 has the highest X_{Mg} (0.80-0.82) among the different generations of biotite and the TiO₂ content varies from 2.5 to 3.1 wt.% (Table 2.7). Very fine-grained biotite occurring along with Opx-Al₂SiO₅-Spl in the symplectites replacing cordierite has low X_{Mg} (ca. 0.65) and moderate TiO₂ (2.0-3.0 wt.%). Coarse-grained second generation of retrograde biotite occurring along with needles of kyanite, sillimanite and andalusite and replacing garnet and cordierite has moderate X_{Mg} (0.67-0.74) and TiO₂ (2.7-3.7 wt.%).

Table 2.2: Representative garnet analyses

Rock Sample	Grt-Sil-Spl-Qz granulite			TK7			Grt-Crd-Opx granulite			TK35-6			Charnockite			Enderbite			Basic granulite		
	TK1	TK8-1	TK8-1	TK7	TK7	TK7	TK73-1	TK73-1	TK73-1	TK35-6	TK35-6	TK35-6	TK39-4	TK39-4	TK39-4	TK4B2	TK4B2	TK4B2	TK38-1	TK38-1	TK38-1
Texture	coarse grained core	Around spinel corona	coarse grained core	coarse grained core	coarse grained core	coarse grained core	late stage rim	coarse grained core	late stage rim	coarse grained core	late stage rim	coarse grained core	late stage rim	coarse grained core	late stage rim	coarse grained core	late stage rim	coarse grained core	coarse grained core	coarse grained core	late stage rim
Position Analysis	93	153	288	415	57	57	41	243	164	100	100	319	304	224	235	78	102	178			
SiO ₂	38.89	39.22	39.29	38.99	38.87	38.87	38.75	38.81	38.49	38.90	38.85	38.05	38.00	38.39	38.19	37.73	37.93	37.94			
ThO ₂	0.05	0.03	0.00	0.01	0.00	0.00	0.03	0.00	0.00	0.00	0.09	0.06	0.00	0.00	0.00	0.26	0.19	0.11			
Al ₂ O ₃	22.74	22.61	22.10	22.03	22.27	22.04	22.04	21.91	21.35	21.74	21.67	21.98	21.92	21.85	21.53	20.75	20.75	20.91			
FeO	26.95	27.46	27.57	28.71	29.56	28.48	28.48	30.22	31.04	29.55	29.92	33.25	29.72	30.10	28.38	31.71	31.79	29.76			
MnO	0.38	0.29	0.52	0.49	0.57	0.43	0.43	0.60	0.74	0.36	0.25	0.87	0.77	1.49	1.40	1.23	1.32	1.97			
MgO	10.07	9.37	9.93	8.90	8.13	7.66	7.66	8.00	7.33	8.57	8.73	4.70	3.83	5.87	4.74	2.30	2.30	2.55			
CaO	0.86	1.01	0.85	1.31	1.02	2.47	2.47	0.86	1.39	1.12	0.54	2.45	6.64	2.61	5.76	6.62	6.31	7.53			
Total	99.94	99.99	100.27	100.44	100.42	99.87	99.87	100.40	100.34	100.24	100.05	101.36	100.88	100.31	100.00	100.60	100.59	100.77			
Oxygen	12	12	12	12	12	12	12	12	12	12	12	12	12	12	12	12	12	12			
Si	2.98	3.00	3.01	3.00	3.00	3.00	3.00	3.01	3.00	3.01	3.01	2.98	2.98	3.00	3.00	3.01	3.02	3.01			
Ti	0.00	0.00	0.00	0.00	0.00	0.00	0.00	0.00	0.00	0.00	0.01	0.00	0.00	0.00	0.00	0.02	0.01	0.01			
Al	2.05	2.04	1.99	2.00	2.03	2.02	2.02	2.00	1.96	1.98	1.98	2.03	2.03	2.02	2.00	1.95	1.95	1.95			
Fe	1.72	1.76	1.76	1.85	1.91	1.85	1.85	1.96	2.03	1.91	1.94	2.18	1.95	1.97	1.87	2.11	2.12	1.97			
Mn	0.02	0.02	0.03	0.03	0.04	0.03	0.03	0.04	0.05	0.02	0.02	0.06	0.05	0.10	0.09	0.08	0.09	0.13			
Mg	1.15	1.07	1.13	1.02	0.94	0.89	0.89	0.92	0.85	0.99	1.01	0.55	0.45	0.68	0.56	0.27	0.27	0.30			
Ca	0.07	0.08	0.07	0.11	0.08	0.21	0.21	0.07	0.12	0.09	0.05	0.21	0.56	0.22	0.49	0.57	0.54	0.64			
Total	8.00	7.98	8.00	8.00	7.99	7.99	7.99	8.00	8.01	8.00	8.00	8.00	8.01	7.99	8.00	8.00	8.00	8.01			
XSpS	0.01	0.01	0.01	0.01	0.01	0.01	0.01	0.01	0.02	0.01	0.01	0.02	0.02	0.03	0.03	0.03	0.03	0.04			
XPrp	0.39	0.37	0.38	0.34	0.32	0.30	0.30	0.31	0.28	0.33	0.33	0.18	0.15	0.23	0.19	0.09	0.09	0.10			
XAlm	0.58	0.60	0.59	0.61	0.64	0.62	0.62	0.65	0.67	0.63	0.65	0.73	0.65	0.66	0.62	0.70	0.70	0.65			
XGrs	0.024	0.028	0.023	0.036	0.028	0.069	0.069	0.024	0.038	0.031	0.015	0.069	0.186	0.074	0.162	0.186	0.179	0.210			
XMg	0.400	0.378	0.391	0.356	0.329	0.324	0.324	0.320	0.296	0.341	0.342	0.201	0.187	0.258	0.229	0.115	0.114	0.132			

Table 2.3: Representative pyroxene analyses

Rock	Grt-Crd-Opx granulite		Charnockite		Enderbite		Mafic granulite		Mafic granulite (clinopyroxene)	
Sample	TK73-1	TK73-2	TK73-5	TK39-4	TK4B2	TK33-1	TK82-5	TK33-1	TK33-1	TK82-5
Texture	porph.		porph.		porph.		coarse grained		coarse grained	
Position	core	core	core	core	core	core	core	core	core	core
Analysis	179	100	81	221	368	367	238	427	273	225
SiO ₂	47.55	47.39	47.97	50.70	50.45	50.65	50.63	50.63	50.57	51.12
ThO ₂	0.03	0.08	0.00	0.43	0.19	0.11	0.10	0.44	0.03	0.28
Al ₂ O ₃	7.96	7.42	8.95	6.67	2.73	1.07	0.90	2.31	1.01	1.60
Cr ₂ O ₃	0.13	0.01	0.09	0.00	0.00	0.05	0.03	0.11	0.06	0.08
FeO	27.06	27.99	26.80	32.16	27.69	29.84	31.23	30.68	11.70	11.58
MnO	0.22	0.38	0.35	0.25	0.26	0.53	0.49	0.85	0.21	0.23
MgO	16.89	16.15	16.32	15.36	18.28	16.55	16.88	15.52	16.22	11.33
CaO	0.09	0.03	0.05	0.51	0.32	0.82	0.57	0.59	22.01	22.14
Na ₂ O	0.02	0.04	0.01	0.02	0.00	0.00	0.01	0.01	0.38	0.39
K ₂ O	0.02	0.00	0.00	0.00	0.00	0.00	0.02	0.00	0.00	0.00
Total	99.97	99.47	100.45	100.33	99.92	99.62	100.16	99.65	100.01	99.42
Oxygen	6	6	6	6	6	6	6	6	6	6
Si	1.81	1.82	1.81	1.97	1.93	1.97	1.98	1.98	1.97	1.95
Ti	0.00	0.00	0.00	0.01	0.01	0.00	0.00	0.01	0.00	0.01
Al	0.36	0.34	0.40	0.30	0.12	0.05	0.04	0.04	0.05	0.10
Cr	0.00	0.00	0.00	0.00	0.00	0.00	0.00	0.00	0.00	0.00
Fe	0.86	0.90	0.85	1.05	0.89	0.97	0.96	1.02	1.00	0.37
Mn	0.01	0.01	0.01	0.01	0.01	0.02	0.02	0.03	0.03	0.01
Mg	0.96	0.93	0.92	0.89	1.04	0.96	0.97	0.91	0.94	0.65
Ca	0.00	0.00	0.01	0.02	0.01	0.03	0.02	0.02	0.02	0.90
Na	0.00	0.00	0.00	0.00	0.00	0.00	0.00	0.00	0.00	0.03
K	0.00	0.00	0.00	0.00	0.00	0.00	0.00	0.00	0.00	0.00
Total	4.01	4.01	3.99	4.01	4.00	4.00	4.00	4.00	4.01	4.02
XMg	0.527	0.507	0.520	0.460	0.541	0.497	0.502	0.470	0.485	0.633
Al(tot)	0.36	0.34	0.40	0.30	0.12	0.05	0.04	0.04	0.05	0.10
Al(IV)	0.19	0.18	0.19	0.03	0.07	0.03	0.02	0.02	0.03	0.06
Al(VI)	0.17	0.16	0.21	0.01	0.05	0.02	0.02	0.02	0.01	0.04

porph., porphyroblastic

Table 2.4: Representative cordierite analyses

Rock	Grt-Crd-Opx granulite											
Sample	TK73-1			TK73-2		TK73-5			TK35-6		TK35-3	
Texture	porphyroblast		inc in Grt	porphyroblastic		porphyroblastic		inc in Grt	porphyroblastic		porphyroblastic	
	beside Grt			in matrix		beside Grt			beside Grt			
Position	core	rim		core	rim	core	rim		core	rim	core	rim
Analysis	40	55	330	186	171	138	147	186	190	198	273	278
SiO ₂	48.36	48.15	49.13	47.98	48.29	48.73	49.56	48.96	49.18	49.15	48.92	49.08
TiO ₂	0.00	0.06	0.00	0.00	0.00	0.00	0.02	0.00	0.00	0.05	0.00	0.00
Al ₂ O ₃	33.76	33.57	33.14	33.36	33.26	32.84	33.02	33.24	32.63	32.34	31.27	31.79
Cr ₂ O ₃	0.03	0.00	0.00	0.00	0.00	0.00	0.00	0.00	0.03	0.01	0.00	0.01
FeO	7.11	4.84	4.62	7.00	5.62	6.70	5.20	4.62	4.02	4.04	5.28	4.32
MnO	0.09	0.02	0.07	0.07	0.12	0.10	0.04	0.05	0.00	0.00	0.06	0.03
MgO	9.29	10.54	10.67	9.27	9.86	9.33	10.73	10.91	10.99	10.98	10.21	10.79
CaO	0.01	0.00	0.01	0.01	0.02	0.02	0.01	0.01	0.01	0.01	0.02	0.00
Na ₂ O	0.09	0.12	0.00	0.00	0.00	0.00	0.00	0.00	0.04	0.07	0.03	0.01
K ₂ O	0.02	0.01	0.00	0.00	0.00	0.00	0.00	0.00	0.00	0.02	0.00	0.00
Total	98.76	97.31	97.64	97.69	97.17	97.73	98.58	97.79	96.90	96.67	95.78	96.03
Oxygens	18	18	18	18	18	18	18	18	18	18	18	18
Si	4.93	4.93	5.00	4.94	4.97	5.01	5.01	4.98	5.03	5.04	5.09	5.07
Ti	0.00	0.00	0.00	0.00	0.00	0.00	0.00	0.00	0.00	0.00	0.00	0.00
Al	4.06	4.06	3.98	4.05	4.04	3.98	3.94	3.99	3.94	3.91	3.84	3.87
Cr	0.00	0.00	0.00	0.00	0.00	0.00	0.00	0.00	0.00	0.00	0.00	0.00
Fe	0.61	0.41	0.39	0.60	0.48	0.58	0.44	0.39	0.34	0.35	0.46	0.37
Mn	0.01	0.00	0.01	0.01	0.01	0.01	0.00	0.00	0.00	0.00	0.01	0.00
Mg	1.41	1.61	1.62	1.42	1.51	1.43	1.62	1.65	1.68	1.68	1.58	1.66
Ca	0.00	0.00	0.00	0.00	0.00	0.00	0.00	0.00	0.00	0.00	0.00	0.00
Na	0.02	0.02	0.00	0.00	0.00	0.00	0.00	0.00	0.01	0.01	0.01	0.00
K	0.00	0.00	0	0.00	0.00	0.00	0.00	0.00	0.00	0.00	0.00	0.00
Total	11.05	11.05	11.01	11.03	11.01	11.00	11.02	11.02	11.00	11.00	10.99	10.99
XMg	0.700	0.795	0.805	0.702	0.758	0.713	0.786	0.808	0.830	0.829	0.775	0.817

Table 2.5: Representative spinel analyses

Rock	Grt-Sil-Spl-Qz granulite				Grt-Crd±Opx granulite			
Sample	TK1	TK8-1	TK7	TK8C2	TK73-2	TK73-2	TK73-5	TK35-6
Texture	Coarse grained	Coarse grained	Coarse grained	Coarse grained	Coarse grained	Symp	Coarse grained	Coarse grained
Position	core	core	core	core	core	core	core	core
Analysis	34	408	240	196	223	125	118	159
SiO ₂	0.08	0.02	0.00	1.08	0.04	0.02	0.00	0.02
TiO ₂	0.01	0.02	0.01	0.00	0.05	0.00	0.03	0.02
Al ₂ O ₃	61.45	59.78	58.41	58.76	54.36	56.97	59.03	58.15
Cr ₂ O ₃	0.50	0.27	0.41	0.29	2.69	0.00	0.81	1.28
Fe ₂ O ₃	1.68	2.790	3.80	1.26	4.85	4.10	1.43	2.55
FeO	26.37	27.410	28.21	29.84	30.80	32.10	29.71	29.65
MnO	0.04	0.08	0.04	0.05	0.16	0.11	0.11	0.03
MgO	9.55	8.78	7.59	7.48	5.28	4.94	5.65	6.90
CaO	0.00	0.01	0.00	0.02	0.00	0.00	0.00	0.01
ZnO	1.21	0.49	1.47	1.63	1.78	1.16	3.15	0.91
Total	100.88	99.644	99.94	100.41	100.01	99.40	99.93	99.51
Oxygen	4	4	4	4	4	4	4	4
Si	0.00	0.001	0.00	0.03	0.00	0.00	0.00	0.00
Ti	0.00	0.000	0.00	0.00	0.00	0.00	0.00	0.00
Al	1.95	1.935	1.91	1.91	1.84	1.91	1.95	1.92
Cr	0.01	0.006	0.01	0.01	0.06	0.00	0.02	0.03
Fe ³⁺	0.03	0.058	0.08	0.03	0.10	0.09	0.03	0.05
Fe ²⁺	0.59	0.629	0.65	0.69	0.74	0.76	0.70	0.69
Mn	0.00	0.002	0.00	0.00	0.00	0.00	0.00	0.00
Mg	0.38	0.359	0.31	0.31	0.22	0.21	0.24	0.29
Ca	0.00	0.000	0.00	0.00	0.00	0.00	0.00	0.00
Zn	0.02	0.010	0.03	0.03	0.04	0.02	0.07	0.02
Total	3.00	3.00	3.00	3.00	3.00	3.00	3.00	3.00
XMg	0.39	0.36	0.324	0.309	0.232	0.215	0.253	0.293
Magnetite	0.027	0.029	0.040	0.013	0.050	0.044	0.015	0.027
Hercynite	0.558	0.598	0.611	0.671	0.658	0.722	0.673	0.653
Spinel	0.386	0.360	0.314	0.299	0.223	0.210	0.237	0.288
Gahnite	0.023	0.010	0.010	0.032	0.039	0.024	0.065	0.019
Chromite	0.006	0.003	0.004	0.003	0.030	0.000	0.009	0.014

Table 2.6: Representative feldspar analyses

Rock	Grt-Sil-Spl-Qz granulite						Grt-Crd±Opx granulite				
Sample	TK1		TK8C2		TK73-5		TK35-6				
Texture	Perthite in matrix		matrix Pl	rim	matrix Pl	matrix Kfs	matrix Pl	matrix Kfs	Antiperthite in matrix		
Analysis	host	exsol	core	rim	core	179	core	197	host	exsol	
	107	201	119	122	146		209	197	255	251	
SiO ₂	64.07	62.74	59.98	60.66	59.27	64.26	58.24	64.10	59.89	64.58	
Al ₂ O ₃	18.68	21.79	25.37	24.56	25.59	19.06	26.83	19.31	25.40	19.00	
Fe ₂ O ₃	0.05	0.10	0.07	0.04	0.08	0.06	0.13	0.10	0.02	0.07	
MgO	0.00	0.00	0.00	0.00	0.00	0.00	0.00	0.00	0.00	0.00	
CaO	0.11	5.37	6.61	5.65	6.77	0.09	8.16	0.41	6.36	0.30	
BaO	0.35	0.00	0.02	0.00	0.00	0.28	0.00	0.25	0.00	0.22	
Na ₂ O	1.57	8.93	7.51	7.92	7.30	2.21	6.88	2.00	7.70	1.50	
K ₂ O	14.70	0.17	0.14	0.23	0.26	13.74	0.23	13.68	0.41	14.39	
Total	99.53	99.40	99.71	99.06	99.27	99.71	100.47	99.85	99.78	100.07	
Oxygens	8	8	8	8	8	8	8	8	8	8	
Si	2.97	2.81	2.68	2.72	2.66	2.97	2.59	2.95	2.67	2.97	
Al	1.02	1.15	1.33	1.30	1.35	1.04	1.41	1.05	1.34	1.03	
Fe	0.00	0.00	0.00	0.00	0.00	0.00	0.00	0.00	0.00	0.00	
Mg	0.00	0.00	0.00	0.00	0.00	0.00	0.00	0.00	0.00	0.00	
Ca	0.01	0.26	0.32	0.27	0.33	0.00	0.39	0.02	0.30	0.01	
Ba	0.01	0.00	0.00	0.00	0.00	0.01	0.00	0.00	0.00	0.00	
Na	0.14	0.76	0.65	0.69	0.64	0.20	0.60	0.18	0.67	0.13	
K	0.87	0.01	0.01	0.01	0.01	0.81	0.01	0.80	0.02	0.85	
Total	5.02	5.01	4.99	4.99	4.99	5.02	5.00	5.01	5.00	5.00	
An	0.006	0.252	0.324	0.279	0.334	0.005	0.390	0.020	0.306	0.015	
Ab	0.139	0.738	0.667	0.708	0.651	0.196	0.597	0.178	0.671	0.135	
Or	0.856	0.010	0.008	0.013	0.015	0.800	0.013	0.801	0.023	0.850	

Sample	Charnockite			Enderbite			Mafic granulite		TK82-5		Antiperthite		
Texture	TK39-4		matrix Kfs	TK4B2		matrix Kfs	TK33-1		matrix Pl	TK82-5		Antiperthite	
Analysis	core	rim	94	core	rim	450	core	rim	core	rim	host	exsol	
	79	77		419	409		447	439	297	302	353	350	
SiO ₂	58.61	59.52	64.12	58.46	57.50	62.82	54.11	53.43	48.57	46.38	47.48	64.03	
Al ₂ O ₃	26.21	25.71	19.31	26.39	26.85	19.53	28.75	29.10	32.32	33.80	33.16	18.83	
Fe ₂ O ₃	0.08	0.19	0.20	0.13	0.34	0.12	0.16	0.19	0.12	0.31	0.34	0.07	
MgO	0.00	0.00	0.00	0.00	0.00	0.00	0.00	0.00	0.00	0.00	0.00	0.00	
CaO	7.74	7.17	0.66	7.86	8.25	0.72	10.96	11.44	15.52	17.54	16.15	0.08	
BaO	0.01	0.02	0.20	0.01	0.05	1.11	0.00	0.00	0.00	0.00	0.00	0.00	
Na ₂ O	7.07	7.57	2.18	6.50	6.22	1.12	4.92	4.66	2.64	1.68	2.14	0.96	
K ₂ O	0.22	0.16	13.51	0.41	0.27	14.63	0.27	0.33	0.09	0.06	0.05	15.45	
Total	99.94	100.33	100.18	99.76	99.48	100.05	99.17	99.15	99.26	99.77	99.33	99.42	
Oxygens	8	8	8	8	8	8	8	8	8	8	8	8	
Si	2.62	2.65	2.95	2.62	2.59	2.92	2.46	2.44	2.24	2.14	2.19	2.97	
Al	1.38	1.35	1.05	1.39	1.42	1.07	1.54	1.56	1.76	1.84	1.80	1.03	
Fe	0.00	0.01	0.01	0.00	0.01	0.00	0.01	0.01	0.00	0.01	0.01	0.00	
Mg	0.00	0.00	0.00	0.00	0.00	0.00	0.00	0.00	0.00	0.00	0.00	0.00	
Ca	0.37	0.34	0.03	0.38	0.40	0.04	0.53	0.56	0.77	0.87	0.80	0.00	
Ba	0.00	0.00	0.00	0.00	0.00	0.02	0.00	0.00	0.00	0.00	0.00	0.00	
Na	0.61	0.65	0.19	0.56	0.54	0.10	0.43	0.41	0.24	0.15	0.19	0.09	
K	0.01	0.01	0.79	0.02	0.02	0.87	0.02	0.02	0.01	0.00	0.00	0.91	
Total	5.00	5.01	5.02	4.98	4.98	5.02	4.99	4.99	5.00	5.01	5.00	5.00	
An	0.372	0.341	0.030	0.391	0.416	0.040	0.543	0.565	0.760	0.850	0.804	0.004	
Ab	0.000	0.000	0.000	0.000	0.001	0.020	0.000	0.000	0.000	0.000	0.000	0.000	
Or	0.615	0.650	0.188	0.585	0.568	0.099	0.441	0.416	0.234	0.147	0.193	0.086	

exsol: exsolution

2.6.2. Charnoenderbitic gneisses

Garnet

Garnet 1 in the charnoenderbitic gneisses is also almandine rich, pyrope-almandine-grossular solid solution with minor amounts of spessartine (X_{Sps} : 0.02-0.04). Garnet 1 in the charnockites is richer in Fe (X_{Alm} : 0.71-0.76, X_{Prp} : 0.13-0.20, X_{Mg} : 0.15-0.20) than their counterparts in the enderbites (X_{Alm} : 0.64-0.70, X_{Prp} : 0.21-0.24, X_{Mg} : 0.23-0.26) (Table 2.2; Fig. 2.6c). The Ca content is similar in both (X_{Grs} : 0.06-0.10). Broad core plateaus with uniform composition are preserved in large porphyroblasts with a slight increase in Ca content near the rims.

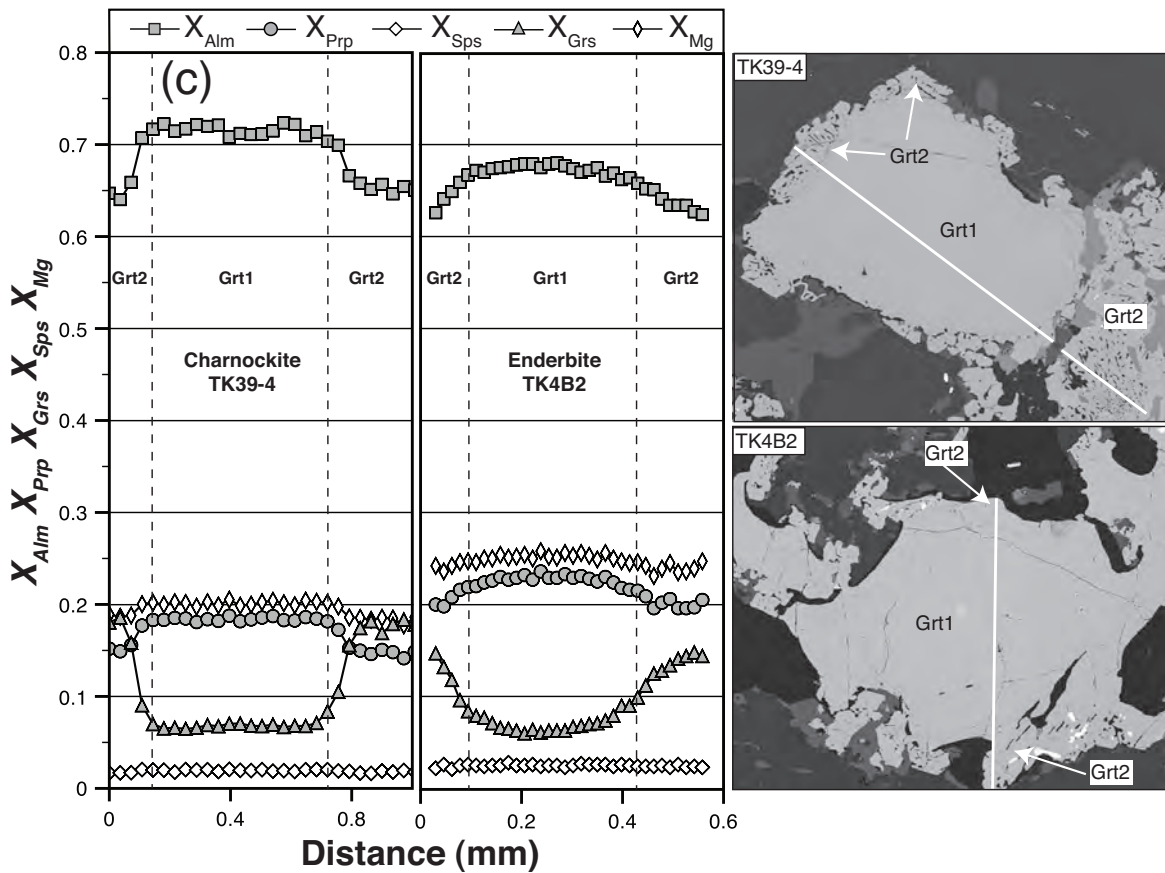


Figure 2.6: (c) Zoning profiles in garnet (BSE image at the side) from a charnockite (TK39-4) and an enderbite (TK4B2).

Garnet 2 forming overgrowths around garnet 1 is compositionally much different from garnet 1 in both charnockites and enderbites (Table 2.2). They are richer in Ca (X_{Grs} : 0.11-0.21 in charnockites; 0.10-0.15 in enderbites) and poorer in Fe and Mg (X_{Alm} : 0.66-0.73; X_{Prp} : 0.10-0.17 in charnockites; X_{Alm} : 0.59-0.67; X_{Prp} : 0.20-0.23 in enderbites) than garnet 1. The Mn content (X_{Sps} : 0.02-0.03) is similar in both. Garnet 2 preserves a broad compositional plateau at their maximum grossular content after a narrow transition zone at the contact with garnet 1.

Orthopyroxene

Orthopyroxene in the charnoenderbites is Fe rich, but orthopyroxene in enderbites is slightly richer in Mg (X_{Mg} : 0.52-0.55) than that of charnockites (X_{Mg} : 0.44-0.47). In most samples orthopyroxene is slightly zoned with respect to the Al_2O_3 content with cores of porphyroblasts preserving 3-5 wt.% Al_2O_3 and rims having only 1.0-2.5 wt.% (Table 2.3).

Biotite

Late-stage biotite in the enderbites is slightly richer in Mg and Ti contents (TiO_2 : 3-5 wt.%; X_{Mg} : 0.61-0.69) than that of charnockites (TiO_2 : 2.5-5 wt.%; X_{Mg} : 0.52-0.60). Rare biotite inclusions in garnet have rather similar compositions as the matrix biotite (Table 2.7).

Feldspar

Perthitic K-feldspar exhibits Na+Ca rich exsolution lamellae (An_{40}) in a potassium rich host ($\text{An}_{0.1}\text{Ab}_{6.13}\text{Or}_{86.94}$). Plagioclase in both charnockite and enderbite is nearly unzoned and Na rich ($\text{An}_{35.46}\text{Ab}_{52.63}\text{Or}_{02}$), but in enderbite it shows slightly more calcic compositions than charnockite (Table 2.6).

2.6.3. Mafic granulites

Garnet

Garnet 1 in a mafic granulite is almandine rich, pyrope-almandine-grossular solid solution (X_{Alm} : 0.69-0.71, X_{Prp} : 0.09-0.11, X_{Grs} : 0.17-0.18, X_{Mg} : 0.11-0.12) with minor amounts of spessartine (X_{Sps} : 0.03-0.04). Garnet 2 growing around pyroxenes has similar X_{Alm} (0.64-0.67), X_{Prp} (0.09-0.10) and X_{Mg} (0.11-0.13) but higher X_{Grs} (0.19-0.24) and X_{Sps} (0.04-0.06) (Table 2.2).

Clinopyroxene

Clinopyroxene is the most Mg rich mineral in the mafic rocks (X_{Mg} : 0.61-0.66) with low Al_2O_3 contents (1.0-2.5 wt.%) and no significant Fe-Mg zoning (Table 2.3).

Orthopyroxene

Orthopyroxene is compositionally homogeneous and is Fe rich (X_{Mg} : 0.47-0.51). Al_2O_3 content varies from 1.0-1.5 wt.% (Table 2.3).

Plagioclase

Plagioclase is quite calcic ($\text{An}_{55-85}\text{Ab}_{15-44}\text{Or}_{1-2}$). In some samples zoning is observed in plagioclase in contact with clinopyroxene having Ca poor cores (An_{74-76}) and Ca rich rims (An_{83-85} ; Table 2.6). Antiperthite exhibits K rich exsolved blebs ($\text{An}_1\text{Ab}_9\text{Or}_{91}$) in a Ca rich host ($\text{An}_{80-82}\text{Ab}_{17-19}\text{Or}_1$).

Amphibole

Amphibole in mafic rocks has variable composition and is rich in Al_2O_3 (13.5-15.3 wt.%). According to Leake et al. (1997) the amphiboles are calcic amphiboles and plot in the fields of hastingsite, magnesiohastingsite and ferrohastingsite (Table 2.8).

Table 2.8: Representative amphibole analyses

Rock	Basic granulite		TK38-1		
Sample	TK33-1		TK38-1		
Texture	late stage	late stage	coarse grained		
Position	rim	rim	core	core	core
Analysis	491	488	208	210	285
SiO ₂	39.47	38.22	41.61	43.09	41.97
TiO ₂	0.69	0.14	1.57	2.02	1.65
Al ₂ O ₃	13.45	14.91	10.99	9.38	10.46
Cr ₂ O ₃	0.09	0.00	0.00	0.02	0.00
FeO	18.13	19.91	19.27	19.29	19.03
MgO	8.63	7.77	8.79	9.08	8.98
MnO	0.12	0.12	0.15	0.22	0.16
CaO	11.70	11.26	11.46	11.09	11.31
Na ₂ O	1.09	0.95	1.69	1.80	1.55
K ₂ O	2.53	3.02	2.09	1.79	1.99
Total	95.90	96.30	97.61	97.78	97.10
Oxygen	23	23	23	23	23
Si	6.12	5.93	6.38	6.57	6.44
Al	2.46	2.73	1.99	1.69	1.89
Ti	0.08	0.02	0.18	0.23	0.19
Cr	0.01	0.00	0.00	0.00	0.00
Fe ³⁺	0.37	0.64	0.14	0.13	0.17
Fe ²⁺	1.98	1.94	2.33	2.33	2.28
Mg	1.99	1.80	2.01	2.06	2.06
Mn	0.02	0.02	0.02	0.03	0.02
	0.00	0.00	0.00	0.00	0.00
Ca	1.94	1.87	1.88	1.81	1.86
Na	0.33	0.29	0.50	0.53	0.46
K	0.50	0.60	0.41	0.35	0.39
Total	15.80	15.81	15.83	15.73	15.76
	Pargasite	Ferro pargasite	Ferro pargasite	Ferro edenite	Ferro pargasite

2.7. Thermobarometry

Several conventional geothermobarometers were applied to infer the peak (and retrograde) metamorphic conditions. These are summarized in Table 2.9 and 10.

2.7.1. Feldspar thermometer

The coarse perthite and mesoperthite grains in the metapelites and the charnoenderbites coexisting with plagioclase display fine exsolution lamellae (0.5-5 μ m wide). These lamellae are homogeneously distributed in the central parts of the grains while the rims are clear and devoid of any exsolution lamellae. As the exsolved lamellae were too fine-grained (<5 μ m) to be analyzed separately with the electron microprobe, reintegration was done by using a slightly defocussed beam (diameter 20 μ m; 20kv accelerating voltage) and analyzing a broader area comprising several exsolution lamellae. An average of 15-20 analyses on a single grain is generally sufficient to reproduce the original feldspar compositions. These were done along a few (2-3) line traverses through the central parts of the grains with 20-25 μ m steps between the points. The traverses were carefully selected to avoid imperfections in the polish and inhomogeneously exsolved parts. Several perthite grains and coexisting plagioclase grains were analyzed from each sample, mostly chosen from the leucosomes where the other K-Na bearing phases are absent, thereby limiting the K-Na exchange to plagioclase and K-feldspar. This process of reintegration was evaluated by Raase (1998) and was consistent with other processes of reintegration mentioned therein. This process of reintegration applied here is the easiest for homogeneously distributed fine scale exsolved lamellae.

Four samples each from metapelites and charnoenderbites have been analyzed for perthitic or mesoperthitic K-feldspar and plagioclase. After the reintegration of plagioclase lamellae in their K-feldspar host, the K-feldspar-plagioclase pairs were

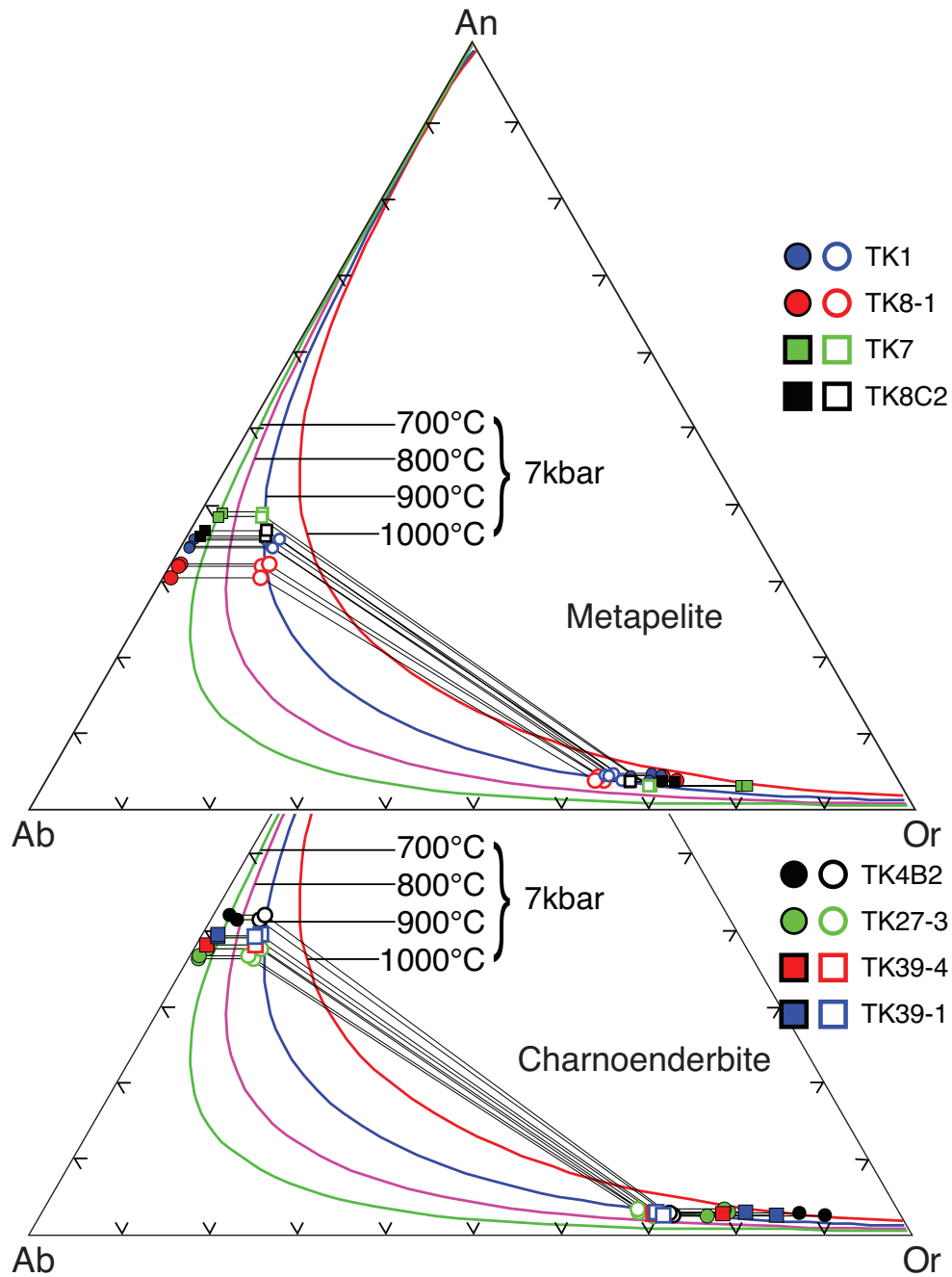


Figure 2.7: Analyzed (closed symbols) and calculated compositions (open symbols) of mesoperthite-plagioclase pairs from metapelites and charnoenderbites. Calculation of feldspar composition and temperature after Benisek et al. (2010).

plotted on the An-Ab-Or triangular diagram (Fig. 7). The isothermal sections of the solvus are calculated using the Margules parameters of Benisek et al. (2010) and drawn using the computer program SOLV CALC (Wen and Nekvasil, 1994) at 700°, 800°, 900° and 1000°C. The K-feldspar and plagioclase do not lie on the same isotherm, which is mainly caused by retrograde reequilibration due to differential

Table 2.9: Compositions (analyzed and calculated) and temperatures for feldspar pairs from metapelites and charnoenderbites of the Ongole domain

Sample	Feldspar	Analyzed composition			Calculated composition			T	Sample	Feldspar	Analyzed composition			Calculated composition			T
		Ab	Or	An	Ab	Or	°C	Ab			Or	An	Ab	Or	°C		
TK1	Kfs	0.274	0.679	0.047	0.317	0.636	937	TK8C2	Kfs	0.267	0.696	0.037	0.303	0.660	909		
	Pl	0.637	0.010	0.352	0.541	0.106	TK4B2		Pl	0.620	0.016	0.364	0.550	0.086			
	Kfs	0.281	0.680	0.038	0.312	0.649			905	Kfs	0.087	0.888	0.025	0.259	0.716	880	
	Pl	0.638	0.010	0.351	0.556	0.091			919	Pl	0.560	0.029	0.411	0.534	0.055		
	Kfs	0.264	0.690	0.045	0.327	0.627			921	Kfs	0.115	0.857	0.028	0.262	0.710	896	
	Pl	0.647	0.010	0.343	0.555	0.102			TK27-3	Pl	0.565	0.018	0.417	0.525	0.058		
	Kfs	0.299	0.657	0.044	0.324	0.632				921	Kfs	0.194	0.776	0.029	0.296	0.674	875
Pl	0.649	0.010	0.341	0.555	0.104	885		Pl		0.629	0.011	0.360	0.567	0.073			
TK8-1	Kfs	0.268	0.694	0.038	0.342	0.620	885	Kfs		0.197	0.769	0.033	0.295	0.671	896		
	Pl	0.689	0.009	0.302	0.588	0.110	908	Pl		0.612	0.015	0.373	0.552	0.075			
	Kfs	0.263	0.694	0.043	0.336	0.621	892	Kfs		0.221	0.755	0.024	0.282	0.694	860		
	Pl	0.673	0.010	0.317	0.569	0.111	TK39-4	Pl		0.626	0.010	0.364	0.570	0.066			
	Kfs	0.250	0.712	0.038	0.332	0.630		892	Kfs	0.202	0.771	0.027	0.280	0.693	878		
Pl	0.669	0.011	0.320	0.579	0.104	897		Pl	0.611	0.011	0.378	0.555	0.067				
TK7	Kfs	0.181	0.788	0.031	0.283	0.686		897	TK39-1	Kfs	0.175	0.796	0.029	0.276	0.695	891	
	Pl	0.589	0.025	0.386	0.544	0.070		895		Pl	0.593	0.018	0.389	0.542	0.066		
	Kfs	0.174	0.795	0.031	0.285	0.684	895	Kfs		0.142	0.833	0.025	0.270	0.705	873		
TK8C2	Kfs	0.253	0.711	0.036	0.304	0.660	905	Pl	0.591	0.017	0.392	0.550	0.061				
	Pl	0.628	0.015	0.356	0.555	0.088											

K-Na exchange (Kroll et al., 1993). The retrodiffusion method of Kroll et al. (1993) was systematically applied using the excel spreadsheet of Benisek et al. (2010). Readjusted compositions lie on the same isotherm. Temperatures were calculated after Benisek et al. (2010) at 7 kbar pressure. The resulting temperatures vary between 850-950°C (Table 2.9; Fig. 2.7).

2.7.2. Garnet-orthopyroxene thermometer

The garnet-orthopyroxene Fe-Mg exchange thermometer was applied to several orthopyroxene bearing metapelitic samples (TK73-1, TK73-5 and TK82-2). The estimated temperature ranges for the first stage of metamorphism, taking the unzoned cores of minerals, are at 950-980°C, 980-990°C, and 860-870°C respectively, using the calibration of Lee and Ganguly (1988) at 6kbar pressure.

In the charnoenderbites, garnet 1 and orthopyroxene 1 yielded temperatures between 790 and 840°C at 7 kbar pressure using the calibration of Lee and Ganguly (1988). These temperature estimates are ~100°C lower than those from feldspar thermometry. Temperatures estimated from garnet 2 and orthopyroxene 2 by using the same calibration are lower, between 750 and 790°C at 9 kbar pressure. Though it has been discussed in detail in earlier studies that Fe-Mg exchange thermometers often do not preserve the peak temperatures due to retrograde Fe-Mg exchange (Fitzsimons and Harley, 1994; Harley, 1998), the garnet-orthopyroxene thermometer gives a rough idea about the peak metamorphic temperature.

2.7.3. Al solubility in orthopyroxene thermometer

The Al content and X_{Mg} of orthopyroxene coexisting with garnet, sillimanite (or cordierite) and quartz are potential indicators of metamorphic P-T conditions (Harley, 1998; Hensen and Harley, 1990). For the estimates coarse-grained orthopyroxene (Al_2O_3 : 7-8.2 wt.%, $Al^{VI} = 0.1- 0.18$ cation p.f.u) coexisting with garnet and cordierite has been used, because these are likely to preserve near peak composition. Application of the thermometer by Aranovich and Berman (1997) produced temperatures of around 940-990°C (TK73-1), 970-980°C (TK73-5) and 900-920°C (TK82-2) (Table 2.10). Application of revised isopleth diagrams of Harley (2004a) on the core compositions of orthopyroxene in sample TK73-1 and TK73-5

indicates UHT metamorphic conditions of 900-950°C at 7kbar pressure. The obtained temperature estimates are nearly similar to the temperatures obtained from garnet-orthopyroxene Fe-Mg exchange and the feldspar thermometer.

Table 2.10: Summary of calculated thermobarometric data

Sample	Texture	Mineral composition						Temperature			Pressure				
		Grt		Opx		Pl	P	Grt-Opx		T	Grt-Opx-Pl-Qz		Grt-A ₂ SiO ₅ -Qz-Pl		
		XMg	XGrS	XMg	Xal (tot)	Xan	(kbar)	LG	AB	(°C)	B	PC	GS	HC	KN
Grt-Opx-Crd granulite															
TK73-1	Grt-Opx-Pl (core)	0.32	0.033	0.51	0.33	0.39	6	950	960	950	5.6	6.3			
TK73-1	Grt-Opx-Pl (core)	0.33	0.030	0.50	0.33	0.38	6	990	970	950	5.5	6.1			
TK73-5	Grt-Opx-Pl (core)	0.33	0.032	0.50	0.35	0.39	6	970	980	950	5.7	6.6			
TK73-5	Grt-Opx-Pl (core)	0.32	0.031	0.49	0.34	0.38	6	980	980	950	5.4	6.2			
TK73-1	Grt-Opx-Pl (rim)	0.33	0.033	0.53	0.32	0.37	6	920	940	950	5.6	6.3			
TK73-5	Grt-Opx-Pl (rim)	0.32	0.033	0.51	0.30	0.38	6	930	940	950	5.6	6.3			
Grt-Opx granulite															
TK82-2	Grt-Opx-Pl (core)	0.27	0.063	0.48	0.22	0.45	6.5	880	910	900	6.5	8			
TK82-2	Grt-Opx-Pl (rim)	0.21	0.210	0.52	0.09	0.43	8	740	820	800	8.4	11.7			
Grt-Sil-Spl-Qz granulite (M1)															
TK1	Grt-Pl (core)	0.40	0.024			0.33				950			6.4	6.6	7.7
TK8-1	Grt-Pl (core)	0.39	0.023			0.31				950			6.4	6.8	7.9
TK7	Grt-Pl (core)	0.34	0.030			0.38				950			5.8	6.4	7.3
TK8C2	Grt-Pl (core)	0.33	0.027			0.34				950			5.6	6.4	7.3
Grt-Sil-Spl-Qz granulite (M2)															
TK8-1	Grt-Pl (rim)	0.36	0.040			0.25				800			8.3	8.4	9.5
TK7	Grt-Pl (rim)	0.30	0.063			0.34				800			8.8	9.1	10
Charnoeenderbite (M1)															
TK39-4	Grt-Opx-Pl (core)	0.21	0.071	0.44	0.04	0.37	7	800		900	6.8	8.4			
TK4B2	Grt-Opx-Pl (core)	0.26	0.074	0.51	0.06	0.39	7	800		900	7.0	8.4			
TK8A	Grt-Opx-Pl (core)	0.26	0.064	0.49	0.18	0.41	7	830		900	6.4	8.1			
Charnoeenderbite (M2)															
TK39-4	Grt-Opx-Pl (rim)	0.18	0.183	0.46	0.43	0.34	9	750		750	8.6	11.4			
TK4B2	Grt-Opx-Pl (rim)	0.23	0.166	0.53	0.07	0.39	9	750		750	8.3	10.6			
TK8A	Grt-Opx-Pl (rim)	0.23	0.142	0.50	0.10	0.41	9	790		750	8.0	10.1			

LG, Lee and Ganguly (1988); AB, Aranovich and Berman (1997); B, Bhattacharya et al. (1991); PC, Perkins & Chipera (1985); GS, Ganguly and Saxena (1984); HC, Hodges and Crowley (1985); KN, Koziol and Newton (1988); M1, First metamorphic event (UHT); M2, Second metamorphic event.

2.7.4. Garnet-orthopyroxene-plagioclase-quartz barometer

For Grt-Opx bearing metapelites pressures are estimated by the garnet-orthopyroxene-plagioclase-quartz barometer (Bhattacharya et al., 1991; Perkins and Chipera, 1985) yielding values of 5.5-6.3 kbar (TK73-1), 5.4-6.6 kbar (TK73-5) and 6.5-8.0 kbar (TK82-2) at 950°C. Garnet 2 and orthopyroxene 2 in sample TK82-2 yielded pressures of 8.4-11.7 kbar at 800°C, which is higher than the pressures obtained from garnet 1 and orthopyroxene 1.

In charnoenderbites, garnet 1 and orthopyroxene 1 yielded pressures of 6.4-8.4 kbar at 900°C using the same calibrations. The X_{Grs} rich garnet 2 and the orthopyroxene 2 yielded pressures of 8.0-11.4 kbar at 750°C.

2.7.5. Garnet – Al_2SiO_5 – quartz – plagioclase (GASP) barometer

Due to the absence of orthopyroxene and the presence of coarse-grained sillimanite in the Grt-Sil-Spl-Qz bearing metapelitic granulites, this barometer was applied to garnet 1 and plagioclase in association with sillimanite and quartz in several samples (e.g. TK1, TK7, TK8-1, TK8C2) (Table 2.10). Peak metamorphic temperatures for the first stage of metamorphism as obtained through feldspar thermometry lie between 900-950°C. The corresponding pressures are estimated to be 5.6 to 8.0 kbar by using several calibrations (Ganguly and Saxena, 1984; Hodges and Crowley, 1985; Koziol and Newton, 1988). Application of GASP barometer to garnet 2, occurring as rims, yielded higher pressures of 8.5 to 10.0 kbar at 800°C using the above calibrations.

2.8. Thermodynamic modeling – P-T pseudosection

To further constrain the P-T evolution of the Fe-Al rich granulites, pseudosections in the $\text{Na}_2\text{O}-\text{CaO}-\text{K}_2\text{O}-\text{FeO}-\text{MgO}-\text{Al}_2\text{O}_3-\text{SiO}_2-\text{TiO}_2-\text{H}_2\text{O}$ (NCKFMASHT) system have been calculated using the THERIAK-DOMINO software (v – 01/08/09; De Capitani 2009) of De Capitani and Brown (1987) with the internally consistent thermodynamic dataset of Holland and Powell (1998) (filename: tcdb55c2d). The activity models of Baldwin et al. (2005) are used for feldspar, White et al. (2007) for garnet, biotite, orthopyroxene, ilmenite, spinel and liquid and activity models of Holland and Powell (1998) for cordierite.

The bulk compositions of the samples used for calculation are provided on the diagram (Fig. 8a,b). Additional components (eg, Mn, Zn) are present only in trace amount (<1 wt.%), and thus will not significantly affect the topology of the pseudosections. Chemical analyses of the minerals also reveal negligible Fe^{3+} in the bulk composition. The water content is taken from the ‘loss of ignition’ (LOI) during XRF analyses. The low water contents are consistent with the granulite facies conditions. Still thermodynamic modeling of high-grade rocks has several problems. In migmatitic rocks melt loss is a common phenomenon during the prograde evolution. Thus constraining the prograde path is often uncertain. The main chemical change during retrogression is the increase in water content. So the stability conditions of the peak assemblage and the retrograde evolution could not be modeled by using the same water content. Moreover, the post peak evolutions of high-grade dry rocks are characterized by the development of mineralogical and chemical microdomains that may form in response to chemical potential gradients rather than changing P-T conditions (Dunkley et al., 1999), often leading to misinterpretations. Therefore, the P-T conditions from pseudosections have been supplemented by conventional thermobarometric calculations, as discussed above, for the observed two metamorphic events.

assemblage and chemical compositions of the minerals. The stability of Spl+Qz indicates peak temperatures of metamorphism above 970°C and pressures above 6.3kbar. The composition of garnet 1 (X_{Mg}) coexisting with Spl+Qz indicates that the peak metamorphic condition lies in the Grt-Sil-Ilm-Kfs-Pl-Spl-Qz-Liq field at P-T conditions of 970-1000°C and 6.4-6.7 kbar. X_{Mg} of 0.38-0.39 documented from the cores of garnet 1 lies well within the field. Subsequent cooling led to the destabilization of Spl+Qz assemblage and the development of concentric sillimanite and garnet rims around spinel marking the entry into the Grt-Sil-Ilm-Kfs-Pl-Qz-Liq field. The X_{Mg} of the garnet rims vary from 0.35-0.36, which is consistent with this field.

The inclusion of the Spl+Qz assemblage within porphyroblastic garnet indicates major garnet growth during cooling outside the stability field of Spl+Qz. This inference is consistent with the isopleths of vol% of garnet (inset in Fig. 8a) that increases from 15 to 35% from inside the Spl-Qz stability field to just outside the stability field at lower temperatures. Biotite is only stable up to 800°C giving a minimum temperature for the biotite-free assemblage. As cordierite is missing as a late-stage product a strong pressure drop after peak metamorphism seems unlikely. Thus the P-T pseudosection indicates that a near-isobaric heating-cooling path is most likely.

2.8.2. Grt-Sil-Spl-Qz granulite (TK7)

This sample exhibits several reaction textures that allow a more detailed reconstruction of the P-T evolution. Similar to sample TK8-1 (Fig. 2.8a) the peak metamorphic conditions are constrained by the stability of Spl+Qz in the Grt-Sil-Ilm-Kfs-Pl-Spl-Qz-Liq field at P-T conditions of 6.3-6.8 kbar and 970-1000°C (Fig. 2.8b). The cores of porphyroblastic garnet exhibiting the highest X_{Mg} values of 0.36 are consistent with the calculated X_{Mg} isopleths, which pass through the stability

field of the assemblage. The rims, showing slightly lower X_{Mg} values (0.34-0.35), indicate garnet growth during cooling outside the Spl-Qz stability field in the Grt-Sil-Ilm-Kfs-Pl-Qz-Liq field. The observed X_{Grs} (0.02-0.03) also matches well (Fig. 2.8b).

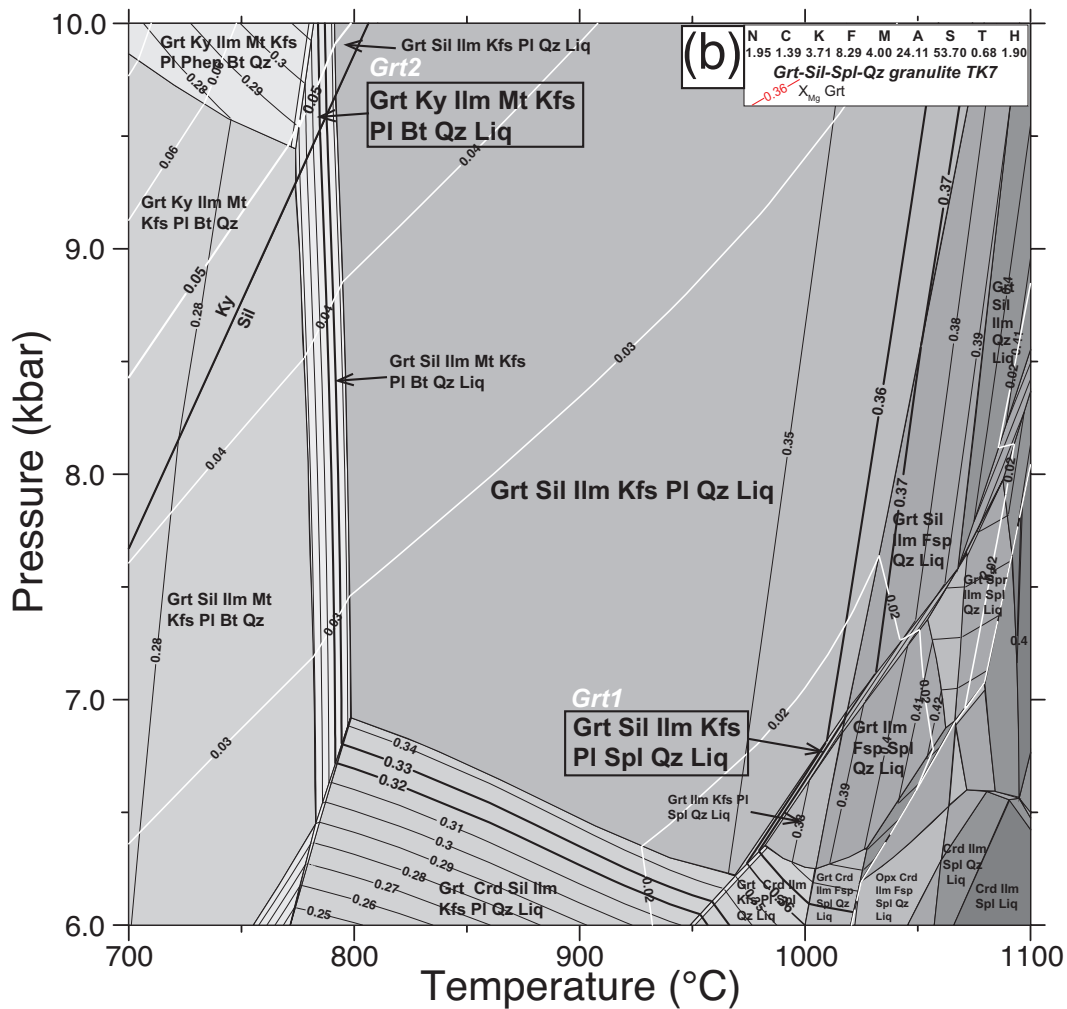


Figure 2.8 (continued): (b) Grt-Sil-Spl-Qz granulite (TK7). The bold contour lines in both diagrams represent the actual X_{Mg} and X_{Grs} values obtained from microprobe analyses.

The second generation of garnet with X_{Mg} values in the range of 0.32-0.33 has higher X_{Grs} of ca. 0.05. The intersection of these isopleths lies in the Grt-Ky-Ilm-Mt-Kfs-Pl-Bt-Qz-Liq field near the Sil-Ky phase boundary. This marks the P-T

conditions for the development of the garnet 2 at 9.5 kbar and 770-780°C. The presence of Bt-Ky symplectites replacing locally the primary coarse-grained assemblage is in agreement with the conditions during the second metamorphism near the Sil-Ky phase transition zone.

2.9. Discussion and conclusions

Petrographic observations as well as thermobarometric results indicate that the Ongole domain experienced two phases of mineral growth under granulite facies condition. The first one occurred under UHT metamorphic condition at low pressures and the second one at a higher pressure but lower temperature.

2.9.1. UHT stage of metamorphism.

Petrological data from the metapelitic granulites and the charnoenderbites from the Ongole domain provide several lines of evidence indicating that this domain experienced crustal metamorphism at UHT conditions. The most convincing piece of evidence is the stability of spinel+quartz bearing assemblages, frequently included in garnet 1 in many of the metapelitic granulites. Though spinel and quartz are now separated from each other by narrow garnet and sillimanite rims, the texture clearly indicates that spinel and quartz were in equilibrium at the peak metamorphic conditions.

Available petrogenetic grids suggest that spinel+quartz is stable at $T > 900^\circ\text{C}$ and $P < 8\text{ kbar}$ (Hensen and Green, 1973) or $T > 950^\circ\text{C}$ at 7 kbar (Bertrand et al., 1991; Hensen and Harley, 1990) or $T > 900^\circ\text{C}$ at $P > 5\text{ kbar}$ (Waters, 1991). Recent thermodynamic calculations in the KFMASH system also support high temperature conditions for the stability of this assemblage (Aït-Djafer et al., 2009; Kelsey, 2008). The computed P-T pseudosection in the NCKFMASH system for the Grt-Sil-Spl-Qz

granulite indicate metamorphic conditions of 970-1000°C at 6.4-6.7 kbar, which is in agreement with the already above mentioned grids and phase diagrams. Similar spinel+quartz assemblages, often enclosed in garnet have also been reported from many other granulite terrains such as Rogaland, southern Norway (Kars et al., 1980), Napier complex (Ellis et al., 1980), Rayner complex and Prydz Bay (Clarke et al., 1989; Stüwe and Powell, 1989), Eastern Ghats Belt (Dasgupta et al., 1995; Lal et al., 1987), Madurai block (Tsunogae and Santosh, 2009), Highland complex (Sajeev and Osanai, 2004), Labwor Hills (Sandiford et al., 1987), Madagascar (Jöns and Schenk, 2011), Namaqualand (Waters, 1991), Brazil (Barbosa et al., 2006) and Hoggar (Aït-Djafer et al., 2009). In many of these occurrences, the association is considered as a strong evidence for UHT metamorphism.

The stability of the spinel+quartz assemblage alone as a diagnostic indicator of UHT metamorphism is debatable as the available experimental and thermodynamic data indicate that the incorporation of elements such as Fe^{3+} , Zn and Cr in spinel extends the stability field of spinel+quartz toward higher pressure and/or lower temperature (e.g. Hensen and Harley, 1990; Nichols et al., 1992; Sengupta et al., 1991). The spinel of the metapelites of the Ongole domain has very low ZnO and Cr_2O_3 contents in some samples ($\text{ZnO} < 0.49$ wt.%; $\text{Cr}_2\text{O}_3 < 0.4$ wt.%). So, this assemblage is considered as an evidence for UHT metamorphism along with other evidence discussed below.

Feldspar thermometry of mesoperthite-plagioclase pairs also provides evidence for UHT metamorphism in metapelites as well as in charnoenderbites. The temperatures ($T = 850\text{-}950^\circ\text{C}$) calculated according to Benisek et al. (2010) are slightly lower than the temperatures calculated by thermodynamic modeling, which is a commonly encountered feature as discussed by Harley, (2004b). The calculated feldspar temperatures ($T = 850\text{-}900^\circ\text{C}$) from the charnoenderbites are slightly lower ($\sim 30^\circ\text{C}$) than those from the metapelites (Table 2.9).

The high Al_2O_3 content of orthopyroxene (up to 8.2 wt.% in TK73-1) coexisting with garnet and cordierite in a metapelitic granulite is yet another indicator of UHT

metamorphism in the Ongole domain. The established P-T conditions of $T > 950^{\circ}\text{C}$ at 7 kbar (Aranovich and Berman, 1997; Harley, 2004a) is consistent with the other P-T estimates discussed above. In addition, conventional thermobarometric methods like garnet-orthopyroxene Fe-Mg exchange thermometry by Lee and Ganguly (1988) yield temperatures from 950 to 990°C at 6 kbar (Table 2.10).

Corundum+quartz, now separated by garnet rims (Fig. 2.4d) is present in the Ongole domain metapelites similar to many other UHT terrains (Guiraud et al., 1996; Motoyoshi et al., 1990; Perchuk et al., 1989; Shaw and Arima, 1998; Tsunogae and Van Reenen, 2006). Still the application of corundum+quartz as the only UHT indicator remains debatable (Kelsey, 2008; Kriegsman and Hensen, 1998) as the assemblage may be metastable due to late-stage crystallization of quartz from anatectic melts.

Combining the several lines of evidence we infer that the granulites of the Ongole domain experienced peak metamorphic conditions at $T=950\text{--}1000^{\circ}\text{C}$ at 6-7.5 kbar pressure. These estimates are almost consistent with the available P-T data from metapelitic granulites of Kondapalle by Sengupta et al. (1999). These authors estimated the temperatures from reintegrated spinel compositions that contain >19 mol % Fe_2TiO_4 and >10 mol % Al_2O_3 in spinel structure, which requires temperatures in excess of 1000°C .

2.9.2. Higher pressure - lower temperature stage of metamorphism.

The key evidence for a second phase of mineral growth at higher pressure but lower temperature comes from the distinct garnet 2 in metapelites and charnoenderbites, developing as rims or overgrowths over garnet 1 or replacing retrograde biotite (2.6c). In metapelites garnet 2 has higher X_{Grs} and slightly lower X_{Mg} than garnet 1

(Fig. 2.6a). Also in charnoenderbites garnet 2 has distinctly higher X_{Grs} and lower X_{Mg} than garnet 1 (Fig. 2.6c).

As shown by the computed P-T pseudosection for the metapelite, the isopleths of X_{Mg} and X_{Grs} for garnet 2 intersect in the stability field of kyanite, just above the sillimanite-kyanite phase transition at 9.5 kbar pressure and 780°C. This piece of evidence is supported by the presence of Bt-Ky symplectites replacing the prograde coarse-grained assemblage.

P-T conditions as obtained from several conventional geothermobarometers further support the second metamorphic event. In the metapelite, the GASP barometer using garnet 2 and rim plagioclase yield pressures from 8.5 to 10.0 kbar at 800°C using several calibrations (Ganguly and Saxena, 1984; Hodges and Crowley, 1985; Koziol and Newton, 1988). In the charnoenderbite, garnet-orthopyroxene-plagioclase-quartz barometer (Bhattacharya et al., 1991; Perkins and Chipera, 1985) using second generation minerals yield pressures of up to 11.4 kbar at 750°C (Table 2.10).

2.9.3. P-T trajectories and geodynamic interpretation

Detailed petrographic observations, geothermobarometric data as well as results from thermodynamic modeling (P-T pseudosection) have been compiled to reconstruct the P-T trajectory of the granulites from the Ongole domain (Fig. 2.9). Though there are good correlations between the textures and the P-T conditions, it is not easy to conclude on petrological data alone whether these are related to two metamorphic events or two phases of mineral growth during a single polyphase metamorphism. However, zircon and monazite dating performed on the same rocks (chapter 3) indicates two metamorphic events separated by 60-80 Ma rather than a single polyphase metamorphism. Despite good petrological and geochronological evidence for two metamorphic events, the reconstruction of the detailed P-T path for

each of the two events is not straightforward and univocal, as some late-stage textures could be equally attributed to the first or the second event.

The prograde path of the UHT event is difficult to trace as most of the mineral assemblages have equilibrated and crystallized at the peak metamorphic conditions except for the inclusions in garnet and cordierite. The absence of cordierite as inclusions or in the retrograde mineral assemblage of the Grt-Sil-Spl-Qz granulites

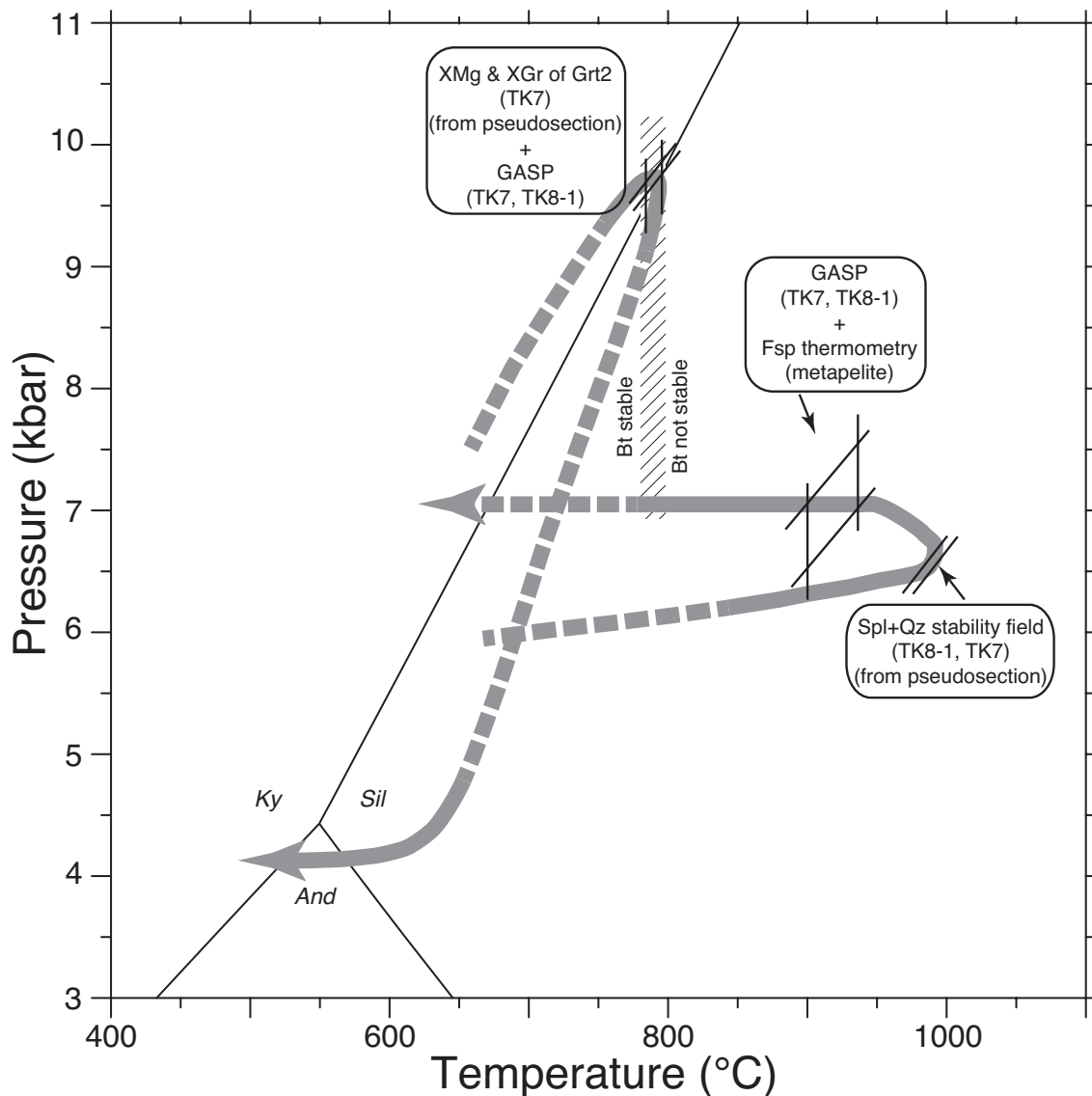


Figure 2.9: Pressure-temperature evolution of the rocks from the Ongole domain during two subsequent metamorphic events as deduced from P-T pseudosections, feldspar thermometry, conventional geothermobarometry and reaction textures in metapelites and charnoenderbites.

indicates that a near isobaric heating-cooling path is most likely since cordierite bearing assemblages would only form at low pressures (Fig. 2.8a). Whether the rocks cooled down to the kyanite stability field after peak metamorphism is a matter of speculation. A possible evidence of reaching the kyanite stability field is the formation of late Bt-Ky symplectites. But the symplectites could have formed during the second metamorphism at higher pressures, which is near the Ky-Sil boundary at a temperature range where biotite is also stable in this rock (Fig. 2.8b). Though it has not much relevance, we prefer to attribute the formation of these symplectites after the first metamorphic event.

After the peak conditions of the second metamorphic event that are well constrained, not much information is available about the P-T path. But late-stage sillimanite, andalusite and kyanite along with retrograde biotite, forming at the expense of garnet and cordierite are present in the same rocks. The subsequent retrograde formation of the three polymorphs of aluminosilicates is best explained by a near isobaric cooling path slightly below the aluminosilicate triple point (Schenk, 1989). If this is attributed to the late-stage of the second metamorphic event, then it should have occurred subsequent to near isothermal decompression from peak metamorphic conditions. The late-stage polymorphs of aluminosilicate could also have formed after the first metamorphism. In this case, decompression followed by near isobaric cooling is expected to have occurred during the late-stage evolution after the first metamorphism. However, this would imply that cordierite should have formed as a retrograde mineral in the Grt-Sil-Spl-Qz granulite (Fig. 2.8a,b), which is not the case. Therefore, the aluminosilicates are more likely to be formed after the second metamorphism.

Opx-Sil \pm Ky symplectites replacing cordierite in the Grt-Crd \pm Opx granulite can form during the peak conditions of the second metamorphism or at lower pressures under extremely dry conditions (Ballèvre et al., 1997). As no andalusite has been detected in the symplectites, formation at higher pressures, during the second metamorphic event, is more likely.

The first metamorphic event with UHT peak conditions that is characterized by an isobaric heating-cooling trajectory, points towards a magmatic heat source for the metamorphism. If the above interpretation of late-stage formation of Sil-Ky-And bearing symplectites is correct, a considerable pressure drop is required after the second metamorphic event. This indicates that a crustal thickening event should have preceded the rapid exhumation of the rocks of the Ongole domain. The two subsequent P-T trajectories of the rocks of the Ongole domain are those expected for magmatic arcs. During the growth stage of the magmatic arc the heat budget of the arc is mainly controlled by the magmatic input into the arc, which leads to UHT metamorphism at lower pressures. At a later stage, when the arc gets attached to the continent, the margin of the arc and the continent builds up a thickened crust, in which a higher pressure but lower temperature metamorphism should take place. The latter is characterized by an isothermal decompression after crustal thickening (e.g. Thompson and England, 1984). The development of an arc and the collision with a continent as envisaged here as the likely geodynamic evolution of the Ongole domain may well take place chronologically unrelated to the major collision of continents that may have lead to supercontinent formations.

2.10 Acknowledgements

We are thankful to P. Appel and B. Mader for their assistance with electron microprobe analyses and A. Fehler for high quality thin-section preparation. We thank M. Menneken for her help during Raman spectroscopic measurements at the University of Münster. Constructive comments from P. Sengupta helped in improving the article.

References

- Aït-Djafer, S., Adjerid, Z., Badani, A., Ouzegane, K., Kienast, J.R., 2009. Spinel–quartz high temperature paragenesis in Al–Fe granulites from the Ihouhaouene area (NW Hoggar, Algeria). *Journal of African Earth Sciences* 55, 79–91.
- Aranovich, L.Y., Berman, R.G., 1997. A new garnet-orthopyroxene thermometer based on reversed Al₂O₃ solubility in FeO-Al₂O₃-SiO₂ orthopyroxene. *American Mineralogist* 82, 345–353.
- Armstrong, J.T., 1995. Citzaf: a package of correction programs for the quantitative electron microbeam X-ray analysis of thick polished materials, thin-films, and particles. *Microbeam Analysis* 4, 117–200.
- Baldwin, J.A., Powell, R., Brown, M., 2005. Modelling of mineral equilibria in ultrahigh-temperature metamorphic rocks from the Anápolis–Itauçu Complex, central Brazil. *Journal of metamorphic Geology* 23, 511–531.
- Ballèvre, M., Hensen, B.J., Reynard, B., 1997. Orthopyroxene-andalusite symplectites replacing cordierite in granulites from the Strangways Range (Arunta block, central Australia): A new twist to the pressure-temperature history. *Geology* 25, 215–218.
- Barbosa, J., Nicollet, C., Leite, C., Kienast, J.R., Fuck, R.A., Macedo, E.R., 2006. Hercynite–quartz-bearing granulites from Brejões Dome area, Jequié Block, Bahia, Brazil: Influence of charnockite intrusion on granulite facies metamorphism. *Lithos* 92, 537–556.
- Benisek, A., Dachs, E., Kroll, H., 2010. A ternary feldspar-mixing model based on calorimetric data: development and application. *Contributions to Mineralogy and Petrology* 160, 327–337.
- Bertrand, P., Ellis, D.J., Green, D.H., 1991. The stability of sapphirine-quartz and

hypersthene-sillimanite-quartz assemblages: an experimental investigation in the system FeO–MgO–Al₂O₃–SiO₂ under H₂O and CO₂ conditions. *Contributions to Mineralogy and Petrology* 108, 55–71.

Bhattacharya, A., Krishnakumar, K.R., Raith, M.M., Sen, S.K., 1991. An Improved Set of a-X Parameters for Fe-Mg-Ca Garnets and Refinements of the Orthopyroxene–Garnet Thermometer and the Orthopyroxene-Garnet-Plagioclase-Quartz Barometer. *Journal of Petrology* 32, 629–656.

Bhui, U., Sengupta, P., Sengupta, P., 2007. Phase relations in mafic dykes and their host rocks from Kondapalle, Andhra Pradesh, India: Implications for the time–depth trajectory of the Palaeoproterozoic (late Archaean?) granulites from southern Eastern Ghats Belt. *Precambrian Research* 156, 153–174.

Bose, S., Dunkley, D.J., Dasgupta, S., Das, K., Arima, M., 2011. India-Antarctica-Australia-Laurentia connection in the Paleoproterozoic-Mesoproterozoic revisited: Evidence from new zircon U-Pb and monazite chemical age data from the Eastern Ghats Belt, India. *Geological Society of America Bulletin* 123, 2031–2049.

Chetty, T.R.K., Murthy, D.S.N., 1994. Collision tectonics in the late Precambrian Eastern Ghats Mobile Belt: mesoscopic to satellite-scale structural observations. *Terra Nova* 6, 72–81.

Clarke, G.L., Powell, R., Guiraud, M., 1989. Low-pressure granulite facies metapelitic assemblages and corona textures from MacRobertson Land, east Antarctica: the importance of Fe₂O₃ and TiO₂ in accounting for spinel-bearing assemblages. *Journal of metamorphic Geology* 7, 323–335.

Dasgupta, S., Bose, S., Das, K., 2013. Tectonic evolution of the Eastern Ghats Belt, India. *Precambrian Research* 227, 247–258.

- Dasgupta, S., Sengupta, P., 2003. Indo-Antarctic Correlation: a perspective from the Eastern Ghats Granulite Belt, India. Geological Society, London, Special Publications 206, 131–143.
- Dasgupta, S., Sengupta, P., Ehl, J., Raith, M.M., Bardhan, S., 1995. Reaction textures in a suite of spinel granulites from the Eastern Ghats Belt, India: evidence for polymetamorphism, a partial petrogenetic grid in the system KFMASH and the roles of ZnO and Fe₂O₃. *Journal of Petrology* 36, 435–461.
- de Capitani, C., Brown, T.H., 1987. The computation of chemical equilibrium in complex systems containing non-ideal solutions. *Geochimica et Cosmochimica Acta* 51, 2639–2652.
- Dharma Rao, C.V., Santosh, M., 2011. Continental arc magmatism in a Mesoproterozoic convergent margin: Petrological and geochemical constraints from the magmatic suite of Kondapalle along the eastern margin of the Indian plate. *Tectonophysics* 510, 151–171.
- Dharma Rao, C.V., Santosh, M., Dong, Y., 2012. U-Pb zircon chronology of the Pangidi-Kondapalle layered intrusion, Eastern Ghats belt, India: Constraints on Mesoproterozoic arc magmatism in a convergent margin setting. *Journal of Asian Earth Sciences* 49, 362–375.
- Dobmeier, C.J., Raith, M.M., 2003. Crustal architecture and evolution of the Eastern Ghats Belt and adjacent regions of India. Geological Society, London, Special Publications 206, 145–168.
- Downs, R.T., 2006. The RRUFF Project: an integrated study of the chemistry, crystallography, Raman and infrared spectroscopy of minerals. Program and abstracts of the 19th general meeting of the International Mineralogical Association in Kobe, Japan, O03-13.

- Dunkley, D.J., Clarke, G.L., Harley, S.L., 1999. Diffusion metasomatism in silica-undersaturated sapphirine-bearing granulite from Rumdoodle Peak, Framnes Mountains, east Antarctica. *Contributions to Mineralogy and Petrology* 134, 264–276.
- Ellis, D.J., Sheraton, J.W., England, R.N., Dallwitz, W.B., 1980. Osumilite-sapphirine-quartz granulites from Enderby Land Antarctica—mineral assemblages and reactions. *Contributions to Mineralogy and Petrology* 72, 123–143.
- Fitzsimons, I., Harley, S.L., 1994. The Influence of Retrograde Cation Exchange on Granulite P-T Estimates and a Convergence Technique for the Recovery of Peak Metamorphic Conditions. *Journal of Petrology* 35, 543–576.
- Ganguly, J., Saxena, S.K., 1984. Mixing properties of aluminosilicate garnets; constraints from natural and experimental data, and applications to geothermobarometry. *American Mineralogist* 69, 88–97.
- Guiraud, M., Kienast, J.R., Ouzegane, K., 1996. Corundum–quartz-bearing assemblage in the Ihouhaouene area (In Ouzzal, Algeria). *Journal of metamorphic Geology* 14, 755–761.
- Harley, S.L., 1998. On the occurrence and characterization of ultrahigh-temperature crustal metamorphism. Geological Society, London, Special Publications 138, 81–107.
- Harley, S.L., 2004a. Extending our understanding of ultrahigh temperature crustal metamorphism. *Journal of Mineralogical and Petrological Sciences* 99, 140–158.
- Harley, S.L., 2004b. An experimental study of the partitioning of Fe and Mg between garnet and orthopyroxene. *Contributions to Mineralogy and Petrology* 86, 359–373.

- Hensen, B.J., Green, D.H., 1973. Experimental study of the stability of cordierite and garnet in pelitic compositions at high pressures and temperatures. *Contributions to Mineralogy and Petrology* 38, 151–166.
- Hensen, B.J., Harley, S.L., 1990. Graphical analysis of P–T–X relations in granulite facies metapelites, in: *High-Temperature Metamorphism and Crustal Anatexis*. Springer Netherlands, Dordrecht, pp. 19–56.
- Hodges, K.V., Crowley, P.D., 1985. Error estimation and empirical geothermobarometry for pelitic systems. *American Mineralogist* 70, 702–709.
- Holland, T.J.B., Powell, R., 1998. An internally consistent thermodynamic data set for phases of petrological interest. *Journal of metamorphic Geology* 16, 309–343.
- Jöns, N., Schenk, V., 2011. The ultrahigh temperature granulites of southern Madagascar in a polymetamorphic context: implications for the amalgamation of the Gondwana supercontinent. *European Journal of Mineralogy* 23, 127–156.
- Kars, H., Jansen, J.B.H., Tobi, A.C., Poorter, R.P.E., 1980. The metapelitic rocks of the polymetamorphic Precambrian of Rogaland, SW Norway. *Contributions to Mineralogy and Petrology* 74, 235–244.
- Kelsey, D.E., 2008. On ultrahigh-temperature crustal metamorphism. *Gondwana Research* 13, 1–29.
- King, H.E., Plumper, O., Geisler, T., Putnis, A., 2011. Experimental investigations into the silicification of olivine: Implications for the reaction mechanism and acid neutralization. *American Mineralogist* 96, 1503–1511.
- Korsch, R.J., Kositcin, N., Champion, D.C., 2011. Australian island arcs through time: Geodynamic implications for the Archean and Proterozoic. *Gondwana Research* 19, 716–734.

- Kovach, V.P., Simmat, R., Rickers, K., Berezhnaya, N.G., Salnikova, E.B., Dobmeier, C., Raith, M.M., Yakovleva, S.Z., Kotov, A.B., 2001. The western charnockite zone of the Eastern Ghats Belt, India-an independent crustal province of late Achaean (2.8 Ga) and Palaeoproterozoic (1.7-1.6 Ga) terrains. *Gondwana Research* 4, 666–667.
- Koziol, A.M., Newton, R.C., 1988. Redetermination of the anorthite breakdown reaction and improvement of the plagioclase-garnet-Al₂SiO₅-quartz geobarometer. *American Mineralogist* 73, 216–223.
- Kriegsman, L.M., Hensen, B.J., 1998. Back reaction between restite and melt: Implications for geothermobarometry and pressure-temperature paths. *Geology* 26, 1111.
- Kroll, H., Evangelakakis, C., Voll, G., 1993. Two-feldspar geothermometry: a review and revision for slowly cooled rocks. *Contributions to Mineralogy and Petrology* 114, 510–518.
- Lal, R.K., Ackermann, D., Upadhyay, H., 1987. P-T-X Relationships Deduced from Corona Textures in Sapphirine-Spinel-Quartz Assemblages from Paderu, Southern India. *Journal of Petrology* 28, 1139–1168.
- Leake, B.E., Woolley, A.R., Arps, C.E.S., Birch, W.D., Gilbert, M.C., Grice, J.D., Hawthorne, F.C., Kato, A., Kisch, H.J., Krivovichev, V.G., Linthout, K., Laird, J., Mandarino, J.A., Maresch, W.V., Nickel, E.H., Rock, N.M.S., Schumacher, J.C., Smith, D.C., Stephenson, N.C., Ungaretti, L., Whittaker, E.J., Youzhi, G., 1997. Nomenclature of amphiboles: report of the subcommittee on amphiboles of the International Mineralogical Association, Commission on New Minerals and Mineral Names. *The Canadian Mineralogist* 35, 219–246.
- Lee, H.Y., Ganguly, J., 1988. Equilibrium compositions of coexisting garnet and orthopyroxene: experimental determinations in the system FeO-MgO-Al₂O₃-

- SiO₂, and applications. *Journal of Petrology* 29, 93–113.
- Mezger, K., Cosca, M.A., 1999. The thermal history of the Eastern Ghats Belt (India) as revealed by U–Pb and ⁴⁰Ar/³⁹Ar dating of metamorphic and magmatic minerals: implications for the SWEAT correlation. *Precambrian Research* 94, 251–271.
- Motoyoshi, Y., Hensen, B.J., Matsueda, H., 1990. Metastable growth of corundum adjacent to quartz in a spinel-bearing quartzite from the Archaean Napier Complex, Antarctica. *Journal of metamorphic Geology* 8, 125–130.
- Möller, A., Appel, P., Mezger, K., Schenk, V., 1995. Evidence for a 2 Ga subduction zone: eclogites in the Usagaran belt of Tanzania. *Geology* 23, 1067–1070.
- Nichols, G.T., Berry, R.F., Green, D.H., 1992. Internally consistent gahnitic spinel-cordierite-garnet equilibria in the FMASHZn system: geothermobarometry and applications. *Contributions to Mineralogy and Petrology* 111, 362–377.
- Perchuk, L., Gerya, T., Nozhkin, A., 1989. Petrology and retrograde P-T path in granulites of the Kanskaya formation, Yenisey range, Eastern Siberia. *Journal of metamorphic Geology* 7, 599–617.
- Perkins, D., III, Chipera, S.J., 1985. Garnet-orthopyroxene-plagioclase-quartz barometry: refinement and application to the English River subprovince and the Minnesota River valley. *Contributions to Mineralogy and Petrology* 89, 69–80.
- Raase, P., 1998. Feldspar thermometry; a valuable tool for deciphering the thermal history of granulite-facies rocks, as illustrated with metapelites from Sri Lanka. *The Canadian Mineralogist* 36, 67–86.
- Ramakrishnan, M., Nanda, J.K., Augustine, P.F., 1998. Geological evolution of the Proterozoic Eastern Ghats mobile belt. *Geological Survey of India Special Publications* 44, 1–21.

- Rickers, K., Mezger, K., Raith, M.M., 2001. Evolution of the continental crust in the Proterozoic Eastern Ghats Belt, India and new constraints for Rodinia reconstruction: implications from Sm–Nd, Rb–Sr and Pb–Pb isotopes. *Precambrian Research* 112, 183–210.
- Rogers, J.J.W., Santosh, M., 2009. Tectonics and surface effects of the supercontinent Columbia. *Gondwana Research* 15, 373–380.
- Sajeev, K., Osanai, Y., 2004. Osumilite and spinel+ quartz from Sri Lanka: Implications for UHT conditions and retrograde PT path. *Journal of Mineralogical and Petrological Sciences* 99, 320–327.
- Sandiford, M., Neall, F.B., Powell, R., 1987. Metamorphic evolution of aluminous granulites from Labwor Hills, Uganda. *Contributions to Mineralogy and Petrology* 95, 217–225.
- Schenk, V., 1989. P-T-t path of the lower crust in The Hercynian fold belt of southern Calabria. Geological Society, London, Special Publications 43, 337–342.
- Sengupta, P., Karmakar, S., Dasgupta, S., Fukuoka, M., 1991. Petrology of spinel granulites from Araku, Eastern Ghats, India, and a petrogenetic grid for sapphirine-free rocks in the system FMAS. *Journal of metamorphic Geology* 9, 451–459.
- Sengupta, P., Sen, J., Dasgupta, S., Raith, M.M., Bhui, U.K., Ehl, J., 1999. Ultra-high temperature metamorphism of metapelitic granulites from Kondapalle, Eastern Ghats Belt: implications for the Indo-Antarctic correlation. *Journal of Petrology* 40, 1065–1087.
- Shaw, R.K., Arima, M., 1998. A corundum–quartz assemblage from the Eastern Ghats Granulite Belt, India: evidence for high P–T metamorphism? *Journal of metamorphic Geology* 16, 189–196.

- Simmat, R., Raith, M.M., 2008. U–Th–Pb monazite geochronometry of the Eastern Ghats Belt, India: Timing and spatial disposition of poly-metamorphism. *Precambrian Research* 162, 16–39.
- Stüwe, K., Powell, R., 1989. Metamorphic evolution of the Bunge Hills, East Antarctica: evidence for substantial post-metamorphic peak compression with minimal cooling in a Proterozoic orogenic event. *Journal of metamorphic Geology* 7, 449–464.
- Thompson, A.B., England, P.C., 1984. Pressure—Temperature—Time Paths of Regional Metamorphism II. Their Inference and Interpretation using Mineral Assemblages in Metamorphic Rocks. *Journal of Petrology* 25, 929–955.
- Tsunogae, T., Santosh, M., 2009. Ultrahigh-temperature metamorphism and decompression history of sapphirine granulites from Rajapalayam, southern India: implications for the formation of hot orogens during Gondwana assembly. *Geol. Mag.* 147, 42.
- Tsunogae, T., Van Reenen, D.D., 2006. Corundum+quartz and Mg-staurolite bearing granulite from the Limpopo Belt, southern Africa: Implications for a P–T path. *Lithos* 92, 576–587.
- Upadhyay, D., 2008. Alkaline magmatism along the southeastern margin of the Indian shield: Implications for regional geodynamics and constraints on craton–Eastern Ghats Belt suturing. *Precambrian Research* 162, 59–69.
- Veevers, J.J., 2004. Gondwanaland from 650–500 Ma assembly through 320 Ma merger in Pangea to 185–100 Ma breakup: supercontinental tectonics via stratigraphy and radiometric dating. *Earth-Science Reviews* 68, 1–132.
- Vijaya Kumar, K., Leelanandam, C., Ernst, W., 2011. Formation and fragmentation of the Palaeoproterozoic supercontinent Columbia: evidence from the Eastern

Ghats Granulite Belt, southeast India. *International Geology Review* 53, 1297–1311.

Waters, D.J., 1991. Hercynite-quartz granulites; phase relations, and implications for crustal processes. *European Journal of Mineralogy* 3, 367–386.

Wen, S., Nekvasil, H., 1994. SOLVALC: An interactive graphics program package for calculating the ternary feldspar solvus and for two-feldspar geothermometry. *Computers and Geosciences* 20, 1025–1040.

White, R.W., Clarke, G.L., 2007. Garnet-forming reactions and recrystallization in high-grade mylonite zones, MacRobertson Land, east Antarctica. *Journal of metamorphic Geology* 25, 853–865.

Zhao, G., Cawood, P.A., Wilde, S.A., Sun, M., 2002. Review of global 2.1–1.8 Ga orogens: implications for a pre-Rodinia supercontinent. *Earth-Science Reviews* 59, 125–162.

Zhao, G., Sun, M., Wilde, S.A., Li, S., 2003. Assembly, Accretion and Breakup of the Paleo-Mesoproterozoic Columbia Supercontinent: Records in the North China Craton. *Gondwana Research* 6, 417–434.

Zhao, G., Sun, M., Wilde, S.A., Li, S., 2004. A Paleo-Mesoproterozoic supercontinent: assembly, growth and breakup. *Earth-Science Reviews* 67, 91–123.

Chapter 3

Two-stage granulite formation in the Ongole domain, Eastern Ghats Belt, India: LA-ICP-MS zircon dating and texturally controlled in-situ monazite dating

Abstract

To quantify the Mesoproterozoic pressure-temperature-time evolution of the granulite-facies Ongole domain, deep crustal Proterozoic magmatic arc in the Eastern Ghats Belt, LA-ICP-MS U-Pb zircon dating and in-situ electron microprobe U-Th-total Pb monazite dating are integrated with the petrologic observations. Zircon grains in the metapelites often preserve oscillatory-zoned, sometimes partly resorbed cores yielding a spread of $^{207}\text{Pb}/^{206}\text{Pb}$ ages between ca. 2700 and ca.1750 Ma, interpreted to reflect the age of detrital grains from the surrounding crustal blocks. Metamorphic zircon overgrowths and rims yield Palaeoproterozoic concordia ages from about 1625 to 1600 Ma, indicating the timing and duration of an ultrahigh-temperature (UHT) metamorphic event.

Texturally controlled in-situ monazite dating however reveals two metamorphic events separated by 60-80 Ma. In metapelites, the monazite inclusions in garnet and cores of some matrix monazite yield weighted mean ages of ca. 1610 Ma, similar to the concordia ages from zircon and indicate the timing of the UHT

metamorphism. The monazite grains in the matrix, growing along with a second generation of garnet and in late-stage symplectites are highly recrystallized and yield weighted mean ages of ca. 1540 Ma, indicating the timing of a second metamorphism at higher pressures but lower temperatures. The weighted mean ages obtained from metapelites in the adjoining Vinjamuru domain are the same as those obtained from the Ongole domain. The chemical differences between the two generations of monazite (Th, Y and HREE contents) support the above interpretation of monazite growth under different conditions and at different times. Monazite in the charnoenderbites records the second metamorphic event but only rarely the earlier UHT event. In addition, they show evidence for later imprints of ductile to brittle deformation between ca. 1450 and 1360 Ma, which may correlate with Mesoproterozoic crustal extension and alkaline plutonism along the western boundary of the Eastern Ghats Belt. Though the Ongole domain was not involved in major crustal reworking during the Neoproterozoic, monazites do record minor disturbances at ca. 730 Ma and ca. 510 Ma. Hence the combination of zircon and monazite dating unveils the sequence of tectonothermal events in the Ongole domain in a hitherto unknown exactness: UHT metamorphism at ca. 1610 Ma due to magmatic heat advection, 60 to 80 Ma later a second metamorphic event at medium-pressure and lower-temperature due to the collision of the arc with the Indian continent, and finally minor disturbances due to rifting between ca. 1450 and 1360 Ma.

3.1. Introduction

In chapter 2 we have presented petrological data leading to the reconstruction of a complex pressure-temperature history of the rocks of a Proterozoic magmatic arc (Ongole domain) in the Eastern Ghats Belt of India, reflecting either two separate

metamorphic events or a single polyphase metamorphism. However, based only on petrological data, it was not possible to arrive to a conclusion whether the rocks experienced polymetamorphism or a single polyphase metamorphism. This points towards the importance of isotopic age dating, which is normally inevitable for a proper geodynamic interpretation of petrological data. In low-grade terrains there are several geochronometers, as micas, which can be dated by using a couple of isotopic systems if the conditions during the reworking event were below the closing temperatures of the applied isotopic system. But above those closing temperature, i.e. in high-grade rocks (upper amphibolite-facies and granulite-facies), micas are not suitable. So we have often to rely on the U-Pb system where zircon and monazite are preeminent geochronometers. These minerals have high closing temperatures for isotopic exchange and Pb diffusion is negligible even at high temperatures of 900°C (Cherniak et al., 2004).

Zircon has long been recognized as a robust U-Pb geochronometer. Small diameter laser beam and high precision mass spectrometry combined with high resolution cathodoluminescence imaging allow us to obtain ages from tiny zones of texturally complex zircon crystals that record the different times of their growth. But sometimes, weaker tectonothermal events, or even a second granulite-facies event might not be recorded by zircon (e.g. Boniface et al., 2012; Schenk et al., 2005), whereas monazite might record. If the geological interpretations are based only on zircon, it might well be misleading. Like the zircon ages of eclogites of the Belomorian Mobile Belt in Russia that are interpreted to reflect Mesoarchean subduction metamorphism (Mints et al., 2010), while recent Lu-Hf dating of the eclogitic garnets proved that the eclogite-facies metamorphism is Palaeoproterozoic in age (Herwartz et al., 2012). In-situ monazite dating using an electron microprobe has high spatial resolution and provides rapid and reliable information on age distribution down to small, recrystallized domains of a single grain. Most importantly, in-situ techniques reveal the textural position of the monazite before dating and can be readily correlated with the textures of the rock that developed

during different tectonometamorphic stages or events. Monazite inclusions in garnet, in late-stage symplectites or in shear zones can be used to date different events. So, careful dating of monazite grains from different textural positions may resolve complex P-T-t evolutions. However, the disadvantage of monazite dating is that monazite is very easily modified, and resetting of the isotopic ratios may occur in response to fluid induced weak tectonothermal impulses that may partially erase memories of past events. As zircon may remain unreactive, the combination of zircon and monazite dating of the same samples is ideal to look through the timings of events in multiply deformed and metamorphosed high-grade terrains.

Several attempts have been made separately with zircon and monazite to characterize the sequence of events that have taken place in the polymetamorphic Ongole domain. But a comprehensive geochronological study and its correlation with the P-T evolution to gain a sound knowledge on the geodynamic setting of the domain is still lacking. In this contribution we have undertaken LA-ICP-MS zircon dating on mineral separates and in-situ monazite dating of grains that are correlated with their textural settings. Applying this technique we can distinctly relate the ages obtained from monazite and zircon to the different P-T paths established in our companion contribution and we develop a geodynamic evolution model of the Ongole domain. This includes the stage of UHT metamorphism due to magma accretion and a later collisional stage when the magmatic arc was attached to the Indian continent.

3.2. Geological background

The Eastern Ghats Belt (EGB), which includes the Ongole domain, is a polycyclic granulite terrain (Mukhopadhyay and Basak, 2009) extending for ca. 1000 km along the east coast of peninsular India and thrust over the Archean cratonic units of

the Indian shield to the west along several shear zones. Earlier subdivisions of the EGB were based on lithology (Ramakrishnan et al., 1998) and isotopic signatures (Rickers et al., 2001). Here we adopt the subdivision scheme of Dobmeier and Raith (2003) in which the Eastern Ghats Belt was divided into several crustal provinces which themselves were subdivided into crustal domains on the basis of their distinct geological histories and separated from each other by tectonic boundaries (Fig. 3.1). The granulite-facies Ongole domain and the medium to low-grade Vinjamuru and Udayagiri domains build up the Krishna province in the southern part of the EGB (Fig. 3.1). The primary focus of the present work is on the Ongole domain that is squeezed between the Archean Eastern Dharwar craton to the west and the Neoproterozoic Eastern Ghats Province to the east. The age of attachment of the Ongole domain with the craton is still debated to be either Mesoproterozoic (Dasgupta et al., 2013) or Neoproterozoic (Simmat and Raith, 2008).

The Ongole domain is characterized by the occurrence of large volumes of multi intrusive charnoenderbites with enclaves of migmatitic metasedimentary rocks (diatexitic Grt-Sil-Spl-Qz granulite, Grt-Crd±Opx granulite) ranging from meter to outcrop scale. A relatively small mafic-ultramafic complex within the northern part of the Ongole domain is interpreted to have formed in a magmatic arc setting based on geochemical data (Dharma Rao and Santosh, 2011). Our own geochemical data of the charnoenderbites (unpublished data) also indicate that they were emplaced in a magmatic arc setting. Previous studies show that the felsic magmatism occurred at ~1.7 Ga (Kovach et al., 2001) and was followed by a high-grade metamorphic event at 1.6 Ga (Bose et al., 2011; Kovach et al., 2001; Simmat and Raith, 2008) reflecting that the Ongole domain is dominantly a Mesoproterozoic terrain. Bose et al. (2011) recently identified a 1760 Ma age from concentrically zoned zircon cores from a single metapelite and interpreted it to be the age of a pre-intrusion early UHT metamorphic event. Alkaline magmatism along the western margin of the domain from 1.5 to 1.3 Ga (Upadhyay, 2008) was interpreted to have occurred during rifting, thereby slightly disturbing the isotopic system of monazite (Simmat and Raith,

2008). Except for minor disturbances reflected in an Ar-Ar age of 1.1 Ga (Mezger and Cosca, 1999), the Ongole domain did not experience a major tectonothermal reworking after the Mesoproterozoic.

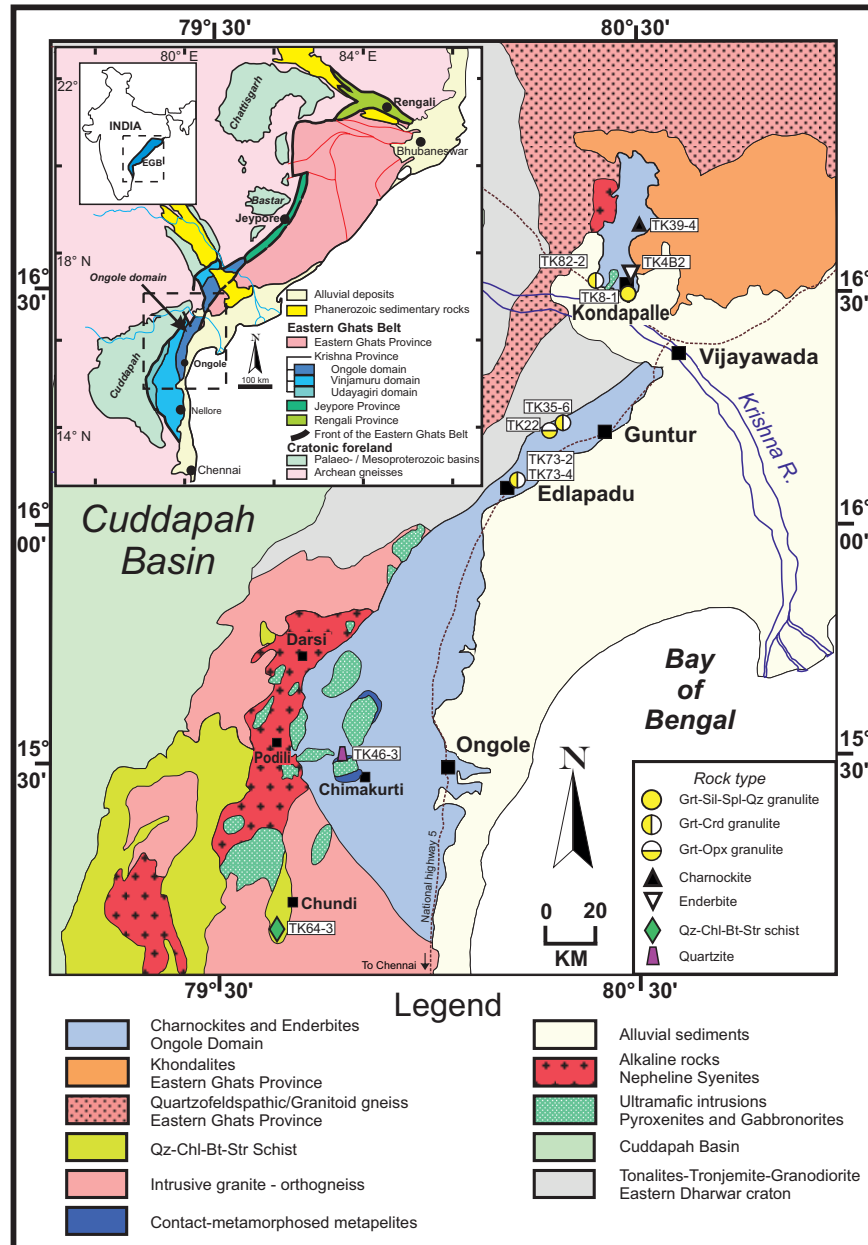


Figure 3.1: Geological map of the southern part of the Eastern Ghats Belt (EGB) showing the position of the Ongole domain and the adjoining areas (adapted and simplified from the Geological Survey of India map of Andhra Pradesh, published in 2001), showing the rock type and locations of geochronological samples. Geological outline of the Eastern Ghats Belt and adjacent regions modified after Dobmeier and Raith (2003) (inset).

The amphibolite-facies Vinjamuru domain, adjacent to the southwestern part of the Ongole domain, is essentially composed of felsic to intermediate metavolcanic rocks along with some metasediments and granitoids (for summary see Dobmeier and Raith, 2003). Although there are significant Archean components towards the south (Nellore greenstone belt), the metavolcanic sequence exposed in the northern part of the domain (close to the Ongole domain) has a late Palaeoproterozoic history (Ravikant, 2010). Recently, Ravikant et al. (2013) established from zircon dating (Pb evaporation method) of the metavolcanic rocks from this northern part that the major magmatic activity was in the Palaeoproterozoic (~1.78 Ga). This was followed by an amphibolite-facies metamorphism between 1.65 and 1.55 Ga.

3.3. Petrography of the investigated lithologies

In the Ongole domain the rocks are exposed along freshly cut large quarries providing a good opportunity to collect and study fresh rock samples. The investigated samples comprise charnockites and enderbites and the included migmatitic metapelites covering a geographically large area within the Ongole domain. A metapelite sample from the adjoining Vinjamuru domain has also been investigated. The sample locations are shown in Fig. 3.1.

3.3.1. Charnockite (TK39-4) and enderbite (TK4B2)

The charnockites and enderbites have a dark, homogenous and massive appearance in quarry exposures. Careful observation reveals fine-grained massive, coarse-grained gneissic and pegmatoidal varieties. Multiple stages of intrusion are evident from complex crosscutting relationships among the different varieties, which are

preserved in several outcrops. Thin leucosome layers point to migmatization of these rocks.

Sample TK39-4 and TK4B2 are from the Kondapalle region (Fig. 3.1). Mineralogically the rocks are composed of a quartzofeldspathic matrix along with garnet, orthopyroxene, biotite, ilmenite and some magnetite. The proportion of K-feldspar varies depending on the rock type. Two stages of mineral growth, especially garnet are evident from the texture. The second generation of garnet (garnet 2) develops as beaded overgrowth around the garnet porphyroblasts (garnet 1). Evidence of post-peak deformation of these rocks is plenty. Recrystallization of coarse-grained quartz and feldspars along grain boundaries resulted in a fine-grained granoblastic texture. Undulose extinction of quartz and myrmekite formation is common.

3.3.2. Metapelites (TK8-1, TK8C1, TK35-6, TK73-2, TK73-4)

The metapelites are Fe-Al rich and occur as enclaves within the charnoenderbites. They are strongly migmatitic and show a well developed gneissic banding, defined by some millimeters to some centimeters scale of alternating leucosome and melanosome layers.

Sample TK8-1 and TK8C1 are Grt-Sil-Spl-Qz granulites from Kondapalle (Fig. 3.1) where melanosome layers are mainly composed of garnet-sillimanite-spinel-quartz-ilmenite-corundum-perthite-plagioclase while the leucosome layers are composed of perthite and quartz with some plagioclase. Two generations of garnet are present: porphyroblastic garnet (garnet 1) forming aggregates with coarse-grained sillimanite and spinel, and garnet coronas (garnet 2) developing around garnet 1, spinel, ilmenite and corundum. Spinel and quartz, now separated by garnet and sillimanite rims, were stable at peak metamorphic conditions along with

garnet. Major garnet growth took place outside the spinel quartz stability field (chapter 2). Biotite is rare and locally replaces garnet and other prograde minerals.

Sample TK35-6, TK73-2 and TK73-4 are Grt-Crd±Opx granulites from the Guntur region (Fig. 3.1). The melanosome layers are dominated by garnet-cordierite±orthopyroxene-spinel-ilmenite-quartz-plagioclase±biotite while the leucosome patches are dominated by quartz-perthite-plagioclase±cordierite±biotite. Two generations of garnet are present. Porphyroblastic garnet (garnet 1) forms clusters with cordierite and orthopyroxene, while the second generation of garnet (garnet 2) occurs as small granular overgrowths over garnet 1 or small grains replacing biotite. Coarse-grained cordierite is partially replaced along grain boundaries by symplectites of Opx-Sil-Ky-Spl±Bt. A second type of replacement texture consisting of coarse-grained late biotite along with kyanite, sillimanite and andalusite replaces garnet and cordierite.

Sample TK64-3 is a staurolite bearing muscovite schist (near Chundi village) from the Vinjamuru domain (Fig. 3.1). The rock is mainly composed of muscovite-biotite-quartz±ilmenite and centimeter scale staurolite porphyroblasts. The foliation is defined by muscovite and biotite that wraps around the staurolite porphyroblasts. Former coarse quartz grains are now deformed and elongated to form spindles with clusters of numerous recrystallized quartz grains having sutured grain boundaries. The mica flakes wrap around these spindles too. Textures clearly suggest continuation of deformation after peak metamorphic conditions.

3.4. LA-ICP-MS zircon dating of metapelites

Six samples have been selected for U-Pb spot analyses with laser ablation inductively coupled plasma mass spectrometry (LA-ICP-MS). Zircon of the five metapelitic samples, (TK8C1, TK35-6, TK73-4, TK22 and TK82-2) and one quartzite

(TK46-3) taken from spatially separated areas (Fig. 3.1) are expected to provide the timings of the UHT metamorphism and partial melting and shed some light on the source area of the sediments. The results of the U-Pb isotopic analyses are presented in Table A.1 (Appendix A).

3.4.1. Analytical techniques

Zircon was separated from the hand specimen by standard heavy mineral separation techniques. The rocks were first crushed, followed by magnetic separation using hand magnet and Franz isodynamic magnetic separator to exclude the magnetic minerals. The separate was washed, cleaned and dried to exclude very fine-grained material. Then it was subjected to heavy mineral separation using bromoform liquid. The individual zircon grains were carefully hand picked from the heavy mineral residue, to include all the varieties of zircon grains in terms of shape and size. Selected grains were mounted on epoxy resin discs and polished. Before analysis the polished mounts were photographed and imaged with cathodoluminescence (CL) to study their internal structure (Fig. 3.2) using the JEOL JSM-6490 Scanning Electron Microscope at the Institute for Geosciences, University of Frankfurt. Points were selected on several zircon grains to include all texturally distinct domains in CL images. U-Pb isotopic analyses were carried out by using a ThermoFinnigan Element2 sector field ICP-MS coupled to a New Wave UP193HE ArF Excimer laser system at the Institute for Mineralogy, Westfälische Wilhelms-University, Münster. The analytical details for the measurement of U and Pb isotopes using the LA-ICP-MS are further elaborated by Kooijman et al. (2012). Analyses only with a degree of concordance of more than 98% have been considered here.

3.4.2. TK8C1

Sample TK8C1 is a Grt-Sil-Spl-Qz bearing metapelite from the Kondapalle region. The selected zircon grains are subhedral to anhedral, rounded to oval and ranging in size from 100 to 200 μm along with a few larger grains up to 300 μm . CL images reveal highly luminescent zoned or unzoned cores surrounded by only one luminescent rim (Fig. 3.2a) or by a weakly luminescent inner mantle and a moderately luminescent rim (Fig. 3.2c). Other grains show an unzoned and weakly luminescent core surrounded by a narrow to broad moderately luminescent rim (Fig. 3.2b). The U content of the mantles and the rims vary widely from 176 – 1404 ppm.

A total of 27 spots on 11 zircon grains have been considered for age calculations. The highly luminescent zoned or unzoned cores (Fig. 3.2a,c) yield a range of Palaeoproterozoic Pb-Pb ages from 1897 ± 23 Ma to 1797 ± 21 Ma (Table A.1 in Appendix A). The weakly luminescent (dark) mantles and the luminescent narrow to broad rims yield a late Palaeoproterozoic concordia age of 1622.3 ± 4.8 Ma defined by 9 concordant analyses (concordance 99.7 – 100.3%; Fig. 3.3a). There is only a single grain (3 spots) that yielded Archean Pb-Pb ages from 2652 ± 28 Ma to 2597 ± 27 Ma (Table A.1 in Appendix A).

3.4.3. TK35-6

Sample TK35-6 is a Grt-Crd bearing metapelite from the Guntur region. The zircon grains are subhedral to anhedral, elongated as well as rounded ranging in size from 100 to 300 μm . CL images reveal that in some grains weakly luminescent, elongated, oscillatory-zoned cores are surrounded by narrow luminescent mostly unzoned rims (Fig. 3.2d). Only occasionally these rims display fine-scale oscillatory zoning. The other grains are rounded with highly luminescent oscillatory-zoned or

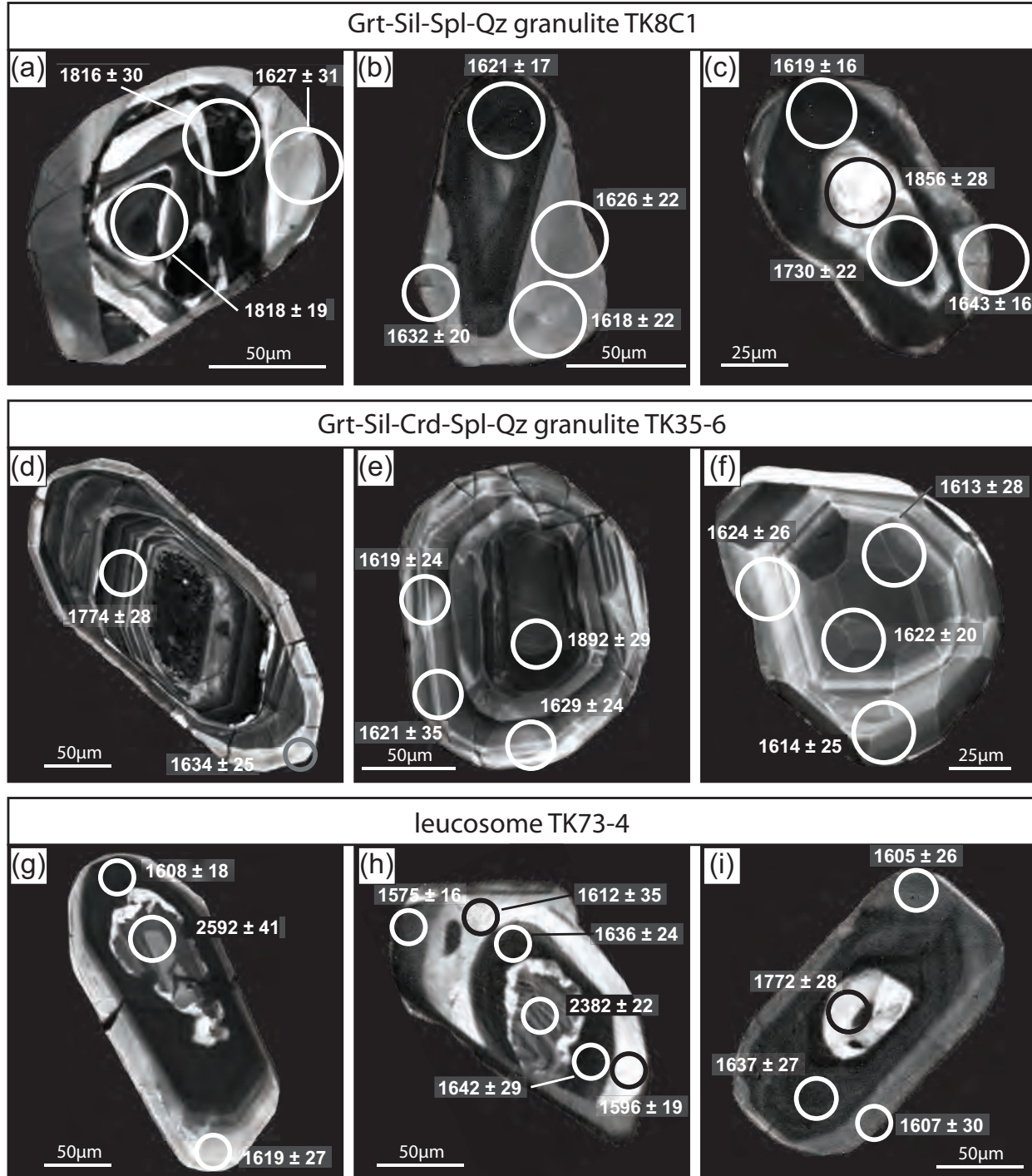
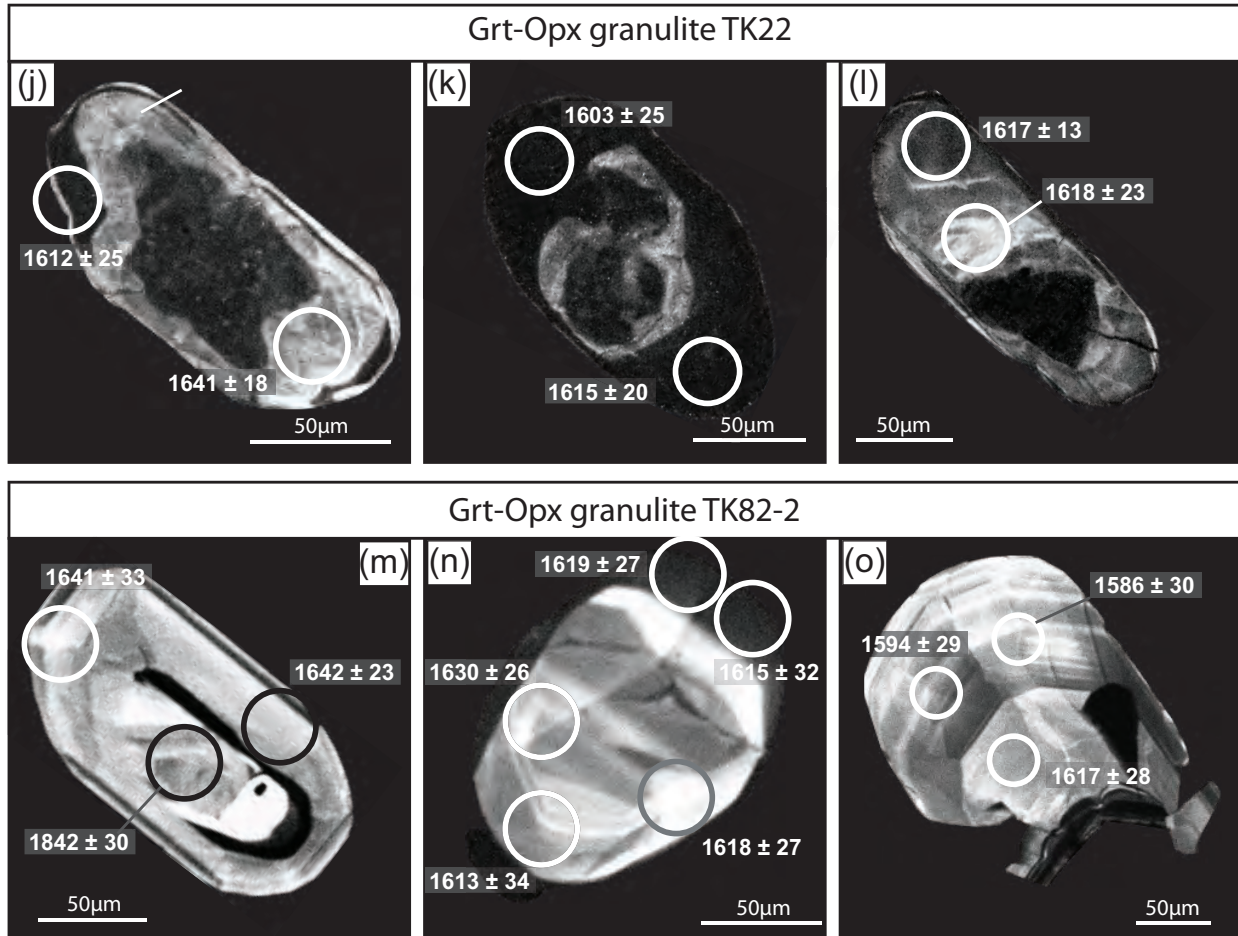


Figure 3.2: Cathodoluminescence (CL) images of selected zircon grains from different regions of the Ongole domain. (a-c) Grt-Sil-Spl-Qz granulite TK8C1 from Kondapalle; (d-f) Grt-Crd granulite TK35-6 from Guntur; (g-i) Grt-Opx-Crd granulite TK73-4 from Guntur; (j-l) Grt-Opx granulite TK22 from Guntur and (m-o) Grt-Opx granulite TK82-2 from west of Kondapalle. The circles mark the position of the laser spot. $^{207}\text{Pb}/^{206}\text{Pb}$ ages are shown on the zircons (in Ma) with 2σ errors. The laser



spots are scaled to size. (a) Zoned core surrounded by unzoned luminescent rim. (b) Unzoned weakly luminescent core surrounded by bright rim. (c) Brightly luminescent core surrounded by a broad dark mantle and a narrow bright rim. (d) Weakly luminescent oscillatory-zoned subhedral zircon grain surrounded by a bright narrow rim. (e) Subrounded and oscillatory-zoned mantle enclosing a weakly luminescent, zoned older core. (f) Sector zoned, brightly luminescent zircon yielding late Palaeoproterozoic ages. (g) A subhedral zircon grain with slightly resorbed oscillatory-zoned Archean core surrounded by a dark mantle and a bright rim of late Palaeoproterozoic age. (h) Zircon grain with early Palaeoproterozoic oscillatory zoned core surrounded by late Palaeoproterozoic to early Mesoproterozoic mantles and rims. (i) Euhedral zircon grain with a bright rounded core surrounded by a dark mantle showing faint zoning pattern and a brighter rim. (j) Elongated zircon grain with a large metamict core surrounded by a bright mantle and a dark rim. (k) An elliptical zircon grain with an irregular metamict core surrounded broad dark rim. (l) An elongated grain with a small irregular core and bright mantle. (m) Euhedral and bright zircon grain with a mid Palaeoproterozoic core and rim showing faint oscillatory zoning. (n) Subrounded late Palaeoproterozoic zircon with a bright sector-zoned core and a dark rim. (o) Late Palaeoproterozoic to early Mesoproterozoic bright zircon mantle with well preserved oscillatory zoning.

sector-zoned cores and rims (Fig. 3.2e,f). The highly luminescent cores and rims have moderate U contents varying from 97 to 512 ppm, while the dark cores have higher U contents from 272 to 5078 ppm.

A total of 20 spots on 9 zircon grains have been considered for age calculations. The oscillatory-zoned weakly luminescent cores yield a range of Palaeoproterozoic Pb-Pb ages from 1892 ± 29 Ma to 1774 ± 28 Ma (Table A.1). The narrow luminescent rims around these cores and the highly luminescent oscillatory-zoned or sector-zoned grains yield a concordia age of 1619.8 ± 4.6 Ma, defined by 15 concordant analyses (concordance 99.4 – 100.4%; Fig. 3.3b).

3.4.4. TK73-4

Sample TK73-4 is a Grt-Crd-Opx bearing metapelite from the Guntur region. The grains are euhedral to subhedral and range in size from 100 to 250 μm . CL images reveal a complex internal structure. Oscillatory-zoned, highly luminescent corroded cores are surrounded by broad, weakly luminescent mantles (Fig. 3.2g,h,i). The mantles are occasionally surrounded by narrow luminescent rims (Fig. 3.2g,i). The U contents of the weakly luminescent mantles (714-1635 ppm) are higher than the moderately luminescent rims (151-924 ppm).

A total of 30 spots on 12 zircon grains have been considered for age calculations. The cores yield a range of Neoproterozoic to Palaeoproterozoic Pb-Pb ages from 2734 ± 23 Ma to 1772 ± 28 Ma (Fig. 3.3c). Both the broad, weakly luminescent mantles and the luminescent rims yield very similar late Palaeoproterozoic concordant ages of 1625.7 ± 6.4 Ma (Fig. 3.3c) and 1599.7 ± 5.2 Ma (Fig. 3.3d) respectively, each defined by 8 concordant analyses (concordance 99.5 – 100.5%).

3.4.5. TK22

Sample TK22 is a Grt-Opx bearing restitic metapelite. Zircon grains are subhedral to euhedral in shape ranging from 100 to 200 μ m in length. CL images reveal weakly luminescent metamict cores for most zircon grains, surrounded by a narrow to broad highly luminescent mantle and a weakly luminescent rim (Fig. 3.2j,k,l). In some zircon grains the luminescent zone surrounding the metamict core is narrow, but has a weakly luminescent broad rim (Fig. 3.2k). In many grains the metamict cores as well as the luminescent zones are partly resorbed over which the weakly luminescent rims have grown.

A total of 14 spots on 10 zircon grains have been considered for age calculations. The highly luminescent mantles as well as the weakly luminescent rims surrounding it yield a late Palaeoproterozoic concordia age of 1620.8 \pm 5.0 Ma, defined by 11 concordant analyses (concordance 99.3 – 100.3%; Fig. 3.3e), very similar to the age obtained from zircon of other samples.

3.4.6. TK82-2

Sample TK82-2 is a restitic Grt-Opx bearing metapelite from the Kondapalle region. Zircon grains are mostly prismatic, euhedral to subhedral in shape and range from 100 to 250 μ m in length. Some subrounded grains are also present. CL images reveal a varying morphology among the zircon grains. The vast majority of the zircon grains show weakly to moderately luminescent cores where primary magmatic zoning is still visible in some. The cores that are sometimes resorbed are sharply overgrown by a highly luminescent mantle (Fig. 3.2m). In many grains, these mantles are surrounded by very dark rims with practically no luminescence. On the other hand there are some subrounded grains with highly luminescent core

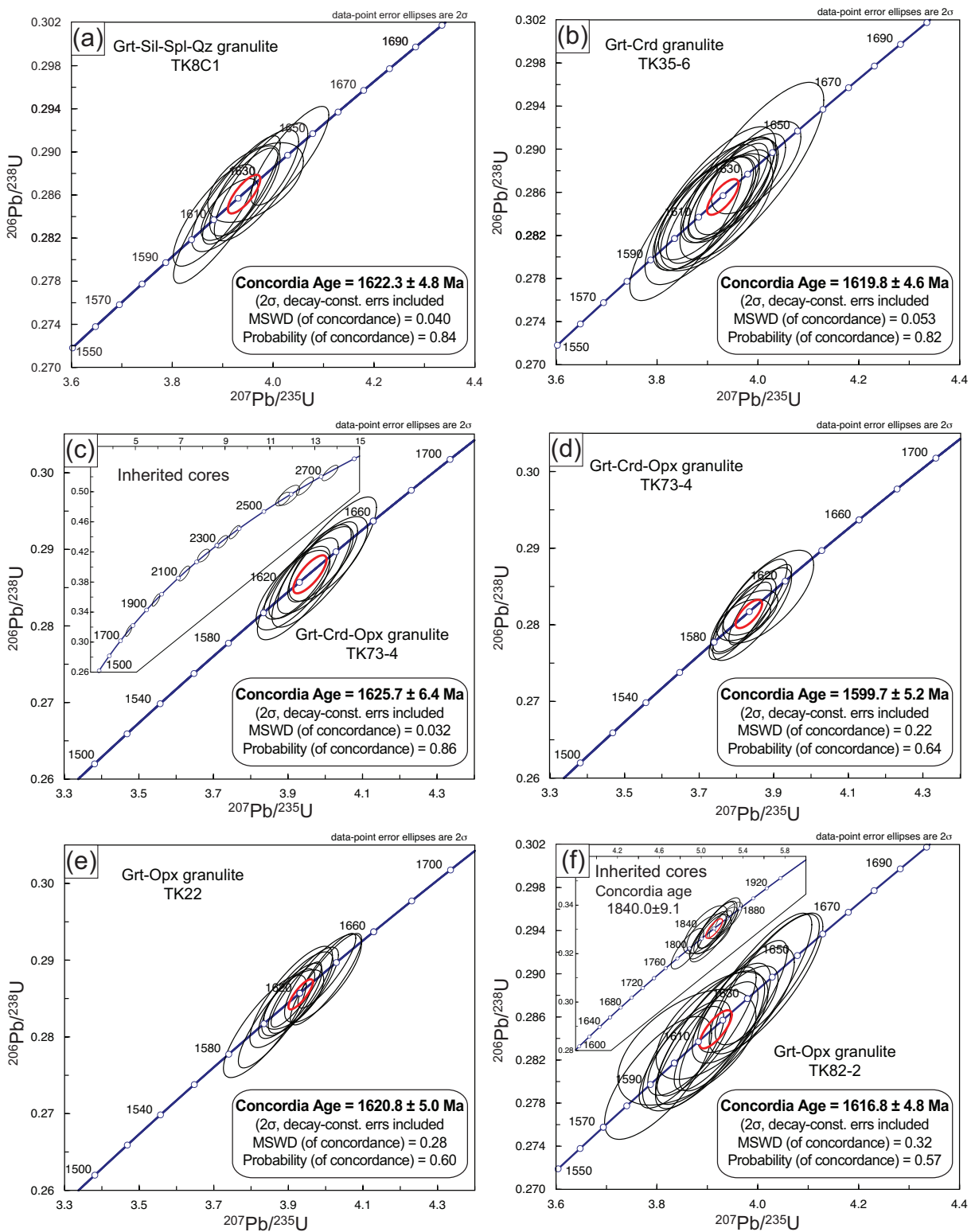


Figure 3.3:

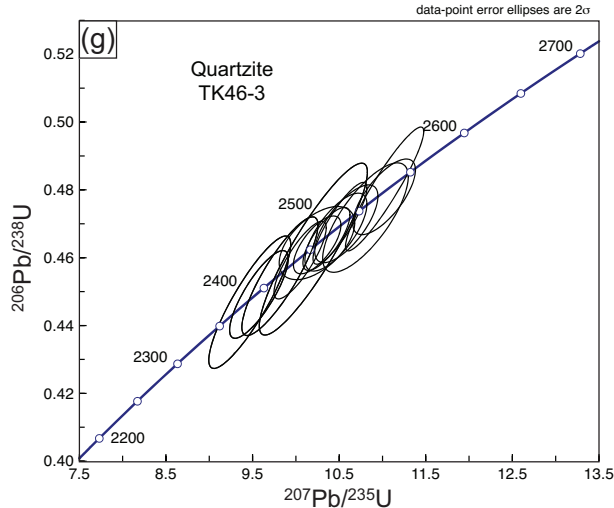


Figure 3.3: U-Pb concordia diagrams for the UHT granulites from the Ongole domain. Sample locations are marked in Fig. 3.1. The data points are from metamorphic mantles and rims of the zircons. Inset (c and f) show ages of inherited cores. (a) Grt-Sil-Spl-Qz granulite. (b) Grt-Crd granulite. (c) Data points from mantle and (d) rims of Grt-Crd-Opx granulite. (e-f) Grt-Opx granulite. (g) Data points from inherited zircon grains in a quartzite.

zones showing weak zoning patterns (Fig. 3.2n). Weakly luminescent rims commonly surround the core zones. A few grains show well-preserved highly luminescent oscillatory-zoned broad rims growing over a bright unzoned core (Fig. 3.2o).

A total of 31 spots on 14 zircon grains have been considered for age calculations. The resorbed cores show a range of spot ages from 1863 ± 24 to 1793 ± 26 Ma, yielding a concordia age of 1840.0 ± 9.1 Ma (11 concordant analyses; Fig. 3.3f). The bright mantles around the cores and the outermost dark rims, the subrounded grains and the oscillatory-zoned mantles found in few grains yield spot ages between 1638 ± 25 and 1593 ± 29 Ma, yielding a concordia age of 1616.8 ± 4.8 Ma, defined by 15 concordant analyses (concordance 99.3 – 100.3%; Fig. 3.3f).

3.4.7. TK46-3

Sample TK46-3 is a quartzite from the southern part of the Ongole domain. The zircon grains are all detrital and vary in shape from prismatic to rounded and range from 50-140 μm in length. CL images reveal fine oscillatory zoning for most grains and narrow to broad unzoned rims around some of these grains (Fig. 3.A1). A total

of 14 spots on 9 grains yield a range of concordant spot ages from 2523 ± 21 to 2887 ± 34 Ma (Fig. 3.3g).

3.4.8. Zircon data results

The varying morphology of the zircon grains in the Grt-Sil-Spl-Qz metapelite (TK8C1) and the range of ages from Neoproterozoic to late Palaeoproterozoic exhibited by the zircon clearly indicate an inherited or a detrital origin for many grains. The concordant late Palaeoproterozoic age of 1622.3 ± 4.8 (Fig. 3.3a) obtained from the narrow to broad mantles is interpreted to be the age of the granulite-facies peak metamorphism, when zircon crystallized on the preexisting detrital zircon grains or formed new rounded grains.

In the Grt-Crd metapelite (TK35-6), the oscillatory-zoned weakly luminescent elongated cores, yielding Pb-Pb spot ages from 1892 ± 29 to 1774 ± 28 , are clearly detrital magmatic zircon grains that were incorporated into the younger sediments. The oscillatory zoning of the rounded zircon grains as well as the zircon overgrowths (occasionally oscillatory-zoned) around weakly luminescent elongated cores indicate their crystallization from anatectic melts. Consequently, we interpret the concordant late Palaeoproterozoic age of 1619.8 ± 4.6 Ma (Fig. 3.3b) to correspond to the timing of partial melting during a granulite-facies metamorphic event. The age is consistent with the age of metamorphism interpreted from sample TK8C1.

In the Grt-Crd-Opx metapelite (TK73-4) the highly luminescent, oscillatory-zoned or unzoned zircon fragments in the cores represent detrital magmatic zircon. The range of Neoproterozoic to Palaeoproterozoic Pb-Pb ages from 2734 ± 23 Ma to 1772 ± 28 Ma indicates varying sources of the sediments (Fig. 3.3c). The late Palaeoproterozoic concordant ages of 1625.7 ± 6.4 Ma and 1599.7 ± 5.2 Ma (Fig. 3.3b,c) obtained from the unstructured mantles and the rims of the grains represent the age of metamorphic zircon growth. The mantles and the rims have different U

contents. Thus the two ages of the metamorphic overgrowth may indicate the temporal extent of the high-grade metamorphism.

In the Grt-Opx metapelite, the partly resorbed metamict cores (TK22) and the resorbed cores yielding a Palaeoproterozoic concordia age of 1840 ± 9 Ma (TK82-2) are interpreted to reflect detrital zircon grains. The concordant age of 1620 ± 5.0 Ma (TK22) 1616.8 ± 4.8 Ma (TK82-2) obtained from mantle and rims of zircon grains from these samples (Fig. 3.3e,f), represent the age of major zircon growth during peak metamorphism that is in accordance with the ages obtained from other samples. We conclude that the concordant metamorphic rim ages from 1626 ± 6 to 1600 ± 5 Ma, from five metapelitic samples, constrain the timing of the UHT granulite-facies metamorphism and partial melting in the Ongole domain. Thus, zircon dating indicates a single pervasive and high-grade metamorphic event that affected the entire Ongole domain and the time span of ~ 26 Ma indicates the duration of the high-grade metamorphism.

3.5. Th-U-total Pb dating of monazite

Monazite grains in the rocks of the granulite-facies Ongole domain are polygenetic and exhibit a diversity of zoning patterns. Dating the different zones in these monazite grains should play an important role in unraveling the complex polymetamorphic history of the Ongole domain. Slow diffusion rate of Pb in monazite under most metamorphic conditions (Cherniak et al., 2004) and the tendency to incorporate negligible common Pb (Parrish, 1990) has made monazite reliable for chemical age dating with U-Th and total Pb contents obtained from electron microprobe analyses. Although low in precision compared to isotope dating, the fact that it can be dated in-situ with 2-3 μm spatial resolution and can be readily correlated with the texture of a rock, rendered the method a valuable tool for the

identification of metamorphic events in polymetamorphic orogenic belts (Brandt et al., 2011; Finger and Krenn, 2007; Jöns and Schenk, 2011; Kelly et al., 2006). Also in the present study, we found in most cases excellent agreement with zircon ages.

Texturally controlled in-situ electron microprobe (EMP) dating was done in five rock samples of the Ongole domain covering three major rock types (Grt-Sil-Spl-Qz granulite, Grt-Crd±Opx granulite and charnoenderbites). A staurolite schist from the adjoining Vinjamuru domain was also dated to investigate the geochronological relationship between the Ongole and the Vinjamuru domain. The results of representative analyses are summarized in Table 1. The results of all monazite analyses are present in Table B.1 (Appendix B).

3.5.1. Analytical techniques

Monazite was analyzed with a JEOL Superprobe JXA 8900R, equipped with five WDS spectrometers, at the Institute for Geosciences, University Kiel, Germany. A total of 17 elements including Th, U, Pb and some common major and rare earth elements were analyzed to understand the origin of chemical differences in different monazite generations. An accelerating voltage of 20kV, a probe current of 60nA (80nA for two samples: TK39-4 and TK64-3) and a focused beam was used for all monazite analyses. The counting time especially for Th, U and Pb were adjusted based on net intensities to achieve the desired objective of a low error for counting statistics at reliable counting times. All monazite grains were measured in-situ in Pb free polished sections. Back-scattered electron images (BSE) were mostly used to visualize the textural position of the monazite grains (Fig. 3.4) and the internal zoning patterns of each grain (Fig. 3.5). Data quality was controlled by repeatedly analyzing the internal lab standard F6 from Manangoutry pass, SE Madagascar, having an age of 545 ± 11 Ma which has been dated by several independent methods (Paquette et al., 1994). Chondrite normalized REE and Y plots and (Th+U+Si) vs.

(REE+Y+P) plots are used to evaluate the chemical differences in the monazite (Fig. 3.6).

For each monazite measurement the apparent age along with the 2σ error was calculated considering the analytical errors of Th, U and Pb and plotted as individual Gaussian probability curves by using the computer program ‘Age Finder’ (Appel, 2010). For a set of data representing a single stage of monazite growth, the age was obtained by calculating the weighted mean value of the individual apparent ages along with the error and plotted as a mean Gaussian curve (Fig. 3.7). This method was first used by Montel et al. (1996) and is now in common use.

Age maps showing the distribution of apparent ages of a grain was calculated from the raw count rates map of U, Th and Pb by using an in-house computer program ‘MacAgeMap’ by Peter Appel (for details of this software follow the links on <http://www.ifg.uni-kiel.de/353.html>). Further detailed analytical techniques of the Th-U-total Pb dating of monazite are summarized in Braun and Appel (2006) and Jöns et al. (2006). Details about background correction and approximation are given at <http://www.ifg.uni-kiel.de/1202.html>.

3.5.2. Monazite texture, chemistry and age

Grt-Sil-Spl-Qz granulite (TK8-1)

Monazite grains in this sample occur in two main textural settings. They occur as inclusions in porphyroblastic garnet (garnet 1) (Fig. 3.4a) and in the quartzofeldspathic matrix (Fig. 3.4b). The monazite inclusions in garnet 1 are small (up to $35\mu\text{m}$) and rounded to subrounded. They are unzoned to very weakly zoned (Fig. 3.5a). The monazite grains in the quartzofeldspathic matrix are larger (up to $130\mu\text{m}$), anhedral in shape and strongly zoned (Fig. 3.5b,c). Monazite grains

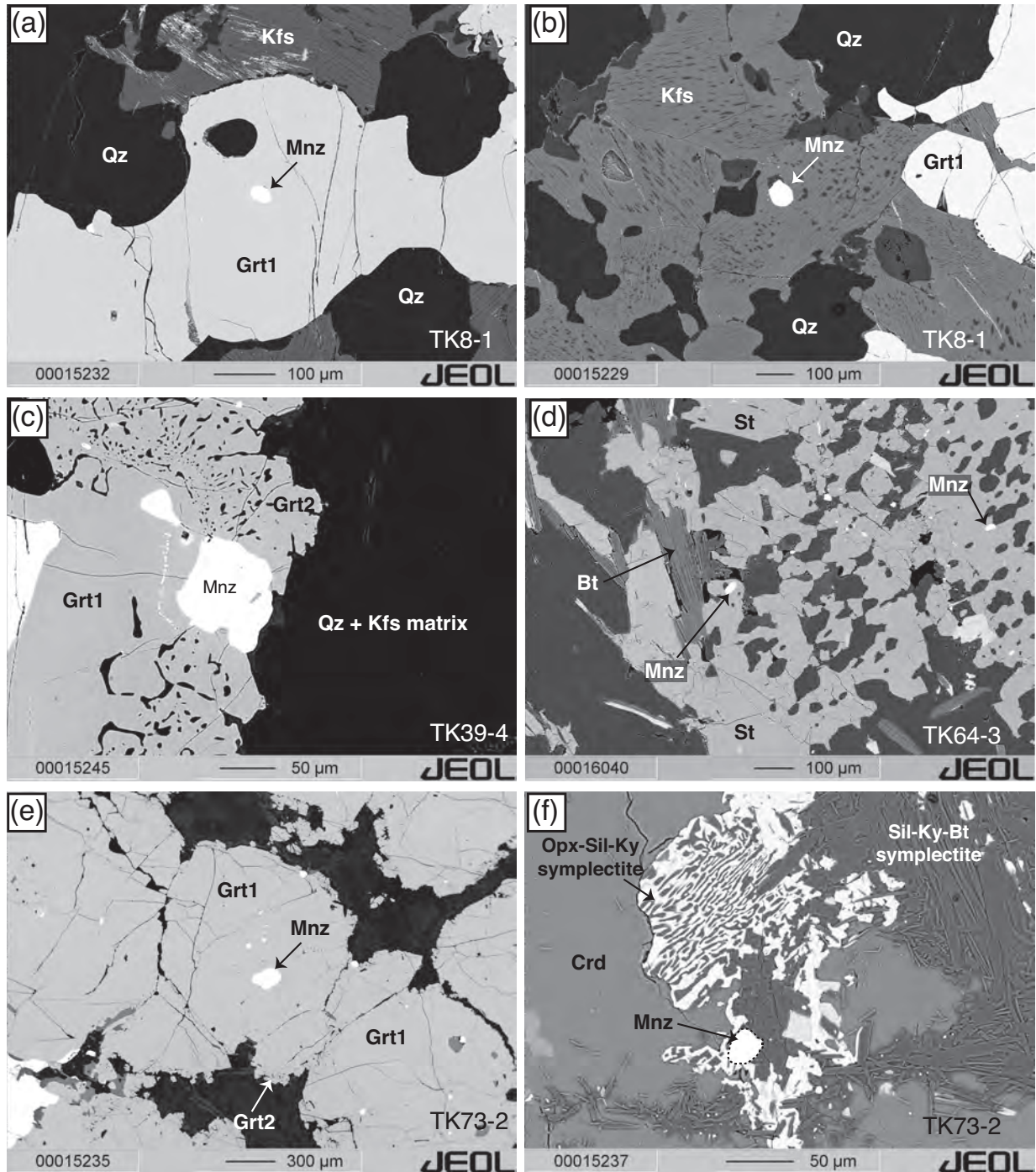


Figure 3.4: Back scattered electron image showing the textural positions of the monazite grains. (a) Monazite as an inclusion in porphyroblastic garnet of Grt-Sil-Spl-Qz granulite TK8-1 and (b) in quartzofeldspathic matrix of the same sample. (c) Monazite growing along with the second generation of garnet in charnockite TK39-4, (d) occurring as inclusion in porphyroblastic staurolite in staurolite schist TK64-3, (e) as an inclusion in a fractured porphyroblastic garnet of Grt-Crd-Opx granulite TK73-2 and (f) within Opx-Sil-Ky-Spl-Bt symplectite replacing cordierite of the same sample.

armored in garnet 1 are of particular importance, as garnet tends to shield the monazite from younger recrystallization events, which might lead to the resetting of the isotopic ratios. These monazite grains have low contents of Th but are rich in Y (ThO_2^* : 4-9 wt.%, Y_2O_3 : 0.3-2.6 wt.%). The monazite grains in the matrix are rich in Th but poor in Y (ThO_2^* : 7-20 wt.%, Y_2O_3 : 0.02-0.06 wt.%). High resolution BSE images reveal a more complex zoning pattern in some of the matrix grains where resorbed portions of a dark, Th-poor, Y-rich core (ThO_2^* : 7-10 wt.%, Y_2O_3 : 0.3-2.6 wt.%) is still preserved and sharply overgrown by Th-rich, Y-poor (ThO_2^* : 14-20 wt.%, Y_2O_3 : 0.02-0.06 wt.%) brighter rims (Fig. 3.5b). In some matrix grains the darker zones are largely replaced by cusped domains of variable BSE contrast that advance from the margin to the interior of the grains, indicating multiple episodes of monazite crystallization (Fig. 3.5c).

Compositional variations of the analyzed monazite grains can be described in terms of the most common substitutions [$\text{Th}/\text{U} + \text{Si} = \text{P} + \text{REE}$ (Huttonite), $\text{Th} + \text{U} + \text{Ca} = 2\text{REE}$ (Cheralite)] taking place in monazite. The influence of these substitutions on the chemical composition of monazite are illustrated in a $(\text{Th}+\text{U}+\text{Si})$ vs. $(\text{REE}+\text{Y}+\text{P})$ diagram, which indicates that the compositional variation is mostly controlled by the huttonitic exchange (Fig. 3.6a). Among the analyzed monazite grains, Th-poor, Y-rich grains included in garnet and cores of matrix grains show a narrow range of chemical variation compared to the matrix grains. Chondrite normalized REE+Y plots (normalizing values from McDonough and Sun, 1995) show a distinct difference between the heavy rare earth element (HREE) content of the monazite inclusions and cores of some matrix monazite grains compared to the majority of matrix grains (Fig. 3.6e). The matrix monazite grains are strongly depleted in Er, while Dy is normally below detection limit compared to higher concentrations of the cores.

In most cases the Th-poor, Y-rich monazite inclusions in garnet record the oldest ages and the complex-zoned Th-rich, Y-poor matrix grains yield younger ages.

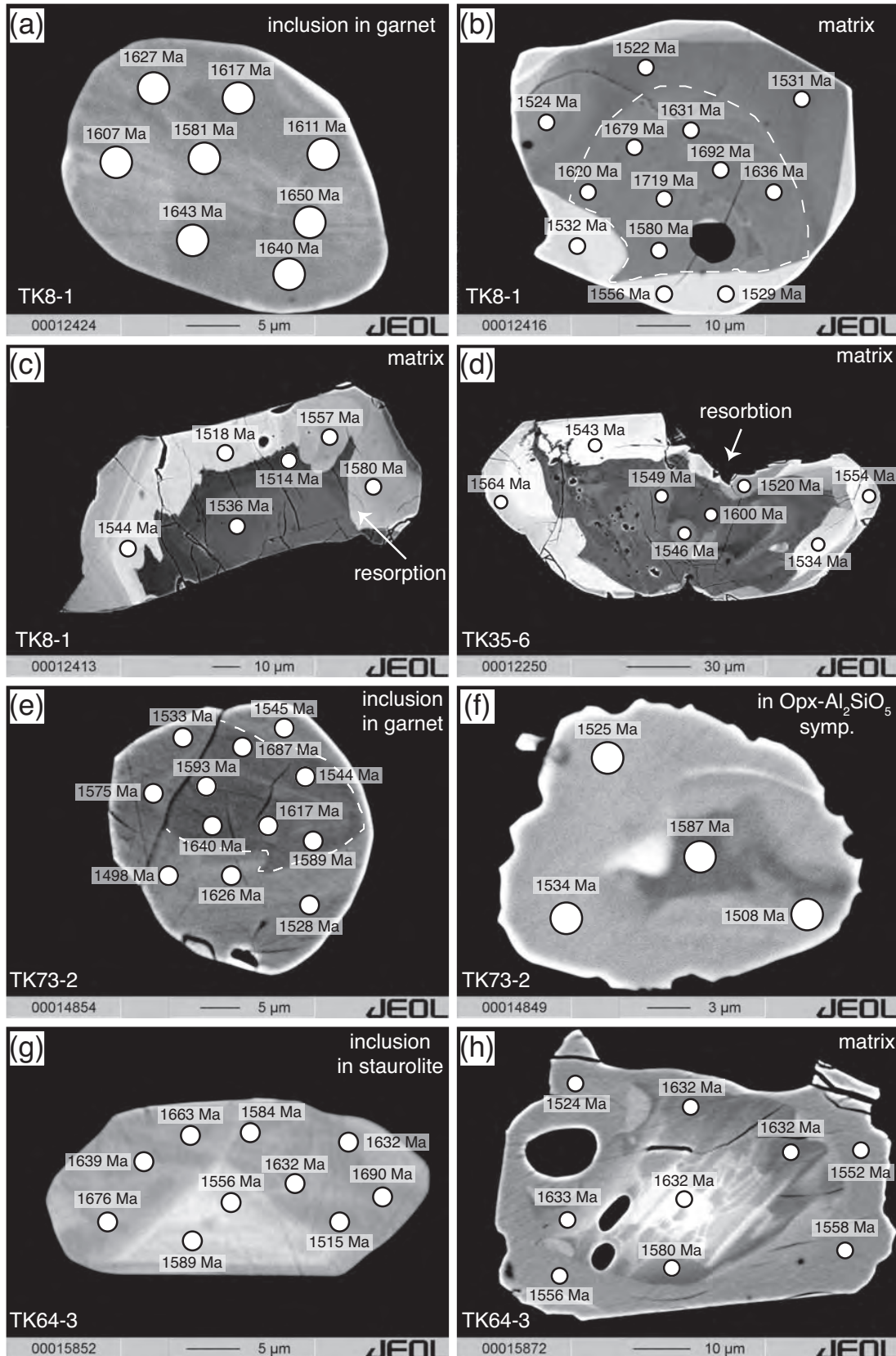


Figure 3.5: (descriptions in the following page)

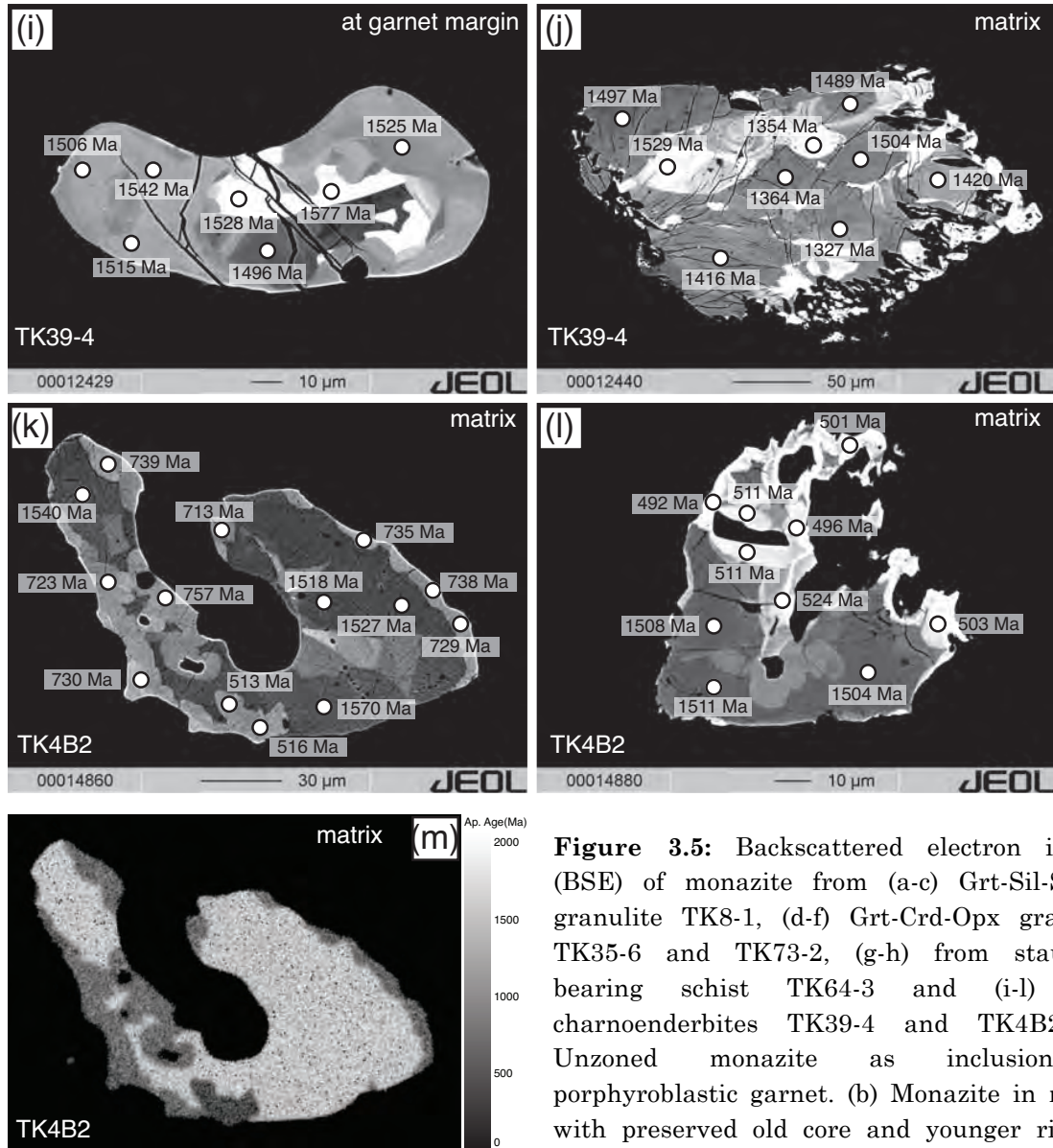


Figure 3.5: Backscattered electron images (BSE) of monazite from (a-c) Grt-Sil-Spl-Qz granulite TK8-1, (d-f) Grt-Crd-Opx granulite TK35-6 and TK73-2, (g-h) from staurolite bearing schist TK64-3 and (i-l) from charnoenderbites TK39-4 and TK4B2. (a) Unzoned monazite as inclusion in porphyroblastic garnet. (b) Monazite in matrix with preserved old core and younger rim. (c) Strongly zoned monazite in the matrix having

uniform age distribution. (d) Irregular monazite in the matrix showing a dark resorbed core and a bright rim, which is also resorbed in some parts. (e) Inclusion in garnet with partially resorbed old core surrounded by a broad younger rim. (f) Small irregular monazite in a Opx-Sil-Ky-Spl-Bt symplectite replacing cordierite. (g) Unzoned monazite inclusion in staurolite. (h) Monazite in the matrix with a resorbed older core surrounded by a broad rim. (i) Zoned monazite at the margin of a porphyroblastic garnet. (j) Large irregular monazite in the matrix with high degrees of resorption and recrystallization. (k) Large monazite grain of the matrix with distinct younger recrystallized zones. (l) Large, highly resorbed matrix monazite with bright younger rims. (m) Apparent age map of the monazite in Fig. 3.5k showing distinct age differences correlating very well with the zonation in the BSE image.

But only occasionally the larger monazite grains in the quartzofeldspathic leucosome domains preserve older cores sharply overgrown by brighter and younger rims. The calculated weighted mean age for older monazite grains is 1619 ± 6 Ma, while the brighter rims yield an age of 1542 ± 4 Ma (Fig. 3.7a).

Grt-Crd±Opx granulite (TK35-6, TK73-2)

In the Grt-Crd±Opx granulites, monazite grains commonly occur as inclusions in garnet 1 or cordierite (Fig. 3.4e), in the matrix and occasionally in coronal garnet 2. In sample TK73-2, monazite grains also occur in the late-stage Opx-Sil-Ky-Spl-Bt symplectite replacing cordierite, attributed to the second metamorphic event (Fig. 3.4f). Monazite grains included in garnet 1 or cordierite are small (up to 40 μm), rounded to subrounded and weakly zoned in BSE. This zonation is attributed to several fractures in the garnet grain providing pathways for fluids (Fig. 3.4e). Monazite grains in the matrix are generally large (up to 200 μm), anhedral and strongly zoned (Fig. 3.5d), while those in the symplectite are small (up to 35 μm) with irregular grain boundaries and weakly zoned (Fig. 3.5f).

The unzoned grains that were well shielded by garnet 1 or large cordierite are Th-poor and Y-rich (ThO_2^* : 5-10.5 wt.%, Y_2O_3 : 0.2-2.8 wt.% in both samples), compared to the complexly zoned grains of the matrix (ThO_2^* : 6-11 wt.% in TK73-2; 9-17 wt.% in TK35-6, Y_2O_3 : 0.1-1.5 wt.% in TK73-2; 0.1-0.5 wt.% in TK35-6). The preserved monazite inclusions as well as the recrystallized matrix grains show a moderate range of chemical substitutions. The incorporation of Th and Si in the monazite grains was mainly due to huttonitic substitution.

Similar to the monazite inclusions in garnet 1 of the Grt-Sil-Spl-Qz granulite (TK8-1), the included monazite grains in the Grt-Crd±Opx granulite are enriched in HREE+Y while the recrystallized grains show depleted values. The oldest ages are recorded from the core domains of monazite included in garnet 1 or cordierite (TK73-2), the weighted mean age being 1608 ± 11 Ma (Fig. 3.7c). The monazite

inclusions of sample TK35-6 are more strongly recrystallized and did not preserve a prominent older age. The complexly zoned, recrystallized parts of the monazite in the matrix and in garnet 2 yielded younger weighted mean ages of 1541 ± 8 Ma (TK35-6; Fig. 3.7b) and 1542 ± 8 Ma (TK73-2; Fig. 3.7c). The recrystallized parts of the monazite grains included in garnet 1 or cordierite also show ages of ca. 1540 Ma, though mostly preserving their Th-poor, Y-rich initial character.

Staurolite schist of the Vinjamuru domain (TK64-3)

Monazite grains in this sample occur in three textural settings: as inclusions in staurolite, along with muscovite or biotite and in the quartzofeldspathic matrix. The monazite grains occurring as inclusions in the porphyroblastic staurolite are small (up to 40 μm), subhedral and weakly zoned (Fig. 3.5g). The monazite grains occurring along with the phyllosilicates and in the quartzofeldspathic matrix are slightly larger (up to 70 μm) and moderately zoned (Fig. 3.5h). BSE images reveal that most matrix grains have a core zone with irregular boundaries and variable BSE contrast. The core zones commonly have curvilinear margins moving towards the interior of the grains. These core zones are sharply overgrown by a broad unzoned mantle showing uniform BSE contrast and having relatively smooth grain boundaries.

Monazite inclusions in staurolite and the darker portions of the core zones have low Th contents (ThO_2^* : 3.6-9.5 wt.%), while the bright recrystallized parts of the core zone and the broad mantles of the matrix monazite grains have higher Th contents (ThO_2^* : 6.4-16.8 wt.%). Y contents are similar in all monazite grains (Y_2O_3 : 1.1-1.6 wt.%) and U_2O_3 contents are 0.1-0.8 wt.%. All monazite grains have enriched HREE and Y contents reflecting the absence of garnet in the sample, which strongly

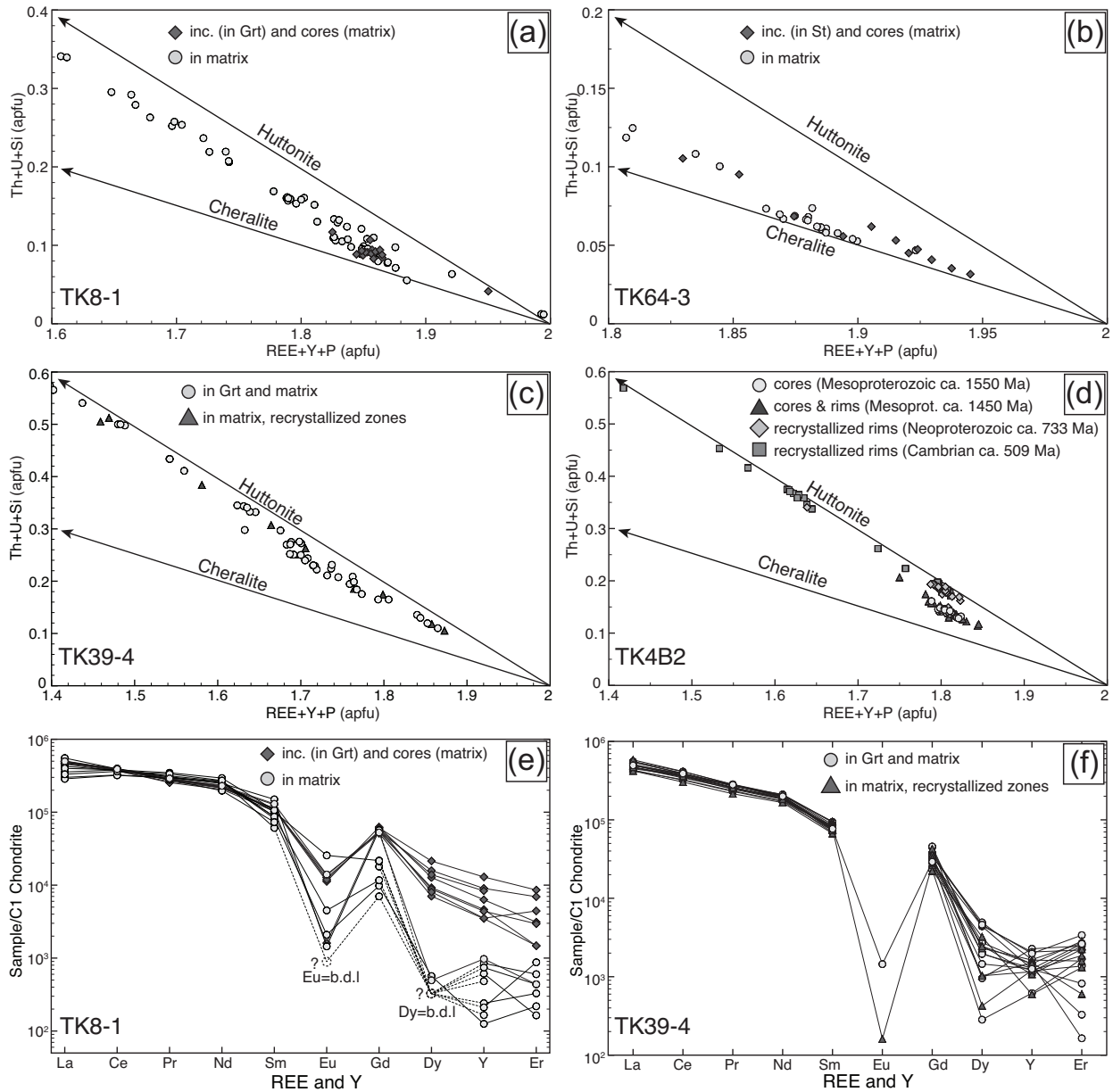


Figure 3.6: Plot of REE+Y+P vs. Th+U+Si from monazites from (a) Grt-Sil-Spl-Qz granulite TK8-1, (b) staurolite bearing schist TK64-3, (c) charnockite TK39-4 and (d) enderbite TK4B2. The linear arrangement of data, which is close to the huttonitic substitution vector in (a), (c) and (d) indicate that the compositional variation was mainly controlled by huttonitic substitution. In contrast, in the staurolite bearing schist (c) the chemical variation is dominated by cheralitic substitution. Chondrite normalized REE+Y plots (normalizing values: McDonough and Sun, 1995) from Grt-Sil-Spl-Qz granulite (e) and from charnockite (f).

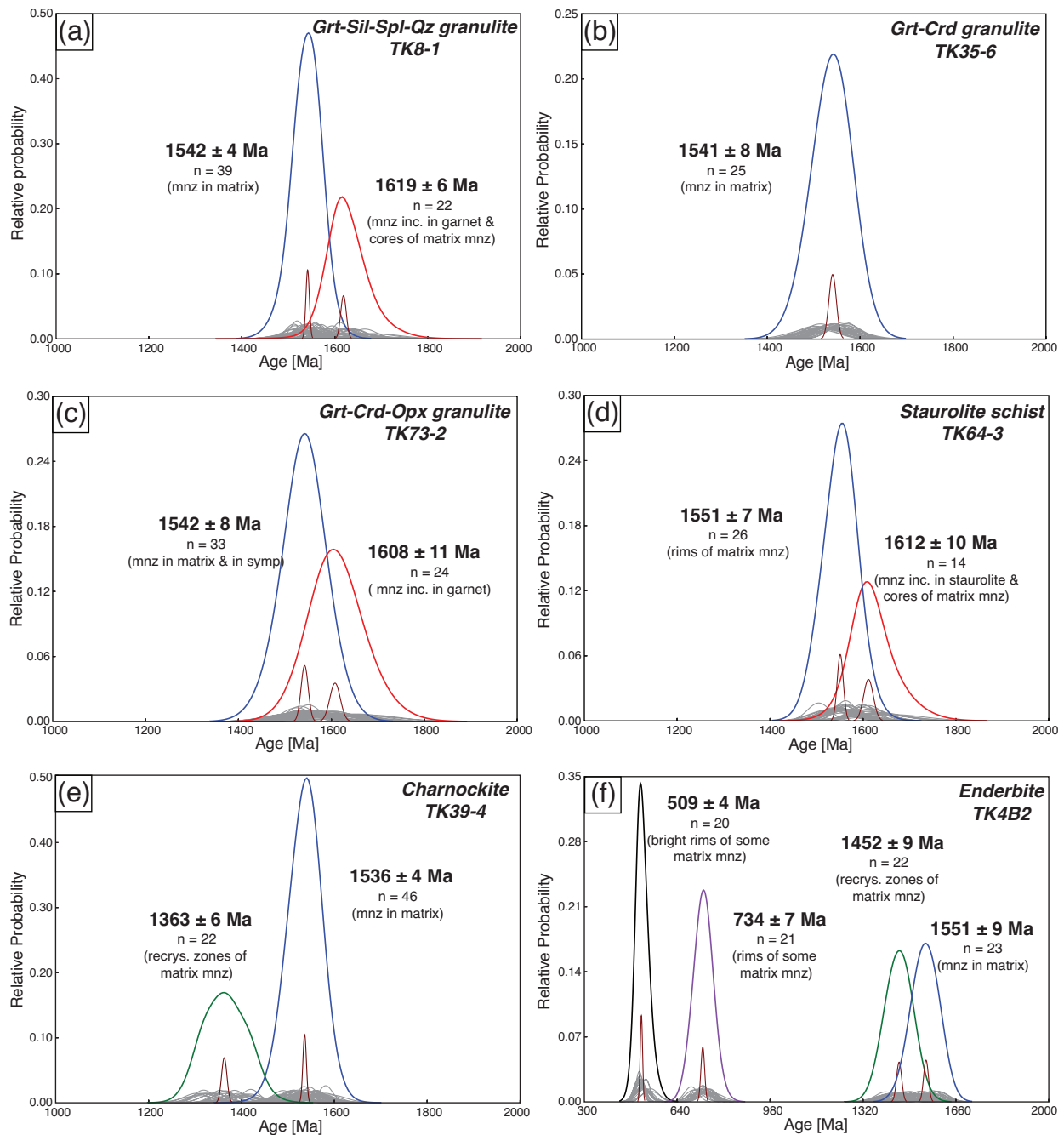


Figure 3.7: Histograms with weighted mean ages for the metapelites and the charnoenderbite from the Ongole domain and a staurolite bearing schist from adjacent Vinjamuru domain. The strong curve is the sum curve for the dates of each age population and the small spiking curve is the curve for weighted mean age (2σ error) for the age population. Most of the samples record at least two stages of monazite growth.

partitions HREE and Y. Unlike the other samples from the granulite-facies Ongole domain the (Th+U+Si) vs. (REE+Y+P) plot reveals that the compositional variation in this sample is controlled mostly by cheralitic substitution (Fig. 3.6b).

Monazite grains recording the oldest spot ages are typically found included in porphyroblastic staurolite and in the non-recrystallized core domains of the matrix grains. These spot ages yield a weighted mean age of 1612 ± 10 Ma (Fig. 3.7d). The broad mantle outside the core domains of the matrix grains as well as some recrystallized parts in the core yield a weighted mean age of 1551 ± 7 Ma (Fig. 3.7d).

Charnoenderbite (TK39-4, TK4B2)

The monazite grains in the charnoenderbite suite of rocks have completely different textural and chemical characters than those in the metapelites. They occur as inclusions in garnet 1 and garnet 2 and in the matrix. The monazite grains are very large (150-450 μm), anhedral and irregular in shape with highly corroded margins (Fig. 3.5j,k,l). Only a few monazite grains armored within garnet 1 are smaller (up to 250 μm) and have smooth margins (Fig. 3.5i). Most grains show complex patchy zoning patterns. The older growth zones are largely to completely replaced by cusped domains of variable BSE contrast advancing from the grain boundary to the interior of the grains (Fig. 3.5k,l). The age and chemistry of the monazite of the charnockite sample (TK39-4) and the enderbite sample (TK4B2) will be discussed separately below.

Charnockite (TK39-4): The different zones of the monazite grains in this sample have highly variable Th contents (ThO_2^* : 7-29 wt.%) while the Y content is very low (Y_2O_3 : 0.09-0.45 wt.%). Individual apparent ages from the monazite range from 1489 to 1577 Ma yielding a weighted mean age of 1536 ± 4 Ma (Fig. 3.7e). But there are some recrystallized zones in several matrix monazite grains that show younger individual apparent ages from 1315 to 1420 Ma. The recrystallized domains yield a weighted mean age of 1363 ± 6 Ma (Fig. 3.7e). The monazite grains hardly

preserve any signature of the older (1620-1600 Ma) event that is prominent in both types of metapelites.

The (Th+U+Si) vs. (REE+Y+P) diagram clearly indicates that the large compositional variation in the analyzed monazite grains is exclusively controlled by the huttonitic substitution for both generations of monazite (Fig. 3.6c). The chondrite normalized REE+Y plot shows depleted HREE contents and strong negative Eu anomalies (Eu mostly below detection limit) for both generations of monazite (Fig. 3.6f).

Enderbite (TK4B2): Due to the complexity of the monazite grains regardless of the textural setting and the large variation in individual apparent ages, a different approach has been adopted to treat the monazite data in this sample. Individual apparent ages (n=86) for this sample range from 489 to 1598 Ma, which are divided into four different groups based on age distribution (Fig. 3.7f). These groups are then treated separately. Individual apparent ages ranging from 496 to 525 Ma (n=20) yield a weighted mean age of 509 ± 4 Ma and apparent ages from 691 to 768 Ma (n=21) yield a mean age of 734 ± 7 Ma (Fig. 3.7f). Apparent ages from 1402 to 1598 Ma has been broadly divided into two groups yielding weighted mean ages of 1452 ± 9 Ma (n=22) and 1551 ± 9 Ma (n=23). A fairly decent correlation could be established between the different ages, when combined with their chemistry and texture (Fig. 3.7f).

An apparent age of ~ 1550 Ma is most common and found in the majority of the analyzed grains regardless of their textural position, but mostly in the core regions (Fig. 3.5k,l). An apparent age map for one of these grains (Fig. 3.5m) clearly indicates that in this particular case the age boundaries within the monazite grains are very sharp and coincide perfectly with the compositional boundaries visible in the BSE image (Fig. 3.5k). Recrystallized marginal parts of some of these grains yield ages of ~ 1450 Ma. These ages are also present throughout some grains. Bright recrystallized cusped domains replacing large parts of the primary grain (with ages of ~ 1550 Ma) yield younger ages with a mean age of 734 ± 7 Ma (Fig. 3.5k). Apparent

ages of ~500 Ma are found from similar coliform recrystallized domains and along the margins of resorbed grain boundaries (Fig. 3.5l). These domains are very bright in BSE image.

The different monazite generations have variable Th and Y contents. The older primary grains yielding Mesoproterozoic ages have moderate Th contents (ThO_2^* : 8-11 wt.%) and high Y contents (Y_2O_3 : 1.3-3.5 wt.%). The Neoproterozoic monazite zones have slightly higher Th contents (ThO_2^* : 9.5-14.4 wt.%) and low to moderate Y contents (Y_2O_3 : 0.28-2.29 wt.%). On the other hand the mid Cambrian monazite grains have highly variable Th contents (ThO_2^* : 11-29 wt.%; avg. 19 wt.%) with low to moderate Y contents (Y_2O_3 : 0.95-2.3 wt.%). The U contents are similar for all the monazite generations ranging from 0.12 to 0.26 wt.% with a few spots having higher contents (up to 0.55 wt.%). The (Th+U+Si) vs. (REE+Y+P) plot reflects the dominance of the huttonitic substitution in controlling the chemical variation of the analyzed monazite grains (Fig. 3.6d), very similar to that of the metapelites and the charnockite. The plot further shows that the Cambrian monazite grains underwent a much stronger huttonitic substitution compared to the older generations.

3.5.3. Monazite data results

Small, Th-poor, Y+HREE-rich monazite grains included in garnet 1 of Grt-Sil-Spl-Qz and Grt-Crd±Opx granulites (Fig. 3.5a,e) clearly suggest that these monazite grains crystallized prior to or along with the growth of garnet 1. By virtue of its textural position these grains are expected to be least affected by younger events. As garnet acts as a sink for Y+HREE, the rock matrix was not yet depleted in these elements before or during the early stages of garnet growth, corroborating the high Y+HREE contents of the included monazite grains. The core domains of some matrix monazite preserving the older age are the remnants of the older monazite that grew

Table 3.1: Electron microprobe U-Th-total Pb representative monazite analyses and calculated ages

Spot	Grain	Texture	Position	Y ₂ O ₃	ThO ₂	err ThO ₂	UO ₂	err UO ₂	PbO	err PbO	ThO ₂ *	err ThO ₂ *	Age	Err ap. Age
				(wt %)	(wt %)	(%)	(wt %)	(%)	(wt %)	(%)	(wt %)	(%)	(Ma)	(Ma)
<i>Gr-Sil-Spl-Qz granulite (TK8-1)</i>														
52	mz6	matrix	core	0.93	7.07	1.05	0.58	1.16	0.66	1.24	9.20	0.85	1631	25
72	mz14	inc. in Grt	unzoned	1.88	7.07	1.05	0.52	1.04	0.63	1.28	8.97	0.85	1595	25
81	mz15	inc. in Grt	unzoned	1.26	6.88	1.06	0.37	0.74	0.59	1.35	8.22	0.90	1628	26
373	mz6	matrix	core	1.80	8.28	0.99	0.67	3.31	0.77	2.30	10.73	1.07	1636	42
38	mz3	matrix	core	0.04	13.76	0.76	0.09	0.18	0.94	1.03	14.08	0.75	1536	20
43	mz3	matrix	rim	0.02	16.52	0.70	0.07	0.15	1.13	0.86	16.79	0.69	1544	17
48	mz5	matrix	rim	0.05	14.78	0.74	0.17	0.33	1.03	0.91	15.38	0.71	1537	18
55	mz6	matrix	rim	0.16	13.27	0.78	0.19	0.39	0.93	0.98	13.97	0.74	1530	19
<i>Gr-Crd granulite (TK35-6)</i>														
62	mz12	matrix	rim	0.40	11.38	0.83	1.65	1.87	1.14	2.09	17.33	0.84	1514	34
174	mz4	matrix	core	0.14	9.36	0.91	0.51	3.53	0.75	2.73	11.20	0.95	1536	44
195	mz21	matrix	core	0.19	9.74	0.89	0.09	7.92	0.68	2.95	10.05	0.90	1547	48
199	mz21	matrix	rim	0.19	16.53	0.70	0.06	6.03	1.13	2.07	16.73	0.69	1544	34
237	mz7	inc. in Grt	core	1.42	6.62	1.08	1.13	2.29	0.71	2.83	10.70	1.10	1530	46
<i>Gr-Crd-Opx granulite (TK73-2)</i>														
129	mz3	inc. in Grt	core	1.10	6.87	1.07	0.44	4.15	0.60	3.22	8.46	1.17	1619	55
192	mz16	inc. in Grt	unzoned	1.23	5.52	1.20	0.70	3.21	0.58	3.30	8.09	1.31	1639	58
361	mz13	inc. in Grt	core	1.45	3.99	1.10	0.35	4.85	0.37	3.54	5.25	1.43	1617	62
365	mz15	inc. in Crd	core	1.42	4.41	1.04	0.63	3.27	0.47	2.93	6.70	1.31	1616	52
125	mz3	inc. in Grt	rim	2.19	6.82	1.07	0.49	3.93	0.58	3.33	8.61	1.18	1553	55
133	mz5	Opx-Sil-Ky sym	unzoned	0.33	8.00	0.99	0.62	3.32	0.68	2.93	10.25	1.06	1525	47
143	mz8	inc. in Grt 2	core	0.14	20.94	0.64	0.40	3.40	1.50	1.72	22.37	0.63	1534	28
357	mz5	Opx-Sil-Ky sym	unzoned	0.28	7.82	0.78	0.56	3.31	0.66	2.28	9.86	0.92	1534	38
<i>St-Ms-Bt schist (TK64-3, Vinjamuru domain)</i>														
135	mz1	inc. in St	unzoned	1.37	3.78	0.79	0.29	5.29	0.35	3.18	4.85	1.32	1633	56
143	mz8	matrix	core	1.11	4.94	0.69	0.23	5.70	0.41	2.70	5.77	1.01	1610	46
165	mz17	matrix	core	1.30	8.68	0.55	0.24	4.77	0.67	1.87	9.56	0.66	1597	32
180	mz25	matrix	rim	1.43	10.44	0.51	0.29	4.07	0.78	1.68	11.51	0.60	1557	28
184	mz32	matrix	rim	1.58	6.18	0.62	0.71	2.67	0.59	2.03	8.74	0.90	1552	34
242	mz17	matrix	rim	1.17	8.47	0.55	0.23	4.97	0.63	1.95	9.29	0.66	1547	32
<i>Charnockite (TK39-4)</i>														
94	m2	at Grt margin	rim	0.25	21.95	0.62	0.17	4.21	1.50	1.44	22.56	0.62	1529	24
99	m2	at Grt margin	core	0.19	14.27	0.75	0.01	7.75	0.95	1.93	14.32	0.75	1516	31
110	m4	inc. in Grt	core	0.24	12.74	0.79	0.11	6.42	0.89	2.01	13.13	0.79	1552	33
131	m11	matrix	core	0.13	24.74	0.60	0.14	4.12	1.68	1.35	25.24	0.59	1529	23
102	m3	in Grt 2	rim	0.33	19.94	0.65	0.36	3.48	1.26	1.60	21.22	0.64	1364	24
132	m11	matrix	rim	0.12	25.20	0.59	0.20	3.79	1.52	1.43	25.90	0.59	1354	21
135	m11	matrix	rim	0.29	16.50	0.71	0.14	5.15	0.98	1.90	17.02	0.70	1327	27
91	m1	matrix	rim	0.23	11.99	0.82	0.04	8.42	0.73	2.35	12.12	0.81	1379	34

Table 3.1: Continued

Spot	Grain	Texture	Position	Y ₂ O ₃	ThO ₂	err ThO ₂	UO ₂	err UO ₂	PbO	err PbO	ThO ₂ *	err ThO ₂ *	Age	Err ap. Age
				(wt %)	(wt %)	(%)	(wt %)	(%)	(wt %)	(%)	(wt %)	(%)	(Ma)	(Ma)
<i>Enderbite (TK4B2)</i>														
202	mz1	matrix	core	3.34	10.09	0.92	0.18	7.92	0.72	3.43	10.75	0.99	1540	55
245	mz17	matrix	core	1.78	9.12	0.93	0.18	6.22	0.65	3.05	9.78	0.96	1520	49
207	mz2	in Grt 2	core	2.11	10.28	0.88	0.17	6.22	0.75	2.77	10.88	0.90	1585	46
261	mz25	inc. in Pl	core	3.57	9.37	0.92	0.23	5.44	0.67	2.98	10.21	0.96	1512	47
209	mz2	in Grt 2	rim	3.18	8.68	0.96	0.20	6.05	0.61	3.20	9.41	1.00	1497	50
238	mz13	in Grt 2	core	1.36	8.82	0.95	0.16	6.78	0.59	3.27	9.38	0.98	1448	49
250	mz17	matrix	rim	1.36	9.89	0.89	0.13	6.83	0.65	3.03	10.37	0.91	1443	46
267	mz28	matrix	unzoned	2.53	10.93	0.85	0.19	5.73	0.73	2.81	11.60	0.87	1448	43
203	mz1	matrix	rim	1.68	10.16	0.90	0.19	6.81	0.33	5.90	10.80	0.94	723	43
298	mz1	matrix	rim	1.58	10.64	0.69	0.18	5.89	0.35	3.95	11.24	0.73	731	29
317	mz13	in Grt 2	rim	0.55	10.10	0.71	0.20	5.46	0.35	3.83	10.77	0.74	754	29
420	mz20	matrix	rim	0.72	13.80	0.61	0.19	4.81	0.45	3.04	14.45	0.62	733	23
258	mz25	inc. in Pl	rim	1.65	18.01	0.68	0.23	4.35	0.41	4.35	18.77	0.68	511	22
314	mz12	matrix	rim	2.30	10.72	0.69	0.19	5.40	0.25	5.10	11.37	0.72	511	26
337	mz25	inc. in Pl	rim	1.37	28.65	0.47	0.31	3.11	0.63	2.39	29.66	0.47	501	12
341	mz33	matrix	rim	1.42	10.22	0.70	0.14	6.24	0.23	5.24	10.67	0.72	511	27

prior to or along with garnet 1. We regard the weighted mean ages of 1619 ± 6 Ma (TK8-1) (Fig. 3.7a) as the timing of the peak metamorphic conditions when spinel+quartz was stable prior to the main garnet growth stage. Many inclusions of spinel and quartz in garnet 1 are in agreement with the fact that garnet grew primarily after or during the peak metamorphic conditions in the spinel-quartz stability field. The weighted mean age of 1608 ± 11 Ma (Fig. 3.7c) from few included grains and core domains of some matrix monazite in the Grt-Crd-Opx granulite (TK73-2) is in accordance with the earlier interpretation that they formed during peak metamorphic conditions prior to or along with garnet 1.

In contrast, Th-rich and Y+HREE poor monazite grains occurring in the rock matrix crystallized subsequent to garnet 1 in a Y+HREE depleted environment. Most likely these monazite grains grew together with garnet 2. The weighted mean age of 1542 ± 4 Ma (TK8-1) (Fig. 3.7a) of these monazite grains is regarded as the timing of the second metamorphism, which was intense enough to isotopically reset or recrystallize most of the matrix monazite grains. Only the grains well armored within garnet 1 survived the re-equilibration. The common occurrence of monazite

grains in a recrystallized quartzofeldspathic matrix indicates that also other minerals recrystallized along with monazite in response to the second metamorphic event. The ages are also in excellent accordance with the weighted mean age of 1541 ± 8 and 1542 ± 8 (Fig. 3.7b,c) from the Grt-Crd \pm Opx granulite (TK35-6 and TK73-2), which is shown by the majority of the monazite grains. Partial to complete re-equilibration of some monazite grains in spite of being shielded by garnet in the Grt-Crd \pm Opx granulite suggests that garnet 1 was not always robust enough to prevent the monazite recrystallization as garnet developed multiple fractures most likely during the second metamorphic event providing fluid pathways (Fig. 3.4e).

The monazite grains in the charnoenderbites show additional ages besides those of the two main metamorphic events that correspond to some events not recorded by monazite in metapelites. The majority of monazite grains from both charnockite (TK39-4) and enderbite (TK4B2) show Mesoproterozoic ages (1536 ± 4 in TK39-4 and 1551 ± 9 in TK4B2, Fig. 3.7e,f), which is in accordance with the age of the second metamorphism obtained from the metapelites. But they hardly preserve any signature of the older (~ 1620 Ma) UHT metamorphism. Consequently, the Mesoproterozoic age of ~ 1550 Ma is interpreted to be the age of the second metamorphism when most of the monazite crystallized or underwent extreme recrystallization. Locally some monazite grains from the charnoenderbites record a further Mesoproterozoic event at 1363 ± 6 Ma (TK39-4) and 1452 ± 9 Ma (TK4B2) (Fig. 3.7e,f). Unlike any other sample the enderbite (TK4B2) record a further Neoproterozoic and early Phanerozoic event along recrystallized margins of some monazite grains. The extreme enrichment of Th in these zones indicates fluid induced recrystallization by dissolution-precipitation processes (see below).

In the staurolite schist (TK64-3) of the Vinjamuru domain the age of 1612 ± 10 Ma (Fig. 3.7d) from monazite inclusions and cores of matrix monazite is the same as the age of the first metamorphism recorded from the monazite inclusions in the granulite-facies metapelites from the Ongole domain. The broad mantle around partly recrystallized cores of the matrix monazite grains yielded a mean age of

1551±6.5 Ma, which is same as the age of a major reequilibration of monazite from the Ongole domain. This indicates that the rocks of both the domains experienced the same tectonothermal events.

The unzoned to weakly zoned older monazite grains included in garnet and in the cores of matrix grains show a narrow range of variation in its chemical composition reflecting a stable physico-chemical environment during their growth. On the other hand the patchy zoned recrystallized matrix monazite grains show a wide range of compositional variability mainly controlled by the huttonitic substitution reflecting a dynamic physico-chemical environment. This is in contrast to other high-Th monazite in the staurolite schist (TK64-3; Fig. 3.6b) from the Vinjamuru domain (this study) and monazite from other areas of the world which usually incorporates Th and Si by cheralitic ($\text{Th}^{4+} + \text{Ca}^{2+} = 2\text{REE}^{3+}$) substitution (Spear and Pyle, 2002). It has been experimentally shown by Harlov et al. (2011) that monazite develops extensive Th+Si enriched zones along the grain boundaries due to dissolution-precipitation processes characterized by the huttonitic substitution. The substitution occurs in response to interaction with $\text{Na}_2\text{SiO}_5 + \text{H}_2\text{O}$ rich fluids or melts at high temperatures by coupled dissolution-precipitation processes, where the older monazite grains served as the source for Th. Since other fluids, including NaCl and KCl brines, did not result in the formation of these textures, the experiments suggest that the similar textures observed here in nature are indications for the involvement of alkali and silica bearing fluids.

To speculate about the possible sources for a $\text{Na}_2\text{SiO}_5 + \text{H}_2\text{O}$ rich fluids that may have been responsible for the chemistry of the newly grown monazite, the main lithologies of the Ongole domain, i.e. the charnoenderbites, are to be considered. Partial melting of enderbites with $\text{Na}_2\text{O}/\text{K}_2\text{O} > 1$ and charnockites with $\text{Na}_2\text{O}/\text{K}_2\text{O} \leq 1$ in response to the second metamorphism is likely to have produced some Na+Si rich melts. A further possibility is that fluids derived from the subduction zone prior and during the second tectonometamorphic event, may have moved through the overlying Na-rich charnoenderbitic crustal rocks.

3.6. Discussion and conclusions

3.6.1. Correlation of zircon and monazite age data

The age data obtained from zircon and monazite have to be combined to reconstruct the sequence of events that took place in the Ongole domain and to discuss the likely geodynamic evolution. The summary of the obtained ages is presented in Fig. 3.8 and Table 2. In some zircon grains of the metapelites, oscillatory-zoned magmatic cores older than the surrounding mantles or rims are preserved. The cores are interpreted as detrital grains from the source areas of the sediments. The zircon grains in the quartzite (TK46-3) from the southern part of the Ongole domain yielding late Archean to early Palaeoproterozoic ages (2.52-2.39 Ga) are also detrital grains. As the Ongole domain was formed in a magmatic arc setting most likely near the Indian continent, the possible source areas of the sediments are the Archean Eastern Dharwar craton, the adjoining Vinjamuru domain, the mafic dykes and sills emplaced within the Proterozoic Cuddapah basin or the magmatic rocks of the Ongole domain itself (Fig. 3.1). The Archean inherited zircon grains (e.g. Fig. 3.2g,h) are most likely to be derived from the Eastern Dharwar craton, as it is the only Archean crust in the surrounding. Moreover, Nd model ages (T_{DM}) of the migmatitic metapelites range between 2.8 and 2.6 Ga (Rickers et al., 2001). These are similar to the Nd model ages of granitoids of the Eastern Dharwar craton, indicating that it is a possible source of the sediments. But the approaching and then subducting continental margin (East Antarctic craton as speculated by Dasgupta et al., 2013), acting as the source of the sediments cannot be ruled out. The few detrital cores showing ages of ~ 1.9 Ga (e.g. Fig. 3.2a,e) can possibly be derived from mafic dykes and sills emplaced within the Cuddapah basin and parts of the Vinjamuru domain at the same time (Anand et al., 2003). The detrital cores showing ages of ~ 1.75 -1.80 Ga (Fig. 3.2d,i) can be derived from the widespread volcanic rocks of the Vinjamuru

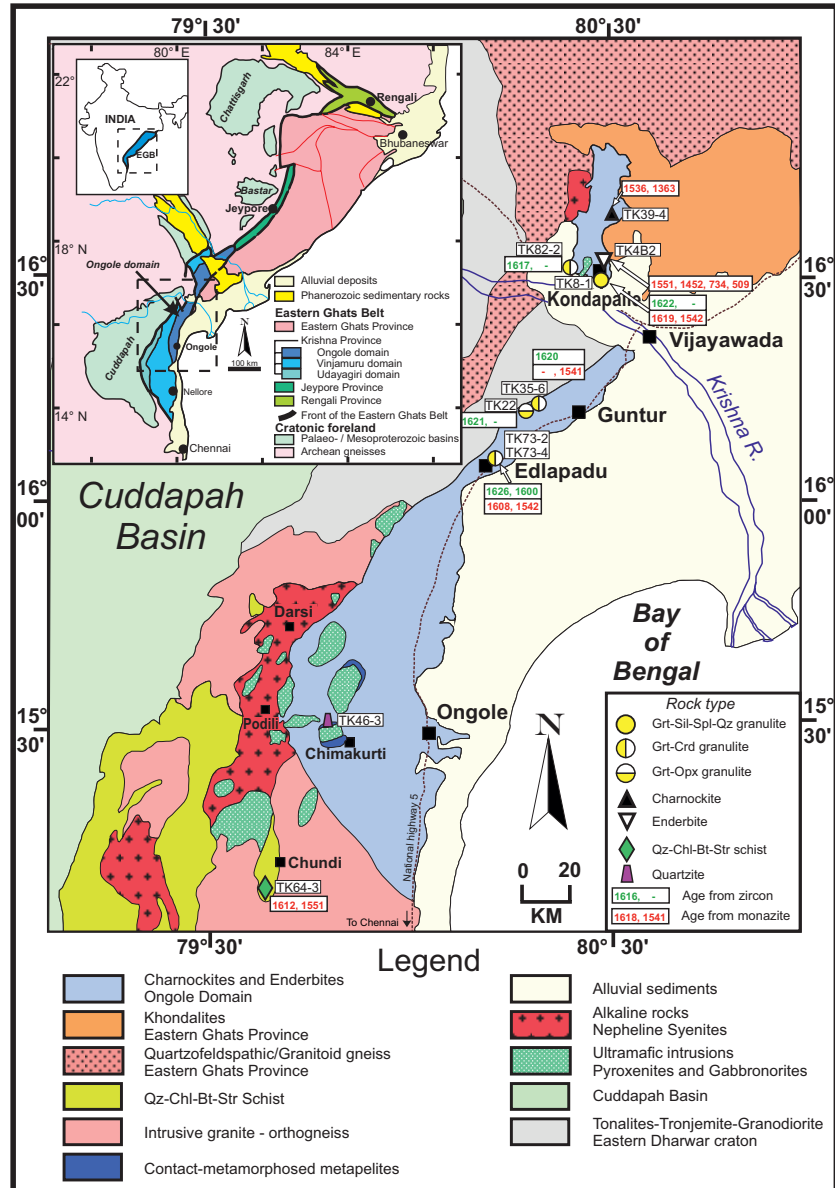


Figure 3.8: Distribution of metamorphic ages in the Ongole and the Vinjamuru domain. LA-ICP-MS zircon dating and texturally controlled in-situ monazite dating by electron microprobe analyses revealed two metamorphic events in the Ongole domain separated by 60-80 Ma. A staurolite bearing schist from the Vinjamuru domain (TK64-3) yielded the same ages as that of the Ongole domain.

domain that were emplaced at ~ 1.78 Ga (Ravikant et al., 2013). As the Ongole domain is characterized by multiple intrusions of different ages starting from ~ 1.76 Ga (Kovach et al., 2001 and unpublished own data) the oscillatory-zoned detrital cores of that age (Fig. 3.2d) can well be derived from the earlier magmatic intrusions

within the Ongole domain itself. Bose et al. (2011) obtained a concordia age of ~ 1.76 Ga from oscillatory-zoned zircon grains of a single metapelite from the Ongole domain and interpreted it to be the age of an earlier UHT metamorphism, although they explored the possibility that these oscillatory-zoned zircon grains might be detrital and represent magmatic activity in the source region. We have found no metamorphic zircon rims or overgrowths with ages of ~ 1.76 Ga from five metapelite samples dated from the Ongole domain. Therefore, we prefer to interpret these oscillatory-zoned cores in the metapelites (e.g. Fig. 3.2d) to represent detrital zircon grains recording the age of the magmatic activity in the source area of the sediments. The zircon rims and overgrowths around these cores and some ellipsoidal metamorphic zircon grains yielding concordia ages of ~ 1.60 Ga (e.g. Fig. 3.3b) indicate a single metamorphic event and represent the timing of the pervasive UHT metamorphism in the Ongole domain. From field relations it is evident that the migmatitic metapelites occur as enclaves within the charnoenderbites (chapter 2). This situation gives rise to two possibilities. The metapelites were metamorphosed in high-grade conditions prior to the emplacement of the charnoenderbites at ca. 1.76 Ga and were taken up as huge blocks by the precursor magma of the charnoenderbites. The other possibility is that the metapelites were metamorphosed in high-grade conditions during the emplacement of the precursor magma of the charnoenderbites. In either of the cases a metamorphic event older or at least contemporaneous to the age of emplacement of the charnoenderbites is most likely and should lead to zircon growth or regrowth. However, no metamorphic growth zones of that age have been found. The absence of a metamorphic age older than ca. 1.62 Ga from the zircon grains that have been dated here does not exclude the possibility of an older metamorphism.

As discussed before, because zircon dating might not provide complete information even in high-grade terrains, age data from in-situ monazite dating have been compared and combined with those of the zircon dating. The ages of monazite inclusions in garnet (ca. 1.62 Ga; e.g. Fig. 3.7a) correlate perfectly with the concordia

Table 3.2: Summary of zircon and monazite ages

Sample	Rock type	Assemblage	Mnz/Zrc	Grain size (μm)	Age (2σ error)	Figures
TK8C1	Metapelite	Grt-Sil-Spl-Qz	Zrc	100-300	2652 \pm 28 Ma to 1797 \pm 21 Ma (detrital cores) 1622.3 \pm 4.8 Ma (n=9; MSWD=0.04)	Fig. 3.3a
TK8-1	Metapelite	Grt-Sil-Spl-Qz	Mnz	20-130	1619 \pm 6 Ma (n=22) 1542 \pm 4 Ma (n=39)	Fig. 3.7a
TK35-6	Metapelite	Grt-Crd	Zrc	100-300	1892 \pm 29 Ma to 1774 \pm 28 Ma (detrital cores) 1619.8 \pm 4.6 Ma (n=15; MSWD=0.05)	Fig. 3.3b
TK73-4	Metapelite	Grt-Opx Crd	Mnz Zrc	30-200 100-250	1541 \pm 8 Ma (n=25) 2734 \pm 23 Ma to 1772 \pm 28 Ma (detrital cores) 1625.7 \pm 6.4 Ma (n=8; MSWD=0.03) 1599.7 \pm 5.2 Ma (n=8; MSWD=0.64)	Fig. 3.7b Fig. 3.3c Fig. 3.3c Fig. 3.3d
TK73-2	Metapelite	Grt-Opx-Crd	Mnz	15-180	1608 \pm 11 Ma (n=24) 1542 \pm 8 Ma (n=33)	Fig. 3.7c
TK22	Metapelite	Grt-Opx	Zrc	100-200	1620.8 \pm 5.0 Ma (n=11; MSWD=0.28)	Fig. 3.3e
TK82-2	Metapelite	Grt-Opx	Zrc	100-250	1840.0 \pm 9.1 Ma (n=11; MSWD=) (detrital cores) 1616.8 \pm 4.8 Ma (n=15; MSWD=0.32)	Fig. 3.3f Fig. 3.3f
TK46-3	Quartzite	Qz	Zrc	50-140	2523 \pm 21 Ma to 2387 \pm 34 Ma (detrital cores)	Fig. 3.3g Fig. 3.3g
TK39-4	Charnockite	Grt-Opx-Kfs-Qz-Pl	Mnz	150-450	1536 \pm 4 Ma (n=46) 1363 \pm 6 Ma (n=22)	Fig. 3.7e
TK4B2	Enderbite	Grt-Opx-Pl-Qz-Kfs	Mnz	100-300	1551 \pm 9 Ma (n=23) 1452 \pm 9 Ma (n=22) 734 \pm 7 Ma (n=21) 509 \pm 4 Ma (n=20)	Fig. 3.7f
TK64-3	Metapelite (Vinjamuru domain)	St-Ms-Bt	Mnz	20-70	1612 \pm 10 Ma (n=14) 1551 \pm 7 Ma (n=26)	Fig. 3.7d

ages (ca. 1.62 Ga) obtained from the metamorphic rims and overgrowths on zircon grains (Fig. 3.3a), thus confirming the interpretation of this age as the age of the pervasive UHT metamorphism in the Ongole domain. The monazite grains in the matrix rarely preserve ages of \sim 1.62 Ga, but mostly show younger ages of \sim 1.54 Ga. Monazite grains growing along with the second generation of garnet also show these younger ages. Therefore we interpret this age as the age of the second metamorphic event. This interpretation is also supported by the monazite chemistry that is different in HREE+Y contents in the two generations of monazite. Though this second metamorphic event occurred under high-grade conditions, it is not recorded

by zircon. As the two events recorded by monazite are closely spaced they could have been easily misinterpreted to be part of a single long-lived metamorphic event rather than two separate metamorphic events, if there were no strong textural and chemical control on the different generations of monazite grains. Thus, only zircon dating, or even monazite dating without textural control would have revealed a single polyphase metamorphism. But the combination of zircon dating and texturally controlled in-situ monazite dating revealed two closely spaced separate metamorphic events.

The geochemistry of the metamorphosed felsic to intermediate volcanic rocks from the Vinjamuru domain indicates that they were emplaced in a convergent magmatic arc tectonic setting (Ravikant et al., 2013). The emplacement age of these rocks at ~ 1.78 Ga is constrained from zircon dating and are very similar to the emplacement ages of the charnoenderbites from the Ongole domain. Monazite dating of the staurolite schist (TK64-3) from the Vinjamuru domain also yielded ages at ~ 1.61 Ga and ~ 1.55 Ga (Fig. 3.7d), indicating two separate metamorphic events, identical to those of the Ongole domain. This evidence suggests that the Ongole domain and at least the northern part of the Vinjamuru domain are tectonically related, but the latter experienced a lower-grade metamorphism than the former.

3.6.2. Possible interpretation of the post 1.54 Ga events

Mesoproterozoic ages younger than that of the second metamorphism at 1.54 Ga were obtained at 1452 ± 9 - 1363 ± 6 Ma from a charnockite and an enderbite (Fig. 3.7e,f). They can be tentatively correlated to an extensional event (Simmat and Raith, 2008) that led to the emplacement of alkaline complexes along the western margin of the Eastern Ghats Belt between 1480 and 1260 Ma (Upadhyay, 2008). The ages also correlate with the 1.35 Ga age obtained from allanite of a sheared

syenitic pegmatite, possibly indicating the timing of a late ductile deformation (Mezger and Cosca, 1999).

The significance of the age population at ~ 734 Ma obtained from the narrow recrystallized rims of several matrix monazite grains of the enderbite is not clear (TK4B2; Fig. 3.7f). We tentatively correlate them with phases of renewed monazite recrystallization in response to some weak tectonic activities in the region. Similar ages of 880-750 Ma have been reported from matrix monazite of the northern part of the Eastern Ghats Province (Simmat and Raith, 2008), which have been correlated to ductile deformation and associated fluid infiltration that produced a mylonitic fabric in the granulites. On a global perspective, widespread continental rifting occurred between ca. 850 Ma and 740 Ma during the break-up of the Rodinia supercontinent (Li et al., 2008). Therefore, minor disturbances in the Eastern Ghats Belt at this time are likely.

Similar to the Cambrian age of 508 ± 4 Ma obtained from the enderbite (TK4B2), also Simmat and Raith (2008) reported some monazite grains in a single sample near a shear zone from the Ongole domain showing ages of ~ 513 Ma. A well-defined age population of 530-470 Ma, mainly from matrix monazite was also documented by the same workers in the Eastern Ghats Province. It was interpreted as the time of the NNW directed deformation during the Neoproterozoic collision of the Eastern Ghats Province – Rayner complex terrain with cratonic India.

3.6.3. Geodynamic interpretation

The timing of the first metamorphic event in the Ongole domain has been constrained between 1625 and 1600 Ma by zircon dating and in-situ monazite dating. No older metamorphic growth zones have been found. This metamorphic event was under UHT metamorphic conditions and is characterized by a near-isobaric heating-cooling trajectory at low pressures (Fig. 3.9), pointing towards a

magmatic heat source for the metamorphism (chapter 2). An evidence for magmatic activity is a mafic-ultramafic complex in the northern part of the Ongole domain near Kondapalle, which was emplaced in a magmatic arc setting at ~1630 Ma (Dharma Rao et al., 2012). Moreover, magmatic activity was still persistent at ~1600 Ma as some intrusions are of that age (author's unpublished data). The

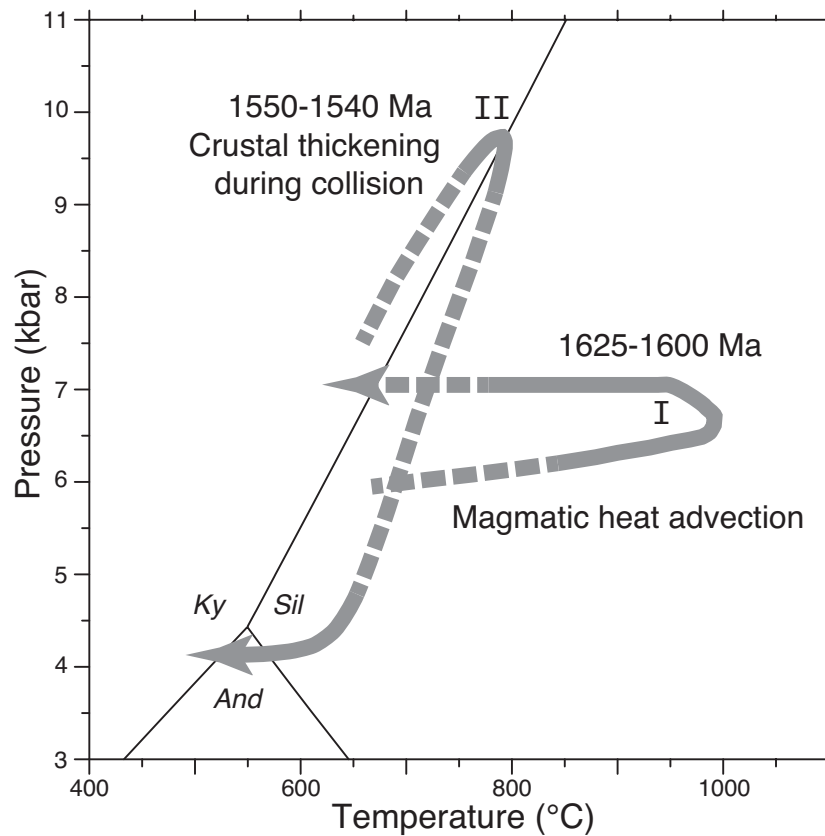


Figure 3.9: Pressure-temperature evolution of the rocks from the Ongole domain during two subsequent metamorphic events.

timing of the second metamorphic event at ~1540 Ma is constrained by monazite ages. It implies a gap of 60-80 Ma between the two metamorphic events. During this time the rocks may have cooled isobarically from the peak metamorphic conditions. The second metamorphic event occurred at higher pressures but lower temperatures and is characterized by a clockwise P-T path with a strong pressure drop after peak pressures (Fig. 3.9). It has been attributed to a crustal thickening event during the

collision of the magmatic arc (Ongole domain) with the Eastern Dharwar craton (chapter 2). Though there is evidence for Meso- to Neoproterozoic disturbances, the Ongole domain did not experience a major tectonothermal reworking after ca. 1.54 Ga. In summary, the combination of LA-ICP-MS zircon dating and texturally controlled in-situ monazite dating by electron microprobe allowed us to unravel a two-stage metamorphic history of a Proterozoic magmatic arc that may represent a likely evolution of magmatic arcs in general. First, during its growth stage, the arc experienced a UHT metamorphism due to magmatic heat advection, which then several tens of million years later was followed by a second metamorphic event in an overthickened crust during the collision of the arc with a continent.

3.7 Acknowledgements

We thank A. Fehler for the preparation of high quality thin-sections and B. Mader for her assistance with microprobe analyses.

References

- Anand, M., Gibson, S.A., Subbarao, K.V., Kelly, S.P., Dickin, A.P., 2003. Early Proterozoic Melt Generation Processes beneath the Intra-cratonic Cuddapah Basin, Southern India. *Journal of Petrology* 44, 2139–2171.
- Appel, P., 2010. “AgeFinder” A Mac OS X computer program to evaluate electron microprobe data of monazite for chemical age dating. *Computers and Geosciences* 36, 559–563.
- Boniface, N., Schenk, V., Appel, P., 2012. Paleoproterozoic eclogites of MORB-type chemistry and three Proterozoic orogenic cycles in the Ubendian Belt (Tanzania): Evidence from monazite and zircon geochronology, and geochemistry.

- Precambrian Research 192-195, 16–33.
- Bose, S., Dunkley, D.J., Dasgupta, S., Das, K., Arima, M., 2011. India-Antarctica-Australia-Laurentia connection in the Paleoproterozoic-Mesoproterozoic revisited: Evidence from new zircon U-Pb and monazite chemical age data from the Eastern Ghats Belt, India. *Geological Society of America Bulletin* 123, 2031–2049.
- Brandt, S., Schenk, V., Raith, M.M., Appel, P., Gerdes, A., Srikantappa, C., 2011. Late Neoproterozoic P-T evolution of HP-UHT Granulites from the Palni Hills (South India): New Constraints from Phase Diagram Modelling, LA-ICP-MS Zircon Dating and in-situ EMP Monazite Dating. *Journal of Petrology* 52, 1813–1856.
- Braun, I., Appel, P., 2006. U-Th-total Pb dating of monazite from orthogneisses and their ultra-high temperature metapelitic enclaves implications for the multistage tectonic evolution of the Madurai Block, southern India. *European Journal of Mineralogy* 18, 415–427.
- Cherniak, D.J., Watson, E.B., Grove, M., Harrison, T.M., 2004. Pb diffusion in monazite: a combined RBS/SIMS study. *Geochimica et Cosmochimica Acta* 68, 829–840.
- Dasgupta, S., Bose, S., Das, K., 2013. Tectonic evolution of the Eastern Ghats Belt, India. *Precambrian Research* 227, 247–258.
- Dharma Rao, C.V., Santosh, M., 2011. Continental arc magmatism in a Mesoproterozoic convergent margin: Petrological and geochemical constraints from the magmatic suite of Kondapalle along the eastern margin of the Indian plate. *Tectonophysics* 510, 151–171.
- Dharma Rao, C.V., Santosh, M., Dong, Y., 2012. U-Pb zircon chronology of the

- Pangidi-Kondapalle layered intrusion, Eastern Ghats belt, India: Constraints on Mesoproterozoic arc magmatism in a convergent margin setting. *Journal of Asian Earth Sciences* 49, 362–375.
- Dobmeier, C.J., Raith, M.M., 2003. Crustal architecture and evolution of the Eastern Ghats Belt and adjacent regions of India. Geological Society, London, Special Publications 206, 145–168.
- Finger, F., Krenn, E., 2007. Three metamorphic monazite generations in a high-pressure rock from the Bohemian Massif and the potentially important role of apatite in stimulating polyphase monazite growth along a PT loop. *Lithos* 95, 103–115.
- Harlov, D.E., Wirth, R., Hetherington, C.J., 2011. Fluid-mediated partial alteration in monazite: the role of coupled dissolution–reprecipitation in element redistribution and mass transfer. *Contributions to Mineralogy and Petrology* 162, 329–348.
- Herwartz, D., Skublov, S.G., Berezin, A.V., Mel'nik, A.E., 2012. First Lu-Hf garnet ages of eclogites from the Belomorian Mobile Belt (Baltic Shield, Russia). *Doklady Earth Sciences* 443, 377–380.
- Jöns, N., Schenk, V., 2011. The ultrahigh temperature granulites of southern Madagascar in a polymetamorphic context: implications for the amalgamation of the Gondwana supercontinent. *European Journal of Mineralogy* 23, 127–156.
- Jöns, N., Schenk, V., Appel, P., Razakamanana, T., 2006. Two-stage metamorphic evolution of the Bemarivo Belt of northern Madagascar: constraints from reaction textures and in situ monazite dating. *Journal of metamorphic Geology* 24, 329–347.
- Kelly, N.M., Clarke, G.L., Harley, S.L., 2006. Monazite behaviour and age

- significance in poly-metamorphic high-grade terrains: A case study from the western Musgrave Block, central Australia. *Lithos* 88, 100–134.
- Kooijman, E., Berndt, J., Mezger, K., 2012. U-Pb dating of zircon by laser ablation ICP-MS: recent improvements and new insights. *European Journal of Mineralogy* 24, 5–21.
- Kovach, V.P., Simmat, R., Rickers, K., Berezhnaya, N.G., Salnikova, E.B., Dobmeier, C., Raith, M.M., Yakovleva, S.Z., Kotov, AB, 2001. The western charnockite zone of the Eastern Ghats Belt, India-an independent crustal province of late Achaean (2.8 Ga) and Palaeoproterozoic (1.7-1.6 Ga) terrains. *Gondwana Research* 4, 666–667.
- Li, Z., Bogdanova, S., Collins, A., Davidson, A., De Waele, B., Ernst, R., Fitzsimons, I., Fuck, R., Gladkochub, D., Jacobs, J., 2008. Assembly, configuration, and break-up history of Rodinia: a synthesis. *Precambrian Research* 160, 179–210.
- McDonough, W.F., Sun, S.S., 1995. The composition of the Earth. *Chemical Geology* 120, 223–253.
- Mezger, K., Cosca, M.A., 1999. The thermal history of the Eastern Ghats Belt (India) as revealed by U–Pb and $^{40}\text{Ar}/^{39}\text{Ar}$ dating of metamorphic and magmatic minerals: implications for the SWEAT correlation. *Precambrian Research* 94, 251–271.
- Mints, M.V., Belousova, E.A., Konilov, A.N., Natapov, L.M., Shchipansky, A.A., Griffin, W.L., O'Reilly, S.Y., Dokukina, K.A., Kaulina, T.V., 2010. Mesoarchean subduction processes: 2.87 Ga eclogites from the Kola Peninsula, Russia. *Geology* 38, 739–742.
- Montel, J., Foret, S., Veschambre, M., Nicollet, C., Provost, A., 1996. Electron microprobe dating of monazite. *Chemical Geology* 131, 37–53.

- Mukhopadhyay, D., Basak, K., 2009. The Eastern Ghats Belt... A Polycyclic Granulite Terrain. *Journal Geological Society of India* 73, 489–518.
- Paquette, J.L., Nédélec, A., Moine, B., Rakotondrazafy, M., 1994. U-Pb, Single Zircon Pb-Evaporation, and Sm-Nd Isotope Study of a Granulite Domain in SE Madagascar. *The Journal of Geology* 102, 523–538.
- Parrish, R.R., 1990. U–Pb dating of monazite and its application to geological problems. *Canadian Journal of Earth Sciences* 27, 1431–1450.
- Ramakrishnan, M., Nanda, J.K., Augustine, P.F., 1998. Geological evolution of the Proterozoic Eastern Ghats mobile belt. *Geological Survey of India Special Publications* 44, 1–21.
- Ravikant, V., 2010. Palaeoproterozoic (~1.9Ga) extension and breakup along the eastern margin of the Eastern Dharwar Craton, SE India: New Sm–Nd isochron age constraints from anorogenic mafic magmatism in the Neoproterozoic Nellore greenstone belt. *Journal of Asian Earth Sciences* 37, 67–81.
- Ravikant, V., Kröner, A., Vasudevan, D., 2013. Zircon evaporation ages and geochemistry of metamorphosed volcanic rocks from the Vinjamuru domain, Krishna Province: evidence for 1.78 Ga convergent tectonics along the southeastern margin of the Eastern Dharwar Craton. *Geological Journal* 48, 293–309.
- Rickers, K., Mezger, K., Raith, M.M., 2001. Evolution of the continental crust in the Proterozoic Eastern Ghats Belt, India and new constraints for Rodinia reconstruction: implications from Sm–Nd, Rb–Sr and Pb–Pb isotopes. *Precambrian Research* 112, 183–210.
- Schenk, V., Appel, P., Jöns, N., Loose, D., Schumann, A., Wegner, H., 2005. Pan-African reworking of the northeastern corner of the Congo Craton in Uganda.

Supercontinents and Earth Evolution Symposium.

Simmat, R., Raith, M.M., 2008. U–Th–Pb monazite geochronometry of the Eastern Ghats Belt, India: Timing and spatial disposition of poly-metamorphism. *Precambrian Research* 162, 16–39.

Spear, F.S., Pyle, J.M., 2002. Apatite, monazite, and xenotime in metamorphic rocks. *Reviews in Mineralogy and Geochemistry* 48, 293–335.

Upadhyay, D., 2008. Alkaline magmatism along the southeastern margin of the Indian shield: Implications for regional geodynamics and constraints on craton–Eastern Ghats Belt suturing. *Precambrian Research* 162, 59–69.

Chapter 4

Formation and evolution of a Proterozoic magmatic arc: geochemical and geochronological constraints from meta-igneous rocks of the Ongole domain, Eastern Ghats belt, India.

Abstract

Geochemical data and U-Pb zircon results are presented for the intrusive meta-igneous rocks of the Ongole domain, a granulite-facies terrain of the Eastern Ghats Belt in India, with the aim of inferring the tectonic setting and the timing of their formation. Geochemical data suggest that the intrusive meta-igneous rocks (mafic granulites and charnoenderbites) possess trace and rare earth element composition that are typical of magmatic arcs. They are subalkaline, enriched in light rare earth elements (LREEs) and large ion lithophile elements (LILEs) and depleted in heavy rare earth elements (HREEs) and high field strength elements (HFSEs) like Nb, Ta and Ti. These characteristics indicate that the primary magmas of these rocks were derived by partial melting of a depleted mantle wedge that had been metasomatized by fluids derived from a subducted slab. Zircon grains collected from 5 charnoenderbites are large, euhedral to subhedral and display fine-scale oscillatory growth zoning in CL images, implying a magmatic origin. The grains are frequently surrounded by narrow to broad unzoned overgrowths, implying a metamorphic

origin. The oscillatory-zoned cores yield Palaeoproterozoic concordia ages of ca. 1750-1710 Ma, indicating the time of magma emplacement. The unzoned overgrowths yield very late Palaeoproterozoic ages of ca. 1630-1600 Ma, indicating the timing of metamorphism. An enderbite showing both magmatic and metamorphic concordia ages of ca. 1605 Ma point to the existence of syn-metamorphic intrusions. Together, the presented geochemical and geochronological evidence suggest that the Ongole domain was a magmatic arc near the Indian continent during the Palaeoproterozoic. Subsequently, the rocks were metamorphosed during late Palaeoproterozoic and the terrain was accreted to the Indian craton during early Mesoproterozoic. In context to the relation of the Ongole domain to the Columbia supercontinent, the terrain grew by subduction related accretion during the growth stage of Columbia (1.8-1.2 Ga) and was accreted to the Indian craton during a time apparently unrelated to the formation of Columbia (2.1-1.8 Ga) on a global scale.

4.1. Introduction

The formation and subsequent evolution of continental crust from the Archean to the present is one of the key topics in earth sciences that is widely debated (Arndt, 2013; Condie, 2000; Hawkesworth and Kemp, 2006). Continental crust grew mainly along subduction zones of active continental margins by tectonic accretion and emplacement of juvenile magmatic rocks besides minor magmatism in intra-plate tectonic settings (Jagoutz et al., 2007; Şengör et al., 1993; Windley and Garde, 2009), though the nature of geodynamic processes that generated Archean continental crust still remains controversial (Polat, 2012 and references therein). Trace element similarities, such as enrichment of light rare earth elements (LREE), depletion of Nb, Ta and Ti, enrichment of Pb with respect to REE, between Proterozoic

magmatic sequences and volcanic rocks at modern subduction zones imply that post-Archean continental crust formed in a similar way as in the Phanerozoic (Cawood et al., 2006; Rudnick, 1995; Taylor and McLennan, 1985). Magmatic arcs have always been important entities in models of continental growth and preserve unique geochemical characteristics (Polat, 2012) and tectono-metamorphic histories (Chapter 3). They are often formed during the process of continental amalgamation through the subduction of the intervening oceanic lithosphere in a prolonged subduction-accretion-collision regime (Korsch et al., 2011). Thus the knowledge about the timing of formation of magmatic arcs helps to anticipate the timings of continental amalgamations, which led to the formations of the various supercontinents in the geological history.

The Ongole domain in the southern part of the Eastern Ghats Belt exposes a variety of granulite-facies rocks mainly dominated by charnoenderbites (Dobmeier and Raith, 2003; Chapter 2). Geochemical data from discrete magmatic bodies around and within the Ongole domain indicate their formation in a continental arc setting (Dharma Rao and Santosh, 2011). However, a systematic geochemical and geochronological study of the now granulite-facies meta-igneous rocks of the Ongole domain itself has not yet been undertaken.

In this contribution we present field relationships, trace and rare earth element geochemistry and U-Pb zircon (LA-ICPMS) geochronological data of the meta-igneous rocks of the Ongole domain (mostly charnoenderbites and some associated mafic granulites). Our data constrain the timing and tectonic setting of crust formation: The Ongole domain was formed in a continental arc setting during a short time interval of the late-Palaeoproterozoic. The geochronological data further constrain also the timing of metamorphism in addition to the data presented in Chapter 3. This study reconstructs the history of a magmatic arc from its growth via subduction related accretion to its attachment with the craton and provides new insights into the evolution of Proterozoic continental crust in Peninsular India.

4.2. Geological setting

The Eastern Ghats Belt (EGB), which includes the Ongole domain, is a Proterozoic crustal segment extending for ca. 1000 km along the eastern margin of the Indian peninsula in a NE-SW direction (Fig. 1). It is an assembly of intensely deformed, polymetamorphosed and deeply eroded high-grade terrains bounded to the west along several shear zones by the Archean cratons of the Indian shield (for summary: see Dobmeier and Raith, 2003).

Earlier subdivisions of the EGB were based on lithology (Ramakrishnan et al., 1998) and isotopic signatures (Rickers et al., 2001). Dobmeier and Raith (2003) divided the EGB into 4 crustal provinces, which were further divided into crustal domains based on their distinct geological histories and separated from each other by tectonic boundaries. The Krishna Province in the southern part of the EGB comprises the granulite-facies Ongole domain and the medium to low-grade Vinjamuru and Udayagiri domains (Fig. 1). The present work is focused on the Ongole domain that lies in between the Archean Eastern Dharwar craton to the west and the Mesoproterozoic Eastern Ghats Province to the east (Fig. 1).

The Ongole domain is characterized by the occurrence of large volumes of multi-intrusive charnoenderbites with enclaves of migmatitic metasedimentary rocks from meter to outcrop scale (Dobmeier and Raith, 2003; Chapter 2). Geochemical data of the relatively small Kondapalle mafic-ultramafic complex within the northern part of the Ongole domain has been interpreted as indications for a formation in a magmatic arc setting (Dharma Rao and Santosh, 2011). A preliminary study revealed that charnoenderbites were emplaced at ca. 1.7 Ga (Kovach et al., 2001). The Nd model ages (T_{DM}) of 2.5-2.3 Ga from the charnoenderbites suggest a mantle-derived magma with substantial input of Archean crustal material (Rickers et al., 2001). This was followed by a high-grade metamorphic event at ca. 1.6 Ga (Bose et al., 2011; Simmat and Raith, 2008;

Chapter 3) indicating that the Ongole domain is dominantly a Palaeoproterozoic terrain.

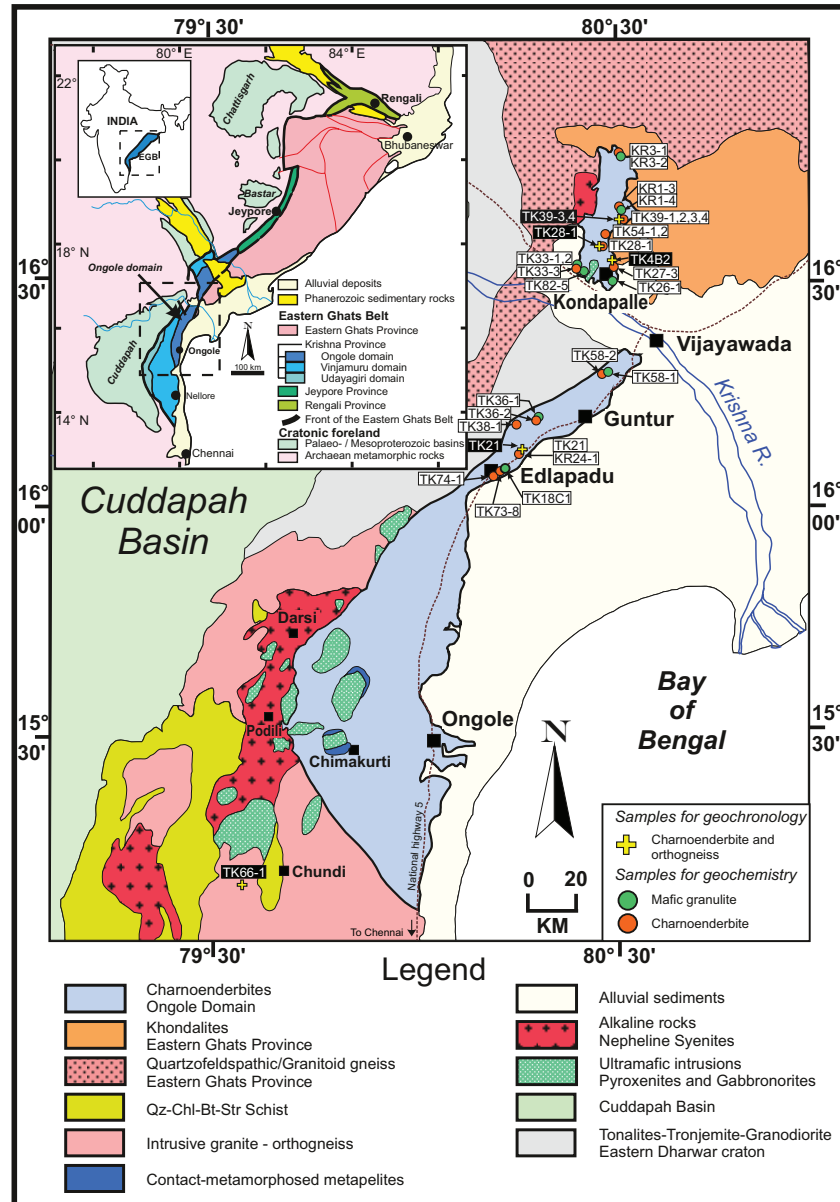


Figure 4.1: Geological map of the southern part of the Eastern Ghats Belt (EGB) showing the position of the Ongole domain and the adjoining areas (adapted and simplified from the Geological Survey of India map of Andhra Pradesh, published in 2001) with the rock type and locations of geochemistry and geochronology samples. Geological outline of the Eastern Ghats Belt and adjacent regions modified after Dobmeier and Raith (2003) (inset).

Field relations show that the mafic-ultramafic complex near Kondapalle has been intruded and dismembered by charnoenderbites (Sengupta et al., 1999) that

were thought to have been emplaced at 1.7 Ga. Very recently the emplacement of the same mafic-ultramafic complex has been dated at 1.69-1.63 Ga (Dharma Rao et al., 2012) indicating different generations of magmatic rocks in the area. A N-S array of a suite of alkaline rocks ranging from quartz syenite to alkali granite, interpreted to have been emplaced during rifting, marks the boundary between the Ongole domain and the Eastern Dharwar craton (Fig. 1; Upadhyay, 2008).

The amphibolites-facies Vinjamuru domain, adjacent to the southwestern part of the Ongole domain (Fig. 1) is essentially composed of felsic to intermediate metavolcanic rocks in addition to some metasediments and granitoids (see Dobmeier and Raith, 2003). Recently Ravikant et al. (2013) established from zircon dating (Pb evaporation method) of the metavolcanic rocks from the northern part of the Vinjamuru domain that a major magmatic activity was in the Palaeoproterozoic (ca. 1.78 Ga). This was followed by an amphibolite facies metamorphism at 1.61 Ga (Chapter 3). From geochemical data, the rocks are interpreted to have formed in a continental magmatic arc tectonic setting (Ravikant et al., 2013).

4.3. Field relationship and petrography

The Ongole domain is dominantly composed of large volumes of multi-intrusive intermediate (enderbite) to felsic (charnockite) granulites, collectively referred to as charnoenderbites (Fig. 2a). It covers a substantial part of the Ongole domain. The metapelitic granulites constitute only a small portion (<10 vol %) of the exposed rocks and occur as enclaves (Fig. 2b) within the charnoenderbites (for details see Chapter 2). The mafic rocks are rare and occur as big enclaves, dykes and xenoliths within the charnoenderbites (Fig. 2c,d,e) and as a separate layered mafic intrusion in the northern part of the Ongole domain near Kondapalle. All the rocks are exposed along freshly cut quarry faces throughout the Ongole domain.

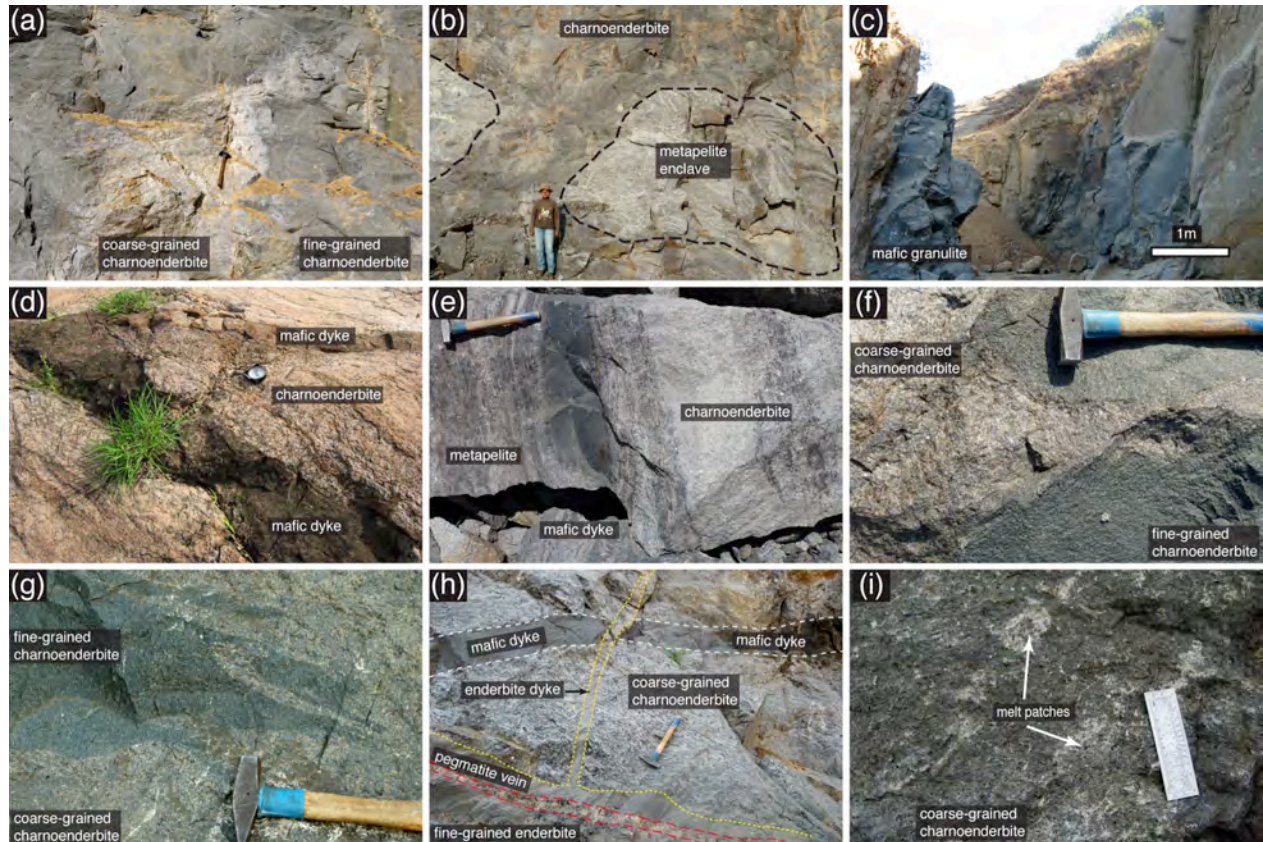


Figure 4.2: (a) Coarse-grained charnoenderbite intruding into fine-grained charnoenderbite; (b) enclaves of metapelitic granulite within charnoenderbite; (c) mafic granulite associated with charnoenderbite; (d) charnoenderbite cut by a mafic dyke; (e) metapelitic enclave cut by mafic dyke near the contact of metapelite and charnoenderbite; (f, g) contact between coarse-grained and fine-grained charnoenderbites; (h) interrelation among the different generations of magmatic rocks. A charnockite (1) has been intruded by a mafic dyke (2) and a fine-grained enderbite (3). A pegmatite vein (4) has cut through all the rock units (Chapter 2); (i) leucosome patches within charnoenderbite.

The charnoenderbites have a homogenous and massive appearance in the outcrop. Meticulous observation reveals that the enderbites are generally fine-grained massive to medium-grained gneissic rocks whereas the charnockites are generally medium to coarse-grained gneissic to pegmatoidal (Fig. 2a,f,g). However, the gneissic nature is clearly observed only on weathered surfaces. Complex crosscutting relationships among the different varieties of rocks are preserved in outcrops, indicating multiple stages of intrusion (Fig. 2h).

Mineralogically the rocks are composed of a quartzofeldspathic matrix together with garnet, orthopyroxene, biotite and ilmenite. The rocks underwent granulite-

facies metamorphic events and migmatization (Chapter 2), which is also evident from the thin leucosome patches (Fig. 2i). It is, however, not clear if orthopyroxene is a product of this metamorphism or inherited from the magmatic protolith.

4.4. Analytical techniques

4.4.1. Geochemistry

A representative part of each sample was washed with distilled water and pulverized to very fine powder in an agate mill at the Institute for Geosciences, University of Kiel. Major element concentrations of whole rocks were obtained from XRF analyses at the University of Kiel. Fused glass discs were prepared by mixing 0.6g of sample powder with 3.6g of $\text{Li}_2\text{B}_4\text{O}_7$ and 2g of NH_4NO_3 (flux), then subjecting the mixture to the OXIFLUX 5-stage burner. The glass discs were analyzed with a Philips PW 1400 X-ray fluorescence analyzer to acquire the major element concentrations.

Trace and rare earth element analyses were carried out at GeoForschungZentrum (GFZ) in Potsdam, Germany. Trace element concentrations were determined by Inductively Coupled Plasma Mass Spectrometry (ICP-MS) using a VG Plasma Quad PG2. Sample powders were decomposed using HF, Aqua regia and HClO_4 in pressure vessels. The decomposed samples were dissolved in HNO_3 and diluted to a volume of 50ml for analysis. Rare earth elements (REE) and Y contents were determined by inductively coupled plasma-atomic emission spectroscopy (ICP-AES) following the procedure of Zuleger and Erzinger (1988). The samples were decomposed and dissolved using the Na_2O_2 sinter method and the REE were separated and concentrated using ion-exchange methods. The standards GM, JG-3, GSR-1 and JG-1a (Govindaraju, 1994) were prepared and analyzed together with the unknown samples. The accuracy of each analysis was assessed by

comparing the standards with certified values (Liang and Grégoire, 2000; Dulski, 2001) and estimated to be better than 10% for each element.

4.4.2. U-Pb zircon geochronology by LA-ICP-MS

Zircon grains were separated from hand specimens by standard heavy mineral separation techniques. The rocks (hand specimen size) were first crushed followed by magnetic separation using a hand magnet and a Franz isodynamic magnetic separator to exclude the magnetic minerals. The separate was then subjected to heavy mineral separation using bromoform liquid. To include all the varieties of zircon grains in terms of shape and size, the individual zircon grains were carefully hand picked from the heavy mineral residue. Selected grains were mounted on epoxy resin discs and polished. To study their internal structure, the polished mounts were photographed and cathodoluminescence (CL) images were obtained before analyses using the JEOL JSM-6490 Scanning Electron Microscope at the Institute for Geosciences, University of Frankfurt. Points were carefully selected on several zircon grains to include all petrographically distinct domains under CL images. U-Pb isotopic analyses were carried out by using a Element2 sector field ICP-MS coupled to a New Wave UP193HE ArF Excimer laser system at the Institute for Mineralogy of the University of Münster. The analytical details for the measurement of U and Pb isotopes using the LA-ICP-MS are further elaborated by Kooijman et al. (2012).

4.5. Geochemistry

4.5.1. Alteration and element mobility

The meta-igneous rocks of the Ongole domain have undergone granulite-facies metamorphism. This high-grade metamorphism might have led to the mobility of some elements, which would render them useless to decipher the primary petrogenetic processes. Thus, fresh samples were carefully selected and big sample specimens were crushed to avoid trace element partitioning on a local scale due to different mineral assemblages. Altogether, a total of 28 samples are selected forming the basis of all subsequent discussions.

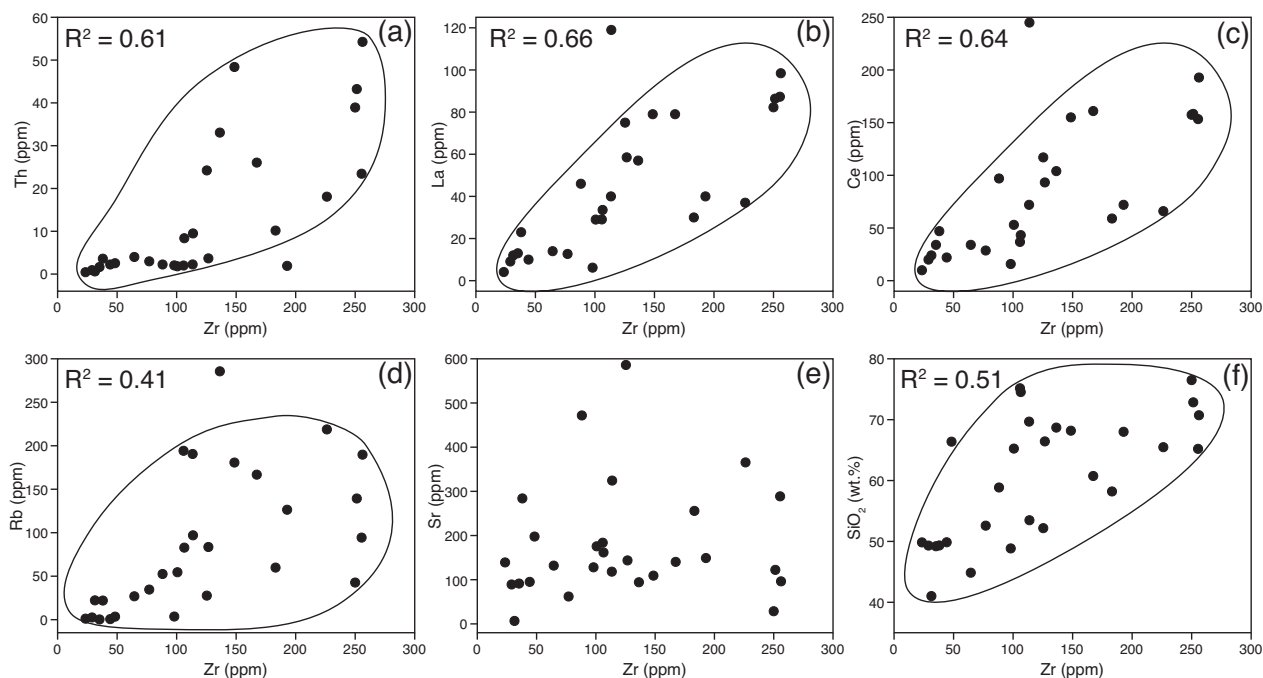


Figure 4.3: Zr vs. selected major and trace elements for the magmatic rocks of the Ongole domain.

Most workers (e.g. Polat and Hofmann, 2003) consider the large-ion lithophile elements (LILE) as being easily mobilized during metamorphism or alteration processes whereas the high field strength elements (HFSE) and the rare earth elements (REE) are regarded relatively immobile. The HFSE (represented by Th),

the REE (represented by La and Ce) and the LILE (represented by Rb and Sr) are plotted against Zr (Fig. 3), considered as the least mobile element, to assess the degree of mobility in different groups of elements. SiO₂ is also plotted to assess the mobility of major elements. Th, La, Ce and SiO₂ show strong correlation with Zr (r^2 values of 0.61, 0.66, 0.64, 0.51 respectively) for most of the samples, whereas Rb ($r^2=0.41$) and Sr shows scattered trends. The apparent positive correlation between Zr and Th, La, Ce and SiO₂ suggests that the HFSE, REE and major element concentrations of the rocks were not much affected during granulite-facies metamorphism and mostly reflect primary magmatic signatures. This view is supported by the coherent patterns in the chondrite and primitive mantle normalized rare earth and trace element plots. The poor correlation between Zr and (Rb and Sr) indicates that LILE were definitely modified during the subsequent granulite-facies metamorphism and were therefore not used for significant interpretations.

4.5.2. Rock classification

In order to apply a coherent nomenclature based on widely used rock classification schemes, the magmatic rocks of the Ongole domain are plotted in the total alkalis against SiO₂ (TAS) classification diagram (Fig. 4a; Le Bas et al., 1986). The boundary line between alkaline and subalkaline series is from Irvine and Baragar (1971). The rocks plot in the sub-alkaline series and range from the field of basalt to rhyolite. On this diagram, 9 samples plot in the field of basalt, micro basalt and basaltic andesite. From now onwards these 9 samples will be referred to as mafic granulites. Out of the remaining 19 samples, 14 samples plot in the field of dacite, trachydacite and rhyolite, 2 each in the field of basaltic trachy-andesite and andesite and 1 in the field of trachy-andesite. Henceforth, all of these 19 samples, ranging from intermediate to acidic in composition, will be referred to as charnoenderbites.

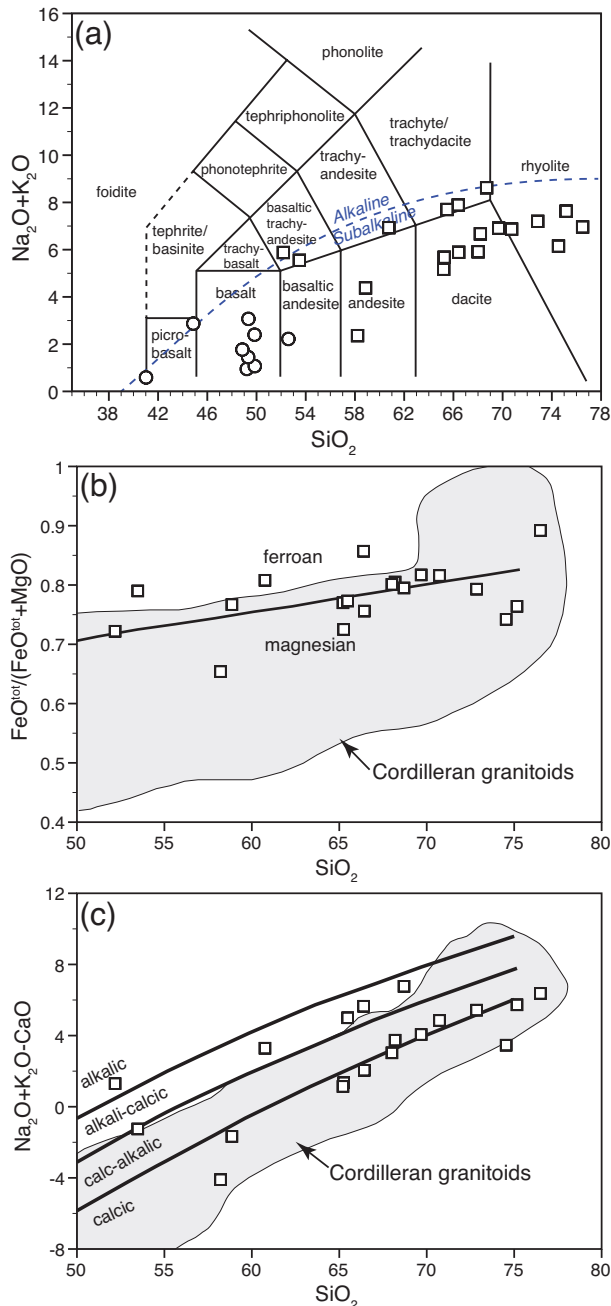


Figure 4.4: (a) Classification of magmatic rocks of the Ongole domain on the total alkali vs. SiO_2 (TAS) diagram of Irvine and Baragar (1971). All samples show subalkaline affinity. The mafic granulites are represented by circles and the charnoenderbites are represented by squares; (b) & (c) $\text{FeO}^{\text{tot}}/(\text{FeO}^{\text{tot}}+\text{MgO})$ and $\text{K}_2\text{O}+\text{Na}_2\text{O}-\text{CaO}$ (MALI: modified alkali-lime index) versus SiO_2 plots. The composition fields of Cordilleran-type granites as well as (b) the boundary between ferroan and magnesian plutons and (c) the ranges of alkalic, alkali-calcic, calc-alkalic, and calcic rock series are from Frost et al. (2001).

According to the plot of Fe^* [$\text{Fe}^* = \text{FeO}^{\text{tot}}/(\text{FeO}^{\text{tot}}+\text{MgO})$] and weight percent SiO_2 (Fig.; Frost et al., 2001), that is used to classify granitoid rocks into magnesian and ferroan types, the charnoenderbites plot around the boundary of magnesian and ferroan. In terms of the modified alkali-lime index (MALI) plot ($\text{Na}_2\text{O}+\text{K}_2\text{O}-\text{CaO}$ against weight percent SiO_2 ; Fig. 4c) by Frost et al., (2001), the charnoenderbites

are mostly calcic to calc-alkalic. Only 4 samples are alkali-calcic and 1 alkalic. In Fig. 4b and c, the compositional range of Cordilleran granitoids is shown on the above-mentioned plots, which demonstrates that the charnoenderbites have composition similar to the Cordilleran granitoids of the USA.

4.5.3. Major and trace element composition

Mafic granulites

Major and trace element composition of the mafic granulites from the Ongole domain are presented in Table 1. The samples have $\text{SiO}_2 = 44.9\text{-}52.6$ wt.%, $\text{TiO}_2 = 1.0\text{-}2.1$ wt.%, total $\text{Fe}_2\text{O}_3 = 13.1\text{-}18.4$ wt.%, $\text{MgO} = 6.2\text{-}7.6$ wt.%, $\text{Al}_2\text{O}_3 = 13.2\text{-}15.0$ wt.%, $\text{CaO} = 7.5\text{-}10.8$ wt.%, and $\text{Na}_2\text{O}+\text{K}_2\text{O} = 1.0\text{-}3.1$ wt.%. Mg#, calculated as $100\text{Mg}^{2+}/(\text{Mg}^{2+}+\text{Fe}_{\text{tot}}^{2+})$, vary from 40.8 to 48.8. One sample (TK18C1) with a picro basalt chemistry has lower SiO_2 (41.0 wt.%), Al_2O_3 (8.11 wt.%), CaO (3.4 wt.%), $\text{Na}_2\text{O}+\text{K}_2\text{O}$ (0.59 wt.%), Mg# (23.9) and higher total Fe_2O_3 (36.43 wt.%) than the above mentioned range. Major and trace element variation diagrams of selected elements (Fig. 5) show that SiO_2 is negatively correlated with MgO, total Fe_2O_3 , CaO, Ni and Cr and positively correlated with K_2O .

The mafic granulites have low Sr contents (6-284 ppm, average 114 ppm) and high Y contents (26-39 ppm, average 31 ppm), resulting in very low Sr/Y ratios (0.19-10.92, average 3.85). Nb contents vary from 1.31 to 10.0 ppm (average 6.21 ppm). The high Y contents result in a low Nb/Y ratio (0.04-0.23), which attest to their sub-alkaline affinity. This fact is also prominent in the TAS diagram (Fig. 4a). The mafic granulites show moderate Th/Yb (0.12-1.38) and Ta/Yb (0.12-0.30) ratios.

On the chondrite normalized (normalizing values after McDonough and Sun, 1995) rare earth element (REE) diagram (Fig. 6a), the mafic granulites display coherent REE patterns characterized by relative enrichment in LREE and nearly flat HREE pattern as indicated by $\text{La}/\text{Yb}_{\text{CN}}$ of 0.75-6.01 (average 2.46) and $\text{Tb}/\text{Yb}_{\text{CN}}$

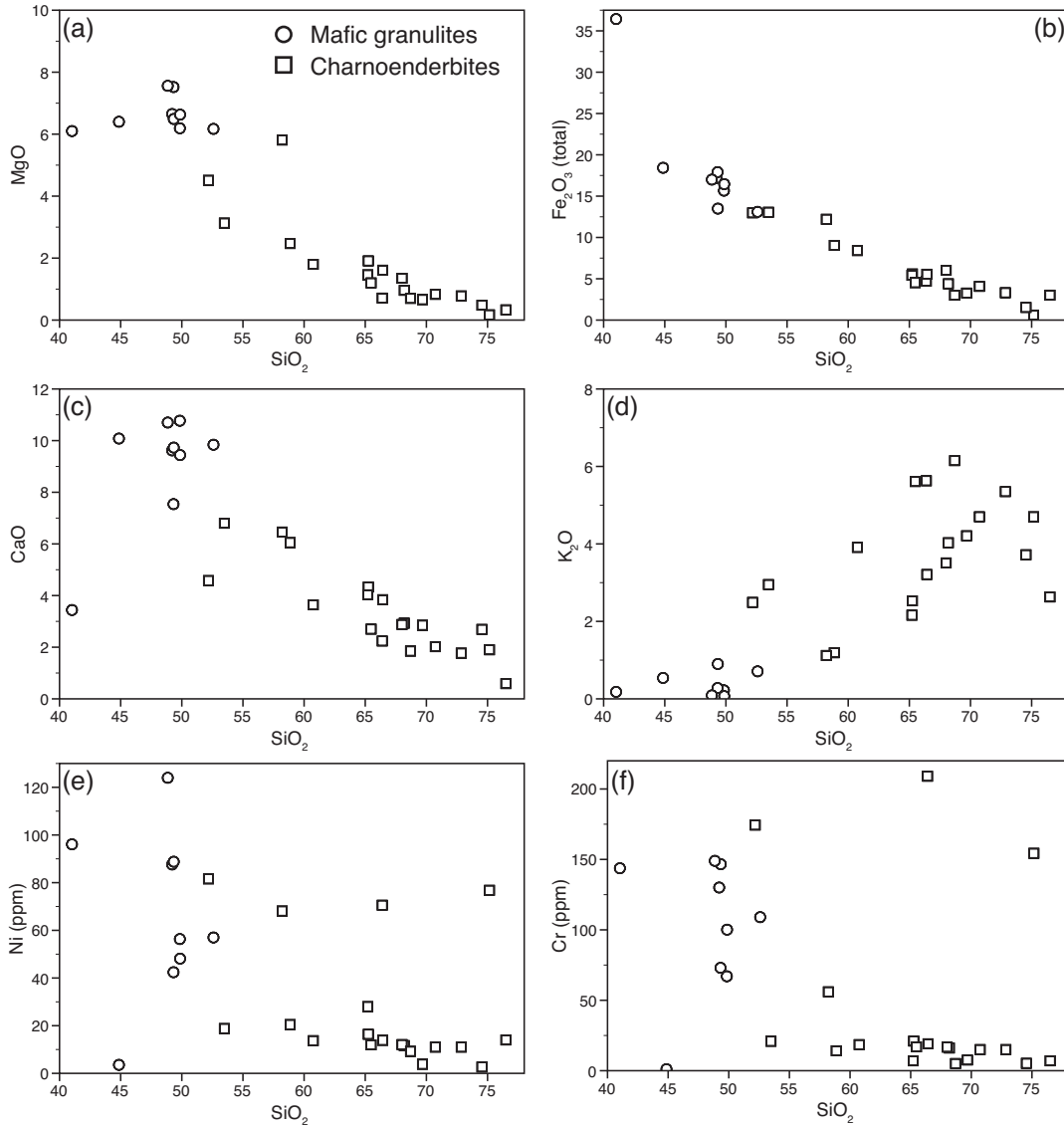


Figure 4.5: SiO_2 vs. selected major and trace element variation diagram for the rocks of the Ongole domain.

of 1.01-1.66 (average 1.25). CN refers to the respective chondrite normalized values. The samples show very minor negative or no Eu anomalies ($\text{Eu}/\text{Eu}^* = 0.664$ -1.044, mean 0.88). These patterns are very similar to the patterns shown by the average values of continental and island arc basalts (Fig. 6a) as compiled by Kelemen et al. (2003).

On the primitive mantle normalized (normalizing values after Sun and McDonough, 1989) extended trace element diagram (Fig. 6b), the mafic granulites

display negative anomalies of Nb ($Nb/La_{PM}=0.31-0.94$, mean 0.54), and negative to slightly positive anomalies of Zr ($Zr/Nd_{PM}=0.18-1.03$, mean 0.43) relative to elements of similar degree of incompatibility. PM represents respective primitive normalized values. Except for two, the samples show a slightly negative Ta anomaly (Fig. 6b). Ti shows minor negative anomalies. Like the chondrite normalized REE patterns, the primitive mantle normalized trace element patterns of the mafic granulites from the Ongole domain are also similar (Fig. 6b) to that of the average values of continental and island arc basalts (Kelemen et al., 2003).

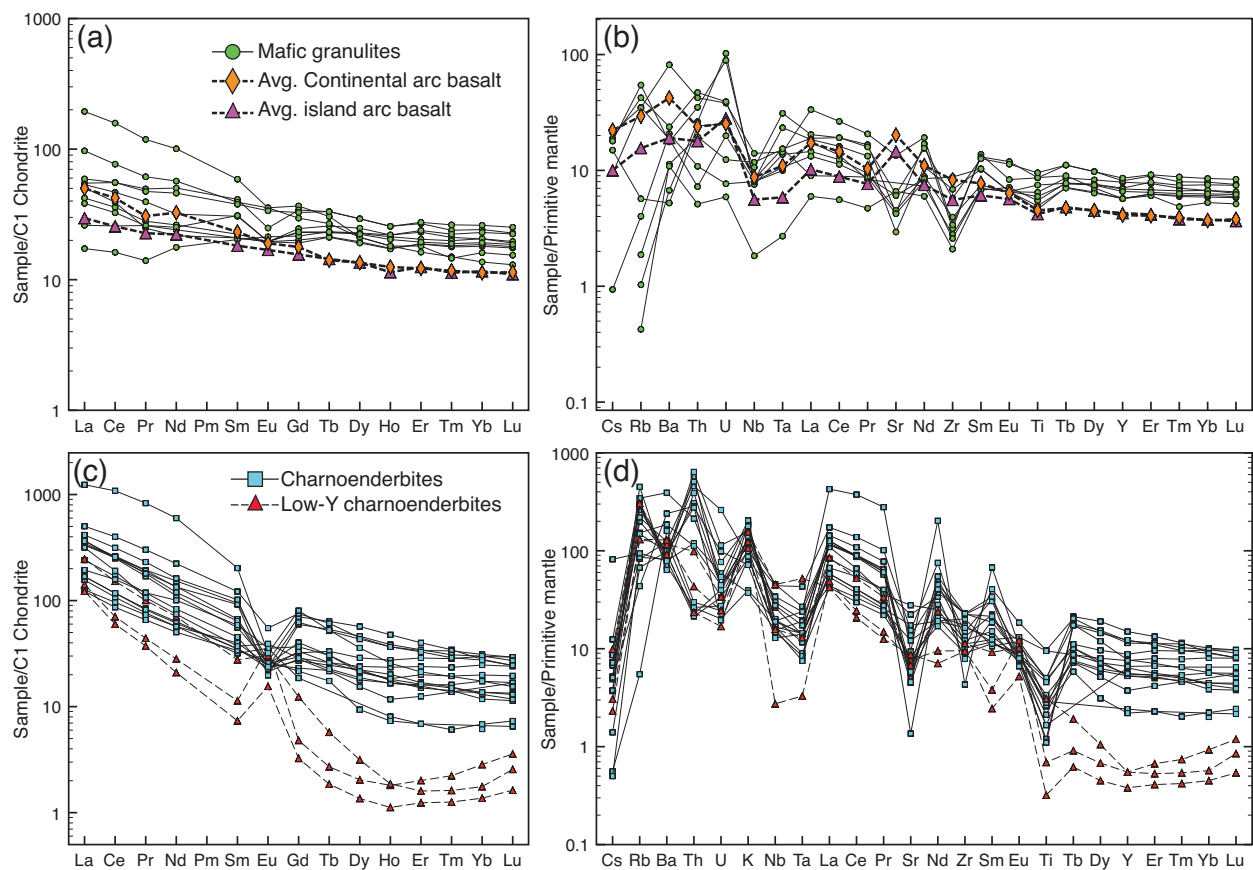


Figure 4.6: (a) REE plot of mafic granulites normalized to C1 chondrite (McDonough and Sun, 1995); (b) trace element plot of mafic granulites normalized to primitive mantle (Sun and McDonough, 1989). In (a) & (b) average REE and trace element values of continental and island arc basalts (Keleman et al., 2003) are plotted to compare with the analyzed data. (c) REE plot of charnoenderbites normalized to C1 chondrite (McDonough and Sun, 1995); (d) trace element plot of charnoenderbites normalized to primitive mantle (Sun and McDonough, 1989).

Charnoenderbites

Major and trace element composition of the charnoenderbites from the Ongole domain are presented in Table 1. The samples have $\text{SiO}_2 = 52.2\text{-}75.2$ wt.% (average 66.1 wt.%), $\text{TiO}_2 = 0.1\text{-}2.1$ wt.%, total $\text{Fe}_2\text{O}_3 = 0.61\text{-}13.1$ wt.%, $\text{MgO} = 0.2\text{-}5.8$ wt.%, $\text{Al}_2\text{O}_3 = 13.0\text{-}16.7$ wt.%, $\text{CaO} = 1.8\text{-}6.0$ wt.%, and $\text{Na}_2\text{O}+\text{K}_2\text{O} = 2.4\text{-}7.9$ wt.%. $\text{Mg\#} = 29.8\text{-}40.8$. Major and trace element variation diagrams show that SiO_2 is negatively correlated with MgO , total Fe_2O_3 , CaO , Ni and Cr and positively correlated with K_2O (Fig. 5).

Similar to the mafic granulites, the charnoenderbites have variable but low Sr contents (28-586 ppm, average 211 ppm) and high Y contents (10-68 ppm, average 33ppm) resulting in low Sr/Y ratios (2.1-33.0, average 9.2). There are 3 samples (TK21, TK36-2 and TK58-2) that have low Sr contents (143-183 ppm) and very low Y contents (1.8-2.5 ppm) resulting in high Sr/Y ratios (57-105), which is very different from the rest of the samples. Henceforth, these 3 samples will be referred to as low Y charnoenderbites. Nb contents (11-32 ppm) and the high Y contents of the remaining samples result in low Nb/Y ratio (0.2-1.2, average 0.6) conforming the sub-alkaline nature of these rocks, which is also evident from the TAS diagram (Fig. 4a). The charnoenderbites show variable Th/Yb (1.1-25.5) and high Ta/Yb (0.1-0.6) ratios while the low Y charnoenderbites have similar Th/Yb ratios (9.1-18.3) but higher Ta/Yb ratios (0.3-5.1) than the other charnoenderbites.

On the chondrite normalized rare earth element diagram (McDonough and Sun, 1995; Fig. 6c), the charnoenderbites display highly fractionated REE patterns characterized by the relative enrichment in the LREE compared to the HREE as indicated by the high ratios of $\text{La}/\text{Yb}_{\text{CN}} = 4.2\text{-}71.1$ (average 19.1). The HREE patterns are rather flat as indicated by the low ratios of $\text{Tb}/\text{Yb}_{\text{CN}} = 1.1\text{-}3.0$ (average 1.6). They are characterized by negative to no Eu anomalies ($\text{Eu}/\text{Eu}^* = 0.25\text{-}0.99$) with the exception of two samples with slightly positive Eu anomalies (1.2 and 1.5).

Table 4.1: Major (wt.%) and trace (ppm) element compositions for the meta-igneous rocks.

Sample	Mafic granulites									Charnoenderbites				
	TK18-C1	TK26-1	TK33-1	TK33-2	TK36-1	TK58-1	TK82-5	KR1-4	KR3-2	TK27-3	TK39-1	TK39-2	TK39-3	TK39-4
SiO ₂	41.02	49.21	49.34	49.84	49.86	44.86	49.32	52.59	48.85	60.75	65.48	58.86	66.39	68.19
Al ₂ O ₃	8.11	13.98	14.70	13.15	14.99	13.84	13.68	14.48	13.49	15.76	15.13	16.37	14.50	14.52
Fe ₂ O ₃ (t)	36.43	17.19	13.49	15.66	16.45	18.43	17.91	13.10	17.00	8.41	4.53	9.04	4.71	4.39
MgO	6.10	6.65	6.49	6.19	6.63	6.40	7.52	6.17	7.56	1.80	1.20	2.47	0.71	0.96
CaO	3.44	9.62	9.73	10.77	9.44	10.08	7.54	9.84	10.70	3.64	2.70	6.05	2.24	2.93
Na ₂ O	0.41	0.88	2.17	2.18	1.00	2.33	1.17	1.51	1.68	3.02	2.09	3.19	2.26	2.64
K ₂ O	0.18	0.07	0.90	0.22	0.07	0.54	0.28	0.71	0.09	3.91	5.61	1.19	5.63	4.03
TiO ₂	1.41	1.87	1.88	1.19	1.00	2.07	1.07	1.29	1.62	1.07	0.63	1.05	1.09	0.56
P ₂ O ₅	0.15	0.22	0.57	0.11	0.07	0.24	0.12	0.13	0.14	0.42	0.18	0.41	0.30	0.18
MnO	1.81	0.22	0.18	0.23	0.30	0.25	0.38	0.20	0.19	0.10	0.05	0.10	0.07	0.06
LOI	0.11	0.12	0.10	0.16	0.21	0.31	0.24	n.d	n.d	0.12	0.50	0.40	0.16	0.45
Total	99.17	100.03	99.55	99.70	100.02	99.35	99.23	100.02	101.32	99.00	98.10	99.13	98.06	98.91
FeO (t)	34.62	15.49	12.15	14.11	14.82	16.60	16.14	11.80	15.32	7.58	4.08	8.14	4.24	3.95
Mg#	24	43	49	44	44	41	45	48	47	30	34	35	23	30
Na ₂ O +K ₂ O	0.59	0.95	3.07	2.40	1.07	2.87	1.45	2.22	1.77	6.93	7.70	4.38	7.89	6.67
FeO/(FeO+MgO)	0.85	0.70	0.65	0.70	0.69	0.72	0.68	0.66	0.67	0.81	0.77	0.77	0.86	0.80
Na ₂ O +K ₂ O-CaO	-2.85	-8.67	-6.66	-8.37	-8.37	-7.21	-6.09	-7.62	-8.93	3.29	5.00	-1.67	5.65	3.74
Cs	0.678	0.000	0.300	0.000	0.000	0.604	0.030	0.573	0.478	0.162	0.398	0.216	0.018	0.275
Rb	22.2	0.3	22.0	1.2	0.7	26.9	2.6	34.6	3.6	166.8	218.8	52.5	33.5	180.7
Ba	130	79	570	76	47	166	145	123	37	639	2736	856	1117	556
Sr	7	91	284	139	95	132	89	62	128	140	365	472	198	109
Pb	0.9	1.2	7.0	2.2	3.6	44.9	4.9	7.2	1.7	17.5	23.9	10.4	3.9	18.8
Th	0.6	1.7	3.6	0.4	2.2	4.0	0.9	3.0	2.0	26.0	18.1	2.2	2.5	48.4
U	0.42	0.26	0.80	0.12	2.15	0.82	0.16	1.87	0.53	0.93	0.94	0.42	0.51	0.88
Zr	31.4	35.2	38.0	23.4	44.2	64.5	28.9	77.0	98.0	167.3	226.2	88.2	48.3	148.6
Ta	0.41	0.63	0.59	b.d.1	0.56	1.28	0.44	0.96	0.63	1.10	0.59	0.58	0.98	0.80
Y	36.0	37.0	26.0	32.0	26.0	39.0	26.0	31.4	29.9	68.0	11.0	25.0	35.0	24.0
Nb	5.70	8.37	10.00	1.31	5.40	7.57	5.70	5.87	6.03	32.48	11.86	13.96	13.68	21.28
Sc	17.0	52.2	32.6	49.4	45.7	7.5	46.7	38.0	52.0	20.0	9.0	19.4	50.6	9.2
Cr	143.7	130.0	146.6	67.0	100.1	1.1	73.0	109.0	149.0	18.5	16.9	14.2	209.1	16.1
Ni	96.09	87.63	88.79	56.34	48.12	3.57	42.43	57.00	124.00	13.72	11.96	20.46	70.54	11.65
Co	35.34	53.56	46.51	49.97	55.24	8.05	47.20	26.00	67.00	15.62	9.70	19.07	58.17	8.83
V	101.8	378.8	230.2	316.5	279.0	35.5	313.6	311.0	397.0	97.9	102.0	153.9	323.1	49.3
Ga	9.9	20.4	16.1	15.1	16.3	17.8	15.5	13.0	16.0	21.0	16.4	20.5	19.0	17.0
Zn	210.42	78.55	87.48	92.64	151.49	59.98	119.90	123.00	142.00	55.78	44.98	88.48	139.37	39.69
Cu	1426	74	29	49	60	13	28	n.d	309	28	24	73	70	19
La	12.0	13.0	23.0	4.1	10.0	14.0	9.1	12.7	6.2	79.0	37.0	46.0	293.0	79.0
Ce	24.0	34.0	47.0	9.9	22.0	34.0	20.0	28.6	15.8	161.0	66.0	97.0	665.0	155.0
Pr	2.3	4.6	5.7	1.3	2.6	4.4	2.4	3.7	2.4	18.0	7.1	11.0	77.0	17.0
Nd	9.9	23.0	26.0	8.1	12.0	21.0	11.0	14.5	11.5	70.0	26.0	46.0	274.0	62.0
Sm	3.10	6.10	5.80	3.00	3.30	5.60	3.10	4.53	4.59	14.00	4.70	8.70	30.00	9.90
Eu	1.10	1.40	2.00	1.20	1.10	1.90	1.10	1.10	1.10	1.50	2.00	2.00	1.80	1.40
Gd	4.90	6.80	5.90	4.30	4.00	6.50	3.80	4.57	4.61	14.00	3.70	7.30	16.00	8.00
Tb	0.93	1.20	0.97	0.84	0.77	1.20	0.76	0.83	0.84	2.30	b.d.1	1.10	1.90	1.10
Dy	6.10	7.20	5.20	5.60	4.80	7.20	4.70	5.56	5.49	14.00	2.30	5.20	8.80	5.50
Ho	1.20	1.40	0.99	1.20	0.95	1.40	0.94	1.16	1.11	2.60	0.44	0.99	1.40	0.96
Er	3.70	4.30	2.90	3.80	3.00	4.40	3.00	3.26	3.10	6.40	1.10	2.60	3.40	2.40
Tm	0.52	0.59	0.36	0.55	0.44	0.65	0.45	0.49	0.47	0.85	b.d.1	0.37		0.35
Yb	3.30	3.90	2.60	3.70	2.90	4.20	3.00	3.31	3.09	4.50	0.99	2.20	2.80	1.90
Lu	0.47	0.56	0.38	0.55	0.43	0.62	0.44	0.48	0.46	0.60	0.16	0.32	0.38	0.28
Eu/Eu*	0.86	0.66	1.04	1.02	0.92	0.96	0.98	0.74	0.73	0.33	1.46	0.77	0.25	0.48
K	1494	581	7471	1826	581	4483	2324	5894	747	32458	46570	9879	46736	33454
Ti	8402	11143	11203	7091	5959	12335	6376	7687	9654	6376	3754	6257	6495	3337
P	655	960	2488	480	306	1048	524	567	611	1833	786	1789	1309	786
Sr/Y	0.19	2.47	10.92	4.35	3.66	3.38	3.43	1.97	4.28	2.06	33.22	18.87	5.65	4.55
Th/Yb	0.19	0.42	1.38	0.12	0.77	0.95	0.31	0.90	0.66	5.79	18.27	1.02	0.91	25.47
Ta/Yb	0.12	0.16	0.23	b.d.1	0.19	0.30	0.15	0.29	0.20	0.24	0.59	0.26	0.35	0.42
Nb/Y	0.16	0.23	0.38	0.04	0.21	0.19	0.22	0.19	0.20	0.48	1.08	0.56	0.39	0.89
Y+Nb	n.d	n.d	n.d	n.d	n.d	n.d	n.d	n.d	n.d	100.48	22.86	38.96	48.68	45.28
Nb/La _{PM}	0.46	0.62	0.42	0.31	0.52	0.52	0.60	0.45	0.94	0.40	0.31	0.29	0.04	0.26
Zr/Nd _{PM}	0.38	0.19	0.18	0.35	0.45	0.37	0.32	0.64	1.03	0.29	1.05	0.23	0.02	0.29
La/Yb _{CN}	2.47	2.26	6.01	0.75	2.34	2.26	2.06	2.60	1.36	11.93	25.39	14.20	71.09	28.25
Tb/Yb _{CN}	1.26	1.37	1.66	1.01	1.18	1.27	1.13	1.11	1.21	2.28	0.00	2.23	3.03	2.58
DF1	-1.03	-1.71	-1.95	-4.09	-3.21	-3.56	-1.69	-3.43	-2.87	n.d	n.d	n.d	n.d	n.d
DF2	1.64	0.21	-1.40	0.86	-0.41	-0.91	1.02	-0.93	-0.28	n.d	n.d	n.d	n.d	n.d

Note: LOI: Loss on ignition. Mg# = 100Mg²⁺/(Mg²⁺+Fetot²⁺). Eu/Eu* = Eu_{CN}/(Gd_{CN}+Sm_{CN})/2. Nb/La_{PM} = (Nb/0.713)/(La/0.687). Zr/Nd_{PM} = (Zr/11.20)/(Nd/1.354). La/Yb_{CN} = (La/0.687)/(Yb/0.161). Tb/Yb_{CN} = (Tb/0.0361)/(Yb/0.161); n.d = not determined; b.d.1 = below detection limit.

Table 4.1: Continued

Sample	Charnoenderbites													
	TK54-1	TK54-2	TK74-1	TK 73-8	TK38-1	TK28-1	TK33-3	KR1-3	KR3-1	KR24-1	KR11-1	TK 36-2	TK 21	TK 58-2
SiO ₂	68.01	69.68	65.25	58.21	53.48	68.70	52.18	65.21	76.50	72.85	70.73	74.54	66.43	75.16
Al ₂ O ₃	13.17	15.15	16.15	15.39	13.59	14.11	16.65	16.74	13.23	13.54	14.70	13.03	14.59	13.62
Fe ₂ O ₃ (t)	6.02	3.27	5.58	12.20	13.05	3.01	12.98	5.42	3.02	3.31	4.08	1.53	5.55	0.61
MgO	1.35	0.66	1.91	5.81	3.13	0.70	4.51	1.46	0.33	0.78	0.83	0.48	1.61	0.17
CaO	2.88	2.85	4.33	6.46	6.80	1.85	4.58	4.03	0.59	1.77	2.02	2.69	3.84	1.90
Na ₂ O	2.40	2.70	3.15	1.24	2.60	2.47	3.39	3.01	4.33	1.85	2.17	2.43	2.68	2.93
K ₂ O	3.51	4.21	2.53	1.12	2.95	6.15	2.49	2.16	2.63	5.35	4.70	3.72	3.21	4.70
TiO ₂	0.73	0.36	0.57	0.99	2.10	0.36	2.07	0.61	0.26	0.46	0.24	0.15	0.67	0.07
P ₂ O ₅	0.20	0.17	0.19	0.12	0.74	0.15	0.04	0.15	0.14	0.08	0.19	0.02	0.15	0.02
MnO	0.07	0.04	0.05	0.24	0.18	0.04	0.15	0.06	0.01	0.04	0.04	0.03	0.05	0.01
LOI	0.13	0.19	0.09	0.02	0.52	0.34	0.27	n.d	n.d	n.d	n.d	0.25	0.14	0.19
Total	98.47	99.28	99.80	101.80	99.14	97.88	99.31	98.85	101.04	100.03	99.70	98.87	98.92	99.38
FeO (t)	5.42	2.95	5.03	10.99	11.76	2.71	11.69	4.88	2.72	2.98	3.68	1.38	5.00	0.55
Mg#	31	29	40	49	32	32	41	35	18	32	29	38	36	36
Na ₂ O +K ₂ O	5.91	6.91	5.68	2.36	5.55	8.62	5.88	5.17	6.96	7.20	6.87	6.15	5.89	7.63
FeO/(FeO+MgO)	0.80	0.82	0.72	0.65	0.79	0.79	0.72	0.77	0.89	0.79	0.82	0.74	0.76	0.76
Na ₂ O +K ₂ O-CaO	3.03	4.06	1.35	-4.10	-1.25	6.77	1.30	1.14	6.37	5.43	4.85	3.46	2.05	5.73
Cs	0.118	0.167	0.016	2.620	0.233	0.120	0.156	0.232	0.045	0.163	0.230	0.098	0.074	0.316
Rb	126.4	190.5	54.6	59.9	97.0	285.6	27.7	94.4	42.7	139.4	189.8	82.8	83.6	194.2
Ba	661	487	571	550	1295	445	1676	681	690	869	626	817	899	645
Sr	149	118	176	256	324	94	586	289	29	122	96	162	144	184
Pb	15.9	17.3	18.2	14.0	17.1	21.9	18.2	15.9	8.4	34.6	29.2	24.3	15.8	24.2
Th	1.9	2.2	1.8	10.2	9.5	33.1	24.2	23.4	38.9	43.2	54.3	8.4	3.7	2.0
U	0.84	0.57	0.70	1.24	0.94	1.13	0.41	2.07	5.48	1.61	2.39	0.71	0.52	0.36
Zr	192.8	113.4	100.7	183.1	113.7	136.3	125.3	255.4	250.0	251.3	256.2	106.4	126.7	105.8
Ta	0.57	0.48	0.37	0.78	1.77	0.35	0.98	0.58	0.31	0.59	0.71	0.14	0.53	1.13
Y	24.0	29.0	10.0	40.0	52.0	17.0	30.0	25.5	54.7	34.5	55.7	2.5	2.5	1.7
Nb	18.76	14.34	11.87	11.06	31.37	10.58	24.29	9.18	11.22	13.46	19.70	1.95	11.27	32.26
Sc	14.4	8.7	11.2	40.9	32.1	7.7	23.3	11.0	13.0	17.0	9.0	5.5	16.1	30.6
Cr	16.7	7.6	21.0	56.0	20.9	5.1	174.4	7.0	7.0	15.0	15.0	5.2	19.1	154.3
Ni	12.07	3.83	16.39	68.10	18.80	9.24	81.58	28.00	14.00	11.00	11.00	2.67	13.86	76.81
Co	11.92	5.70	12.08	41.44	29.74	5.23	31.64	9.00	11.00	3.41	21.00	2.96	12.11	26.60
V	68.7	29.9	115.5	234.6	296.3	31.1	373.5	54.0	5.0	33.0	29.0	5.2	75.7	189.3
Ga	17.2	16.9	18.4	15.8	19.5	15.3	21.2	21.0	16.0	16.0	20.0	10.6	17.6	22.6
Zn	59.73	23.54	85.93	98.57	132.37	20.86	76.10	64.00	19.00	38.00	39.00	11.52	68.91	156.92
Cu	25	6	10	57	30	8	66	31	n.d	n.d	n.d	5	24	36
La	40.0	40.0	29.0	30.0	119.0	57.0	75.0	87.3	82.3	86.4	98.5	33.6	58.5	29.1
Ce	72.0	72.0	53.0	59.0	245.0	104.0	117.0	153.4	157.5	158.3	192.8	43.2	93.2	36.8
Pr	7.8	7.6	6.1	6.8	28.0	11.0	9.9	15.7	17.8	16.7	21.4	4.1	9.3	3.5
Nd	29.0	28.0	23.0	26.0	102.0	38.0	34.0	50.7	61.2	54.6	74.0	12.9	32.3	9.6
Sm	5.20	5.20	5.00	5.90	18.00	6.70	5.50	8.24	13.61	9.51	15.09	1.68	4.09	1.09
Eu	1.40	1.30	1.50	1.40	3.10	1.20	2.20	1.44	1.11	1.28	1.34	2.06	1.71	0.88
Gd	4.60	5.40	4.30	6.40	15.00	5.60	5.70	5.83	11.87	6.62	12.41	0.96	2.46	0.65
Tb	0.79	b.d.l	0.63	1.20	2.20	0.78	0.94	0.82	1.93	0.94	1.87	0.10	0.21	0.07
Dy	4.40	5.80	2.30	7.10	11.00	3.80	5.30	4.61	11.34	5.89	10.65	0.50	0.77	0.33
Ho	0.91	1.10	0.40	1.50	2.00	0.64	1.00	0.90	2.10	1.28	2.00	0.10	0.10	0.06
Er	2.50	2.70	1.10	4.60	5.40	2.00	3.20	2.57	5.50	3.82	5.26	0.32	0.26	0.20
Tm	0.34	0.38	0.15	0.70	0.83	0.00	0.48	0.40	0.76	0.58	0.71	0.06	0.04	0.03
Yb	2.20	2.10	1.10	4.80	5.00	3.10	3.20	2.80	4.83	3.97	4.42	0.46	0.28	0.22
Lu	0.33	0.29	0.18	0.72	0.72	0.41	0.48	0.41	0.67	0.59	0.60	0.09	0.06	0.04
Eu/Eu*	0.87	0.75	0.99	0.70	0.58	0.60	1.20	0.64	0.27	0.49	0.30	4.96	1.65	3.19
K	29138	34948	21002	9297	24489	51053	20670	17931	21832	44412	39016	30881	26647	39016
Ti	4350	2145	3397	5899	12514	2145	12335	3635	1549	2741	1430	894	3993	417
P	873	742	829	524	3230	655	175	655	611	349	829	87	655	87
Sr/Y	6.21	4.08	17.56	6.39	6.24	5.54	19.54	11.34	0.52	3.55	1.73	64.48	56.92	105.05
Th/Yb	0.87	1.07	1.65	2.12	1.90	10.67	7.57	8.39	8.06	10.88	12.28	18.29	12.98	9.05
Ta/Yb	0.26	0.23	0.34	0.16	0.35	0.11	0.31	0.21	0.06	0.15	0.16	0.29	1.89	5.13
Nb/Y	0.78	0.49	1.19	0.28	0.60	0.62	0.81	0.36	0.21	0.39	0.35	0.78	4.46	18.44
Y+Nb	42.76	43.34	21.87	51.06	83.37	27.58	54.29	34.64	65.89	47.91	75.43	4.46	13.79	34.01
Nb/La _{PM}	0.45	0.35	0.39	0.36	0.25	0.18	0.31	0.10	0.13	0.15	0.19	0.06	0.19	1.07
Zr/Nd _{PM}	0.80	0.49	0.53	0.85	0.13	0.43	0.45	0.61	0.49	0.56	0.42	1.00	0.47	1.33
La/Yb _{CN}	12.35	12.94	17.91	4.25	16.17	12.49	15.92	21.21	11.58	14.76	15.13	49.80	140.47	89.33
Tb/Yb _{CN}	1.60	0.00	2.55	1.11	1.96	1.12	1.31	1.30	1.79	1.05	1.88	0.95	3.26	1.35

Note: LOI: Loss on ignition. Mg# = 100Mg²⁺/(Mg²⁺+Fetot²⁺). Eu/Eu* = Eu_{CN}/(Gd_{CN}+Sm_{CN})/2. Nb/La_{PM} = (Nb/0.713)/(La/0.687). Zr/Nd_{PM} = (Zr/11.20)/(Nd/1.354). La/Yb_{CN} = (La/0.687)/(Yb/0.161). Tb/Yb_{CN} = (Tb/0.0361)/(Yb/0.161); n.d = not determined; b.d.l = below detection limit.

On the other hand, the low Y charnoenderbites (Fig. 6c) are characterized by highly enriched LREE compared to HREE ($\text{La/Yb}_{\text{CN}} = 49.8\text{-}140.5$), distinct concave-up trends in the HREE and positive Eu anomalies ($\text{Eu/Eu}^* = 1.65\text{-}4.96$). Overall, the MREE and HREE in the low Y charnoenderbites are highly depleted compared to the other charnoenderbites (Fig. 6c).

On the extended trace element plot normalized to primitive mantle (Sun and McDonough, 1989; Fig. 6d), the charnoenderbites possess relative enrichment of the fluid mobile large ion lithophile elements (LILE, except Cs) and are characterized by large negative Nb-Ta anomalies ($\text{Nb/La}_{\text{PM}} = 0.04\text{-}0.45$, mean 0.26) and negative Zr anomalies ($\text{Zr/Nd}_{\text{pm}} = 0.02\text{-}1.05$, mean 0.48). They also possess negative Ti and Sr anomalies. The low Y charnoenderbites show negative to slightly positive Nb-Ta anomalies ($\text{Nb/La}_{\text{pm}} = 0.06\text{-}1.07$).

4.6. U-Pb zircon geochronology

A total of six samples were selected for laser ablation inductively coupled plasma mass spectrometry (LA-ICP-MS) U-Pb spot analyses on separate zircon grains. Out of these five separates derive from charnoenderbites (TK4B2, TK21, TK28-1, TK39-3, TK39-4) of different parts of the Ongole domain. They are expected to provide the ages of emplacement of the precursor magmas of the charnoenderbites and the age of their metamorphism. In addition, zircon grains from one orthogneiss (TK66-1) of the Vinjamuru domain were analyzed and are expected to provide the emplacement age of the granitic precursor into this adjoining crustal block. The results of the U-Pb isotopic analyses are presented in Table C.1 (appendix C). Analyses only with a degree of concordance of $100 \pm 2\%$ have been considered for concordant age calculation.

4.6.1. TK4B2

The enderbite (TK4B2) from Kondapalle preserves a peak assemblage of Grt-Opx-Pl-Kfs-Qz. The zircon grains are prismatic, euhedral to subhedral and range from 150 to 300 μm in length. CL images reveal weakly luminescent well-developed oscillatory-zoned cores for most zircon grains, surrounded by broad, unzoned overgrowths having slightly higher luminescence (Fig. 7a). The oscillatory-zoned cores are sometimes partly corroded, over which broad unzoned rims have grown (Fig. 7a). A few grains exhibit a narrow, unzoned, highly luminescent intermediate part surrounding the partly corroded zoned cores (Fig. 7a). In most of the grains these intermediate zones are too narrow to be analyzed with the LA-ICP-MS. The oscillatory-zoned cores have varying U contents (461-2787), while the rims have lower U contents (262-1144 ppm).

A total of 30 spots on 11 zircon grains were analyzed. The oscillatory-zoned core domains of the zircon grains yield a Palaeoproterozoic concordia age of 1717.0 ± 13.0 Ma, defined by 9 concordant analyses (Fig. 8a). The unzoned broad overgrowths around the core domains define a late-Palaeoproterozoic concordia age of 1626.4 ± 9.1 Ma from 15 concordant analyses (Fig. 8a), which is ca. 90 Ma younger than the oscillatory-zoned core domains. A single grain (Fig. 7a) in which the highly luminescent intermediate zone is broad enough to be analyzed yielded a Pb-Pb age of 1652 ± 48 Ma, which is slightly older than the concordant age obtained from the rims. However, within error it gives the same age as that of the broad rims.

4.6.2. TK21

The charnockite (TK21) from the south of the Guntur region preserves a peak mineral assemblage of Grt-Opx-Pl-Kfs-Qz. The zircon grains are prismatic, euhedral to subhedral, mostly ranging from 200 to 350 μm in length, with a few larger grains

up to 450 μm . CL images reveal moderately luminescent well-developed oscillatory zoning for most zircon grains (Fig. 7b). Most of the zircon grains show two consecutive narrow unstructured overgrowths with some resorption of the marginal parts of the oscillatory-zoned grains (Fig. 7b). A highly luminescent inner zone around the core is normally very narrow (<20 μm) making it difficult for precise measurement with the LA-ICP-MS. The weakly luminescent outer overgrowths are normally very narrow along the length, but are wider (up to 50 μm) around the corner, where it could be analyzed comfortably (Fig. 7b). The cores and the rims have similar U contents (230-1017 ppm).

A total of 35 spots on 13 grains were analyzed. The oscillatory-zoned core domains of the zircon grains yield a Palaeoproterozoic concordia age of 1743.0 ± 10.0 Ma, defined by 13 concordant analyses (Fig. 8c). The weakly luminescent, zoned outer overgrowths define a very late-Palaeoproterozoic concordia age of 1600.5 ± 9.8 Ma from 13 concordant analyses (Fig. 8d). This age is ca. 143 Ma younger than the age obtained from the core.

4.6.3. TK28-1

The charnockite (TK28-1) from Kondapalle preserves a peak assemblage of Grt-Opx-Kfs-Pl-Qz. The zircon grains are mostly subhedral to anhedral. Some are rounded to elliptical. They are in the size range of 150 to 300 μm in length. CL images reveal very weakly luminescent, oscillatory or sector zoning in the core domains of most zircon grains (Fig. 7c). Due to the very low luminescence, the very fine oscillatory zoning in the cores is not very prominent in most of the grains. The majority of the cores exhibit resorption along their margins and are overgrown by narrow to broad unzoned luminescent rims (Fig. 7c). The dark cores have very high U contents (1111-4277 ppm) while the brighter rims have lower contents (188-969 ppm).

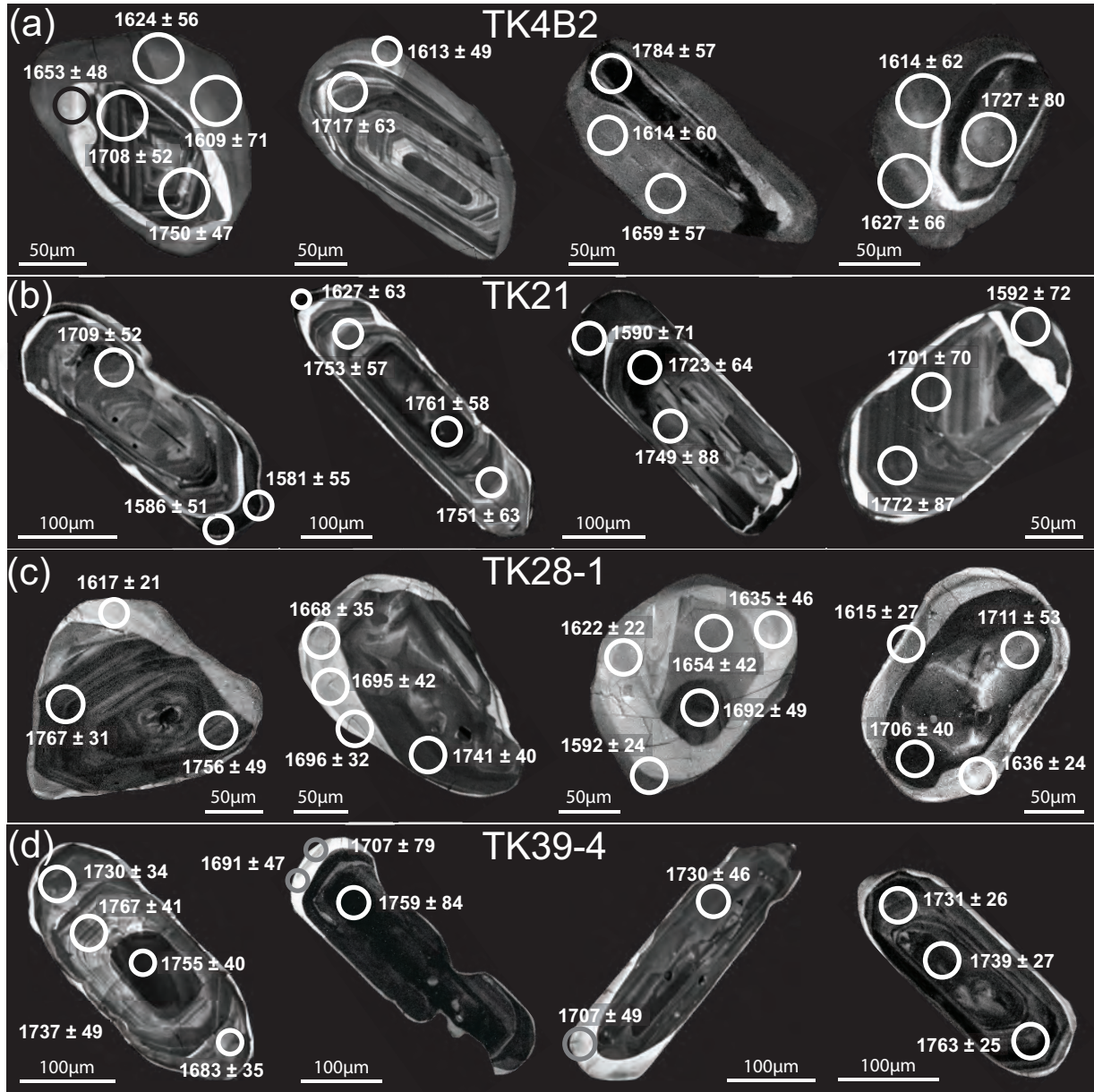


Figure 4.7: CL images of selected zircon grains from the samples of the Ongole domain (a-e) and the adjoining Vinjamuru domain (f). Circles mark the position of the laser spot (scaled to size). Ages are presented as $^{207}\text{Pb}/^{206}\text{Pb}$ ages (in Ma) with 2σ error. (a) Well-developed oscillatory-zoned cores surrounded by broad unzoned rims. Sometimes a bright zone in between the core and the rims is present; (b) elongated zircon grains with well-developed oscillatory-zoned cores surrounded by two consecutive bright and dark narrow rims; (c) anhedral zircon grains with resorbed cores (sometimes oscillatory-zoned) surrounded by broad and bright rims; (d) prismatic zircon grains having dark oscillatory-zoned cores surrounded by narrow to broad bright rims.

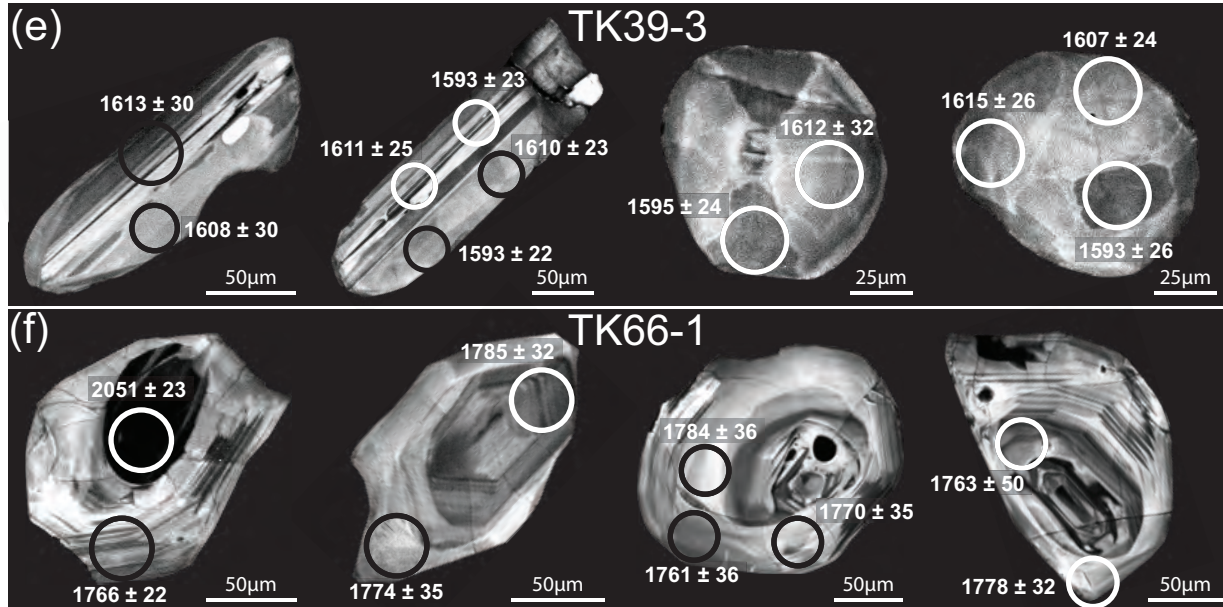


Figure 4.7 (continued): (e) Elongated and rounded zircon grains. The elongated grains show resorbed zoned cores and unzoned rims having variable thickness. The rounded grains show sector zoning. (f) anhedral zircon grains with preserved oscillatory-zoned xenocrystic cores. The cores are partly resorbed and overgrown by oscillatory-zoned mantles that truncate the zoning pattern of the cores.

A total of 44 spots on 12 zircon grains were analyzed. The weakly luminescent oscillatory-zoned core domains yield a concordia age of 1719.6 ± 9.5 Ma, defined by 11 concordant analyses (Fig. 8e). The luminescent narrow to broad rims around the core domains display two different age populations. The rims from most of the grains define a concordia age of 1687.7 ± 8.3 Ma from 13 concordant analyses (Fig. 8f). The rims of the other grains define an upper intercept age of 1620 ± 9 Ma from 16 analyses (Fig. 8g). Among them, 7 concordant analyses yield a concordia age of 1612.1 ± 14.0 Ma from 7 concordant analyses (Fig. 8h), similar to that of the upper intercept age. However, the rims with two different ages could not be separated petrographically under CL images or chemically from U contents.

4.6.4. TK39-4

The charnockite (TK39-4) from the north of the Kondapalle region preserves a peak assemblage of Grt-Opx-Kfs-Pl-Qz. The zircon grains are prismatic, euhedral to

subhedral and mostly range from 200 to 350 μm in length. CL images reveal weakly luminescent, well-developed oscillatory zoning for most zircon grains (Fig. 7d). Some grains exhibit a slightly zoned or unzoned dark mantle around the oscillatory-zoned core. Very often narrow (<10 μm), moderate to highly luminescent, unzoned rims surround the grains (Fig. 7d). In only a few grains these rims are broader, where they could be analyzed (Fig. 7d). The U content in the cores vary widely from 329 to 3437 ppm, while the rims have low U contents from 179 to 1074 ppm.

A total of 42 spots on 12 zircon grains were analyzed. The weakly luminescent oscillatory-zoned domains yield a concordia age of 1745.8 ± 8.2 Ma, defined by 14 concordant analyses (Fig. 8i). The highly luminescent rims define a concordia age of 1715.6 ± 8.4 Ma from 11 concordant analyses (Fig. 8j). Four discordant analyses from the rims yield Pb-Pb ages from 1683 ± 53 to 1644 ± 48 Ma (Table C.1 in appendix C).

4.6.5. TK39-3

The fine-grained enderbite (TK39-3) is a sheared rock with the mineral assemblage of Grt-Pl-Kfs-Qz intruding into the charnockite (TK39-4). The zircon grains show contrasting morphological features. Some zircon grains are prismatic, euhedral to subhedral ranging from 100 to 250 μm in length (Fig. 7e), while others are spherical to ellipsoidal ranging from 50 to 100 μm in diameter (Fig. 7e). CL images reveal highly luminescent growth banding and sector zoning for the elongated zircon grains and moderately luminescent sector zoning for the spherical to ellipsoidal grains. Many elongated grains show different degrees of resorption of the zoned domains and development of unzoned domains (Fig. 7e). The spherical to ellipsoidal grains do not display such features. The zoned cores and the unzoned domains have similar U contents of 119-450 ppm.

A total of 36 spots on 14 zircon grains were analyzed. The zoned domains of the elongated zircon grains yield a concordia age of 1602.6 ± 7.2 Ma, defined by 12

concordant analyses (Fig. 8k). However, the concordia diagram clearly indicates that there is a spread of ages. The resorbed and recrystallized unzoned domains of the elongated grains and the sector zoned, spherical to ellipsoidal grains define a concordia age of 1602.1 ± 4.5 Ma from 14 concordant analyses (Fig. 8l), the same age as that from the zoned cores.

4.6.6. TK66-1

The amphibolite-facies orthogneiss (TK66-1) of the Vinjamuru domain (near Chundi village) preserves a peak mineral assemblage of Qz-Pl-Kfs-Bt. The zircon grains are subhedral to anhedral, ranging from 100 to 200 μm in length. CL images reveal that most of the zircon grains have a distinct core and mantle. Some grains have weakly luminescent (very dark) spherical to ellipsoidal cores while the others preserve moderately luminescent, well-preserved oscillatory-zoned cores (Fig. 7f). The zoned cores are separated from their mantles by surfaces (sometimes geometrically irregular) that truncate the internal zoning pattern (Fig. 7f). The broad mantles are moderate to highly luminescent and show well-preserved oscillatory growth zoning. The discontinuities between the core and the mantle indicate deep resorption of the early zircon phase and locally they reveal that the new zircon growth occurred in a different crystallographic orientation than the substrate zircon. Both cores and the mantles have very low U contents (114-263 ppm).

A total of 41 spots on 17 zircon grains were analyzed for U-Pb isotopes. The spherical to ellipsoidal dark cores yielded a range of Pb-Pb spot ages from 2436 ± 19 Ma to 1869 ± 41 Ma (Table C.1 in appendix C). Several of these cores were completely metamict and no age could be obtained. The oscillatory-zoned xenocrystic cores yield a concordia age of 1777.9 ± 6.1 Ma, defined by 12 concordant analyses (Fig. 8m). The more luminescent well-preserved oscillatory-zoned mantles also yield the same concordia age of 1777.6 ± 6.4 Ma, defined by 9 concordant analyses (Fig. 8m).

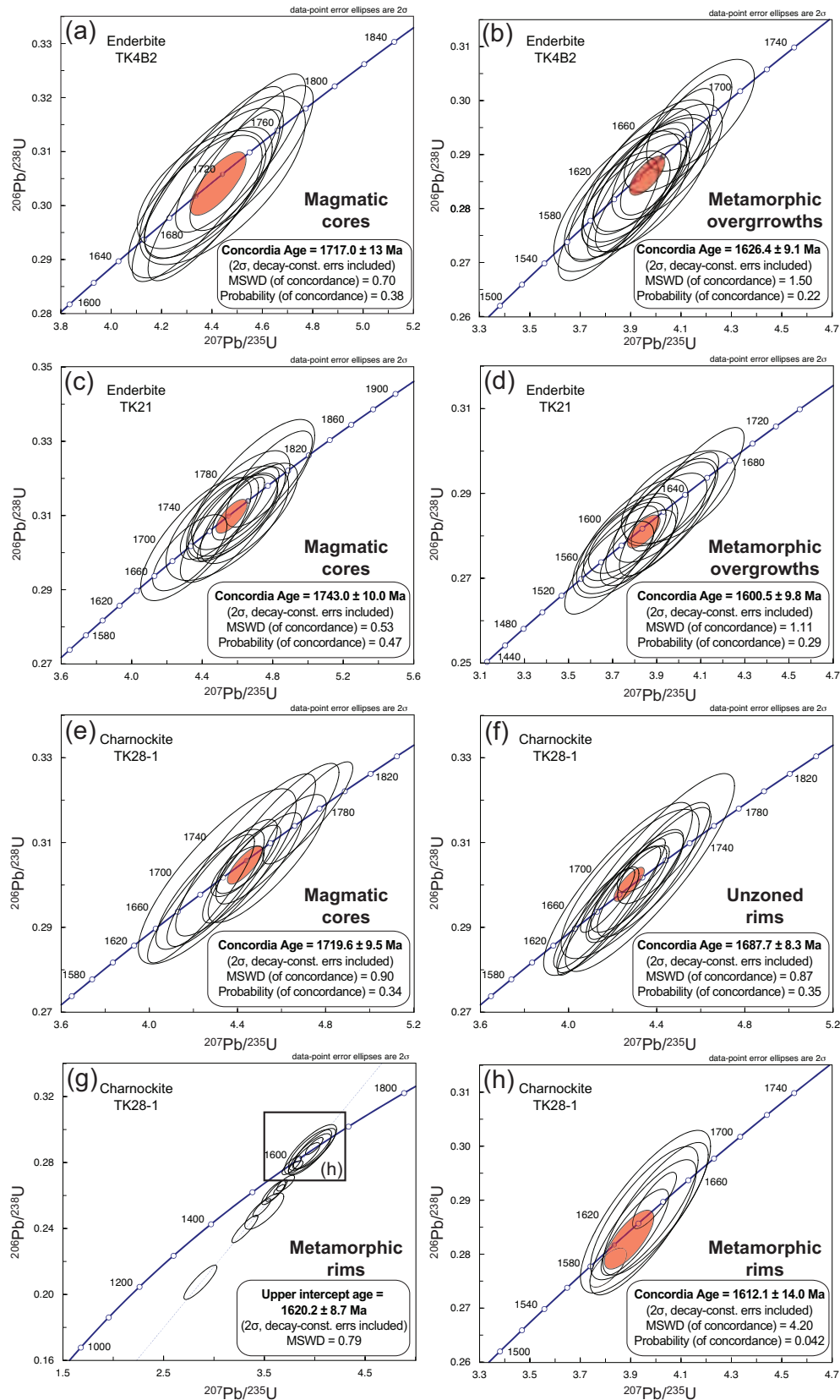


Figure 4.8:

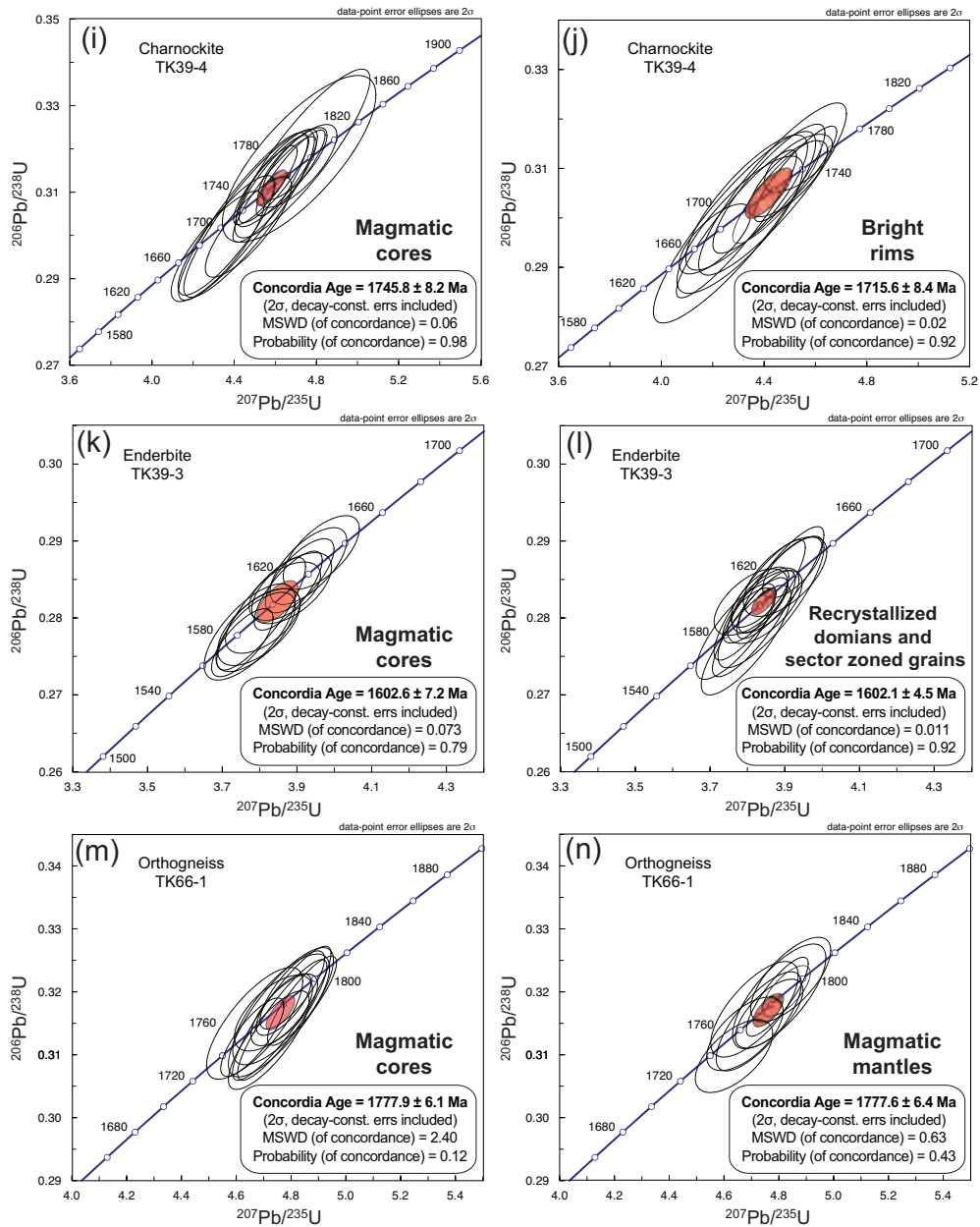


Figure 4.8: U-Pb concordia diagrams for the charnoenderbites of the Ongole domain and an orthogneiss from the adjoining Vinjamuru domain. Concordia ages are given with 2σ standard uncertainties.

4.7. Discussion

4.7.1. Timing of formation and metamorphism of the Ongole domain

The oscillatory zoning in the core domains of the zircon grains of the enderbite gneiss (TK4B2) suggests that they represent parts of the magmatically grown zircon crystals. The zircon grains were partly resorbed before being overgrown by broad unzoned rims. The Palaeoproterozoic age of ca. 1720 Ma obtained from the core domains is interpreted to be the age of intrusion of the granodioritic precursor of the enderbite (Fig. 7a, 8a; Table 2). The late-Palaeoproterozoic age of ca. 1630 Ma obtained from the broad, unzoned rims is interpreted to be the age of granulite-facies peak metamorphism (Fig. 7a, 8b; Table 2).

The large, prismatic, well-developed, oscillatory-zoned zircon grains from the enderbite gneiss (TK21) indicate that they are magmatic zircon grains. Therefore, the Palaeoproterozoic age of ca. 1740 Ma obtained from the oscillatory-zoned domains of the zircon grains (Fig. 7b, 8c; Table 2) reflects the age of the magmatic intrusion. The late-Palaeoproterozoic age of ca. 1600 Ma obtained from the unzoned, weakly luminescent outer rims indicate the age of peak metamorphism (Fig. 7b, 8d; Table 2). The highly luminescent narrow rims between the zoned cores and the unzoned rims in both the samples (TK4B2 and TK21; Fig. 7a,b) could not be measured properly with the LA-ICPMS. Due to the lack of data the exact timing of the formation and hence the geological significance could not be resolved. However, petrographically it seems that these bright rims formed by resorption and subsequent recrystallization of the oscillatory-zoned zircon cores prior to the growth of the broad rims.

The Palaeoproterozoic age of ca. 1720 Ma obtained from the large, oscillatory or sector-zoned zircon grains in the charnockite (TK28-1) is interpreted as the age of intrusion of the granitic protolith of the charnockite (Fig. 7c, 8e; Table 2). The late-

Palaeoproterozoic age of ca. 1610 Ma obtained from the rims of some zircon grains (Fig. 7c, 8h; Table 2) is consistent with the ages obtained from the metamorphic rims and overgrowths in zircon of other charnoenderbites, thereby representing the age of the peak metamorphism. The brightly luminescent rims from the other zircon grains yielding a Palaeoproterozoic age of ca. 1690 Ma is not easy to interpret (Fig. 7c, 8f). Still there is no strong evidence from other rocks to assign this age as the timing of another tectonometamorphic event in the region. However, Kovach et al. (2001) reported concordant U-Pb monazite ages of ca. 1670 Ma and interpreted that as the age of the syn-kinematic formation of the coarse-grained leucosome network in the charnoenderbites, but the geological interpretation is not unambiguous.

Similar to that of other charnoenderbites, the Palaeoproterozoic age of ca. 1750 Ma obtained from the oscillatory-zoned large zircon grains in the charnockite TK39-4 represents the magmatic intrusion age (Fig. 7d, 8i; Table 2). The implications of the Palaeoproterozoic age of ca. 1715 Ma, obtained from the highly luminescent unzoned or weakly-zoned overgrowths (Fig. 7d, 8j; Table 2), are again not straightforward. Considering the lack of evidence from other rocks to correlate this age with any regional event, we interpret this age as a period of renewed zircon growth due to local fluid circulations during the last stage of magma crystallization. The zircon rims in this charnockite do not show any age of ca. 1620 Ma found in most samples.

The prismatic, euhedral zircon grains in the sheared enderbite (TK39-3) strongly argue for a magmatic origin of the zircon grains. Consequently, the concordia age of ca. 1600 Ma obtained from the zoned, elongated grains represent the age of intrusion of the precursor magma (Fig. 7e, 8k; Table 2). On the other hand, the unzoned, recrystallized domains of the elongated grains and the ellipsoidal sector zoned zircon grains indicate a metamorphic origin (Fig. 7e, 8l; Table 2). Therefore, the concordia age of ca. 1600 Ma obtained from these grains is interpreted to be the age of peak metamorphism. The age is very consistent with the metamorphic ages obtained from the other charnoenderbites. Magmatic zircon

grains having the same age as the metamorphic overgrowths have not been encountered before. The most plausible interpretation is that the precursor rock intruded during ongoing metamorphism and deformation, indicating that this enderbite is a syn-metamorphic intrusion. The intrusive relationship of the fine-grained sheared enderbite into the older (ca. 1750 Ma) coarse-grained charnockite (TK39-4) further conforms to the overall interpretation.

The dark, spherical to ellipsoidal core domains of zircon grains of the orthogneiss (TK66-1), from the adjoining Vinjamuru domain, showing a range of Palaeoproterozoic ages from ca. 2430 to 1870 Ma represent inherited cores, which were incorporated into the magma from the surrounding country rocks during intrusion or melting of the source rocks (Fig. 7f; Table 2). The oscillatory-zoned outer parts of the cores clearly indicate that they are magmatically grown zircon grains. These grains were resorbed to different extents before the crystallization of a broad oscillatory-zoned mantle that is also of magmatic origin. The zoned cores as well as the zoned mantles yielding the same concordia age (ca. 1780 Ma; Fig. 8m,n; Table 2) implies that they were formed during the same magmatic event.

The zircon U-Pb geochronological data from the current study (summarized in Table 2) constrain the timing of the intrusion of the precursor magmas of charnoenderbites, the dominant rocks of the Ongole domain, and the timing of the metamorphism. From the 4 charnoenderbite samples, the concordant ages from the oscillatory zoned magmatic cores range from ca. 1750 to 1710 Ma. We interpret this age span (ca. 40 Ma) as the duration of widespread magmatic activity in the region. This implies that the crust formation of the Ongole domain was in the Palaeoproterozoic. The ages from this study are in agreement with the age of emplacement (1.72-1.70 Ga) reported by Kovach et al. (2001) in a preliminary study.

The concordant ages from the unzoned metamorphic overgrowths around the cores, in three charnoenderbite samples, range from ca. 1630 to 1600 Ma, constraining the timing of the granulite-facies metamorphism in the Ongole domain. This age range is identical to the concordant metamorphic ages of ca. 1625-1600 Ma

obtained from zircons of five metapelitic samples that occur as enclaves within these charnoenderbites (Chapter 3). This age is interpreted to reflect the timing of the UHT granulite-facies metamorphism and partial melting in rocks of the Ongole domain that took place at high temperatures and low pressures. Thus, the concordant metamorphic ages (ca. 1630-1600 Ma) from 8 different rocks (3 from this chapter and 5 from Chapter 3) from different localities tightly constrain the timing and duration (ca. 30 Ma) of the UHT granulite-facies metamorphism and partial melting the Ongole domain. The age is further supported by in-situ Th-U-total Pb dating of monazites from the same metapelites, where the monazite inclusions in garnet yield ages of ca. 1610 Ma (Chapter 3). Additionally, monazite dating of 5 different samples (3 metapelites and 3 charnoenderbites) yielded a younger age of ca. 1540 Ma, interpreted to be the age of a second metamorphic event that occurred 60 to 80 Ma after the first. Incidentally, this age was neither preserved in zircon grains from the metapelites (Chapter 3), nor in zircon grains from the charnoenderbites of the present study. This fact once again highlights the importance of a second method of dating (preferably texturally controlled monazite dating in high-grade rocks), so that the two methods can complement each other for precise age determination and consequently to propose a suitable geodynamic model.

The syn-metamorphic charnockite intrusion into the older charnoenderbites is an important finding and sheds some more light on the reason for the UHT metamorphism. It is argued in Chapter 2 based on petrological and thermobarometric constrains that the first metamorphic event with UHT peak conditions (ca. 1620 Ma) is characterized by an isobaric heating-cooling trajectory, which points towards a magmatic heat source for the metamorphism. The syn-metamorphic enderbite intrusion most likely represents a fractionated melt from a bigger mafic intrusion that probably contributed heat for this metamorphic event. Nevertheless, it is an important piece of evidence that supports the proposition made with petrological and thermobarometric constrains.

Table 4.2: Sample locations, descriptions of zircon textures under CL, corresponding U-Pb ages of zircon growth and geological interpretation of the age

Sample	Rock type	GPS coordinates	Zircon populations and textures under cathodoluminescence (CL)	Interpretation of zircon growth	Ages (Ma)	Geological interpretation
Ongole domain						
TK4B2	Enderbite	N 16° 36.374' E 80° 31.982'	Two zircon populations are distinguished (Pop1) Subhedral zircon grains (up to 300 µm) having weakly luminescent well-developed oscillatory-zoned cores (Fig. 7a) (Pop2) Broad, unzoned overgrowths around cores (occasionally resorbed) having slightly higher luminescence Fig. 7a)	(1) Magmatic (2) Metamorphic	(1) Concordia age 1717±13 (Fig. 8a) (2) Concordia age 1626±9 (Fig. 8b)	(1) Magmatic protolith emplacement (2) Granulite facies metamorphism
TK21	Enderbite	N 16° 11.581' E 80° 15.816'	Two zircon populations are identified (Pop1) Elongated zircon grains (up to 350µm) with moderately luminescent well-developed oscillatory zoned cores (Fig. 7b) (Pop2) Two consecutive narrow unstructured overgrowths; (2a) narrow highly luminescent inner zone; (2b) weakly luminescent outer zone (Fig. 7b)	(1) Magmatic (2a) Not known (2b) Metamorphic	(1) Concordia age 1743±10 (Fig. 8c) (2a) Could not be measured (2b) Concordia age 1601±10 (Fig. 8d)	(1) Magmatic protolith emplacement (2) Granulite facies metamorphism
TK28-1	Charnockit	N 16°37.440' E 80°31.978'	Two zircon populations are identified (Pop1) Subhedral (up to 300µm) weakly luminescent, oscillatory or sector zoned cores (Fig. 7c) (Pop2) Moderately luminescent narrow to broad unzoned overgrowths surrounding the zoned cores (Fig. 7c). Pop2 yields two concordia ages.	(1) Magmatic (2) Metamorphic	(1) Concordia age 1720±10 (Fig. 8e) (2a) Concordia age 1688±8 (2b) Concordia age 1612±14 (Fig. 8f & h)	(1) Magmatic protolith emplacement (2a) Interpretation no clear (2b) Granulite facies metamorphism
TK39-4	Charnockit	N 16°40.545' E 80°34.253'	CL-images reveal two zircon populations (Pop1) Prismatic zircon grains (up to 350 µm) having weakly luminescent well-developed oscillatory-zoned cores (Fig. 7d) (Pop2) Highly luminescent narrow unzoned rims surrounding the zoned cores (Fig. 7d)	(1) Magmatic (2) Magmatic	(1) Concordia age 1746±8 (Fig. 8i) (2) Concordia age 1716±8 (Fig. 8j)	(1) Magmatic protolith emplacement (2) Crystallization from late stage magmatic fluids
TK39-3	Enderbite	N 16°40.545' E 80°34.253'	Two zircon populations are distinguished (Pop1) Prismatic, euhedral zircon grains (up to 250µm) with highly luminescent growth banding (Fig. 7e) (Pop2) Unzoned or planar banded overgrowths that embay and truncate the early zoning. Pop2 zircon also form anhedral grains showing patchy or sector zoning (Fig. 7e)	(1) Magmatic (2) Anatectic & metamorphic	(1) Concordia age 1603±7 (Fig. 8k) (2) Concordia age 1602±5 (Fig. 8l)	(1) Magmatic protolith emplacement (2) Granulite facies metamorphism (Syn-metamorphic intrusion)
Vinjamuru domain						
TK66-1	Orthogneis	N 15°09.809' E 79°33.562'	Three zircon populations are recognized in the subhedral zircon grains (up to 200µm) (Pop1) Weakly luminescent rounded to ellipsoidal cores (Fig. 7f) (Pop2) Oscillatory-zoned, moderately to weakly luminescent xenocrystic cores (Fig. 7f) (Pop3) Broad, moderately to highly luminescent, oscillatory zoned overgrowths that may truncate the core zoning but also form conformable to the cores (Fig. 7f)	(1) Inherited (2) Magmatic (3) Magmatic	(1) ²⁰⁷ Pb/ ²⁰⁶ Pb ages 2436-11 (1) (2) Concordia age 1778±6 (Fig. 8m) (3) Concordia age 1778±6 (Fig. 8n)	(1) Magmatic or metamorphic event (2) Magmatic protolith emplacement (3) Resorption and overgrowth during magmatic activity

Concordant magmatic ages of ca. 1780 Ma from the oscillatory-zoned cores and mantles of the zircon grains from the orthogneiss of the Vinjamuru domain (TK66-1; Fig. 8m,n) clearly indicate the age of emplacement, which is slightly older but similar to the emplacement age of the charnoenderbites in the Ongole domain. The age is in agreement with the age (ca. 1790-1770 Ma) obtained from zircon (evaporation method) from similar metamorphosed felsic rocks that show major and trace element chemistry of a volcanic arc granite (Ravikant et al., 2013).

4.7.2. Petrogenesis of the mafic granulites

The mafic granulites of the Ongole domain show negative correlations between SiO_2 and MgO , Fe_2O_3 and CaO and a positive correlation between SiO_2 and K_2O (Fig. 5). The negative correlations suggest the fractionation of ferromagnesian minerals like pyroxene and hornblende. The positive correlation can also be explained by the fractionation of ferromagnesian minerals, which make the magma progressively richer in K_2O .

As ratios of incompatible elements mostly remain unchanged during partial melting as well as fractional crystallization (Pearce and Peate, 1995), the incompatible elements can be used as tracers for magmatic processes. The two important elements for tracing subduction zone processes are Nb and Ta as depletion of primitive arc magmas in Nb and Ta relative to Th and La are ubiquitous has been ascribed to many processes (Kelemen et al., 2003). The primary reason for depletion is the preferential retention of Nb and Ta within mineral phases (e.g. rutile, ilmenite) in rocks of subduction zones (e.g. Pearce and Peate, 1995). These minerals are either present as residual phases in the area of melt production and/or separated during fractional crystallization from the magma. Depletion in Zr indicates that the neighboring LREE are relatively enriched compared to Zr, which is the most immobile element. Nb and Ta depletions coupled

with Ti and Zr depletions, like in the mafic granulites of the Ongole domain (Fig. 6b), are therefore a unique characteristic of melts generated in a magmatic arc.

The mafic granulites also display other trace element signatures that are typical of volcanic rocks erupting at modern day volcanic arcs. The rocks are characterized by LREE enrichment (Fig. 6a) and moderate depletion in HREE leading to Sr/Y ratios in the range of 0.19-10.92 (Fig. 9a) and La/Yb_{CN} ratios of 0.75-6.01 (Fig. 9b). These along with low TiO₂ (<0.2wt.%) contents (Pearce and Cann, 1973) suggest that the mafic granulites are typical of calc-alkaline subduction related magmas (e.g. oceanic island arc or continental arc). The mafic granulite suite also falls mainly in the island field of the La-Sm-Th-Yb-Nb log-transformed discrimination diagram (Agrawal et al., 2008; Fig. 9d)

As continental rocks are highly differentiated and enriched in incompatible elements compared to the upper mantle (e.g. Rudnick, 1995), the ratios of incompatible elements are also useful in investigating the role of crustal contamination in mantle-derived melts. Immobile trace element ratios of Th/Yb and Ta/Yb are used to investigate the role of the subcontinental lithosphere in magma genesis at oceanic arcs and active continental margins (Pearce, 1983). The rocks formed at active continental margins have higher Th/Yb (1.0-10.0) and Ta/Yb (0.1-1.0) ratios than rocks formed in oceanic island arcs that have low Th/Yb (0.05-1.0) and Ta/Yb (0.02-1.0) ratios, indicating a Th and Ta enrichment by interaction of the melts with continental crust. The mafic granulites of the Ongole domain have moderate ratios of Th/Yb (0.12-1.38, average 0.63) and high Ta/Yb (0.12-0.30, average 0.21). The Th/Yb values fall in the range of oceanic island arcs while the Ta/Yb ratios lie at the lower end of the range for active continental margins (Fig. 9c). This suggests that the role of crustal contamination in their magma genesis is only low.

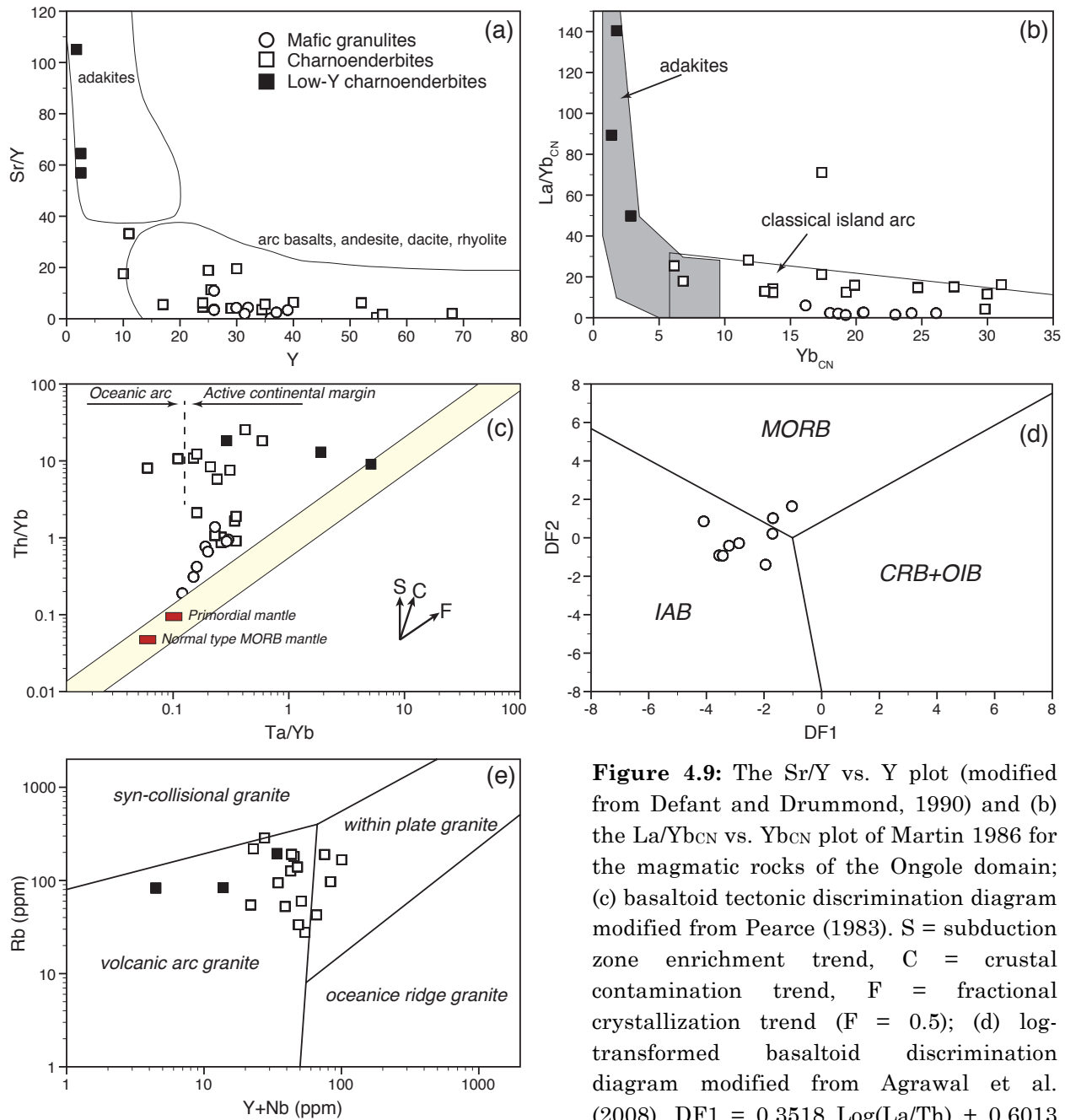


Figure 4.9: The Sr/Y vs. Y plot (modified from Defant and Drummond, 1990) and (b) the La/Yb_{CN} vs. Yb_{CN} plot of Martin 1986 for the magmatic rocks of the Ongole domain; (c) basaltoid tectonic discrimination diagram modified from Pearce (1983). S = subduction zone enrichment trend, C = crustal contamination trend, F = fractional crystallization trend (F = 0.5); (d) log-transformed basaltoid discrimination diagram modified from Agrawal et al. (2008). DF1 = 0.3518 Log(La/Th) + 0.6013

Log(Sm/Th) - 1.3450 Log(Yb/Th) + 2.1056 Log(Nb/Th) - 5.4763; and DF2 = -0.3050 Log(La/Th) - 1.1801 Log(Sm/Th) + 1.6189 Log(Yb/Th) + 1.2260 Log(Nb/Th) - 0.9944. MORB = mid-ocean ridge basalts, IAB = island arc basalt, CRB = continental rift basalt, OIB = ocean island basalt; (e) Rb vs. Y+Nb granitoid tectonic discrimination diagram of Pearce et al., 1984.

4.7.3. Petrogenesis of the charnoenderbites

The charnoenderbites of the Ongole domain have variable SiO_2 content (52.2-72.5 wt. %) and display negative correlations between SiO_2 and MgO , Fe_2O_3 , CaO , Ni and Cr and a positive correlation with K_2O . The large variation in SiO_2 and the element correlations are best explained by magma differentiation. Lower values of Cr and Ni than that of the mafic granulites can be explained by extensive fractionation of pyroxene and hornblende (Fig. 5e,f). In the plot of Fe^* against wt.% SiO_2 and $\text{Na}_2\text{O}+\text{K}_2\text{O}-\text{CaO}$ against wt.% SiO_2 (Fig. 4b,c), the similarity of the charnoenderbites and the Cordillaran granitoids of USA suggests that these rocks were formed in a subduction related arc setting.

In addition, the charnoenderbites show pronounced Nb-Ta depletion ($\text{Nb}/\text{La}_{\text{pm}}=0.04-0.45$, mean 0.26; $\text{Ta}/\text{La}_{\text{pm}}=0.06-0.44$, mean 0.19) relative to the other incompatible elements (Fig. 6d) that are typical of rocks formed in a magmatic arc setting and is primarily due to the preferential retention of the two elements by mineral phases like rutile and ilmenite in the subduction zone. This argument is in agreement with the low contents of TiO_2 (0.1-2.1 wt.%, mean 0.75).

Similar to the mafic granulites, the charnoenderbites are also characterized by highly enriched LREE ($\text{La}/\text{Yb}_{\text{CN}} = 4.2-71.1$) relative to HREE (Fig. 6c), which shows moderate depletion ($\text{Tb}/\text{Yb}_{\text{CN}} = 1.1-3.0$). In the Sr/Y vs. Y plot (Fig. 9a; Drummond and Defant, 1990) and $\text{La}/\text{Yb}_{\text{CN}}$ vs. Yb_{CN} plot (Fig. 9b; Martin, 1986) the charnoenderbites lie in the field of typical island arc rocks. The charnoenderbite suite also plots mainly in the volcanic arc granite field of the Rb vs. $\text{Y}+\text{Nb}$ diagram (Pearce et al., 1984; Fig. 9e).

There are three distinct low Y charnoenderbites with very low Y (1.8-2.5 ppm) and Yb (0.22-0.46 ppm) contents and plot in the field of adakites in the Sr/Y vs. Y and $\text{La}/\text{Yb}_{\text{CN}}$ vs. Yb_{CN} diagrams (Fig. 9a,b). The fact that Sr/Y (which is vulnerable to alteration) and $\text{La}/\text{Yb}_{\text{CN}}$ (which is not) are similarly high suggests that Sr/Y ratios

largely reflect magmatic compositions and not secondary effects. The name 'adakite' is used to describe a large group of rocks whose sole feature is high Sr/Y and La/Yb_{CN} ratios (Moyen, 2009). The original adakites, as defined by Defant and Drummond (1990) and termed as 'high silica adakites' by Martin et al. (2005) have characteristic chemical composition (SiO₂>56%, Al₂O₃>15%, MgO>3.5%, K₂O/Na₂O<0.5, Y and Yb < 18 and 1.9 ppm and Sr>400 ppm). The genesis of these high silica adakites is best explained by the classical 'slab melting' model, where the melts are interpreted to have formed by partial melting of the subducting slab leaving garnet±amphibole as residual phases, which preferentially retain HREE and Y, producing depletion in the magma. But, as plagioclase is not a residual phase the magmas lack a negative Eu anomaly. However, there is a growing evidence that the sole signature of high Sr/Y and La/Yb_{CN}, by which the term adakite is defined, can be achieved through different processes than slab melting but in these cases the rocks lack the other chemical characteristic chemistry of 'high silica adakites' (Moyen, 2009). They may form in geodynamic settings not typically associated with active subduction, as well as in a subduction setting, but not necessarily related to slab melts. For example the adakites can form through differentiation and/or partial melting processes at the base of an arc-crust (Bindeman et al., 2005) or are produced by fractional crystallization of garnet bearing assemblages from metasomatized mantle derived basaltic arc magmas (Macpherson et al., 2006). However, in all cases garnet plays the most important role in fractionating HREE and Y. The three low Y chernoenderbites that plot in the field of adakites are different from the composition of 'high silica adakites'. Therefore, these three rocks are not likely to be produced by slab melts. Instead, they are more likely to be produced by partial melting of older continental crust in a subduction zone setting where garnet was stable. This interpretation is consistent with the genesis of the spatially and timely associated rocks that were clearly formed in a magmatic arc setting.

As discussed in section 7.2, incompatible trace element ratios (e.g. Th/Nb and Ta/Nb) are useful in investigating crustal contamination of mantle derived melts

(Pearce, 1983). The charnoenderbites of the Ongole domain have high and variable ratios of Th/Yb (1.1-25.5) and high Ta/Yb (0.1-0.6) ratios that fall in the range defined for active continental margins (Fig. 9c; Pearce, 1983). This suggests that the role of crustal contamination in the trace element signatures of the charnoenderbites is significant. This interpretation is in agreement with the observation that migmatitic metapelites form enclaves within the charnoenderbites. Crust-magma interaction is typical of continental arcs and can explain some of the trace element signatures like enriched LREE and high Th/Nb ratios. Large variation in LILE/HFSE ratios (e.g. Ba/La = 3.81-73.95) between broadly contemporaneous magmatic phases spatially occurring together can be better explained by varying degrees of crust-magma interaction and fractionation rather than variability within melt sources (Hildreth and Moorbath, 1988).

4.7.4. Geodynamic setting

Based on the geological, geochronological and geochemical evidence presented above we propose that the Ongole domain was formed as a subduction related magmatic arc during the Palaeoproterozoic. The arc was situated near the continental margin of the Eastern Dharwar craton with a remnant oceanic basin in between the arc and the continent (Fig. 10a). This basin was most likely the site of deposition of continental sediments derived from the felsic granitoids of the adjacent Eastern Dharwar craton. This is highlighted by the Nd model ages (T_{DM}) of the migmatitic metapelites (2.8-2.6 Ga) reflecting the mean crustal residence age of the provenance areas, which are similar to the Nd model ages of the granitoids of the Eastern Dharwar craton (Rickers et al., 2001).

When the subduction process continued the oceanic slab dehydrated before melting and releasing aqueous fluids that rose and metasomatized the overlying

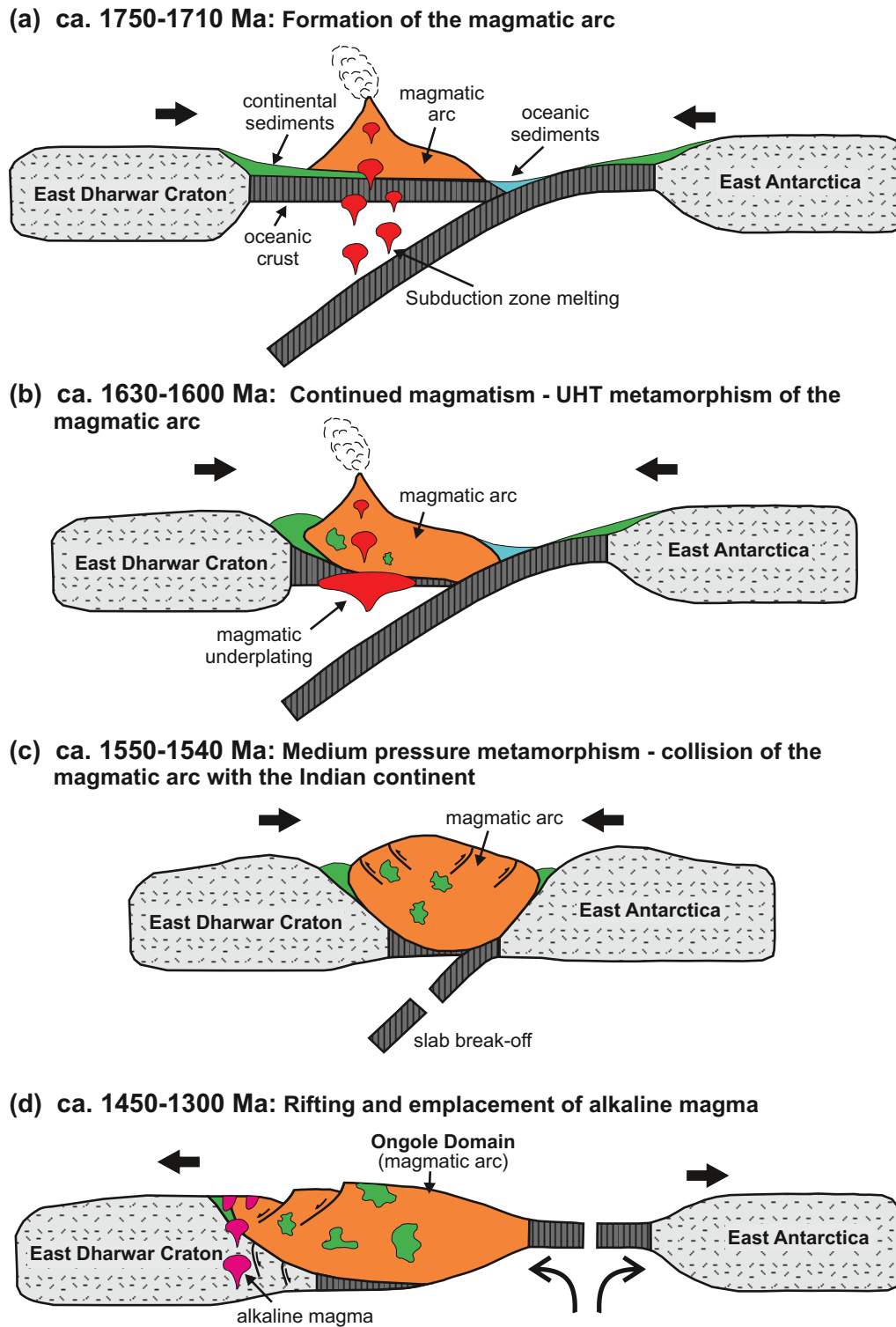


Figure 4.10: Model showing sequences of tectonic evolution of the Ongole domain (simplified after Dasgupta et al. 2013) with constraints from new geochronological data. See text for details of the sequences (a) to (d).

mantle wedge. The fluids triggered partial melting of the mantle peridotite, which generated the parental magma of the mafic granulites (Fig. 10a). These juvenile magmas ascended through the mantle and were probably emplaced at the base of the crust. There they were slightly contaminated by the metasediments of the continental crust resulting in Ta/Yb ratios slightly higher than rocks formed in an oceanic island arc. Subsequent differentiation of the basic magma led to the formation of intermediate to felsic parental magmas of the charnoenderbites. Owing to their buoyancy, they moved upwards taking huge enclaves of undifferentiated basic rocks and the crustal metasediments on the way. These processes resulted in widespread volcanism and plutonism in the Ongole domain between 1750-1710 Ma of these magmas that were contaminated by the crustal sediments with high Th/Yb and Ta/Yb ratios (Fig. 10a). Nd model ages of 2.5-2.3 Ga for the charnoenderbites (Rickers et al., 2001) also argue for the contamination with older crustal sediments. The metapelitic enclaves within the charnoenderbites were most likely metamorphosed during the widespread magma emplacements. Unfortunately, ages reflecting this synmagmatic metamorphism were not found in zircon grains of the metapelitic enclaves (Chapter 3).

The presence of a ca. 1750-1700 Ma old magmatic arc in the Eastern Ghats Belt is critical in understanding the accretionary history of supercontinent Columbia, which formed at ca. 2.1-1.8 Ga (Rogers and Santosh, 2002; Zhao et al., 2002). Columbia is believed to have undergone a long lived (1.8-1.2 Ga) subduction related episodic growth due to the accretion along some of its continental margin involving Laurentia, Baltica, South America, Australia and China (Zhao et al., 2004). Petrological and geochemical studies indicate that the large accretionary magmatic belts include juvenile volcanogenic sequences and granitoid suites resembling those of present day magmatic arcs (Zhao et al., 2004). Bose et al. (2011) proposed the inclusion of SE margin of India as an accretionary magmatic belt during Columbia formation based on geochronological constrains. This proposition can now be consolidated with our extensive geochronological and geochemical data.

The period of ca. 1710-1630 Ma was probably a period of quiescence as evidence for major tectonothermal activity is absent. Reactivation of subduction processes led to mafic magmatism inducing UHT metamorphism at low pressures between ca. 1630 and 1600 Ma (Fig. 10b). The heat from mafic magmas resulted in remelting of some older rocks and emplacement of felsic magmas during the period of metamorphism (Fig. 10b). Subsequent to subduction of the back-arc basin the collision of the arc with the continent resulted in a thickened crust at the arc-continent margin. Consequently, the rocks experienced a higher-pressure lower-temperature second metamorphism dated at ca. 1540 Ma (Fig. 10c). The evolution of the Ongole domain magmatic arc has similarities with the Areachap magmatic arc, which magmatically grew till ca. 1240 Ma and was juxtaposed with the craton at ca. 1200 Ma (Pettersson et al., 2007). The advancing style of tectonism in the Ongole domain is switched to a retreating one at ca. 1450 Ma with the opening of an ocean basin (Upadhyay, 2008) and emplacement of alkaline rocks in a rift setting along the craton-mobile belt contact (Fig. 10d). Thus all the tectonothermal events including the UHT metamorphism are considered to be a part of this accretionary process during the growth of the Palaeo-Mesoproterozoic supercontinent Columbia.

4.8. Conclusions

Based on field observations, U-Pb zircon geochronology and geochemical data presented in this paper we draw the following conclusions.

- 1) U-Pb zircon ages indicate that a widespread magmatic activity in the Ongole domain started in the Palaeoproterozoic at ca. 1750 Ma resulting in the emplacement of evolved calc-alkaline granitoids and some mafic rocks. The magmatic activity lasted for ca. 40 Ma giving rise to different generations of magmatic rocks having complex crosscutting relationship as observed in outcrops.

2) The Palaeoproterozoic magmatic rocks possess trace and rare earth element characteristics that are analogous to modern day continental arcs.

3) These magmatic rocks along with the metapelites occurring as enclaves within them experienced a high-grade (UHT) metamorphism during the late Palaeoproterozoic (ca. 1610 Ma) attributed to further magmatic activities. This was followed by a second metamorphism at lower temperatures but higher pressures during early Mesoproterozoic (ca. 1540 Ma), marking the collision of the magmatic arc with the Indian shield.

4.9. Acknowledgements

The authors would like to thank Prof. J. Erzinger for generously extending the geochemical lab facilities at GeoForschungZentrum in Potsdam and S. Tonn and H. Rothe for their help with geochemical analysis. We extend our thanks to Prof. M. Raith for providing geochemical data of six samples from the Ongole domain and for his insightful discussions.

References

- Agrawal, S., Guevara, M., Verma, S.P., 2008. Tectonic Discrimination of Basic and Ultrabasic Volcanic Rocks through Log-Transformed Ratios of Immobile Trace Elements. *International Geology Review* 50, 1057–1079.
- Arndt, N., 2013. Formation and Evolution of the Continental Crust. *Geochemical Perspectives* 2, 405–533.
- Bindeman, I.N., Eiler, J.M., Yogodzinski, G.M., Tatsumi, Y., Stern, C.R., Grove, T.L., Portnyagin, M., Hoernle, K., Danyushevsky, L.V., 2005. Oxygen isotope

- evidence for slab melting in modern and ancient subduction zones. *Earth and Planetary Science Letters* 235, 480–496.
- Bose, S., Dunkley, D.J., Dasgupta, S., Das, K., Arima, M., 2011. India-Antarctica-Australia-Laurentia connection in the Paleoproterozoic-Mesoproterozoic revisited: Evidence from new zircon U-Pb and monazite chemical age data from the Eastern Ghats Belt, India. *Geological Society of America Bulletin* 123, 2031–2049.
- Cawood, P.A., Kröner, A., Pisarevsky, S., 2006. Precambrian plate tectonics: criteria and evidence. *GSA TODAY*.
- Condie, K.C., 2000. Episodic continental growth models: afterthoughts and extensions. *Tectonophysics*.
- Defant, M.J., Drummond, M.S., 1990. Derivation of some modern arc magmas by melting of young subducted lithosphere. *Nature* 347, 662–665.
- Dharma Rao, C.V., Santosh, M., 2011. Continental arc magmatism in a Mesoproterozoic convergent margin: Petrological and geochemical constraints from the magmatic suite of Kondapalle along the eastern margin of the Indian plate. *Tectonophysics* 510, 151–171.
- Dharma Rao, C.V., Santosh, M., Dong, Y., 2012. U-Pb zircon chronology of the Pangidi-Kondapalle layered intrusion, Eastern Ghats belt, India: Constraints on Mesoproterozoic arc magmatism in a convergent margin setting. *Journal of Asian Earth Sciences* 49, 362–375.
- Dobmeier, C.J., Raith, M.M., 2003. Crustal architecture and evolution of the Eastern Ghats Belt and adjacent regions of India. *Geological Society, London, Special Publications* 206, 145–168.
- Drummond, M.S., Defant, M.J., 1990. A model for Trondhjemite-Tonalite-Dacite Genesis and crustal growth via slab melting: Archean to modern comparisons. *J. Geophys. Res.* 95, 21503.
- Dulski, P., 2001. Reference Materials for Geochemical Studies: New Analytical Data by ICP-MS and Critical Discussion of Reference Values. *Geostandards*

Newsletter 25, 87–125.

- Frost, B.R., Barnes, C.G., Collins, W.J., Arculus, R.J., Ellis, D.J., Frost, C.D., 2001. A geochemical classification for granitic rocks. *Journal of Petrology* 42, 2033–2048.
- Govindaraju, K., 1994. 1994 compilation of working values and sample description for 383 geostandards. *Geostandards Newsletter* 18, 1–158.
- Hawkesworth, C.J., Kemp, A.I.S., 2006. Evolution of the continental crust. *Nature* 443, 811–817.
- Hildreth, W., Moorbath, S., 1988. Crustal contributions to arc magmatism in the Andes of Central Chile. *Contributions to Mineralogy and Petrology* 98, 455–489.
- Irvine, T., Baragar, W., 1971. A guide to the chemical classification of the common volcanic rocks. *Canadian Journal of Earth Sciences* 8, 523–548.
- Jagoutz, O., Muntener, O., Ulmer, P., Pettke, T., Burg, J.P., Dawood, H., Hussain, S., 2007. Petrology and Mineral Chemistry of Lower Crustal Intrusions: the Chilas Complex, Kohistan (NW Pakistan). *Journal of Petrology* 48, 1895–1953.
- Kelemen, P.B., Høghøj, K., Greene, A.R., 2003. One View of the Geochemistry of Subduction-Related Magmatic Arcs, with an Emphasis on Primitive Andesite and Lower Crust, in: *Treatise on Geochemistry*. Elsevier, pp. 593–659.
- Kooijman, E., Berndt, J., Mezger, K., 2012. U-Pb dating of zircon by laser ablation ICP-MS: recent improvements and new insights. *European Journal of Mineralogy* 24, 5–21.
- Korsch, R.J., Kositsin, N., Champion, D.C., 2011. Australian island arcs through time: Geodynamic implications for the Archean and Proterozoic. *Gondwana Research* 19, 716–734.
- Kovach, V.P., Simmat, R., Rickers, K., Berezhnaya, N.G., Salnikova, E.B., Dobmeier, C., Raith, M.M., Yakovleva, S.Z., Kotov, AB, 2001. The western charnockite zone of the Eastern Ghats Belt, India-an independent crustal province of late Achaean (2.8 Ga) and Palaeoproterozoic (1.7-1.6 Ga) terrains. *Gondwana Research* 4, 666–667.

- Le Bas, M.J., Le Maitre, R.W., Streckeisen, A., Zanettin, B., 1986. A chemical classification of volcanic rocks based on the total alkali-silica diagram. *Journal of Petrology* 27, 745–750.
- Liang, Q., Grégoire, D.C., 2000. Determination of Trace Elements in Twenty Six Chinese Geochemistry Reference Materials by Inductively Coupled Plasma-Mass Spectrometry. *Geostandards Newsletter* 24, 51–63.
- Macpherson, C.G., Dreher, S.T., Thirlwall, M.F., 2006. Adakites without slab melting: High pressure differentiation of island arc magma, Mindanao, the Philippines. *Earth and Planetary Science Letters* 243, 581–593.
- Martin, H., 1986. Effect of steeper Archean geothermal gradient on geochemistry of subduction-zone magmas. *Geology* 14, 753–756.
- Martin, H., Smithies, R.H., Rapp, R., Moyen, J.F., 2005. An overview of adakite, tonalite–trondhjemite–granodiorite (TTG), and sanukitoid: relationships and some implications for crustal evolution. *Lithos*.
- McDonough, W.F., Sun, S.S., 1995. The composition of the Earth. *Chemical Geology* 120, 223–253.
- Moyen, J.-F., 2009. High Sr/Y and La/Yb ratios: The meaning of the “adakitic signature.” *Lithos* 112, 556–574.
- Pearce, J.A., 1983. Role of the sub-continental lithosphere in magma genesis at active continental margins. Shiva Press Limited, Cheshire, UK.
- Pearce, J.A., Cann, J.R., 1973. Tectonic setting of basic volcanic rocks determined using trace element analyses. *Earth and Planetary Science Letters* 19, 290–300.
- Pearce, J.A., Harris, N.B.W., Tindle, A.G., 1984. Trace Element Discrimination Diagrams for the Tectonic Interpretation of Granitic Rocks. *Journal of Petrology*.
- Pearce, J.A., Peate, D.W., 1995. Tectonic implications of the composition of volcanic arc magmas. *Annu. Rev. Earth Planet. Sci.* 23, 251–286.
- Pettersson, Å., Cornell, D.H., Moen, H.F.G., Reddy, S., Evans, D., 2007. Ion-probe dating of 1.2Ga collision and crustal architecture in the Namaqua-Natal Province of southern Africa. *Precambrian Research* 158, 79–92.

- Polat, A., 2012. Growth of Archean continental crust in oceanic island arcs. *Geology* 40, 383–384.
- Polat, A., Hofmann, A.W., 2003. Alteration and geochemical patterns in the 3.7–3.8 Ga Isua greenstone belt, West Greenland. *Precambrian Research* 126, 197–218.
- Ramakrishnan, M., Nanda, J.K., Augustine, P.F., 1998. Geological evolution of the Proterozoic Eastern Ghats mobile belt. *Geological Survey of India Special Publications* 44, 1–21.
- Ravikant, V., Kröner, A., Vasudevan, D., 2013. Zircon evaporation ages and geochemistry of metamorphosed volcanic rocks from the Vinjamuru domain, Krishna Province: evidence for 1.78 Ga convergent tectonics along the southeastern margin of the Eastern Dharwar Craton. *Geological Journal* 48, 293–309.
- Rickers, K., Mezger, K., Raith, M.M., 2001. Evolution of the continental crust in the Proterozoic Eastern Ghats Belt, India and new constraints for Rodinia reconstruction: implications from Sm–Nd, Rb–Sr and Pb–Pb isotopes. *Precambrian Research* 112, 183–210.
- Rogers, J.J.W., Santosh, M., 2002. Configuration of Columbia, a Mesoproterozoic Supercontinent. *Gondwana Research* 5, 5–22.
- Rudnick, R.L., 1995. Making continental crust. *Nature* 378, 571–578.
- Sengupta, P., Sen, J., Dasgupta, S., Raith, M.M., Bhui, U.K., Ehl, J., 1999. Ultra-high temperature metamorphism of metapelitic granulites from Kondapalle, Eastern Ghats Belt: implications for the Indo-Antarctic correlation. *Journal of Petrology* 40, 1065–1087.
- Simmat, R., Raith, M.M., 2008. U–Th–Pb monazite geochronometry of the Eastern Ghats Belt, India: Timing and spatial disposition of poly-metamorphism. *Precambrian Research* 162, 16–39.
- Sun, S.S., McDonough, W.F., 1989. Chemical and isotopic systematics of oceanic basalts: implications for mantle composition and processes. *Geological Society, London, Special Publications* 42, 313–345.

- Şengör, A.M.C., Natal'in, B.A., Burtman, V.S., 1993. Evolution of the Altaid tectonic collage and Palaeozoic crustal growth in Eurasia. *Nature* 364, 299–307.
- Taylor, S.R., McLennan, S.M., 1985. *The continental crust: Its composition and evolution*. Blackwell Scientific Publications, Oxford.
- Upadhyay, D., 2008. Alkaline magmatism along the southeastern margin of the Indian shield: Implications for regional geodynamics and constraints on craton–Eastern Ghats Belt suturing. *Precambrian Research* 162, 59–69.
- Windley, B.F., Garde, A.A., 2009. Arc-generated blocks with crustal sections in the North Atlantic craton of West Greenland: Crustal growth in the Archean with modern analogues. *Earth-Science Reviews* 93, 1–30.
- Zhao, G., Cawood, P.A., Wilde, S.A., Sun, M., 2002. Review of global 2.1–1.8 Ga orogens: implications for a pre-Rodinia supercontinent. *Earth-Science Reviews* 59, 125–162.
- Zhao, G., Sun, M., Wilde, S.A., Li, S., 2004. A Paleo-Mesoproterozoic supercontinent: assembly, growth and breakup. *Earth-Science Reviews* 67, 91–123.
- Zuleger, E., Erzinger, J., 1988. Determination of the REE and Y in silicate materials with ICP-AES. *Fresenius' Journal of Analytical Chemistry* 332, 140–143.

List of Figures

1.1 Main geological units in the southern part of the Indian subcontinent	3
2.1 Simplified geological map of the Eastern Ghats Belt (EGB).....	17
2.2 Geological map of the southern part of the Eastern Ghats Belt showing the position of the Ongole domain and the adjoining areas	19
2.3 Field photographs of different rock types in the Ongole domain	21
2.4 Photomicrographs illustrating the reaction textures from the metapelites and charnoenderbites in the Ongole domain.....	24
2.4 Photomicrographs illustrating the reaction textures from the metapelites and charnoenderbites in the Ongole domain (continued).....	28
2.5 Typical Raman spectra of fine-grained aluminosilicate symplectites.....	29
2.6 Chemistry of garnet (metapelite and charnoenderbite) and orthopyroxene	35
2.6 Chemistry of garnet (metapelite and charnoenderbite) and orthopyroxene (continued)	44
2.7 Feldspar thermometry (metapelites and charnoenderbites).....	49
2.8 P-T pseudosections.....	55
2.8 P-T pseudosections (continued)	57
2.9 Pressure-temperature paths of the rocks from the Ongole domain	62
3.1 Geological map of the southern part of the Eastern Ghats Belt showing the rock type and locations of geochronological samples	80
3.2 CL images of selected zircon grains from metapelites.....	86
3.2 CL images of selected zircon grains from metapelites (continued).....	87
3.3 U-Pb concordia diagrams for metapelites and a quartzite	90
3.3 U-Pb concordia diagrams for metapelites and a quartzite (continued)	91

3.4 BSE images showing the textural positions of the monazite grains.....	96
3.5 BSE images of monazite showing ages	98
3.5 BSE images of monazite showing ages (continued)	99
3.6 Monazite substitution and composition	102
3.7 Monazite histogram ages	103
3.8 Distribution of metamorphic ages in the Ongole and the Vinjamuru domain	112
3.9 Geodynamic settings corresponding to P-T paths	117
4.1 Geological map showing the locations of the geochemical and geochronological samples.....	129
4.2 Field photographs of different meta-igneous rocks in the Ongole domain	131
4.3 Zr vs. selected major and trace elements plots for the meta-igneous rocks	134
4.4 Classification of meta-igneous rocks	136
4.5 SiO ₂ vs. selected major and trace elements plots	138
4.6 REE and extended trace plots for mafic granulites and charnoenderbites	139
4.7 CL images of selected zircon grains from charnoenderbites	146
4.7 CL images of selected zircon grains from charnoenderbites (continued)...	147
4.8 U-Pb concordia diagrams for charnoenderbites	150
4.8 U-Pb concordia diagrams for charnoenderbites (continued)	151
4.9 Various trace element ratios for the meta-igneous rocks	159
4.10 Model showing sequences of tectonic evolution of the Ongole domain	163
A.1 CL images of selected zircon grains from a quartzite	175

List of Tables

2.1 Mineral assemblages of the granulites of the Ongole domain.....	32
2.2 Representative garnet analyses	38
2.3 Representative pyroxene analyses	39
2.4 Representative cordierite analyses	40
2.5 Representative spinel analyses	41
2.6 Representative feldspar analyses	42
2.7 Representative biotite analyses	43
2.8 Representative amphibole analyses.....	47
2.9 Reintegrated feldspar compositions and temperatures	50
2.10 Summary of calculated thermobarometric data.....	52
3.1 Electron microprobe U-Th-total Pb representative monazite analyses and calculated ages.....	107
3.1 Electron microprobe U-Th-total Pb representative monazite analyses and calculated ages (continued)	108
3.2 Summary of zircon and monazite ages	114
4.1 Major and trace element compositions of the meta-igneous rocks of the Ongole domain.....	141
4.1 Major and trace element compositions of the meta-igneous rocks of the Ongole domain (continued).....	142
4.2 Sample locations, descriptions of zircon textures under CL, corresponding U-Pb ages of zircon growth and geological interpretation of the age	156
A.1 LA-ICP-MS zircon U-Pb data (metapelites)	176
B.1 EMP monazite U-Th-total Pb data	182
C.1 LA-ICP-MS zircon U-Pb data (charnoenderbites)	191

Appendix A

LA-ICP-MS zircon U-Pb data of metapelites and a quartzite from the Ongole domain

Zircon from five metapelites and one quartzite from the Ongole domain have been analyzed. The cathodoluminescence (CL) images of selected zircon grains from the five metapelites are illustrated in Chapter 3 (Fig. 3.2; pages 86-87). The CL images of zircon grains from the quartzite (TK46-3) are not included in Chapter 3 and is shown below in Fig. A.1. The U-Pb concordia diagrams of all the six samples are included in Chapter 3 (Fig. 3.3; pages 90-91). The isotopic ratios and ages of individual spots on zircon grains from the six samples are listed here in Table A.1.

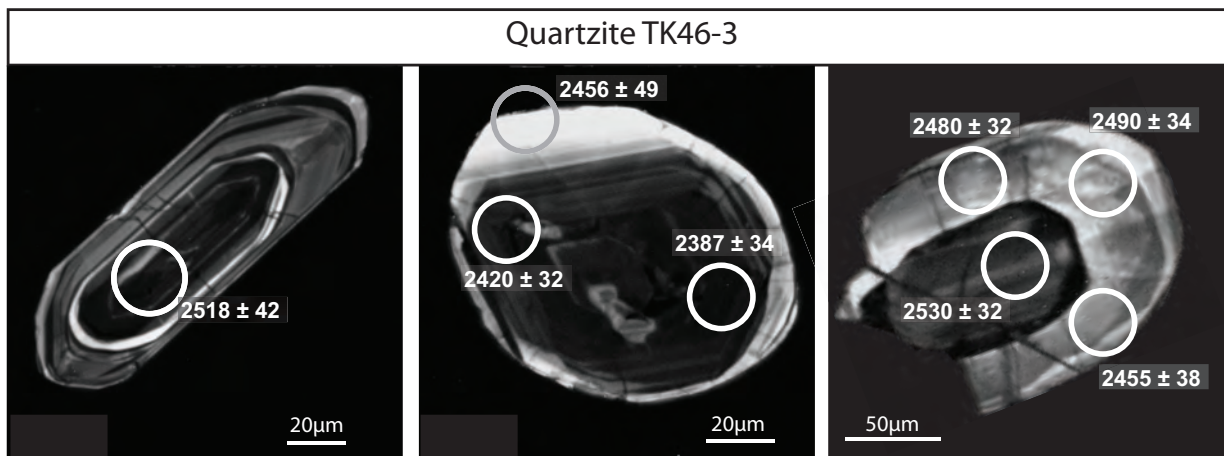


Figure A.1: Cathodoluminescence (CL) images of selected detrital zircon grains from a quartzite. The grains show fine-scale oscillatory zoning indicating crystallization from magma. The grains are inherited from the source region of the sediment.

Table A.1: LA-ICP-MS zircon U-Pb dating data for metapelites and a quartzite of the Ongole domain.

Spot	Grain	Texture	U conc. (ppm)	Radiogenic ratios				Ages (Ma)				Con.						
				$\frac{^{206}\text{Pb}}{^{204}\text{Pb}}$	$\frac{^{206}\text{Pb}}{^{238}\text{U}}$	$\frac{^{207}\text{Pb}}{^{235}\text{U}}$	$\frac{^{207}\text{Pb}}{^{206}\text{Pb}}$	$\frac{^{207}\text{Pb}}{^{238}\text{U}}$	$\frac{^{207}\text{Pb}}{^{206}\text{Pb}}$	$\frac{^{207}\text{Pb}}{^{235}\text{U}}$	$\frac{^{207}\text{Pb}}{^{206}\text{Pb}}$							
1	TK8C1 1-4	inhr. core	149	42319	0.4487	0.0095	10.7702	0.2684	0.1741	0.0023	0.85	2389	42	2503	23	2597	22	92.0
2	TK8C1 1-5	inhr. core	206	8179	0.5031	0.0104	12.3054	0.3044	0.1774	0.0024	0.84	2627	45	2628	23	2629	23	99.9
3	TK8C1 1-6	inhr. core	198	7715	0.5092	0.0124	12.6313	0.3734	0.1799	0.0030	0.83	2653	53	2653	28	2652	28	100.0
4	TK8C1 4-1	inhr. core	980	1746	0.3247	0.0088	4.9718	0.1585	0.1110	0.0019	0.85	1813	43	1815	27	1817	30	99.8
5	TK8C1 4-2	inhr. core	890	6962	0.3244	0.0060	4.9707	0.1056	0.1111	0.0012	0.87	1811	29	1814	18	1818	19	99.6
6	TK8C1 4-4	meta. rim	176	59683	0.2872	0.0030	3.9653	0.0774	0.1002	0.0016	0.54	1627	15	1627	16	1627	31	100.0
7	TK8C1 5-1	mantle	1329	36808	0.2859	0.0036	3.9549	0.0611	0.0998	0.0009	0.82	1621	18	1621	13	1621	17	100.0
8	TK8C1 5-4	meta. rim	219	7301	0.2871	0.0040	3.9624	0.0720	0.1001	0.0012	0.77	1627	20	1627	15	1626	21	100.1
9	TK8C1 5-5	meta. rim	252	b.d.l	0.2857	0.0040	3.9260	0.0715	0.0997	0.0012	0.77	1620	20	1619	15	1618	22	100.1
10	TK8C1 5-6	meta. rim	996	b.d.l	0.2872	0.0045	3.9761	0.0757	0.1004	0.0011	0.82	1628	22	1629	15	1632	20	99.8
11	TK8C1 6-1	inhr. core	287	1370	0.3545	0.0134	5.8507	0.2336	0.1197	0.0016	0.94	1956	64	1954	35	1952	23	100.2
12	TK8C1 6-4	inhr. core	978	7130	0.3141	0.0044	4.6676	0.0764	0.1078	0.0009	0.85	1761	21	1761	14	1762	16	99.9
13	TK8C1 7-1	inhr. core	212	3670	0.3268	0.0120	5.1195	0.2012	0.1136	0.0016	0.93	1823	58	1839	33	1858	26	98.1
14	TK8C1 8-1	inhr. core	601	1287	0.3345	0.0059	5.2332	0.1216	0.1135	0.0017	0.75	1860	28	1858	20	1856	28	100.2
15	TK8C1 8-2	inhr. core	1230	2803	0.3070	0.0054	4.4831	0.0950	0.1059	0.0013	0.82	1726	26	1728	18	1730	22	99.8
16	TK8C1 8-5	meta. rim	424	7773	0.2896	0.0037	4.0331	0.0631	0.1010	0.0009	0.83	1640	19	1641	13	1642	16	99.8
17	TK8C1 8-4	meta. rim	1404	35019	0.2846	0.0023	3.9137	0.0463	0.0997	0.0008	0.69	1615	12	1617	10	1619	16	99.7
18	TK8C1 9-4	meta. rim	213	b.d.l	0.2841	0.0039	3.8826	0.0659	0.0991	0.0010	0.80	1612	19	1610	14	1608	19	100.3
19	TK8C1 9-5	meta. rim	208	14289	0.2846	0.0056	3.9083	0.0864	0.0996	0.0010	0.89	1615	28	1615	18	1616	19	99.9
20	TK8C1 10-1	inhr. core	1377	22108	0.3081	0.0048	4.4968	0.0970	0.1058	0.0016	0.72	1732	23	1730	18	1729	28	100.1
21	TK8C1 10-5	inhr. core	276	1459	0.3133	0.0037	4.6411	0.0823	0.1074	0.0014	0.66	1757	18	1757	15	1756	24	100.0
22	TK8C1 11-1	inhr. core	187	4420	0.3249	0.0051	4.9529	0.1051	0.1106	0.0016	0.74	1813	25	1811	18	1809	26	100.2
23	TK8C1 11-2	inhr. core	103	2375	0.3424	0.0045	5.4816	0.1015	0.1161	0.0015	0.71	1898	22	1898	16	1897	23	100.0
24	TK8C1 12-1	inhr. core	314	12022	0.3220	0.0064	4.8766	0.1124	0.1099	0.0013	0.86	1799	31	1798	19	1797	21	100.1
25	TK8C1 15-1	inhr. core	298	5745	0.3117	0.0049	4.5822	0.0929	0.1066	0.0013	0.78	1749	24	1746	17	1743	23	100.4
26	TK8C1 15-4	inhr. core	1922	87261	0.3166	0.0055	4.7366	0.1015	0.1085	0.0014	0.81	1773	27	1774	18	1775	23	99.9
27	TK8C1 15-5	inhr. core	2583	79263	0.3155	0.0070	4.7042	0.1213	0.1081	0.0014	0.86	1768	34	1768	22	1768	24	100.0

Con., degree of concordance; meta. rim, metamorphic rim; inhr. core, inherited core; b.d.l, below detection limit

Table A.1: Continued

Spot	Grain	Texture	U conc. Radiogenic ratios										Ages (Ma)						
			$\frac{^{206}\text{Pb}}{^{204}\text{Pb}}$ (ppm)	$\frac{^{206}\text{Pb}}{^{238}\text{U}}$	$\frac{^{207}\text{Pb}}{^{235}\text{U}}$	$\frac{^{207}\text{Pb}}{^{206}\text{Pb}}$	$\pm 2\sigma$	$\frac{^{207}\text{Pb}}{^{235}\text{U}}$	$\frac{^{207}\text{Pb}}{^{206}\text{Pb}}$	$\pm 2\sigma$	$\frac{^{206}\text{Pb}}{^{238}\text{U}}$	$\frac{^{207}\text{Pb}}{^{235}\text{U}}$	$\frac{^{207}\text{Pb}}{^{206}\text{Pb}}$	$\pm 2\sigma$	$\frac{^{206}\text{Pb}}{^{238}\text{U}}$	$\frac{^{207}\text{Pb}}{^{235}\text{U}}$	$\frac{^{207}\text{Pb}}{^{206}\text{Pb}}$	$\pm 2\sigma$	Con.
Grt-Crd granulite TK35-6																			
1	TK35-6-6-1	inhr. core	549	3897	0.3178	0.0280	4.7093	0.4627	0.1075	0.0046	0.90	137	1769	82	1757	79	101.3		
2	TK35-6 7-2	inhr. core	1144	790	0.3329	0.00569	5.31473	0.1251	0.1158	0.00187	0.73	28	1871	20	1892	29	97.9		
3	TK35-6 7-4	meta. rim	266	11981	0.2844	0.0041	3.9107	0.0753	0.0997	0.0013	0.75	21	1616	16	1619	24	99.7		
4	TK35-6 7-5	meta. rim	278	75226	0.2841	0.0044	3.9124	0.0958	0.0999	0.0019	0.64	22	1616	20	1622	35	99.4		
5	TK35-6 7-6	meta. rim	318	10439	0.2868	0.0038	3.9645	0.0736	0.1003	0.0013	0.72	19	1627	15	1629	24	99.8		
6	TK35-6 8-1	core	407	90932	0.2858	0.0034	3.9440	0.0665	0.1001	0.0012	0.70	17	1623	14	1626	22	99.7		
7	TK35-6 8-2	core	299	b.d.1	0.2861	0.0036	3.9406	0.0650	0.0999	0.0011	0.77	18	1622	13	1622	20	100.0		
8	TK35-6 8-4	meta. rim	206	b.d.1	0.2851	0.0044	3.9025	0.0815	0.0993	0.0014	0.73	17	1614	17	1611	26	100.4		
9	TK35-6 8-5	meta. rim	183	b.d.1	0.2840	0.0043	3.8940	0.0792	0.0994	0.0014	0.74	22	1612	16	1614	25	99.9		
10	TK35-6 9-1	core	1439	10583	0.3148	0.0057	4.7080	0.1122	0.1085	0.0017	0.76	28	1764	20	1774	28	99.4		
11	TK35-6 9-2	core	2068	2794	0.3353	0.0068	5.2791	0.1275	0.1142	0.0015	0.84	33	1865	21	1867	24	99.8		
12	TK35-6 9-5	meta. rim	645	216904	0.2883	0.0035	3.9964	0.0724	0.1005	0.0014	0.67	17	1633	15	1634	25	99.9		
13	TK35-6 10-4	meta. rim	243	8239	0.2848	0.0060	3.9057	0.1058	0.0995	0.0017	0.78	30	1615	22	1614	32	100.1		
14	TK35-6 11-5	core	496	18494	0.2824	0.0053	3.8570	0.0907	0.0990	0.0014	0.80	27	1605	19	1606	26	99.8		
15	TK35-6 11-6	mantle	282	b.d.1	0.2850	0.0050	3.9220	0.0940	0.0998	0.0016	0.73	25	1618	19	1621	31	99.7		
16	TK35-6 13-1	core	365	6255	0.2841	0.0043	3.8937	0.0832	0.0994	0.0015	0.71	22	1612	17	1613	28	99.9		
17	TK35-6 13-4	meta. rim	97	30822	0.2861	0.0039	3.9461	0.0769	0.1000	0.0014	0.70	20	1623	16	1625	26	99.9		
18	TK35-6 14-1	inhr. core	5078	63807	0.3141	0.0088	4.6595	0.1918	0.1076	0.0032	0.68	43	1760	34	1759	55	100.1		
19	TK35-6 14-5	meta. rim	512	20298	0.2862	0.0040	3.9393	0.0756	0.0998	0.0013	0.73	20	1622	16	1621	24	100.1		
20	TK35-6 15-4	meta. rim	339	12264	0.2880	0.0067	3.9879	0.1165	0.1004	0.0018	0.80	34	1632	24	1632	33	100.0		

Con., degree of concordance; meta. rim, metamorphic rim; inhr. core, inherited core; b.d.1, below detection limit

Table A.1: Continued

Spot	Grain	Texture	U conc. Radiogenic ratios				Ages (Ma)				Con.							
			$^{206}\text{Pb}/^{204}\text{Pb}$	$^{206}\text{Pb}/^{238}\text{U}$	$^{207}\text{Pb}/^{235}\text{U}$	$^{207}\text{Pb}/^{206}\text{Pb}$	$^{206}\text{Pb}/^{238}\text{U}$	$^{207}\text{Pb}/^{235}\text{U}$	$^{207}\text{Pb}/^{206}\text{Pb}$	$^{207}\text{Pb}/^{206}\text{Pb}$								
Grt-Crd-Opx granulite TK73-4																		
1	TK73-4 2-1	inhr. core	b.d.l	0.5250	0.0084	13.6821	0.2898	0.1890	0.0026	0.76	2720	36	2728	20	2734	23	99.5	
2	TK73-4 2-7	meta. rim	48555	0.2806	0.0022	3.8193	0.0590	0.0987	0.0013	0.51	1595	11	1597	12	1600	25	99.7	
3	TK73-4 2-8	meta. rim	1407	0.2816	0.0024	3.8377	0.0599	0.0988	0.0013	0.54	1599	12	1601	13	1603	24	99.8	
4	TK73-4 3-1	inhr. core	238	0.2867	0.0062	4.7069	0.1178	0.1084	0.0017	0.78	1765	30	1768	21	1772	28	99.6	
5	TK73-4 3-2	mantle	1635	0.2888	0.0045	4.0082	0.0861	0.1007	0.0015	0.73	1635	23	1636	17	1637	27	99.9	
6	TK73-4 3-4	meta. rim	879	0.2814	0.0049	3.8420	0.0864	0.0990	0.0014	0.78	1598	25	1602	18	1606	26	99.5	
7	TK73-4 3-5	meta. rim	627	0.2847	0.0058	3.8907	0.1022	0.0991	0.0016	0.78	1615	29	1612	21	1608	31	100.4	
8	TK73-4 4-1	inhr. core	379	0.4464	0.0073	9.4295	0.1958	0.1532	0.0020	0.78	2379	32	2381	19	2382	22	99.9	
9	TK73-4 4-5	mantle	151	0.2837	0.0050	3.8850	0.0997	0.0993	0.0019	0.68	1610	25	1611	21	1612	35	99.9	
10	TK73-4 4-6	mantle	191	0.2805	0.0041	3.8102	0.0683	0.0985	0.0010	0.82	1594	21	1595	14	1596	19	99.9	
11	TK73-4 4-7	mantle	1332	0.2539	0.0050	3.5227	0.0822	0.1006	0.0013	0.84	1458	26	1532	18	1636	24	89.2	
12	TK73-4 4-4	meta. rim	331	b.d.l	0.2654	0.0030	3.5643	0.0504	0.0974	0.0008	0.80	1517	15	1542	11	1575	16	96.4
13	TK73-4 4-8	meta. rim	1308	0.2603	0.0044	3.6242	0.0833	0.1010	0.0016	0.74	1491	23	1555	18	1642	29	90.8	
14	TK73-4 5-1	inhr. core	387	0.4953	0.0109	11.8496	0.3896	0.1735	0.0042	0.67	2593	47	2593	31	2592	41	100.1	
15	TK73-4 5-7	mantle	897	0.2826	0.0043	3.8638	0.0687	0.0991	0.0009	0.85	1605	21	1606	14	1608	17	99.8	
16	TK73-4 5-4	meta. rim	124	0.2847	0.0042	3.9135	0.0810	0.0997	0.0014	0.72	1615	21	1616	17	1619	27	99.8	
17	TK73-4 6-1	inhr. core	183	0.4152	0.0070	9.0370	0.2176	0.1404	0.0030	0.62	2239	32	2235	24	2232	37	100.3	
18	TK73-4 6-7	meta. rim	1459	0.2873	0.0046	3.9734	0.0830	0.1003	0.0013	0.77	1628	23	1629	17	1630	25	99.9	
19	TK73-4 7-4	meta. rim	798	0.2856	0.0039	3.9245	0.0721	0.0996	0.0012	0.74	1620	20	1619	15	1618	23	100.1	
20	TK73-4 7-5	meta. rim	924	0.2811	0.0040	3.8182	0.0720	0.0985	0.0012	0.76	1597	20	1597	15	1596	23	100.1	
21	TK73-4 8-1	inhr. core	240	0.4903	0.0075	11.5877	0.2680	0.1714	0.0030	0.66	2572	32	2572	22	2571	29	100.0	
22	TK73-4 8-2	inhr. core	427	0.5076	0.0099	12.5580	0.3121	0.1794	0.0028	0.79	2647	42	2647	23	2648	26	100.0	
23	TK73-4 8-8	meta. rim	720	0.2884	0.0043	3.9930	0.0765	0.1004	0.0012	0.77	1633	21	1633	16	1632	23	100.1	
24	TK73-4 9-1	inhr. core	906	0.2825	0.0068	5.9273	0.1429	0.1208	0.0018	0.79	1963	32	1965	21	1968	26	99.8	
25	TK73-4 9-7	mantle	714	0.2825	0.0049	3.8359	0.0816	0.0985	0.0012	0.82	1604	25	1600	17	1596	23	100.5	
26	TK73-4 10-1	inhr. core	350	b.d.l	0.3913	0.0082	7.1710	0.2035	0.1329	0.0026	0.74	2129	38	2133	25	2137	34	99.6
27	TK73-4 11-4	meta. rim	369	0.2862	0.0043	3.9418	0.0759	0.0999	0.0012	0.78	1623	22	1622	16	1622	22	100.0	
28	TK73-4 12-1	inhr. core	469	0.4335	0.0068	8.8673	0.2033	0.1484	0.0025	0.69	2321	31	2324	21	2327	29	99.8	
29	TK73-4 13-7	mantle	817	0.2857	0.0061	3.9437	0.1029	0.1001	0.0015	0.82	1620	31	1623	21	1626	27	99.6	
30	TK73-4 13-4	meta. rim	350	0.2883	0.0069	3.9972	0.1147	0.1005	0.0016	0.84	1633	35	1634	23	1634	29	99.9	

Con., degree of concordance; meta. rim, metamorphic rim; inhr. core, inherited core; b.d.l, below detection limit

Table A.1: Continued

Spot	Grain	Texture	U conc. Radiogenic ratios					Ages (Ma)					Con.				
			²⁰⁶ Pb/ ²⁰⁴ Pb	²⁰⁶ Pb/ ²³⁸ U	²⁰⁷ Pb/ ²³⁵ U	²⁰⁷ Pb/ ²⁰⁶ Pb	$\pm 2\sigma$	²⁰⁶ Pb/ ²³⁸ U	$\pm 2\sigma$	²⁰⁷ Pb/ ²³⁵ U	$\pm 2\sigma$	²⁰⁷ Pb/ ²⁰⁶ Pb		$\pm 2\sigma$			
Grt-Opx granulite TK22-2																	
1	TK22 1-7	meta. rim	1352	0.2633	0.0054	3.6819	0.0852	0.1014	0.0011	0.88	1507	27	1567	18	1650	20	91.3
2	TK22 2-7	meta. rim	2627	0.2861	0.0046	3.9402	0.0768	0.0999	0.0011	0.82	1622	23	1622	16	1622	21	100.0
3	TK22 3-5	mantle	613	0.2875	0.0049	4.0008	0.0781	0.1009	0.0010	0.87	1629	24	1634	16	1641	18	99.3
4	TK22 3-7	meta. rim	1518	0.2852	0.0054	3.9075	0.0904	0.0994	0.0013	0.82	1617	27	1615	19	1612	25	100.3
5	TK22 4-8	meta. rim	4031	b.d.l	0.2876	3.9929	0.0842	0.1007	0.0013	0.78	1630	24	1633	17	1637	25	99.6
6	TK22 6-7	meta. rim	2279	0.2750	0.0029	3.8282	0.0703	0.1009	0.0015	0.58	1566	15	1599	15	1642	28	95.4
7	TK22 8-7	meta. rim	3333	0.2700	0.0047	3.7447	0.0830	0.1006	0.0014	0.79	1541	24	1581	18	1635	25	94.2
8	TK22 9-8	meta. rim	2934	0.2618	0.0040	3.6388	0.0749	0.1008	0.0014	0.75	1499	21	1558	16	1639	25	91.5
9	TK22 10-5	mantle	813	0.2856	0.0045	3.9243	0.0779	0.0997	0.0012	0.79	1620	22	1619	16	1618	23	100.1
10	TK22 11-7	meta. rim	5632	0.2814	0.0055	3.8368	0.0906	0.0989	0.0013	0.82	1598	27	1601	19	1604	25	99.7
11	TK22 11-8	meta. rim	4865	b.d.l	0.2847	3.9053	0.0695	0.0995	0.0011	0.79	1615	20	1615	14	1615	20	100.0
12	TK22 13-7	meta. rim	1363	0.2824	0.0053	3.8684	0.0837	0.0993	0.0011	0.86	1603	27	1607	17	1612	20	99.5
13	TK22 14-4	mantle	1118	0.2855	0.0035	3.9211	0.0551	0.0996	0.0007	0.86	1619	17	1618	11	1617	13	100.1
14	TK22 14-5	mantle	603	0.2849	0.0032	3.9147	0.0655	0.0997	0.0012	0.66	1616	16	1617	14	1618	23	99.9

Con., degree of concordance; meta. rim, metamorphic rim; b.d.l, below detection limit

Table A.1: Continued

Spot	Grain	Texture	U conc. Radiogenic ratios					Ages (Ma)					Con.				
			²⁰⁶ Pb/ ²⁰⁴ Pb	²⁰⁶ Pb/ ²³⁸ U	²⁰⁷ Pb/ ²³⁵ U	²⁰⁷ Pb/ ²⁰⁶ Pb	$\pm 2\sigma$	²⁰⁶ Pb/ ²³⁸ U	$\pm 2\sigma$	²⁰⁷ Pb/ ²³⁵ U	$\pm 2\sigma$	²⁰⁷ Pb/ ²⁰⁶ Pb		$\pm 2\sigma$			
Quartzite TK46-3																	
1	TK46-3 5-3	inhr. core	508	0.4718	0.0132	10.8037	0.4039	0.1661	0.0041	0.75	2492	58	2506	35	2518	42	98.9
2	TK46-3 6-1	inhr. core	1212	0.4545	0.0143	9.8160	0.3589	0.1566	0.0029	0.86	2415	63	2418	34	2420	32	99.8
3	TK46-3 6-2	inhr. core	1114	0.4469	0.0160	9.4678	0.3864	0.1537	0.0030	0.87	2381	71	2384	38	2387	34	99.8
4	TK46-3 6-4	inhr. core	165	0.4643	0.0088	10.2431	0.3556	0.1600	0.0047	0.55	2459	39	2457	32	2456	49	100.1
5	TK46-3 8-1	inhr. core	367	0.4779	0.0091	11.0191	0.2951	0.1672	0.0032	0.71	2518	40	2525	25	2530	32	99.5
6	TK46-3 8-4	inhr. core	260	0.4676	0.0094	10.4627	0.2923	0.1623	0.0032	0.72	2473	41	2477	26	2480	33	99.7
7	TK46-3 8-5	inhr. core	238	b.d.l	0.4700	10.5826	0.2981	0.1633	0.0033	0.71	2484	41	2487	26	2490	34	99.7
8	TK46-3 8-6	inhr. core	304	0.4625	0.0207	10.2022	0.5098	0.1600	0.0036	0.90	2451	91	2453	46	2455	38	99.8
9	TK46-3 9-4	inhr. core	387	b.d.l	0.4593	10.0496	0.2461	0.1587	0.0022	0.83	2436	41	2439	23	2442	23	99.8
10	TK46-3 10-4	inhr. core	1433	0.4655	0.0076	10.3533	0.2220	0.1613	0.0022	0.76	2464	33	2467	20	2469	24	99.8
11	TK46-3 11-1	inhr. core	671	0.4492	0.0106	9.5741	0.2765	0.1546	0.0026	0.81	2392	47	2395	27	2397	29	99.8
12	TK46-3 11-4	inhr. core	809	0.4638	0.0070	10.2462	0.2237	0.1602	0.0025	0.69	2456	31	2457	20	2458	27	99.9
13	TK46-3 12-1	inhr. core	624	0.4701	0.0098	10.5098	0.2543	0.1621	0.0020	0.86	2484	43	2481	22	2478	21	100.2
14	TK46-3 13-1	inhr. core	484	0.4803	0.0149	11.0250	0.3690	0.1665	0.0021	0.93	2528	65	2525	31	2523	21	100.2

Con., degree of concordance; inhr. core, inherited core; b.d.l, below detection limit

Table A.1: Continued

Spot	Grain	Texture	U conc. (ppm)	Radiogenic ratios				Ages (Ma)				Con.				
				$\frac{^{206}\text{Pb}}{^{204}\text{Pb}}$	$\frac{^{206}\text{Pb}}{^{238}\text{U}}$	$\pm 2\sigma$	$\frac{^{207}\text{Pb}}{^{206}\text{Pb}}$	$\frac{^{207}\text{Pb}}{^{235}\text{U}}$	$\pm 2\sigma$	$\frac{^{206}\text{Pb}}{^{238}\text{U}}$	$\pm 2\sigma$		$\frac{^{207}\text{Pb}}{^{206}\text{Pb}}$	$\pm 2\sigma$		
<i>Grt-Opx granulite TK22-2</i>																
1	TK82-2 1-1	inhr. core	247	7881	0.3326	0.0053	5.2138	0.1108	0.1137	0.0016	0.76	1855	18	1859	25	99.6
2	TK82-2 1-4	inhr. core	169	5097	0.3419	0.0072	5.4722	0.1427	0.1161	0.0018	0.81	1896	22	1897	28	99.9
3	TK82-2 1-7	meta. rim	986	31388	0.2867	0.0033	3.9605	0.0651	0.1002	0.0012	0.70	1626	13	1628	22	99.8
4	TK82-2 2-1	inhr. core	170	25420	0.3320	0.0077	5.1551	0.1483	0.1126	0.0019	0.81	1848	24	1842	31	100.3
5	TK82-2 2-10	mantle	248	10808	0.2896	0.0045	4.0312	0.0799	0.1010	0.0013	0.78	1639	16	1642	23	99.8
6	TK82-2 2-11	mantle	127	19452	0.2898	0.0063	4.0320	0.1132	0.1009	0.0018	0.77	1641	23	1641	33	100.0
7	TK82-2 3-1	inhr. core	460	3936	0.3349	0.0051	5.2624	0.1065	0.1140	0.0015	0.76	1863	17	1864	24	99.9
8	TK82-2 3-8	meta. rim	1449	155413	0.2831	0.0036	3.8639	0.0669	0.0990	0.0012	0.73	1606	14	1605	22	100.1
9	TK82-2 4-2	inhr. core	663	22114	0.3298	0.0079	5.0392	0.1667	0.1108	0.0025	0.72	1838	28	1813	41	101.4
10	TK82-2 5-7	meta. rim	301	116821	0.2844	0.0054	3.9112	0.0931	0.0997	0.0015	0.79	1616	19	1619	27	99.7
11	TK82-2 5-8	meta. rim	190	b.d.1	0.2838	0.0053	3.8925	0.0988	0.0995	0.0017	0.74	1610	21	1615	32	99.7
12	TK82-2 5-10	mantle	213	34833	0.2871	0.0044	3.9713	0.0827	0.1003	0.0014	0.74	1627	22	1628	17	99.8
13	TK82-2 5-11	mantle	159	b.d.1	0.2852	0.0041	3.9094	0.0907	0.0994	0.0018	0.62	1617	20	1616	19	100.2
14	TK82-2 7-1	inhr. core	239	12732	0.3306	0.0086	5.1245	0.1555	0.1124	0.0018	0.86	1841	42	1840	26	100.1
15	TK82-2 7-2	inhr. core	269	25442	0.3220	0.0066	4.8679	0.1227	0.1096	0.0016	0.82	1797	21	1794	26	100.3
16	TK82-2 7-7	meta. rim	1203	50020	0.2834	0.0048	3.8988	0.0831	0.0998	0.0013	0.80	1608	24	1613	17	99.3
17	TK82-2 12-2	inhr. core	322	13411	0.3283	0.0065	5.0744	0.1691	0.1121	0.0030	0.60	1832	28	1834	48	99.8
18	TK82-2 12-7	meta. rim	818	71681	0.2832	0.0044	3.8594	0.1119	0.0988	0.0024	0.53	1607	22	1605	23	100.3
19	TK82-2 13-7	meta. rim	1845	367453	0.2823	0.0039	3.8488	0.0866	0.0989	0.0011	0.77	1603	14	1603	21	100.0
20	TK82-2 13-8	meta. rim	1751	61885	0.2874	0.0067	3.9759	0.1073	0.1003	0.0013	0.87	1628	34	1629	22	99.9
21	TK82-2 14-10	mantle	159	b.d.1	0.2848	0.0058	3.9111	0.0989	0.0996	0.0015	0.80	1616	20	1617	28	99.9
22	TK82-2 14-12	mantle	130	10366	0.2782	0.0058	3.7576	0.0994	0.0980	0.0016	0.78	1584	21	1586	31	99.8
23	TK82-2 14-11	mantle	136	21188	0.2803	0.0047	3.8024	0.0867	0.0984	0.0015	0.73	1593	18	1594	29	100.0
24	TK82-2 16-2	inhr. core	591	2304	0.3276	0.0080	5.0686	0.1487	0.1122	0.0018	0.83	1831	25	1836	29	99.5
25	TK82-2 18-1	inhr. core	302	33093	0.3319	0.0048	5.1776	0.0959	0.1132	0.0013	0.77	1847	16	1851	21	99.8
26	TK82-2 18-7	meta. rim	1532	136992	0.2846	0.0049	3.8985	0.0802	0.0993	0.0011	0.83	1615	25	1613	17	100.2
27	TK82-2 18-8	meta. rim	2176	68652	0.2895	0.0049	4.0188	0.0843	0.1007	0.0012	0.81	1639	25	1638	17	100.1
28	TK82-2 19-1	inhr. core	299	4886	0.3298	0.0106	5.1308	0.1924	0.1128	0.0022	0.86	1837	52	1841	32	99.5
29	TK82-2 20-1	inhr. core	387	11541	0.3291	0.0057	5.1020	0.1125	0.1124	0.0016	0.78	1834	27	1836	19	99.7
30	TK82-2 22-7	meta. rim	2951	127250	0.2861	0.0057	3.9462	0.0915	0.1000	0.0012	0.86	1623	19	1625	22	99.8
31	TK82-2 22-8	meta. rim	2679	268772	0.2891	0.0053	4.0163	0.0921	0.1008	0.0014	0.80	1637	27	1638	25	99.9

Con., degree of concordance; meta. rim, metamorphic rim; inhr. core, inherited core; b.d.1, below detection limit

Appendix B

EMP U-Th-total Pb in-situ monazite data from metapelites and charnoenderbites from the Ongole domain and a metapelite from the Vinjamuru domain

Electron Microprobe U-Th-total Pb in-situ monazite dating was performed on five samples from the Ongole domain (three metapelites and two charnoenderbites) and one metapelite from the adjoining Vinjamuru domain. Backscattered electron (BSE) images (Fig. 3.5; pages 98-99) and histograms with weighted mean ages (Fig. 3.7; page 103) included in Chapter 3. Representative monazite analyses and calculated ages (Table 3.1; pages 107-108) are also included in Chapter 3. However, all the individual monazite analyses and the calculated ages used for calculating the weighted mean histogram ages are listed here in Table B.1.

Table B.1: EMP U-TH-total Pb monazite analyses and calculated ages

Spot	Grain	Y ₂ O ₃	ThO ₂	err ThO ₂	UO ₂	err UO ₂	PbO	err PbO	ThO ₂ *	err ThO ₂ *	Age	Err ap. Age
		(wt %)	(wt %)	(%)	(wt %)	(%)	(wt %)	(%)	(wt %)	(%)	(Ma)	(Ma)
<i>Grt-Sil-Spl-Qz granulite (TK8-1)</i>												
36	mz2	0.01	2.11	2.28	0.05	0.10	0.16	5.51	2.30	2.09	1633	96
38	mz3	0.04	13.76	0.76	0.09	0.18	0.94	1.03	14.08	0.75	1536	20
39	mz3	0.02	12.90	0.78	0.08	0.16	0.87	1.05	13.19	0.77	1514	20
40	mz3	0.02	22.23	0.62	0.04	0.07	1.48	0.73	22.36	0.61	1519	14
41	mz3	0.03	18.89	0.66	0.06	0.11	1.30	0.79	19.09	0.65	1558	16
43	mz3	0.02	16.52	0.70	0.07	0.15	1.13	0.86	16.79	0.69	1544	17
44	mz3	0.03	19.63	0.65	0.13	0.26	1.42	0.74	20.11	0.63	1611	16
45	mz5	0.04	12.66	0.79	0.09	0.19	0.91	0.99	12.99	0.77	1594	20
48	mz5	0.05	14.78	0.74	0.17	0.33	1.03	0.91	15.38	0.71	1537	18
50	mz5	0.04	16.12	0.71	0.10	0.20	1.12	0.87	16.49	0.70	1558	17
51	mz6	0.10	6.97	1.06	0.44	0.88	0.61	1.31	8.59	0.87	1620	25
52	mz6	0.93	7.07	1.05	0.58	1.16	0.66	1.24	9.20	0.85	1631	25
53	mz6	0.17	4.88	1.28	0.46	0.92	0.44	1.71	6.54	0.98	1531	30
54	mz6	0.04	10.50	0.87	0.34	0.68	0.79	1.10	11.74	0.78	1533	21
55	mz6	0.16	13.27	0.78	0.19	0.39	0.93	0.98	13.97	0.74	1530	19
57	mz9	0.15	10.25	0.88	0.14	0.27	0.73	1.15	10.75	0.84	1565	22
58	mz9	0.13	10.52	0.87	0.12	0.25	0.74	1.15	10.97	0.83	1543	22
60	mz9	0.15	10.05	0.88	0.15	0.29	0.72	1.16	10.58	0.83	1553	22
61	mz10	0.14	5.90	1.14	0.26	0.51	0.46	1.62	6.82	0.99	1529	29
63	mz10	0.15	10.18	0.87	0.15	0.30	0.72	1.16	10.72	0.83	1539	22
64	mz10	0.07	7.16	1.04	0.22	0.43	0.54	1.44	7.94	0.94	1544	27
65	mz10	0.06	5.65	1.17	0.20	0.40	0.43	1.69	6.38	1.04	1548	31
67	mz13	0.28	6.62	1.08	0.36	0.72	0.56	1.38	7.94	0.91	1619	27
68	mz13	0.84	6.72	1.07	0.38	0.75	0.53	1.44	8.07	0.90	1515	26
71	mz13	0.16	6.32	1.10	0.20	0.40	0.46	1.60	7.03	0.99	1511	28
72	mz14	1.88	7.07	1.05	0.52	1.04	0.63	1.28	8.97	0.85	1595	25
74	mz14	0.14	6.95	1.05	0.49	0.99	0.60	1.31	8.75	0.86	1581	25
75	mz14	0.12	8.14	0.97	0.57	1.13	0.70	1.17	10.20	0.81	1568	22
76	mz14	0.01	14.72	0.74	0.11	0.23	1.03	0.90	15.13	0.72	1565	18
77	mz14	0.03	14.89	0.73	0.08	0.15	1.04	0.90	15.16	0.72	1571	18
78	mz14	0.16	7.16	1.03	0.81	1.62	0.68	1.20	10.10	0.87	1547	23
79	mz14	0.08	8.10	0.97	0.31	0.62	0.63	1.27	9.24	0.86	1568	24
80	mz14	0.19	6.17	1.12	0.55	1.10	0.57	1.36	8.17	0.88	1586	26
81	mz15	1.26	6.88	1.06	0.37	0.74	0.59	1.35	8.22	0.90	1628	26
82	mz15	0.22	6.73	1.07	0.27	0.53	0.54	1.41	7.71	0.94	1612	27
83	mz15	0.69	7.16	1.04	0.26	0.52	0.58	1.35	8.12	0.92	1639	27
84	mz15	1.51	6.71	1.08	0.38	0.76	0.58	1.36	8.11	0.91	1643	27
144	mz14	1.19	6.91	1.06	0.59	1.19	0.62	1.29	9.07	0.85	1562	24
145	mz14	0.88	7.06	1.05	0.42	0.83	0.61	1.30	8.57	0.87	1622	25
146	mz14	0.02	14.95	0.73	0.11	0.23	1.01	0.92	15.36	0.71	1512	18
147	mz14	0.10	7.94	0.99	0.58	1.17	0.67	1.21	10.05	0.82	1535	22
148	mz14	2.58	6.82	1.08	0.44	0.87	0.61	1.31	8.42	0.89	1665	26
372	mz6	0.77	6.87	1.09	0.31	5.50	0.60	2.84	8.03	1.22	1692	52
373	mz6	1.80	8.28	0.99	0.67	3.31	0.77	2.30	10.73	1.07	1636	42
374	mz6	0.07	7.17	1.05	0.46	4.12	0.59	2.75	8.82	1.15	1524	45

Table B.1: Continued

Spot	Grain	Y ₂ O ₃	ThO ₂	err ThO ₂	UO ₂	err UO ₂	PbO	err PbO	ThO ₂ *	err ThO ₂ *	Age	Err ap. Age
		(wt %)	(wt %)	(%)	(wt %)	(%)	(wt %)	(%)	(wt %)	(%)	(Ma)	(Ma)
<i>Grt-Sil-Spl-Qz granulite (TK8-1)</i>												
375	mz6	0.09	7.44	1.03	0.39	4.48	0.59	2.72	8.84	1.12	1523	45
376	mz6	0.70	7.08	1.06	0.33	4.96	0.61	2.65	8.29	1.16	1679	48
377	mz6	0.02	14.66	0.75	0.11	6.01	1.02	1.85	15.05	0.75	1556	31
378	mz7	0.16	8.23	0.98	0.32	4.85	0.63	2.60	9.39	1.05	1540	43
379	mz7	0.16	8.51	0.97	0.28	5.12	0.65	2.53	9.54	1.03	1554	42
380	mz7	0.09	9.32	0.93	0.18	6.22	0.67	2.46	9.98	0.96	1541	41
381	mz15	1.30	7.09	1.06	0.34	4.83	0.59	2.71	8.33	1.15	1607	47
382	mz15	0.84	6.93	1.07	0.30	5.27	0.57	2.77	8.02	1.17	1617	49
384	mz15	1.67	7.16	1.05	0.40	4.41	0.62	2.59	8.61	1.15	1651	47
385	mz15	0.48	6.84	1.08	0.29	5.36	0.57	2.78	7.89	1.17	1640	49
386	mz16	0.08	9.96	0.89	0.10	7.53	0.70	2.40	10.33	0.90	1549	40
387	mz16	0.08	9.53	0.91	0.11	7.57	0.66	2.50	9.92	0.92	1515	40
388	mz16	0.09	8.55	0.96	0.09	8.65	0.60	2.68	8.86	0.98	1548	44
389	mz16	0.06	8.67	0.96	0.08	8.99	0.59	2.68	8.94	0.97	1521	43
390	mz16	0.12	8.31	0.98	0.12	7.87	0.58	2.73	8.74	1.00	1528	44
391	mz16	0.08	9.80	0.90	0.12	7.08	0.68	2.43	10.25	0.91	1522	40
<i>Grt-Crd granulite (TK35-6)</i>												
60	mz12	2.06	19.98	0.65	0.52	3.17	1.50	1.83	21.88	0.65	1566	30
61	mz12	0.13	9.72	0.89	0.32	4.68	0.73	2.91	10.89	0.94	1527	47
62	mz12	0.40	11.38	0.83	1.65	1.87	1.14	2.09	17.33	0.84	1514	34
168	mz1	0.17	9.69	0.89	0.22	5.61	0.71	2.86	10.47	0.93	1561	47
169	mz1	0.14	12.22	0.80	0.15	5.87	0.84	2.54	12.75	0.80	1503	40
173	mz1	0.15	8.67	0.94	0.24	5.46	0.63	3.09	9.53	0.99	1515	49
174	mz4	0.14	9.36	0.91	0.51	3.53	0.75	2.73	11.20	0.95	1536	44
178	mz4	0.15	7.79	0.99	0.47	3.78	0.62	3.09	9.51	1.06	1499	49
181	mz6	0.09	12.66	0.79	0.64	2.95	1.02	2.20	14.99	0.81	1562	37
184	mz7	0.99	8.13	0.97	1.00	2.43	0.77	2.68	11.72	1.00	1511	43
186	mz17	0.11	16.22	0.70	0.00	7.31	1.09	2.12	16.22	0.70	1542	34
187	mz17	0.04	13.63	0.76	0.06	6.96	0.93	2.37	13.83	0.76	1533	38
188	mz17	0.12	11.03	0.84	0.10	7.01	0.77	2.69	11.39	0.84	1551	44
189	mz17	0.43	9.61	0.90	0.17	6.24	0.69	2.92	10.21	0.92	1549	47
192	mz17	0.11	16.73	0.69	0.05	6.10	1.16	2.03	16.91	0.69	1568	34
193	mz21	0.11	15.42	0.72	0.04	6.74	1.04	2.19	15.55	0.72	1535	35
194	mz21	0.27	14.18	0.75	0.07	6.58	0.98	2.27	14.42	0.74	1555	37
195	mz21	0.19	9.74	0.89	0.09	7.92	0.68	2.95	10.05	0.90	1547	48
197	mz21	0.58	9.73	0.89	0.15	6.44	0.70	2.89	10.28	0.91	1549	47
198	mz21	0.12	14.80	0.73	0.04	6.94	1.02	2.22	14.94	0.73	1564	36
199	mz21	0.19	16.53	0.70	0.06	6.03	1.13	2.07	16.73	0.69	1544	34
200	mz21	0.12	10.14	0.87	0.02	10.02	0.68	2.95	10.20	0.87	1520	47
237	mz7	1.42	6.62	1.08	1.13	2.29	0.71	2.83	10.70	1.10	1530	46
238	mz7	1.52	6.94	1.05	1.30	2.11	0.78	2.65	11.65	1.06	1539	44
240	mz8	1.53	7.71	1.00	1.16	2.25	0.80	2.60	11.92	1.02	1539	43

Table B.1: Continued

Spot	Grain	Y ₂ O ₃	ThO ₂	err ThO ₂	UO ₂	err UO ₂	PbO	err PbO	ThO ₂ *	err ThO ₂ *	Age	Err ap. Age
		(wt %)	(wt %)	(%)	(wt %)	(%)	(wt %)	(%)	(wt %)	(%)	(Ma)	(Ma)
<i>Grt-Crd-Opx granulite (TK73-2)</i>												
122	mz2	0.21	6.91	1.08	0.42	4.86	0.56	3.79	8.42	1.24	1520	61
124	mz3	0.51	7.49	1.02	0.26	5.71	0.57	3.43	8.42	1.11	1541	56
125	mz3	2.19	6.82	1.07	0.49	3.93	0.58	3.33	8.61	1.18	1553	55
126	mz3	2.10	6.74	1.08	0.51	3.84	0.60	3.25	8.59	1.18	1589	55
127	mz3	1.04	7.16	1.05	0.41	4.31	0.61	3.17	8.65	1.14	1621	55
128	mz3	1.09	7.20	1.04	0.51	3.77	0.60	3.24	9.03	1.13	1518	52
129	mz3	1.10	6.87	1.07	0.44	4.15	0.60	3.22	8.46	1.17	1619	55
130	mz3	1.35	6.89	1.07	0.50	3.81	0.59	3.25	8.71	1.16	1563	54
131	mz3	1.20	6.98	1.06	0.49	3.88	0.59	3.24	8.74	1.15	1557	53
133	mz5	0.33	8.00	0.99	0.62	3.32	0.68	2.93	10.25	1.06	1525	47
134	mz5	2.83	3.99	1.43	1.03	2.63	0.51	3.69	7.70	1.47	1508	60
135	mz5	2.27	4.56	1.32	0.82	2.97	0.52	3.59	7.54	1.42	1588	61
136	mz6	0.48	6.57	1.09	0.35	4.79	0.54	3.48	7.84	1.20	1564	58
137	mz6	1.30	6.89	1.07	0.51	3.79	0.58	3.30	8.72	1.16	1522	53
138	mz6	0.79	6.77	1.07	0.32	5.03	0.52	3.57	7.91	1.17	1516	57
142	mz8	0.09	11.97	0.82	0.45	3.72	0.93	2.35	13.60	0.85	1570	39
143	mz8	0.14	20.94	0.64	0.40	3.40	1.50	1.72	22.37	0.63	1534	28
144	mz8	2.05	18.55	0.67	0.12	5.05	1.26	1.94	18.99	0.67	1525	31
145	mz8	0.23	24.88	0.59	0.27	3.60	1.75	1.56	25.86	0.59	1550	26
146	mz10	0.25	8.44	0.96	0.18	6.43	0.60	3.19	9.08	1.00	1522	51
147	mz10	0.22	9.16	0.92	0.08	8.26	0.66	2.97	9.46	0.93	1602	50
148	mz10	0.16	7.95	0.99	0.11	8.19	0.56	3.35	8.33	1.02	1536	54
149	mz10	0.22	8.65	0.95	0.10	8.09	0.61	3.16	9.00	0.97	1553	51
150	mz13	0.27	6.47	1.10	0.38	4.51	0.55	3.43	7.87	1.21	1589	58
151	mz13	1.51	4.12	1.40	0.47	4.19	0.41	4.26	5.84	1.58	1618	74
152	mz13	0.76	6.52	1.10	0.36	4.74	0.56	3.40	7.82	1.21	1626	59
175	mz3	1.90	6.85	1.08	0.46	4.05	0.59	3.26	8.52	1.17	1594	55
177	mz3	1.08	6.96	1.06	0.40	4.40	0.59	3.28	8.42	1.16	1603	56
180	mz13	2.86	5.52	1.20	0.78	3.03	0.58	3.33	8.35	1.30	1588	57
182	mz13	1.48	4.65	1.32	0.33	5.22	0.41	4.29	5.87	1.51	1614	73
187	mz15	0.35	6.32	1.11	0.66	3.31	0.60	3.22	8.72	1.22	1582	54
188	mz15	1.58	8.06	0.99	0.38	4.43	0.65	3.03	9.42	1.06	1587	51
189	mz15	1.00	3.34	1.57	0.66	3.42	0.42	4.22	5.76	1.70	1670	76
190	mz15	0.13	7.38	1.03	0.23	5.88	0.54	3.48	8.22	1.10	1513	55
191	mz15	0.16	7.23	1.04	0.23	5.95	0.54	3.50	8.07	1.12	1529	56
192	mz16	1.23	5.52	1.20	0.70	3.21	0.58	3.30	8.09	1.31	1639	58
347	mz3	1.79	6.78	0.84	0.50	3.60	0.58	2.52	8.58	1.01	1547	42
348	mz3	1.82	6.74	0.84	0.49	3.65	0.57	2.57	8.52	1.01	1532	42
349	mz3	1.75	6.70	0.84	0.50	3.60	0.58	2.52	8.51	1.01	1564	42
350	mz3	1.82	6.78	0.84	0.52	3.51	0.58	2.53	8.67	1.01	1533	42
351	mz3	0.88	7.12	0.82	0.40	4.07	0.59	2.50	8.59	0.97	1566	42
352	mz3	0.89	7.04	0.82	0.40	4.07	0.58	2.54	8.50	0.98	1559	42
353	mz3	0.96	7.13	0.82	0.47	3.73	0.60	2.46	8.81	0.97	1562	41
354	mz3	0.97	7.09	0.82	0.43	3.91	0.61	2.44	8.67	0.98	1605	42
356	mz4	2.16	7.46	0.80	0.72	2.92	0.69	2.24	10.06	0.96	1563	38

Table B.1: Continued

Spot	Grain	Y ₂ O ₃	ThO ₂	err ThO ₂	UO ₂	err UO ₂	PbO	err PbO	ThO ₂ *	err ThO ₂ *	Age	Err ap. Age
		(wt %)	(wt %)	(%)	(wt %)	(%)	(wt %)	(%)	(wt %)	(%)	(Ma)	(Ma)
<i>Grt-Crd-Opx granulite (TK73-2)</i>												
357	mz5	0.28	7.82	0.78	0.56	3.31	0.66	2.28	9.86	0.92	1534	38
359	mz13	1.26	3.94	1.10	0.44	4.10	0.39	3.42	5.56	1.42	1594	59
360	mz13	0.31	6.55	0.85	0.19	6.37	0.48	2.89	7.22	0.97	1533	47
361	mz13	1.45	3.99	1.10	0.35	4.85	0.37	3.54	5.25	1.43	1617	62
362	mz13	0.89	4.52	1.03	0.36	4.61	0.42	3.20	5.85	1.31	1657	57
363	mz13	2.67	6.13	0.88	0.64	3.16	0.59	2.49	8.47	1.08	1589	43
364	mz15	0.61	2.50	1.42	0.90	2.70	0.38	3.50	5.75	1.65	1520	59
365	mz15	1.42	4.41	1.04	0.63	3.27	0.47	2.93	6.70	1.31	1616	52
366	mz15	1.71	5.24	0.95	0.61	3.30	0.50	2.83	7.43	1.18	1540	47
367	mz15	0.45	2.59	1.39	0.66	3.24	0.37	3.54	5.03	1.73	1680	66
368	mz16	1.69	6.84	0.83	0.71	2.95	0.63	2.37	9.41	1.01	1544	40
369	mz16	1.43	6.47	0.86	0.68	3.04	0.62	2.40	8.96	1.05	1593	42
<i>Charnockite (TK39-4)</i>												
90	m1	0.21	11.71	0.83	0.06	7.99	0.80	2.21	11.92	0.83	1537	36
91	m1	0.23	11.99	0.82	0.04	8.42	0.73	2.35	12.12	0.81	1379	34
92	m1	0.25	11.47	0.83	0.07	7.69	0.79	2.20	11.72	0.83	1545	36
93	m2	0.45	6.64	1.09	0.14	8.12	0.47	3.26	7.13	1.16	1496	52
94	m2	0.25	21.95	0.62	0.17	4.21	1.50	1.44	22.56	0.62	1529	24
95	m2	0.23	22.04	0.62	0.14	4.38	1.53	1.42	22.54	0.62	1558	24
96	m2	0.17	11.94	0.81	0.07	7.42	0.81	2.13	12.19	0.81	1526	35
97	m2	0.19	14.07	0.75	0.06	6.78	0.96	1.90	14.28	0.75	1542	31
98	m2	0.13	13.06	0.78	0.04	7.69	0.87	2.04	13.19	0.78	1506	33
99	m2	0.19	14.27	0.75	0.01	7.75	0.95	1.93	14.32	0.75	1516	31
102	m3	0.33	19.94	0.65	0.36	3.48	1.26	1.60	21.22	0.64	1364	24
106	m3	0.33	20.87	0.64	0.21	4.08	1.46	1.46	21.62	0.63	1545	25
107	m3	0.15	15.47	0.72	0.01	7.35	1.05	1.79	15.50	0.72	1557	30
108	m4	0.28	14.49	0.74	0.14	5.54	0.99	1.88	14.99	0.74	1509	30
109	m4	0.23	12.59	0.79	0.05	7.58	0.87	2.03	12.77	0.79	1564	34
110	m4	0.24	12.74	0.79	0.11	6.42	0.89	2.01	13.13	0.79	1552	33
111	m4	0.26	9.47	0.91	0.17	6.26	0.68	2.42	10.10	0.94	1552	40
112	m4	0.21	13.34	0.77	0.06	7.08	0.94	1.93	13.56	0.77	1592	33
113	m4	0.33	9.82	0.89	0.20	5.74	0.64	2.53	10.55	0.92	1405	38
114	m4	0.29	14.63	0.74	0.14	5.51	0.98	1.88	15.13	0.74	1490	30
115	m6	0.39	17.63	0.68	0.21	4.42	1.27	1.59	18.40	0.68	1581	27
116	m6	0.24	17.27	0.69	0.24	4.24	1.24	1.62	18.15	0.69	1569	28
117	m6	0.36	17.55	0.69	0.15	4.92	1.23	1.63	18.09	0.68	1562	28
118	m6	0.09	11.80	0.82	0.03	8.61	0.81	2.17	11.91	0.82	1549	36
119	m6	0.13	11.72	0.82	0.04	8.39	0.80	2.17	11.85	0.82	1547	36
120	m6	0.26	14.13	0.75	0.06	6.90	0.97	1.90	14.33	0.75	1551	32
121	m7	0.34	6.18	1.13	0.17	7.43	0.41	3.53	6.78	1.22	1401	52
122	m7	0.30	6.76	1.08	0.21	6.39	0.46	3.26	7.50	1.16	1401	48
126	m10	0.30	25.16	0.59	0.37	3.18	1.59	1.39	26.47	0.58	1385	21
127	m10	0.14	26.28	0.58	0.12	4.03	1.76	1.31	26.73	0.58	1509	22
129	m10	0.21	15.46	0.73	0.01	7.50	0.89	2.03	15.48	0.73	1321	28
131	m11	0.13	24.74	0.60	0.14	4.12	1.68	1.35	25.24	0.59	1529	23

Table B.1: Continued

Spot	Grain	Y ₂ O ₃	ThO ₂	err ThO ₂	UO ₂	err UO ₂	PbO	err PbO	ThO ₂ *	err ThO ₂ *	Age	Err ap. Age
		(wt %)	(wt %)	(%)	(wt %)	(%)	(wt %)	(%)	(wt %)	(%)	(Ma)	(Ma)
<i>Charnockite (TK39-4)</i>												
132	m11	0.12	25.20	0.59	0.20	3.79	1.52	1.43	25.90	0.59	1354	21
133	m11	0.24	14.44	0.75	0.16	5.45	0.92	1.97	15.00	0.75	1417	30
135	m11	0.29	16.50	0.71	0.14	5.15	0.98	1.90	17.02	0.70	1327	27
136	m11	0.26	14.32	0.75	0.06	6.75	0.95	1.94	14.54	0.75	1497	31
137	m12	0.27	18.18	0.68	0.19	4.53	1.24	1.63	18.86	0.67	1504	27
138	m12	0.31	27.70	0.57	0.52	2.75	1.96	1.22	29.57	0.56	1522	20
139	m12	0.10	24.51	0.60	0.21	3.77	1.71	1.33	25.27	0.59	1555	23
140	m12	0.22	27.61	0.57	0.30	3.27	1.95	1.23	28.68	0.56	1560	21
141	m12	0.15	14.89	0.74	0.03	7.08	1.03	1.82	15.00	0.73	1570	31
142	m12	0.21	28.19	0.56	0.32	3.17	1.94	1.23	29.35	0.56	1513	20
191	m1	0.25	11.82	0.49	0.06	6.91	0.80	1.65	12.02	0.49	1531	26
193	m4	0.33	10.09	0.51	0.21	4.90	0.66	1.90	10.82	0.58	1395	28
194	m4	0.33	9.80	0.52	0.21	4.91	0.63	1.97	10.55	0.60	1365	28
195	m4	0.28	9.93	0.52	0.19	5.15	0.60	2.02	10.60	0.58	1304	27
196	m4	0.24	9.16	0.53	0.15	5.87	0.59	2.03	9.70	0.60	1404	30
197	m7	0.30	6.92	0.60	0.18	5.99	0.49	2.33	7.56	0.75	1490	37
198	m7	0.32	6.59	0.61	0.18	6.05	0.41	2.69	7.23	0.77	1308	37
199	m7	0.32	6.72	0.60	0.21	5.56	0.46	2.46	7.45	0.77	1408	36
203	m11	0.27	15.66	0.44	0.15	4.49	0.93	1.49	16.21	0.46	1319	21
204	m11	0.24	15.20	0.45	0.19	4.23	1.04	1.38	15.89	0.47	1504	22
205	m11	0.24	14.53	0.45	0.19	4.35	0.90	1.52	15.20	0.47	1365	22
207	m11	0.28	18.05	0.43	0.19	3.95	1.16	1.29	18.72	0.44	1420	19
209	m16	0.08	4.82	0.69	0.07	11.09	0.34	3.06	5.06	0.85	1557	49
210	m16	0.08	17.98	0.43	0.15	4.22	1.24	1.24	18.52	0.43	1536	20
211	m16	0.10	16.86	0.44	0.12	4.56	1.18	1.28	17.31	0.44	1561	21
212	m16	0.11	13.49	0.47	0.06	6.14	0.93	1.49	13.71	0.47	1555	24
213	m16	0.13	14.49	0.46	0.02	6.53	0.98	1.44	14.58	0.45	1544	23
214	m16	0.11	14.81	0.45	0.02	6.55	1.01	1.41	14.87	0.45	1558	23
216	m16	0.04	15.27	0.45	0.05	5.85	1.05	1.38	15.44	0.45	1558	23
217	m16	0.14	14.30	0.46	0.04	6.23	0.96	1.46	14.45	0.46	1519	23
218	m17	0.14	26.02	0.39	0.00	4.26	1.76	1.01	26.02	0.39	1547	17
219	m17	0.23	31.45	0.38	0.35	2.59	2.26	0.89	32.73	0.38	1581	15
220	m17	0.04	27.93	0.38	0.08	3.57	1.89	0.97	28.22	0.38	1535	16
252	m4	0.28	10.01	0.52	0.19	5.19	0.62	1.97	10.67	0.58	1341	28
253	m4	0.29	9.93	0.52	0.18	5.25	0.60	2.02	10.58	0.58	1316	28
254	m4	0.30	10.10	0.52	0.20	4.97	0.63	1.95	10.81	0.58	1342	27
257	m4	0.20	11.07	0.50	0.18	5.01	0.78	1.67	11.72	0.55	1534	27
272	m11	0.15	16.47	0.44	0.04	5.69	1.08	1.36	16.60	0.44	1489	21
<i>Enderbite (TK4B2)</i>												
202	mz1	3.34	10.09	0.92	0.18	7.92	0.72	3.43	10.75	0.99	1540	55
203	mz1	1.68	10.16	0.90	0.19	6.81	0.33	5.90	10.80	0.94	723	43
204	mz1	2.96	10.12	0.89	0.15	7.09	0.73	2.95	10.66	0.92	1571	49
205	mz1	3.20	9.93	0.90	0.15	6.79	0.69	3.01	10.49	0.92	1518	48
206	mz1	3.47	9.97	0.90	0.20	5.94	0.70	2.93	10.68	0.93	1511	46
207	mz2	2.11	10.28	0.88	0.17	6.22	0.75	2.77	10.88	0.90	1585	46

Table B.1: Continued

Spot	Grain	Y ₂ O ₃	ThO ₂	err ThO ₂	UO ₂	err UO ₂	PbO	err PbO	ThO ₂ *	err ThO ₂ *	Age	Err ap. Age
		(wt %)	(wt %)	(%)	(wt %)	(%)	(wt %)	(%)	(wt %)	(%)	(Ma)	(Ma)
<i>Enderbite (TK4B2)</i>												
208	mz2	2.07	10.73	0.86	0.18	5.89	0.74	2.80	11.37	0.88	1489	44
209	mz2	3.18	8.68	0.96	0.20	6.05	0.61	3.20	9.41	1.00	1497	50
210	mz2	3.31	9.62	0.91	0.21	5.66	0.64	3.07	10.38	0.94	1420	46
217	mz4	2.30	9.75	0.90	0.22	5.60	0.33	5.21	10.47	0.93	726	38
218	mz7	1.74	10.26	0.88	0.13	6.81	0.72	2.82	10.72	0.89	1546	46
219	mz7	1.77	10.33	0.88	0.14	6.66	0.70	2.91	10.81	0.89	1476	45
220	mz7	1.59	10.36	0.87	0.15	6.42	0.67	2.98	10.89	0.89	1423	44
224	mz9	1.53	10.99	0.85	0.10	7.23	0.72	2.82	11.34	0.85	1460	43
226	mz9	1.05	12.47	0.80	0.38	4.00	0.84	2.52	13.83	0.82	1402	37
228	mz9	2.98	9.98	0.89	0.16	6.37	0.66	3.04	10.55	0.91	1427	45
230	mz10	1.11	11.00	0.85	0.16	6.07	0.72	2.82	11.58	0.86	1435	42
231	mz10	1.40	9.77	0.90	0.19	5.94	0.66	3.02	10.44	0.92	1450	46
232	mz10	1.56	9.65	0.90	0.20	5.88	0.68	2.95	10.35	0.93	1496	46
233	mz10	0.31	9.13	0.93	0.13	7.09	0.32	5.30	9.59	0.94	768	41
234	mz12	2.65	10.46	0.87	0.19	5.74	0.26	6.34	11.10	0.89	542	35
235	mz12	3.36	10.30	0.88	0.19	5.75	0.74	2.79	11.00	0.90	1546	45
236	mz12	3.31	10.46	0.87	0.18	5.91	0.74	2.78	11.11	0.89	1533	45
237	mz12	2.37	10.20	0.88	0.14	6.69	0.73	2.79	10.69	0.90	1573	46
238	mz13	1.36	8.82	0.95	0.16	6.78	0.59	3.27	9.38	0.98	1448	49
240	mz13	2.30	9.51	0.91	0.17	6.24	0.63	3.11	10.13	0.94	1438	47
241	mz13	1.23	10.39	0.87	0.19	5.77	0.35	4.92	11.04	0.89	737	37
242	mz13	0.44	9.95	0.89	0.18	6.01	0.34	5.04	10.56	0.91	750	38
244	mz13	1.34	8.91	0.94	0.16	6.67	0.59	3.25	9.48	0.97	1438	49
245	mz17	1.78	9.12	0.93	0.18	6.22	0.65	3.05	9.78	0.96	1520	49
246	mz17	1.35	9.88	0.89	0.19	5.95	0.34	5.05	10.51	0.91	754	39
247	mz17	1.53	9.07	0.93	0.18	6.22	0.66	3.01	9.73	0.96	1552	49
249	mz17	1.31	9.48	0.91	0.18	6.23	0.67	3.00	10.11	0.94	1513	48
250	mz17	1.36	9.89	0.89	0.13	6.83	0.65	3.03	10.37	0.91	1443	46
251	mz21	2.94	8.04	0.99	0.17	6.70	0.53	3.55	8.66	1.04	1408	52
252	mz21	0.74	10.67	0.86	0.13	6.71	0.75	2.74	11.14	0.87	1552	45
253	mz21	3.12	9.62	0.91	0.21	5.77	0.71	2.87	10.37	0.94	1568	47
256	mz21	1.99	9.71	0.90	0.23	5.42	0.68	2.96	10.54	0.94	1481	46
257	mz25	1.74	18.32	0.67	0.26	4.13	0.41	4.34	19.18	0.67	501	22
258	mz25	1.65	18.01	0.68	0.23	4.35	0.41	4.35	18.77	0.68	511	22
259	mz25	1.61	14.08	0.76	0.19	5.16	0.33	5.19	14.71	0.76	524	28
261	mz25	3.57	9.37	0.92	0.23	5.44	0.67	2.98	10.21	0.96	1512	47
262	mz25	3.10	9.24	0.93	0.19	6.11	0.65	3.06	9.92	0.96	1504	48
264	mz28	3.41	9.87	0.90	0.21	5.72	0.65	3.04	10.60	0.92	1417	45
267	mz28	2.53	10.93	0.85	0.19	5.73	0.73	2.81	11.60	0.87	1448	43
295	mz1	1.24	9.97	0.73	0.19	7.37	0.34	4.96	10.59	0.82	740	37
296	mz1	2.09	9.55	0.74	0.18	6.69	0.31	4.77	10.17	0.80	718	35
297	mz1	1.94	10.27	0.71	0.20	5.78	0.35	4.07	10.96	0.76	747	31
298	mz1	1.58	10.64	0.69	0.18	5.89	0.35	3.95	11.24	0.73	731	29
299	mz1	1.74	10.44	0.70	0.20	5.56	0.36	3.81	11.10	0.74	754	29
300	mz1	1.93	10.56	0.70	0.22	5.23	0.37	3.70	11.29	0.73	758	29

Table B.1: Continued

Spot	Grain	Y ₂ O ₃	ThO ₂	err ThO ₂	UO ₂	err UO ₂	PbO	err PbO	ThO ₂ *	err ThO ₂ *	Age	Err ap. Age
		(wt %)	(wt %)	(%)	(wt %)	(%)	(wt %)	(%)	(wt %)	(%)	(Ma)	(Ma)
<i>Enderbite (TK4B2)</i>												
303	mz1	1.96	9.82	0.72	0.17	5.92	0.23	5.40	10.38	0.75	516	28
304	mz1	1.81	10.19	0.71	0.20	5.42	0.34	3.91	10.87	0.74	730	29
305	mz1	1.40	9.82	0.72	0.20	5.51	0.33	3.95	10.49	0.76	738	30
306	mz1	2.68	10.13	0.71	0.17	5.87	0.70	2.26	10.73	0.75	1491	35
307	mz1	2.69	10.04	0.71	0.14	6.35	0.74	2.16	10.54	0.74	1599	37
308	mz1	2.83	9.85	0.72	0.20	5.46	0.70	2.24	10.57	0.77	1527	36
312	mz10	0.28	9.36	0.73	0.12	6.87	0.29	4.37	9.77	0.76	702	31
313	mz12	2.29	10.45	0.70	0.18	5.61	0.24	5.14	11.05	0.73	517	27
314	mz12	2.30	10.72	0.69	0.19	5.40	0.25	5.10	11.37	0.72	511	26
317	mz13	0.55	10.10	0.71	0.20	5.46	0.35	3.83	10.77	0.74	754	29
318	mz16	3.26	10.13	0.71	0.21	5.33	0.76	2.12	10.89	0.76	1594	36
319	mz16	2.59	9.90	0.71	0.17	5.89	0.70	2.25	10.51	0.76	1525	36
323	mz16	3.17	10.16	0.71	0.20	5.42	0.73	2.18	10.88	0.75	1542	36
325	mz16	2.37	9.85	0.72	0.20	5.52	0.73	2.17	10.57	0.77	1586	36
332	mz25	1.51	19.50	0.54	0.25	3.81	0.45	3.05	20.33	0.54	525	16
333	mz25	1.46	19.20	0.54	0.23	3.97	0.45	3.10	19.96	0.54	524	16
335	mz25	1.39	19.36	0.54	0.26	3.80	0.43	3.20	20.22	0.54	497	16
336	mz25	1.08	18.12	0.55	0.21	4.17	0.40	3.41	18.81	0.55	497	17
337	mz25	1.37	28.65	0.47	0.31	3.11	0.63	2.39	29.66	0.47	501	12
338	mz25	0.96	18.59	0.54	0.25	3.90	0.42	3.28	19.42	0.55	504	17
339	mz33	2.72	8.21	0.77	0.20	5.73	0.57	2.57	8.93	0.85	1463	40
340	mz33	3.01	9.40	0.72	0.19	5.61	0.65	2.34	10.09	0.77	1477	36
341	mz33	1.42	10.22	0.70	0.14	6.24	0.23	5.24	10.67	0.72	511	27
343	mz33	1.02	18.94	0.54	0.34	3.48	0.43	3.17	20.06	0.55	508	16
344	mz33	1.25	21.34	0.52	0.35	3.31	0.48	2.93	22.51	0.52	500	15
345	mz33	1.23	22.86	0.50	0.38	3.16	0.52	2.75	24.13	0.51	504	14
346	mz33	1.52	10.64	0.68	0.15	5.90	0.24	5.08	11.13	0.70	509	26
398	mz1	1.53	10.94	0.67	0.23	4.93	0.37	3.56	11.70	0.71	736	27
400	mz1	2.12	9.79	0.71	0.21	5.26	0.32	4.02	10.50	0.75	713	29
401	mz1	1.75	10.26	0.69	0.18	5.55	0.24	5.14	10.86	0.72	513	27
402	mz1	1.92	9.92	0.70	0.19	5.54	0.33	3.87	10.55	0.74	740	29
403	mz1	0.37	10.00	0.70	0.55	3.25	0.83	1.96	12.01	0.80	1576	33
417	mz16	2.38	9.68	0.71	0.19	5.60	0.24	5.12	10.30	0.75	543	28
420	mz20	0.72	13.80	0.61	0.19	4.81	0.45	3.04	14.45	0.62	733	23
421	mz20	0.96	12.34	0.64	0.16	5.36	0.38	3.49	12.87	0.65	691	25
<i>St-Ms-Bt schist (TK64-3, Vinjamuru domain)</i>												
133	mz1	1.14	3.85	0.80	0.27	6.19	0.35	3.51	4.85	1.43	1640	62
134	mz1	1.40	11.99	0.49	0.30	4.20	0.89	1.61	13.07	0.57	1566	27
135	mz1	1.37	3.78	0.79	0.29	5.29	0.35	3.18	4.85	1.32	1633	56
137	mz5	1.22	8.13	0.56	0.25	4.85	0.61	2.02	9.02	0.70	1538	33
139	mz5	1.56	6.18	0.62	0.52	3.25	0.54	2.18	8.05	0.89	1538	36
140	mz5	1.38	5.49	0.66	0.41	3.82	0.48	2.38	6.98	0.97	1569	40
141	mz8	1.52	6.00	0.63	0.50	3.34	0.53	2.19	7.80	0.91	1565	37
142	mz8	1.32	10.45	0.51	0.21	4.76	0.79	1.66	11.22	0.58	1613	28
143	mz8	1.11	4.94	0.69	0.23	5.70	0.41	2.70	5.77	1.01	1610	46

Table B.1: Continued

Spot	Grain	Y ₂ O ₃	ThO ₂	err ThO ₂	UO ₂	err UO ₂	PbO	err PbO	ThO ₂ *	err ThO ₂ *	Age	Err ap. Age
		(wt %)	(wt %)	(%)	(wt %)	(%)	(wt %)	(%)	(wt %)	(%)	(Ma)	(Ma)
<i>St-Ms-Bt schist (TK64-3, Vinjamuru domain)</i>												
146	mz11	1.14	10.80	0.50	0.16	5.31	0.80	1.65	11.38	0.55	1602	28
149	mz13	1.08	2.59	0.96	0.28	5.52	0.26	3.93	3.62	1.71	1631	70
150	mz13	1.13	3.85	0.78	0.26	5.48	0.33	3.20	4.80	1.25	1567	54
151	mz13	1.48	4.58	0.71	0.67	2.84	0.47	2.40	7.00	1.09	1552	41
152	mz13	1.51	5.47	0.66	0.49	3.43	0.48	2.37	7.22	0.97	1530	39
154	mz14	1.16	11.80	0.49	0.17	4.99	0.84	1.59	12.41	0.52	1555	26
155	mz14	1.21	11.85	0.49	0.11	5.69	0.86	1.57	12.26	0.51	1598	26
156	mz14	1.17	9.88	0.52	0.15	5.61	0.71	1.78	10.43	0.57	1562	29
157	mz14	1.52	5.90	0.64	0.42	3.70	0.50	2.30	7.44	0.92	1541	38
159	mz15	1.13	12.78	0.47	0.24	4.23	0.89	1.52	13.63	0.52	1505	24
163	mz17	1.50	5.08	0.68	0.61	2.96	0.50	2.30	7.30	1.02	1569	40
164	mz17	1.20	7.51	0.58	0.23	5.15	0.59	2.04	8.33	0.73	1618	35
165	mz17	1.30	8.68	0.55	0.24	4.77	0.67	1.87	9.56	0.66	1597	32
166	mz17	1.49	4.87	0.70	0.63	2.92	0.50	2.30	7.19	1.05	1605	41
167	mz19	1.55	6.41	0.62	0.46	3.50	0.55	2.17	8.07	0.87	1550	36
169	mz19	1.44	9.89	0.52	0.27	4.35	0.75	1.74	10.87	0.61	1570	29
170	mz19	1.53	6.18	0.63	0.49	3.39	0.54	2.20	7.96	0.90	1547	37
171	mz20	1.49	5.89	0.64	0.44	3.64	0.51	2.28	7.48	0.92	1559	38
172	mz20	1.48	6.15	0.63	0.45	3.58	0.55	2.15	7.79	0.90	1617	38
175	mz22	1.13	6.14	0.63	0.13	7.37	0.45	2.52	6.61	0.79	1543	41
178	mz25	1.61	5.12	0.68	0.73	2.65	0.53	2.20	7.78	1.01	1566	38
179	mz25	1.50	4.75	0.70	0.48	3.53	0.44	2.56	6.47	1.07	1547	43
180	mz25	1.43	10.44	0.51	0.29	4.07	0.78	1.68	11.51	0.60	1557	28
182	mz32	1.09	16.20	0.44	0.17	4.29	1.15	1.30	16.80	0.45	1563	21
184	mz32	1.58	6.18	0.62	0.71	2.67	0.59	2.03	8.74	0.90	1552	34
185	mz32	1.40	5.56	0.65	0.46	3.54	0.49	2.33	7.23	0.96	1559	39
235	mz1	1.14	2.81	0.92	0.23	6.34	0.27	3.84	3.65	1.63	1664	69
242	mz17	1.17	8.47	0.55	0.23	4.97	0.63	1.95	9.29	0.66	1547	32
246	mz32	1.35	5.60	0.65	0.39	3.93	0.47	2.42	7.01	0.95	1524	40
247	mz32	1.08	4.27	0.74	0.25	5.48	0.37	2.88	5.20	1.15	1633	51
249	mz32	1.18	3.40	0.83	0.24	5.91	0.30	3.40	4.27	1.38	1627	60

Appendix C

LA-ICP-MS zircon U-Pb data for the meta-igneous rocks of the Ongole domain and the adjoining Vinjamuru domain

Zircon from five charnoenderbites from the Ongole domain and one orthogneiss from the adjoining Vinjamuru domain were analyzed. The cathodoluminescence (CL) images of selected zircon grains from the six samples are illustrated in Chapter 4 (Fig. 4.7; pages 146-147). The U-Pb concordia diagrams of all the six samples are included in Chapter 4 (Fig. 4.8; pages 150-151). The isotopic ratios and ages of individual spots on zircon grains from the six meta-igneous samples are listed here in Table C.1.

Table C.1: LA-ICP-MS zircon U-Pb dating data for the meta-igneous rocks of the Ongole domain and the adjoining Vinjamuru domain

Spot	Grain	Texture	U conc. (ppm)	Radiogenic ratios				Ages (Ma)				Con.						
				$\frac{^{206}\text{Pb}}{^{204}\text{Pb}}$	$\pm 2\sigma$	$\frac{^{207}\text{Pb}}{^{235}\text{U}}$	$\pm 2\sigma$	$\frac{^{207}\text{Pb}}{^{206}\text{Pb}}$	$\pm 2\sigma$	$\frac{^{206}\text{Pb}}{^{238}\text{U}}$	$\pm 2\sigma$		$\frac{^{207}\text{Pb}}{^{235}\text{U}}$	$\pm 2\sigma$	$\frac{^{207}\text{Pb}}{^{206}\text{Pb}}$	$\pm 2\sigma$		
Enderbite TK4B2																		
1	TK4B2-1-1	mag. core	1748	274429	0.3121	0.0097	4.6920	0.2069	0.1090	0.0034	0.70	1751	48	1766	37	1784	57	98.2
2	TK4B2-2-1	mag. core	496	8805	0.3047	0.0127	4.4417	0.2688	0.1057	0.0046	0.69	1714	63	1720	50	1727	80	99.3
3	TK4B2-6-1	mag. core	2255	72578	0.3041	0.0114	4.4007	0.2195	0.1049	0.0035	0.75	1712	56	1712	41	1713	61	99.9
4	TK4B2-6-2	mag. core	2787	72012	0.3029	0.0089	4.3585	0.2086	0.1043	0.0039	0.62	1706	44	1705	40	1703	70	100.2
5	TK4B2-9-1	mag. core	1498	166238	0.3024	0.0099	4.3853	0.2077	0.1052	0.0036	0.69	1703	49	1710	39	1717	63	99.2
6	TK4B2-10-1	mag. core	953	49777	0.3040	0.0148	4.3853	0.2467	0.1046	0.0030	0.86	1711	73	1710	47	1708	52	100.2
7	TK4B2-10-2	mag. core	727	125906	0.3088	0.0110	4.5573	0.1998	0.1070	0.0027	0.81	1735	54	1742	37	1750	47	99.2
8	TK4B2-11-1	mag. core	568	19501	0.3019	0.0129	4.4148	0.2194	0.1060	0.0027	0.86	1701	64	1715	41	1733	46	98.2
9	TK4B2-12-1	mag. core	937	b.d.1	0.2998	0.0108	4.3339	0.2169	0.1048	0.0036	0.72	1690	54	1700	41	1712	64	98.8
10	TK4B2-12-2	mag. core	1971	b.d.1	0.3097	0.0120	4.5134	0.2108	0.1057	0.0028	0.83	1739	59	1733	39	1726	48	100.7
11	TK4B2-1-7	meta. ovrgrth.	600	206353	0.2843	0.0116	3.8996	0.2023	0.0995	0.0032	0.78	1613	58	1614	42	1614	60	99.9
12	TK4B2-1-8	meta. ovrgrth.	677	146903	0.2973	0.0085	4.1773	0.1750	0.1019	0.0031	0.68	1678	42	1670	34	1659	57	101.1
13	TK4B2-2-7	meta. ovrgrth.	583	b.d.1	0.2806	0.0082	3.8470	0.1712	0.0994	0.0033	0.66	1594	41	1603	36	1614	62	98.8
14	TK4B2-2-4	meta. ovrgrth.	262	b.d.1	0.2870	0.0108	3.8629	0.2051	0.1002	0.0036	0.72	1626	54	1627	42	1627	66	100.0
15	TK4B2-4-5	meta. ovrgrth.	271	14933	0.2903	0.0058	4.0461	0.1405	0.1011	0.0029	0.58	1643	29	1644	28	1644	53	99.9
16	TK4B2-6-7	meta. ovrgrth.	673	20988	0.2685	0.0102	3.5849	0.1921	0.0968	0.0037	0.71	1533	52	1546	43	1564	71	98.1
17	TK4B2-6-8	meta. ovrgrth.	1136	101553	0.2844	0.0101	3.9616	0.2075	0.1010	0.0039	0.68	1613	51	1626	42	1643	71	98.2
18	TK4B2-7-8	meta. ovrgrth.	652	154113	0.2887	0.0087	4.0445	0.1791	0.1016	0.0033	0.68	1635	44	1643	36	1654	60	98.8
19	TK4B2-10-7	meta. ovrgrth.	597	86957	0.2838	0.0090	3.9138	0.1704	0.1000	0.0030	0.73	1611	45	1617	35	1624	56	99.2
20	TK4B2-10-8	meta. ovrgrth.	557	b.d.1	0.2814	0.0106	3.8476	0.2068	0.0992	0.0038	0.70	1598	54	1603	43	1609	71	99.3
21	TK4B2-10-4	meta. ovrgrth.	332	176810	0.2819	0.0082	3.9470	0.1529	0.1015	0.0026	0.75	1601	41	1623	31	1652	48	97.9
22	TK4B2-11-7	meta. ovrgrth.	662	b.d.1	0.2780	0.0093	3.8114	0.1626	0.0994	0.0026	0.79	1581	47	1595	34	1613	49	98.0
23	TK4B2-12-7	meta. ovrgrth.	516	175069	0.2918	0.0106	4.0809	0.1805	0.1014	0.0025	0.82	1650	53	1651	36	1651	47	100.0
24	TK4B2-12-8	meta. ovrgrth.	502	40534	0.2866	0.0128	3.9794	0.2052	0.1007	0.0026	0.86	1625	64	1630	42	1637	48	99.3
25	TK4B2-13-7	meta. ovrgrth.	535	473126	0.2848	0.0074	3.9391	0.1516	0.1003	0.0029	0.67	1615	37	1622	31	1630	53	99.1
26	TK4B2-13-8	meta. ovrgrth.	583	17934	0.2856	0.0085	3.9421	0.1579	0.1001	0.0027	0.74	1619	43	1622	32	1626	50	99.6
27	TK4B2-4-1	mag. core	2297	b.d.1	0.3102	0.0165	4.7564	0.3081	0.1112	0.0041	0.82	1742	81	1777	54	1819	67	95.7
28	TK4B2-4-4	meta. ovrgrth.	559	b.d.1	0.2877	0.0144	4.1031	0.2959	0.1034	0.0054	0.69	1630	72	1655	59	1686	96	96.7
29	TK4B2-7-1	mag. core	85	1758	0.3267	0.0114	5.2402	0.2857	0.1163	0.0049	0.64	1823	55	1859	47	1900	75	95.9
30	TK4B2-14-7	meta. ovrgrth.	1560	91679	0.2891	0.0106	4.1251	0.1807	0.1035	0.0025	0.84	1637	53	1659	36	1688	44	97.0

Con., degree of concordance; mag. core, magmatic core; meta. ovrgrth., metamorphic overgrowth; b.d.1, below detection limit

Table C.1: Continued

Spot	Grain	Texture	U conc. (ppm)	Radiogenic ratios				Ages (Ma)				Con.						
				$\frac{^{206}\text{Pb}}{^{204}\text{Pb}}$	$\frac{^{206}\text{Pb}}{^{238}\text{U}}$	$\frac{^{207}\text{Pb}}{^{235}\text{U}}$	$\frac{^{207}\text{Pb}}{^{206}\text{Pb}}$	$\frac{^{206}\text{Pb}}{^{238}\text{U}}$	$\frac{^{207}\text{Pb}}{^{235}\text{U}}$	$\frac{^{207}\text{Pb}}{^{206}\text{Pb}}$	$\pm 2\sigma$							
<i>Enderbite TK21</i>																		
1	TK21-1-1	mag. core	431	47105	0.3132	0.0080	4.6463	0.1547	0.1076	0.0023	0.77	1756	39	1758	28	1759	39	99.8
2	TK21-1-2	mag. core	386	b.d.l	0.3090	0.0093	4.5630	0.1555	0.1071	0.0017	0.88	1736	46	1743	28	1751	30	99.2
3	TK21-3-1	mag. core	528	48088	0.3141	0.0109	4.6184	0.2276	0.1066	0.0037	0.70	1761	53	1753	41	1743	64	101.1
4	TK21-3-2	mag. core	643	80438	0.3093	0.0091	4.4974	0.1808	0.1055	0.0029	0.73	1737	45	1730	33	1722	50	100.9
5	TK21-4-2	mag. core	461	b.d.l	0.3096	0.0093	4.5739	0.2080	0.1071	0.0037	0.66	1739	46	1745	38	1751	63	99.3
6	TK21-4-3	mag. core	874	6936	0.3081	0.0131	4.5739	0.2434	0.1077	0.0034	0.80	1731	65	1745	44	1761	58	98.3
7	TK21-4-1	mag. core	296	22811	0.3102	0.0091	4.5868	0.1963	0.1072	0.0033	0.69	1742	45	1747	36	1753	57	99.4
8	TK21-6-1	mag. core	321	b.d.l	0.3106	0.0110	4.6651	0.2254	0.1089	0.0036	0.74	1743	54	1761	40	1782	60	97.8
9	TK21-6-2	mag. core	391	42557	0.3167	0.0156	4.6743	0.2972	0.1070	0.0043	0.78	1774	77	1763	53	1750	73	101.4
10	TK21-7-1	mag. core	818	92123	0.3186	0.0129	4.7596	0.2986	0.1084	0.0052	0.64	1783	63	1778	53	1772	88	100.6
11	TK21-7-2	mag. core	472	b.d.l	0.3036	0.0136	4.3647	0.2559	0.1043	0.0040	0.76	1709	67	1706	48	1701	70	100.5
12	TK21-10-2	mag. core	448	77619	0.3079	0.0126	4.5425	0.2840	0.1070	0.0051	0.65	1730	62	1739	52	1749	87	98.9
13	TK21-11-2	mag. core	363	191004	0.3000	0.0084	4.3296	0.1718	0.1047	0.0029	0.70	1691	42	1699	33	1709	52	99.0
14	TK21-14-1	mag. core	759	9801410	0.3198	0.0106	4.7787	0.2011	0.1084	0.0028	0.79	1789	52	1781	35	1772	48	100.9
15	TK21-1-4	meta. ovgrth.	112	11497	0.2891	0.0089	3.9981	0.2109	0.1003	0.0043	0.59	1637	45	1634	43	1629	80	100.5
16	TK21-4-7	meta. ovgrth.	566	31010	0.2837	0.0112	3.9175	0.2033	0.1002	0.0034	0.76	1610	56	1617	42	1627	63	98.9
17	TK21-6-7	meta. ovgrth.	519	37352	0.2843	0.0086	3.9154	0.1738	0.0999	0.0032	0.68	1613	43	1617	36	1622	61	99.4
18	TK21-7-7	meta. ovgrth.	705	77327	0.2773	0.0097	3.7569	0.1945	0.0983	0.0037	0.68	1578	49	1584	42	1592	71	99.1
19	TK21-9-4	meta. ovgrth.	39	7541	0.2880	0.0084	3.9658	0.1731	0.0999	0.0032	0.67	1631	42	1627	35	1622	60	100.6
20	TK21-9-5	meta. ovgrth.	55	10254	0.2797	0.0084	3.7691	0.1646	0.0977	0.0031	0.69	1590	42	1586	35	1581	59	100.5
21	TK21-10-7	meta. ovgrth.	1133	b.d.l	0.2711	0.0086	3.6158	0.1984	0.0967	0.0043	0.58	1546	44	1553	44	1562	84	99.0
22	TK21-10-8	meta. ovgrth.	1000	25782	0.2799	0.0110	3.7894	0.2068	0.0982	0.0037	0.72	1591	56	1591	44	1590	71	100.0
23	TK21-11-7	meta. ovgrth.	780	873927	0.2795	0.0068	3.7668	0.1434	0.0977	0.0029	0.64	1589	34	1586	31	1581	55	100.5
24	TK21-11-8	meta. ovgrth.	492	114814	0.2756	0.0064	3.7235	0.1331	0.0980	0.0027	0.65	1569	32	1576	29	1586	51	98.9
25	TK21-12-7	meta. ovgrth.	852	32386	0.2743	0.0104	3.6952	0.1738	0.0977	0.0027	0.81	1562	53	1570	38	1581	52	98.8
26	TK21-12-8	meta. ovgrth.	972	249969	0.2889	0.0091	4.0773	0.1807	0.1024	0.0032	0.71	1636	46	1650	36	1667	58	98.8
27	TK21-12-4	meta. ovgrth.	230	11377	0.2881	0.0143	4.0138	0.2311	0.1011	0.0029	0.86	1632	72	1637	47	1644	54	99.3
28	TK21-13-4	meta. ovgrth.	181	213863	0.2881	0.0095	3.9829	0.1621	0.1003	0.0024	0.81	1632	48	1631	33	1629	44	100.1
29	TK21-13-5	meta. ovgrth.	77	58392	0.2772	0.0073	3.8158	0.1400	0.0998	0.0026	0.72	1577	37	1596	30	1621	48	97.6
30	TK21-3-7	meta. ovgrth.	645	29283	0.2393	0.0045	3.2679	0.1075	0.0991	0.0027	0.57	1383	23	1473	26	1607	50	86.1
31	TK21-7-4	mag. core	45	10089	0.3239	0.0434	4.7534	0.6733	0.1065	0.0048	0.95	1808	212	1777	119	1740	84	104.0
32	TK21-10-1	mag. core	2799	51641	0.2975	0.0177	4.3257	0.2989	0.1055	0.0037	0.86	1679	88	1698	57	1723	64	97.4
33	TK21-14-2	mag. core	478	11516	0.3100	0.0163	4.7321	0.2950	0.1107	0.0037	0.84	1741	80	1773	52	1811	61	96.1
34	TK21-16-4	meta. ovgrth.	773	19865	0.2830	0.0118	3.9563	0.2265	0.1014	0.0040	0.73	1606	59	1625	46	1650	73	97.4
35	TK21-15-4	mag. core	1444	130658	0.3300	0.0153	4.9515	0.3418	0.1088	0.0056	0.67	1838	74	1811	58	1780	93	103.3

Con., degree of concordance; mag. core, magmatic core; meta. ovgrth., metamorphic overgrowth; b.d.l, below detection limit

Table C.1: Continued

Spot	Grain	Texture	U conc. (ppm)	U conc. Radiogenic ratios				Ages (Ma)				±2σ	±2σ	Con.				
				$\frac{^{206}\text{Pb}}{^{204}\text{Pb}}$	$\frac{^{206}\text{Pb}}{^{238}\text{U}}$	$\frac{^{207}\text{Pb}}{^{235}\text{U}}$	$\frac{^{207}\text{Pb}}{^{206}\text{Pb}}$	$\frac{^{206}\text{Pb}}{^{238}\text{U}}$	$\frac{^{207}\text{Pb}}{^{235}\text{U}}$	$\frac{^{207}\text{Pb}}{^{206}\text{Pb}}$	$\frac{^{207}\text{Pb}}{^{206}\text{Pb}}$							
Charnockite TK28-1																		
1	TK28-1-1-1	mag. core	1854	8010	0.3161	0.0133	4.7597	0.2345	0.1092	0.0028	0.85	1771	65	1778	41	1786	47	99.1
2	TK28-1-1-2	mag. core	2582	574376	0.3020	0.0169	4.3081	0.2926	0.1034	0.0040	0.82	1701	84	1695	56	1687	71	100.9
3	TK28-1-2-2	mag. core	604	9600	0.2902	0.0105	4.0726	0.2097	0.1018	0.0037	0.71	1643	53	1649	42	1657	68	99.1
4	TK28-1-2-1	mag. core	622	5006	0.3071	0.0156	4.4369	0.2593	0.1048	0.0030	0.87	1726	77	1719	48	1711	53	100.9
5	TK28-1-4-1	mag. core	2962	216149	0.3040	0.0106	4.4666	0.1836	0.1066	0.0023	0.85	1711	53	1725	34	1741	40	98.3
6	TK28-1-5-1	mag. core	2969	87824	0.2968	0.0124	4.2346	0.1982	0.1035	0.0022	0.89	1675	62	1681	38	1688	39	99.3
7	TK28-1-5-2	mag. core	2728	25908	0.3060	0.0066	4.4493	0.1205	0.1054	0.0017	0.79	1721	32	1722	22	1722	30	99.9
8	TK28-1-6-1	mag. core	861	2972	0.3162	0.0127	4.7749	0.2174	0.1095	0.0024	0.88	1771	62	1781	38	1791	39	98.9
9	TK28-1-6-2	mag. core	1152	b.d.l	0.3062	0.0123	4.5351	0.2189	0.1074	0.0029	0.83	1722	61	1737	40	1756	49	98.1
10	TK28-1-6-3	mag. core	1935	24313	0.3170	0.0098	4.7192	0.1667	0.1080	0.0018	0.88	1775	48	1771	30	1766	31	100.5
11	TK28-1-9-1	mag. core	3155	113257	0.3005	0.0122	4.3305	0.2042	0.1045	0.0025	0.86	1694	61	1699	39	1706	44	99.3
12	TK28-1-11-1	mag. core	804	34764	0.2874	0.0092	4.0256	0.1584	0.1016	0.0023	0.81	1628	46	1639	32	1654	42	98.5
13	TK28-1-11-2	mag. core	1111	7867	0.2990	0.0116	4.2757	0.2009	0.1037	0.0028	0.82	1686	57	1689	39	1692	49	99.7
14	TK28-1-12-1	mag. core	1808	11822	0.3121	0.0135	4.5814	0.2281	0.1065	0.0026	0.87	1751	67	1746	42	1740	45	100.6
15	TK28-1-13-2	mag. core	2402	33571	0.3032	0.0049	4.4007	0.0986	0.1053	0.0016	0.72	1707	24	1712	19	1719	29	99.3
16	TK28-1-2-4	meta. ovrgrth.	676	6093	0.3030	0.0125	4.3884	0.2106	0.1050	0.0026	0.86	1706	62	1710	40	1715	45	99.5
17	TK28-1-2-8	meta. ovrgrth.	2476	122149	0.3075	0.0098	4.4319	0.1709	0.1045	0.0023	0.82	1728	48	1718	32	1706	40	101.3
18	TK28-1-3-4	meta. ovrgrth.	549	22277	0.3029	0.0191	4.3693	0.3138	0.1046	0.0036	0.88	1706	94	1707	59	1707	64	99.9
19	TK28-1-4-4	meta. ovrgrth.	317	13215	0.2923	0.0098	4.1260	0.1581	0.1024	0.0019	0.87	1653	49	1659	31	1668	35	99.1
20	TK28-1-4-5	meta. ovrgrth.	299	2862	0.3010	0.0099	4.3109	0.1721	0.1039	0.0024	0.82	1696	49	1695	33	1695	42	100.1
21	TK28-1-4-6	meta. ovrgrth.	563	46158	0.2983	0.0091	4.2742	0.1497	0.1039	0.0018	0.87	1683	45	1688	29	1696	32	99.2
22	TK28-1-5-4	meta. ovrgrth.	482	38733	0.3002	0.0144	4.2793	0.2558	0.1034	0.0037	0.80	1692	71	1689	49	1686	66	100.4
23	TK28-1-6-4	meta. ovrgrth.	411	23009	0.2991	0.0167	4.2243	0.2757	0.1024	0.0035	0.85	1687	83	1679	54	1669	63	101.1
24	TK28-1-8-6	meta. ovrgrth.	974	50979	0.2964	0.0062	4.1771	0.1004	0.1022	0.0012	0.87	1673	31	1670	20	1665	22	100.5
25	TK28-1-10-5	meta. ovrgrth.	617	36111	0.2994	0.0106	4.3007	0.1807	0.1042	0.0024	0.84	1688	53	1693	35	1700	42	99.3
26	TK28-1-10-4	meta. ovrgrth.	194	66097	0.2948	0.0132	4.1947	0.1997	0.1032	0.0017	0.94	1665	66	1673	39	1682	31	99.0
27	TK28-1-12-4	meta. ovrgrth.	860	61808	0.2942	0.0122	4.1824	0.1929	0.1031	0.0021	0.90	1663	61	1671	38	1681	37	98.9
28	TK28-1-13-1	meta. ovrgrth.	2233	173253	0.3037	0.0044	4.3332	0.0919	0.1035	0.0016	0.69	1710	22	1700	17	1687	28	101.3
29	TK28-1-2-7	meta. ovrgrth.	2056	25855	0.2850	0.0102	3.9498	0.1724	0.1005	0.0025	0.82	1616	51	1624	35	1634	46	98.9
30	TK28-1-5-6	meta. ovrgrth.	592	27999	0.2841	0.0065	3.9167	0.1097	0.1000	0.0016	0.82	1612	33	1617	23	1624	30	99.2

Con., degree of concordance; mag. core, magmatic core; meta. ovrgrth., metamorphic overgrowth; b.d.l. below detection limit

Table C.1: Continued

Spot	Grain	Texture	U conc. (ppm)	Radiogenic ratios				Ages (Ma)				Con.						
				$\frac{^{206}\text{Pb}}{^{204}\text{Pb}}$	$\frac{^{206}\text{Pb}}{^{238}\text{U}}$	$\pm 2\sigma$	$\frac{^{207}\text{Pb}}{^{206}\text{Pb}}$	$\pm 2\sigma$	$\frac{^{207}\text{Pb}}{^{235}\text{U}}$	$\pm 2\sigma$	$\frac{^{206}\text{Pb}}{^{238}\text{U}}$		$\pm 2\sigma$	$\frac{^{207}\text{Pb}}{^{206}\text{Pb}}$	$\pm 2\sigma$			
Charnockite TK28-1 (continued)																		
31	TK28-1 6-5	meta. ovrgrth.	193	9799	0.2775	0.0030	3.8107	0.0596	0.0996	0.0011	0.68	1579	15	1595	13	1617	21	97.7
32	TK28-1 8-4	meta. ovrgrth.	926	2167	0.2879	0.0123	3.9589	0.2111	0.0997	0.0032	0.80	1631	62	1626	43	1619	59	100.7
33	TK28-1 8-5	meta. ovrgrth.	227	b.d.l	0.2876	0.0101	3.9544	0.1744	0.0997	0.0027	0.80	1629	51	1625	36	1619	50	100.6
34	TK28-1 9-6	meta. ovrgrth.	721	20957	0.2900	0.0043	3.9948	0.0712	0.0999	0.0010	0.83	1641	21	1633	14	1623	19	101.1
35	TK28-1 11-5	meta. ovrgrth.	161	b.d.l	0.2884	0.0100	3.9989	0.1707	0.1006	0.0025	0.81	1634	50	1634	35	1635	46	99.9
36	TK28-1 11-6b	meta. ovrgrth.	257	11555	0.2783	0.0046	3.7719	0.0788	0.0983	0.0012	0.79	1583	23	1587	17	1592	24	99.4
37	TK28-1 2-5	meta. ovrgrth.	217	b.d.l	0.2674	0.0039	3.7113	0.0718	0.1006	0.0013	0.76	1528	20	1574	15	1636	24	93.4
38	TK28-1 2-6	meta. ovrgrth.	163	10999	0.2618	0.0060	3.5920	0.0973	0.0995	0.0015	0.84	1499	30	1548	22	1615	27	92.8
39	TK28-1 6-7	meta. ovrgrth.	252	8509	0.2505	0.0090	3.4990	0.1578	0.1013	0.0028	0.80	1441	46	1527	36	1648	50	87.5
40	TK28-1 8-6a	meta. ovrgrth.	147	20900	0.2526	0.0045	3.4749	0.0727	0.0998	0.0011	0.85	1452	23	1522	16	1620	21	89.6
41	TK28-1 9-4	meta. ovrgrth.	299	10271	0.2073	0.0085	2.8650	0.1335	0.1002	0.0022	0.88	1215	45	1373	35	1628	41	74.6
42	TK28-1 9-5	meta. ovrgrth.	151	23742	0.2397	0.0068	3.3070	0.1053	0.1001	0.0015	0.89	1385	35	1483	25	1625	27	85.2
43	TK28-1 11-6	meta. ovrgrth.	161	b.d.l	0.2635	0.0024	3.6479	0.0459	0.1004	0.0009	0.74	1508	12	1560	10	1631	16	92.4
44	TK28-1 11-6a	meta. ovrgrth.	110	b.d.l	0.2630	0.0054	3.6213	0.0863	0.0999	0.0012	0.86	1505	28	1554	19	1622	22	92.8

Con., degree of concordance; mag. core, magmatic core; meta. ovrgrth., metamorphic overgrowth; b.d.l, below detection limit

Table C.1: Continued

Spot	Grain	Texture	U conc. (ppm)	Radiogenic ratios				Ages (Ma)				Con.						
				$\frac{^{206}\text{Pb}}{^{204}\text{Pb}}$	$\frac{^{206}\text{Pb}}{^{238}\text{U}}$	$\pm 2\sigma$	$\frac{^{207}\text{Pb}}{^{206}\text{Pb}}$	$\frac{^{207}\text{Pb}}{^{235}\text{U}}$	$\pm 2\sigma$	$\frac{^{206}\text{Pb}}{^{238}\text{U}}$	$\pm 2\sigma$		$\frac{^{207}\text{Pb}}{^{206}\text{Pb}}$	$\pm 2\sigma$				
Charnockite TK39-4																		
1	TK39-4-1-1	mag. core	834	16349	0.3050	0.0157	4.4726	0.2597	0.1064	0.0028	0.89	1716	78	1726	48	1738	49	98.7
2	TK39-4-1-2	mag. core	338	26130	0.3106	0.0100	4.5970	0.1658	0.1073	0.0018	0.89	1744	49	1749	30	1755	30	99.4
3	TK39-4-4-1	mag. core	523	56659	0.3301	0.0202	5.1263	0.3492	0.1126	0.0034	0.90	1839	98	1840	58	1842	55	99.8
4	TK39-4-4-16	mag. core	1281	20192	0.2998	0.0145	4.3128	0.2258	0.1043	0.0021	0.92	1690	72	1696	43	1703	37	99.3
5	TK39-4-4-2	mag. core	511	8990	0.3135	0.0106	4.7296	0.1780	0.1094	0.0018	0.89	1758	52	1772	32	1790	31	98.2
6	TK39-4-5-4	mag. core	1061	41096	0.3000	0.0113	4.3616	0.1920	0.1054	0.0024	0.85	1691	56	1705	36	1722	42	98.2
7	TK39-4-5-1	mag. core	497	19491	0.2955	0.0137	4.1918	0.2375	0.1029	0.0033	0.82	1669	68	1672	46	1677	60	99.5
8	TK39-4-5-15	mag. core	1901	b.d.l	0.3020	0.0095	4.4690	0.1710	0.1073	0.0023	0.82	1701	47	1725	32	1755	40	96.9
9	TK39-4-5-16	mag. core	1921	105776	0.3189	0.0159	4.7320	0.2687	0.1076	0.0029	0.88	1784	78	1773	48	1759	49	101.4
10	TK39-4-6-2	mag. core	1251	417534	0.3216	0.0155	4.8811	0.2811	0.1101	0.0035	0.84	1798	76	1799	49	1801	57	99.8
11	TK39-4-6-3	mag. core	861	44128	0.3166	0.0068	4.6940	0.1288	0.1075	0.0018	0.78	1773	33	1766	23	1758	31	100.9
12	TK39-4-8-1	mag. core	3256	287412	0.3177	0.0157	4.7160	0.3050	0.1077	0.0045	0.77	1778	77	1770	54	1760	76	101.0
13	TK39-4-9-1	mag. core	570	7628	0.3044	0.0158	4.4438	0.2569	0.1059	0.0027	0.90	1713	78	1721	48	1730	46	99.0
14	TK39-4-10-2	mag. core	1512	117558	0.3174	0.0120	4.8047	0.2087	0.1098	0.0023	0.87	1777	59	1786	37	1796	38	98.9
15	TK39-4-14-1	mag. core	836	52092	0.3116	0.0074	4.5518	0.1266	0.1059	0.0015	0.86	1749	37	1740	23	1731	26	101.0
16	TK39-4-14-2	mag. core	930	10671	0.3144	0.0081	4.6747	0.1366	0.1078	0.0015	0.88	1762	40	1763	24	1763	25	100.0
17	TK39-4-14-15	mag. core	1049	7852	0.3130	0.0082	4.5929	0.1387	0.1064	0.0016	0.87	1755	40	1748	25	1739	27	100.9
18	TK39-4-2-3	mag. core	3032	b.d.l	0.3133	0.0092	4.6069	0.1617	0.1066	0.0020	0.84	1757	45	1751	29	1743	35	100.8
19	TK39-4-5-2	mag. core	589	6748	0.3161	0.0078	4.7076	0.1566	0.1080	0.0024	0.74	1770	38	1769	28	1766	41	100.2
20	TK39-4-5-3	mag. core	656	10353	0.2975	0.0104	4.3208	0.1857	0.1053	0.0026	0.81	1679	52	1697	35	1720	46	97.6
21	TK39-4-2-4	bright rims	572	34744	0.3052	0.0085	4.4501	0.1405	0.1057	0.0016	0.88	1717	42	1722	26	1727	28	99.4
22	TK39-4-7-5	bright rims	324	22635	0.3058	0.0142	4.4329	0.2348	0.1051	0.0027	0.88	1720	70	1719	44	1717	47	100.2
23	TK39-4-8-5	bright rims	699	40209	0.3031	0.0112	4.3322	0.1934	0.1037	0.0026	0.82	1707	55	1700	37	1691	47	100.9
24	TK39-4-8-6	bright rim	1291	953706	0.2847	0.0074	3.9325	0.1217	0.1002	0.0017	0.84	1615	37	1620	25	1627	31	99.3
25	TK39-4-9-4	bright rims	146	4353	0.2986	0.0113	4.3060	0.2003	0.1046	0.0028	0.82	1684	56	1695	38	1707	49	98.7
26	TK39-4-10-4	bright rim	91	2860	0.2816	0.0082	3.9006	0.1491	0.1005	0.0025	0.76	1599	41	1614	31	1633	46	98.0
27	TK39-4-10-5	bright rims	414	169301	0.2981	0.0158	4.2850	0.2580	0.1042	0.0030	0.88	1682	79	1690	50	1701	52	98.9
28	TK39-4-11-4	bright rims	462	22875	0.3059	0.0107	4.4188	0.1781	0.1048	0.0021	0.86	1720	53	1716	33	1710	37	100.6
29	TK39-4-11-5	bright rims	244	6005	0.2988	0.0122	4.2926	0.1911	0.1042	0.0018	0.92	1685	61	1692	37	1700	33	99.1

Con., degree of concordance; mag. core, magmatic core; meta.; b.d.l, below detection limit

Table C.1: Continued

Spot	Grain	Texture	U conc. (ppm)	U conc. Radiogenic ratios				Ages (Ma)				$\pm 2\sigma$	Con.					
				$\frac{^{206}\text{Pb}}{^{204}\text{Pb}}$	$\frac{^{206}\text{Pb}}{^{238}\text{U}}$	$\pm 2\sigma$	$\frac{^{207}\text{Pb}}{^{235}\text{U}}$	$\frac{^{207}\text{Pb}}{^{206}\text{Pb}}$	$\pm 2\sigma$	$\frac{^{206}\text{Pb}}{^{238}\text{U}}$	$\frac{^{207}\text{Pb}}{^{235}\text{U}}$			$\pm 2\sigma$	$\frac{^{207}\text{Pb}}{^{206}\text{Pb}}$			
Charnockite TK39-4 (continued)																		
30	TK39-4 1-5	mantle	425	25996	0.3089	0.0079	4.5224	0.1307	0.1062	0.0014	0.88	1735	39	1735	24	1735	25	100.0
31	TK39-4 4-6	bright rim	231	7319	0.3111	0.0047	4.5336	0.1079	0.1057	0.0019	0.64	1746	23	1737	20	1727	34	101.1
32	TK39-4 5-6	mantle	662	4833	0.3079	0.0063	4.4954	0.1235	0.1059	0.0019	0.74	1730	31	1730	23	1730	34	100.0
33	TK39-4 5-6a	mantle	671	7854	0.2957	0.0058	4.2092	0.1141	0.1032	0.0019	0.72	1670	29	1676	22	1683	35	99.2
34	TK39-4 7-6	bright rim	217	5649	0.2953	0.0056	4.1466	0.1085	0.1018	0.0018	0.72	1668	28	1664	21	1658	34	100.6
35	TK39-4 5-5	mantle	724	76950	0.2525	0.0107	3.5190	0.1752	0.1011	0.0026	0.85	1451	55	1532	39	1644	48	88.3
36	TK39-4 7-1	mag. core	1347	34683	0.2940	0.0205	4.2592	0.3692	0.1051	0.0054	0.80	1661	102	1686	71	1716	95	96.8
37	TK39-4 9-5	bright rim	78	150891	0.2621	0.0038	3.6909	0.0785	0.1021	0.0016	0.68	1501	19	1569	17	1663	29	90.2
38	TK39-4 11-5	bright rim	77	2307	0.2868	0.0095	4.0823	0.1786	0.1033	0.0029	0.76	1625	48	1651	36	1683	53	96.5
39	TK39-4 11-5a	bright rims	93	4272	0.2630	0.0079	3.7120	0.1274	0.1024	0.0017	0.87	1505	40	1574	27	1668	31	90.2
40	TK39-4 15-5	mag. core	411	2665	0.3021	0.0120	4.4770	0.2001	0.1075	0.0022	0.89	1702	59	1727	37	1757	37	96.8
41	TK39-4 2-5	bright rim	906	41588	0.2469	0.0080	3.4675	0.1243	0.1019	0.0015	0.91	1422	42	1520	28	1659	28	85.7
42	TK39-4 4-3	mag. core	913	7952	0.2329	0.0043	3.4306	0.0795	0.1068	0.0015	0.80	1350	23	1511	18	1746	25	77.3

Con., degree of concordance; mag. core, magmatic core; meta.; b.d.l., below detection limit

Table C.1: Continued

Spot	Grain	Texture	U conc. (ppm)		Radiogenic ratios						Ages (Ma)				Con.			
			²⁰⁶ Pb/ ²⁰⁴ Pb	²⁰⁶ Pb/ ²³⁸ U	²⁰⁷ Pb/ ²⁰⁶ Pb	^{±2σ}	²⁰⁷ Pb/ ²³⁵ U	^{±2σ}	²⁰⁷ Pb/ ²⁰⁶ Pb	^{±2σ}	²⁰⁶ Pb/ ²³⁸ U	^{±2σ}	²⁰⁷ Pb/ ²³⁵ U	^{±2σ}		²⁰⁷ Pb/ ²⁰⁶ Pb	^{±2σ}	
Enderbite TK39-3																		
1	TK39-3 1-1	mag. core	199	643220	0.2735	0.0065	3.6722	0.1152	0.0974	0.0020	0.75	1558	33	1565	25	1575	39	98.9
2	TK39-3 1-2	mag. core	155	1208418	0.2835	0.0031	3.8674	0.0780	0.0989	0.0017	0.54	1609	16	1607	16	1604	32	100.3
3	TK39-3 1-3	mag. core	114	b.d.l	0.2788	0.0041	3.7982	0.0905	0.0988	0.0019	0.61	1585	21	1592	19	1602	35	99.0
4	TK39-3 2-1	mag. core	328	104425	0.2782	0.0051	3.7732	0.0994	0.0984	0.0019	0.70	1582	26	1587	21	1594	35	99.3
5	TK39-3 2-2	mag. core	310	17440	0.2796	0.0034	3.8085	0.0816	0.0988	0.0017	0.57	1589	17	1595	17	1601	33	99.2
6	TK39-3 3-1	mag. core	312	11449	0.2867	0.0041	3.9305	0.0838	0.0994	0.0016	0.67	1625	20	1620	17	1613	30	100.7
7	TK39-3 5-1	mag. core	232	12907	0.2718	0.0052	3.6471	0.0997	0.0973	0.0019	0.70	1550	26	1560	22	1574	37	98.5
8	TK39-3 5-2	mag. core	218	b.d.l	0.2763	0.0059	3.7043	0.0972	0.0972	0.0015	0.81	1573	30	1572	21	1571	29	100.1
9	TK39-3 6-2	mag. core	266	31977	0.2839	0.0038	3.8857	0.0873	0.0993	0.0018	0.59	1611	19	1611	18	1611	34	100.0
10	TK39-3 8-1	mag. core	166	11636	0.2835	0.0042	3.8766	0.0743	0.0992	0.0012	0.77	1609	21	1609	15	1608	23	100.0
11	TK39-3 8-2	mag. core	178	31632	0.2885	0.0039	3.9650	0.0832	0.0997	0.0016	0.65	1634	20	1627	17	1618	30	101.0
12	TK39-3 10-1	mag. core	203	11332	0.2855	0.0039	3.9072	0.0749	0.0993	0.0013	0.72	1619	20	1615	16	1610	25	100.5
13	TK39-3 10-2	mag. core	253	37653	0.2768	0.0036	3.7537	0.0671	0.0984	0.0012	0.73	1575	18	1583	14	1593	23	98.8
14	TK39-3 12-2	mag. core	176	5811	0.2782	0.0042	3.7893	0.0866	0.0988	0.0017	0.66	1582	21	1590	18	1602	32	98.8
15	TK39-3 14-1	mag. core	245	51946	0.2805	0.0060	3.8040	0.0970	0.0983	0.0014	0.84	1594	30	1594	21	1593	26	100.1
16	TK39-3 1-4	mag. core	192	99849	0.2712	0.0031	3.6355	0.0767	0.0972	0.0017	0.55	1547	16	1557	17	1572	33	98.4
17	TK39-3 1-5	recrys. domains	208	b.d.l	0.2854	0.0042	3.9009	0.0912	0.0991	0.0018	0.63	1618	21	1614	19	1608	34	100.6
18	TK39-3 3-5	recrys. domains	123	58308	0.2814	0.0039	3.8464	0.0816	0.0991	0.0016	0.65	1599	20	1603	17	1608	30	99.4
19	TK39-3 4-4	recrys. domains	183	3867	0.2821	0.0035	3.8093	0.0802	0.0979	0.0017	0.59	1602	18	1595	17	1585	32	101.0
20	TK39-3 4-5	recrys. domains	288	6598	0.2731	0.0044	3.6520	0.0782	0.0970	0.0014	0.76	1557	22	1561	17	1567	26	99.3
21	TK39-3 5-4	recrys. domains	254	32971	0.2823	0.0035	3.8483	0.0735	0.0989	0.0015	0.64	1603	17	1603	15	1603	27	100.0
22	TK39-3 6-4	recrys. domains	282	b.d.l	0.2817	0.0029	3.8420	0.0538	0.0989	0.0009	0.74	1600	15	1602	11	1604	18	99.7
23	TK39-3 7-5	sec. zoned	280	12473	0.2797	0.0026	3.7469	0.0520	0.0971	0.0010	0.67	1590	13	1581	11	1570	19	101.3
24	TK39-3 9-6	sec. zoned	339	26547	0.2771	0.0058	3.7966	0.0981	0.0994	0.0015	0.81	1577	29	1592	21	1612	28	97.8
25	TK39-3 9-5	sec. zoned	307	9985	0.2902	0.0037	4.0021	0.0691	0.1000	0.0012	0.74	1642	18	1635	14	1625	22	101.1
26	TK39-3 9-4	sec. zoned	454	b.d.l	0.2782	0.0051	3.7693	0.0870	0.0983	0.0014	0.79	1582	26	1586	19	1591	26	99.4
27	TK39-3 10-4	recrys. domains	220	36490	0.2827	0.0032	3.8330	0.0633	0.0983	0.0012	0.69	1605	16	1600	13	1593	22	100.8
28	TK39-3 10-5	recrys. domains	213	b.d.l	0.2865	0.0032	3.9205	0.0648	0.0992	0.0012	0.68	1624	16	1618	13	1610	23	100.9
29	TK39-3 11-4	recrys. domains	344	b.d.l	0.2803	0.0029	3.8032	0.0562	0.0984	0.0010	0.70	1593	15	1593	12	1594	20	99.9
30	TK39-3 12-4	recrys. domains	171	b.d.l	0.2729	0.0038	3.6541	0.0774	0.0971	0.0016	0.65	1555	19	1561	17	1569	30	99.1
31	TK39-3 13-4	sec. zoned	377	b.d.l	0.2823	0.0064	3.8328	0.0999	0.0985	0.0013	0.87	1603	32	1600	21	1595	24	100.5
32	TK39-3 13-5	sec. zoned	353	14269	0.2821	0.0070	3.8629	0.1158	0.0993	0.0017	0.83	1602	35	1606	24	1612	31	99.4
33	TK39-3 14-4	sec. zoned	307	b.d.l	0.2792	0.0056	3.8172	0.0905	0.0991	0.0012	0.85	1587	28	1596	19	1608	23	98.7
34	TK39-3 14-5	sec. zoned	237	28192	0.2846	0.0059	3.8882	0.0952	0.0991	0.0013	0.85	1614	30	1611	20	1607	24	100.5
35	TK39-3 2-4	recrys. domains	168	4882	0.2713	0.0036	3.7391	0.0877	0.1000	0.0019	0.57	1547	18	1580	19	1623	36	95.3
36	TK39-3 8-4	recrys. domains	225	7386	0.2633	0.0034	3.5447	0.0606	0.0977	0.0011	0.75	1506	17	1537	14	1580	21	95.4

Con., degree of concordance; mag. core, magmatic core; recrys. domains, recrystallized domains; sec. zoned, sector zoned; b.d.l, below detection limit

Table C.1: Continued

Spot	Grain	Texture	U conc. (ppm)	Radiogenic ratios				Ages (Ma)				$\pm 2\sigma$	Con.					
				$\frac{^{206}\text{Pb}}{^{204}\text{Pb}}$	$\frac{^{206}\text{Pb}}{^{238}\text{U}}$	$\pm 2\sigma$	$\frac{^{207}\text{Pb}}{^{206}\text{Pb}}$	$\frac{^{207}\text{Pb}}{^{235}\text{U}}$	$\pm 2\sigma$	$\frac{^{206}\text{Pb}}{^{238}\text{U}}$	$\pm 2\sigma$			$\frac{^{207}\text{Pb}}{^{206}\text{Pb}}$	$\pm 2\sigma$			
<i>Orthogneiss TK66-1 (Vinjamuru domain)</i>																		
1	TK66-1 16-1	mag. core	115	37900	0.3128	0.0051	4.6589	0.0943	0.1080	0.0013	0.80	1754	25	1760	17	1766	22	99.3
2	TK66-1 11-1	mag. core	117	9859	0.3171	0.0046	4.7752	0.0992	0.1092	0.0016	0.71	1776	23	1781	17	1786	27	99.4
3	TK66-1 11-16	mag. core	175	10826	0.3166	0.0087	4.7661	0.1468	0.1092	0.0015	0.89	1773	43	1779	26	1786	25	99.3
4	TK66-1 2-1	mag. core	128	b.d.1	0.3203	0.0051	4.8045	0.0961	0.1088	0.0013	0.79	1791	25	1786	17	1779	22	100.7
5	TK66-1 3-2	mag. core	191	b.d.1	0.3155	0.0078	4.7677	0.1332	0.1096	0.0014	0.89	1768	38	1779	23	1793	23	98.6
6	TK66-1 4-1	mag. core	135	32324	0.3109	0.0047	4.5539	0.0843	0.1062	0.0011	0.82	1745	23	1741	15	1736	20	100.5
7	TK66-1 5-1	mag. core	121	74667	0.3123	0.0064	4.7189	0.1205	0.1096	0.0017	0.80	1752	31	1771	21	1793	28	97.7
8	TK66-1 6-1	mag. core	158	4607	0.3186	0.0058	4.8401	0.1029	0.1102	0.0012	0.85	1783	28	1792	18	1803	20	98.9
9	TK66-1 7-2	mag. core	146	16027	0.3180	0.0040	4.7728	0.0816	0.1089	0.0013	0.74	1780	20	1780	14	1781	21	100.0
10	TK66-1 8-1	mag. core	150	b.d.1	0.3166	0.0049	4.7359	0.1164	0.1085	0.0021	0.63	1773	24	1774	21	1774	35	99.9
11	TK66-1 11-1	mag. core	127	19255	0.3150	0.0073	4.6670	0.1433	0.1075	0.0022	0.75	1765	36	1761	26	1757	37	100.5
12	TK66-1 12-1	mag. core	121	8772	0.3168	0.0084	4.7629	0.1567	0.1091	0.0021	0.81	1774	41	1778	28	1784	36	99.4
13	TK66-1 12-2	mag. core	156	5207	0.3172	0.0072	4.7638	0.1443	0.1089	0.0022	0.75	1776	35	1779	25	1781	37	99.7
14	TK66-1 14-4	mag. mantle	114	10490	0.3165	0.0045	4.7648	0.1006	0.1092	0.0017	0.67	1773	22	1779	18	1786	29	99.3
15	TK66-1 14-5	mag. mantle	169	8556	0.3161	0.0079	4.8028	0.1544	0.1102	0.0022	0.78	1770	39	1785	27	1803	37	98.2
16	TK66-1 15-4	mag. mantle	114	12003	0.3192	0.0051	4.7943	0.0921	0.1089	0.0011	0.84	1786	25	1784	16	1782	19	100.2
17	TK66-1 3-4	mag. mantle	128	12815	0.3201	0.0033	4.8278	0.0709	0.1094	0.0011	0.70	1790	16	1790	12	1789	19	100.1
18	TK66-1 8-4	mag. mantle	111	28720	0.3262	0.0074	4.9755	0.1706	0.1106	0.0028	0.66	1820	36	1815	29	1810	47	100.6
19	TK66-1 8-5	mag. mantle	97	b.d.1	0.3220	0.0055	4.8432	0.1192	0.1091	0.0019	0.69	1799	27	1792	21	1785	32	100.8
20	TK66-1 9-4	mag. mantle	136	b.d.1	0.3153	0.0064	4.7269	0.1269	0.1087	0.0019	0.76	1767	32	1772	23	1778	32	99.4
21	TK66-1 10-4	mag. mantle	113	5146	0.3172	0.0062	4.7112	0.1302	0.1077	0.0021	0.71	1776	30	1769	23	1761	36	100.8
22	TK66-1 10-5	mag. mantle	101	11154	0.3193	0.0068	4.8013	0.1390	0.1091	0.0021	0.73	1786	33	1785	24	1784	36	100.1
23	TK66-1 10-6	mag. mantle	124	22893	0.3133	0.0048	4.6762	0.1138	0.1082	0.0021	0.62	1757	23	1763	20	1770	35	99.3
24	TK66-1 13-4	mag. mantle	163	10691	0.3098	0.0047	4.6363	0.1152	0.1085	0.0021	0.61	1740	23	1756	21	1775	36	98.0
25	TK66-1 2-15	inhr. core	290	b.d.1	0.3605	0.0083	6.3582	0.2078	0.1279	0.0030	0.70	1984	39	2027	29	2070	41	95.9
26	TK66-1 5-15	inhr. core	558	67126	0.4498	0.0080	9.8052	0.2058	0.1581	0.0017	0.85	2394	36	2417	19	2435	19	98.3
27	TK66-1 6-15	inhr. core	1162	9891	0.1560	0.0106	3.0328	0.2178	0.1410	0.0034	0.94	934	59	1416	55	2240	41	41.7
28	TK66-1 7-1	inhr. core	225	18899	0.3244	0.0079	5.0109	0.1330	0.1120	0.0012	0.91	1811	38	1821	22	1833	20	98.8
29	TK66-1 7-15	inhr. core	739	b.d.1	0.3312	0.0070	5.2186	0.1632	0.1143	0.0026	0.68	1844	34	1856	27	1868	41	98.7
30	TK66-1 11-15	inhr. core	803	3913	0.2936	0.0052	4.6215	0.1232	0.1142	0.0023	0.67	1659	26	1753	22	1867	36	88.9

Con., degree of concordance; mag. core, magmatic core; mag. mantle, magmatic mantle; inhr. core, inherited core; b.d.1, below detection limit

Table C.1: Continued

Spot	Grain	Texture	U conc. (ppm)	Radiogenic ratios				Ages (Ma)				Con.						
				$\frac{^{206}\text{Pb}}{^{204}\text{Pb}}$	$\frac{^{206}\text{Pb}}{^{238}\text{U}}$	$\frac{^{207}\text{Pb}}{^{235}\text{U}}$	$\frac{^{207}\text{Pb}}{^{206}\text{Pb}}$	$\frac{^{206}\text{Pb}}{^{238}\text{U}}$	$\frac{^{207}\text{Pb}}{^{235}\text{U}}$	$\frac{^{207}\text{Pb}}{^{206}\text{Pb}}$	$\pm 2\sigma$							
Orthogneiss TK66-1 (continued)																		
31	TK66-1 12-15	inhr. core	329	7596	0.3095	0.0053	5.0394	0.1258	0.1181	0.0021	0.69	1738	26	1826	21	1927	32	90.2
32	TK66-1 16-16	inhr. core	776	6111	0.2594	0.0059	4.5261	0.1193	0.1266	0.0017	0.87	1487	30	1736	22	2051	23	72.5
33	TK66-1 16-15	inhr. core	600	4192	0.1841	0.0029	3.1613	0.0659	0.1246	0.0017	0.75	1089	16	1448	16	2023	24	53.8
34	TK66-1 17-1	inhr. core	442	7331	0.4082	0.0061	7.8628	0.1568	0.1397	0.0019	0.75	2207	28	2215	18	2223	23	99.2
35	TK66-1 17-15	inhr. core	913	6560	0.3865	0.0049	7.6480	0.1242	0.1435	0.0014	0.78	2106	23	2191	15	2270	17	92.8
36	TK66-1 17-16	inhr. core	675	14639	0.4243	0.0108	9.1261	0.2699	0.1560	0.0024	0.86	2280	49	2351	27	2413	26	94.5
37	TK66-1 1-15	mag. core	524	14929	0.3016	0.0062	4.5032	0.1163	0.1083	0.0017	0.80	1699	31	1732	21	1771	28	95.9
38	TK66-1 4-15	mag. core	449	25265	0.2986	0.0056	4.4470	0.0951	0.1080	0.0011	0.88	1684	28	1721	18	1766	19	95.3
39	TK66-1 5-2	mag. core	123	b.d.1	0.2726	0.0042	4.1235	0.0834	0.1097	0.0014	0.76	1554	21	1659	17	1795	24	86.6
40	TK66-1 8-2	mag. core	173	b.d.1	0.3450	0.0075	5.0362	0.1412	0.1059	0.0019	0.77	1911	36	1825	24	1729	33	110.5
41	TK66-1 9-5	mag. mantle	62	7441	0.3230	0.0055	4.8015	0.1532	0.1078	0.0029	0.53	1804	27	1785	27	1763	49	102.5

Con., degree of concordance; mag. core, magmatic core; mag. mantle, magmatic mantle; inhr. core, inherited core; b.d.1, below detection limit

Publications related to this thesis

Papers

Sarkar, T. and Schenk, V. (in review). Two-stage granulite formation in a Proterozoic island arc (Ongole domain of the Eastern Ghats Belt, India): Part 1. Petrology and pressure-temperature evolution. Submitted to Precambrian Research.

Sarkar, T., Schenk, V., Appel, P., Berndt, J. and Sengupta, P. (in review). Two-stage granulite formation in a Proterozoic island arc (Ongole domain of the Eastern Ghats Belt, India): Part 2. LA-ICP-MS zircon dating and texturally controlled *in-situ* monazite dating. Submitted to Precambrian Research.

Sarkar, T., Schenk, V. and Berndt, J. (in review). Formation and evolution of a Proterozoic continental arc: geochemical and geochronological constraints from meta-igneous rocks of the Ongole domain, Eastern Ghats belt, India. Submitted to Contributions to Mineralogy and petrology.

Conference abstracts

Sarkar, T., Schenk, V., Berndt, J. (2013). Linking petrology with monazite and zircon geochronology: The polymetamorphic Ongole domain, Eastern Ghats Belt, India. Modern Geological and Geophysical Methods and their Applications, Kolkata, India. Abstracts volume, p. 15.

Sarkar, T., Schenk, V., Berndt, J. (2013). Linking petrology with monazite and zircon geochronology: The polymetamorphic Ongole domain, Eastern Ghats Belt, India. DMG 2013. Geofluids: Lubricants of the Dynamic Earth, Tübingen. Abstracts volume, p. 257.

Sarkar, T., Schenk, V. (2013). Correlating petrographic textures with monazite and zircon ages: The granulite-facies Ongole domain, Eastern Ghats Belt, India. Granulites and Granulites 2013, Hyderabad, India. In: Fitzsimons, I.C.W. and Clark, C. (eds.) Programs and Abstracts, p. 54.

Sarkar, T., and Schenk, V. (2012). The granulite-facies Ongole domain of the Eastern Ghats Belt, India – A Proterozoic island arc? European Mineralogical Conference (EMC) 2012, Frankfurt, Germany. Abstracts volume, p. 311.

Sarkar, T., Schenk, V. (2012). The granulite-facies Ongole domain of the Eastern Ghats Belt, India – A Proterozoic island arc? Tectonics, Structural Geology and Geology of Crystalline Rocks (TSK) 14, Kiel, Germany. Program and Abstracts, p. 87.

Acknowledgements

First and foremost I would like to express my sincere gratitude to my supervisor Prof. Dr. Volker Schenk. His effective guidance through my PhD research, his patience, motivation and constructive criticism has been the backbone in achieving the goal. The joy and enthusiasm he has for research has made my PhD experience productive and stimulating. Apart from the academic relationship we shared a close friendship, which I deeply cherish.

I owe my co-supervisor Prof. Dr. Astrid Holzheid a profound gratefulness for her thoughtful discussions, enthusiastic participations in seminars and constructive recommendations. Her support and good advice was invaluable in completing the thesis.

I would like to acknowledge the Institute for Geosciences at the University of Kiel for providing me an opportunity to pursue my doctoral studies in Germany where I have made some fascinating experiences of my life. The library and the laboratory facilities at the university and the institute have been indispensable.

I am greatly indebted to Prof. Dr. Michael Raith and Prof. Dr. Pulak Sengupta for introducing me to the study area in the Ongole domain of the Eastern Ghats Belt. Detailed and insightful discussions with them at any time of need helped to define the project in a better way. Prepared thin sections and some unpublished data provided by Prof. Raith was very helpful and worth a mention.

Plenty of thanks to Prof. Dr. Pulak Sengupta, Dr. Sanjoy Sanyal and Dr. Uttam Kumar Bhui for their guidance during the field trip in 2010 and 2011. It was much easier with them to locate interesting and useful outcrops. Thanks to Shreya Karmakar for obtaining all geological maps from the Geological Survey of India and her assistance during the field trip.

The contributions of Dr. Peter Appel during monazite dating, discussion of results and the guidance of using the electron microprobe analyzer (EPMA) are deeply appreciated. I am grateful to Dr. Peter Raase for his help in thin section microscopy and feldspar thermometry and Dr. Sönke Brandt for judicious petrological discussions with him. I highly appreciate the thorough scientific discussions with Prof. Dr. Romain Bousquet especially in the field of pseudosection and thermodynamic modeling and for his support and cooperation. Very special thanks to Shreya Karmakar for proof-reading all the chapters and giving constructive comments.

My doctoral colleagues (Emmanuel Kazimoto, Shreya Karmakar, Julia Bial, Dr. Rauno Baese, Rashid Benaouda and Marko Gellissen) have always been friendly and cooperative. I was greatly benefitted from academic discussions and personal conversations with them and the social activities we did together always rejuvenated me. Thanks to Rauno Baese for his instructions on sample preparations for XRF analysis and Daniel Wiemer for showing the method of zircon separation.

The contributions of the technical staffs of the Petrology section were of notable importance. Ms. Barbara Mader was extremely helpful in the EPMA lab and Mr. Andreas Fehler efficiently produced all the high-quality thin sections.

Thanks to Dr. Heidi Höfer at the University of Frankfurt for her help in obtaining cathodoluminescence images of zircon grains using the Scanning Electron Microscope. I am grateful to Dr. Jasper Berndt-Gerdes for his help and cooperation in the LA-ICP-MS lab and Dr. Martina Menneken for helping me obtaining Raman Spectroscopic measurements at the University of Münster.

I immensely thank Prof. Dr. Jörg Erzinger for generously extending the geochemical lab facilities at GeoForschungZentrum in Potsdam and lab assistants Sabine Tonn and Heike Rothe for their help with geochemical analysis. Discussions with Dr. Elis Hoffmann were very helpful in interpretation of geochemical data in Chapter 4.

I am greatly indebted to Ms. Barbara Mader and Ms. Maike Zakrotzky for their valuable social and technical assistance during my stay in Kiel at any time of need and helping me to integrate into the German culture.

I thank the other members of the Institute for Geosciences – Dr. Petra Herms, late Prof. Dr. Manfred Schliestedt, and Dr. Oliver Beermann for their help and cooperation.

A heartfelt thanks to all my friends (Shreya, Emmanuel, Julia B., Julia I., Julia L., Ronny, Sandra, Rauno, Daniel, Amrei, Marlene, Alik, Rahul, Vinoth, Priyadarshi, Sujoy, Mahasweta, Sajid and others) for always being there and providing a rejuvenating social ambiance during my stay in Kiel, making it a home away from home.

Last but not the least, a very precious thanks to all my family members, especially my parents for their immense support, inspiration and motivation with which I have felt strong and focused enough to achieve my goal. I take this opportunity to thank my beloved late sister who had always inspired me set appropriate goals, believe in myself and work hard to achieve the goal. She would have been the happiest person to witness this day.

Curriculum vitae

Personal particulars

Name	Tapabrato Sarkar
Address	Ludewig-Meyn Strasse 10 Kiel University 24118 Kiel, Germany
E-mail	ts@min.uni-kiel.de / tapabrato@gmail.com
Date of birth	7 th June 1987
Nationality	Indian

Education profile

Julien Day School

2003-2005 Indian School Certificate
(Higher Secondary)

Jadavpur University, Kolkata, India.

2005-2008 B.Sc., Geological Sciences

2008-2010 M.Sc., Applied Geology

University of Kiel, Germany

2010 – Present PhD research (Mineralogy)

Erklärung

Hiermit erkläre ich, Tapabrato Sarkar, daß die vorgelegte Abhandlung, abgesehen von der Beratung durch meine akademischen Lehrer, nach Inhalt und Form meine Arbeit ist und ausschließlich unter Verwendung der angegebenen Hilfsmittel entstanden ist. Ferner erkläre ich, daß ich weder diese noch eine ähnliche Arbeit an anderer Stelle im Rahmen eines Prüfungsverfahrens vorgelegt habe.

Kiel, June 2014

Tapabrato Sarkar